STRUCTURE, RHEOLOGY AND APPLICATIONS OF THERMALLY-GELLING NANOEMULSIONS

by

Li-Chiun Cheng

B.S. in Chemical Engineering, National Taiwan University

M.S. in Chemical Engineering Practice, Massachusetts Institute of Technology

Submitted to the Department of Chemical Engineering

in partial fulfillment of the requirements of the degree of

Doctor of Philosophy in Chemical Engineering

at the

MASSACHUSETTS INSTITUTE OF TECHNOLOGY

May ~~February~~ 2020

Author_____

Department of Chemical Engineering

February 10th, 2020

Certified by_____

Patrick S. Doyle

Robert T. Haslam (1911) Professor of Chemical Engineering

Thesis Supervisor

Accepted by_____

Patrick S. Doyle

Robert T. Haslam (1911) Professor of Chemical Engineering

Chairman, Department Committee on Graduate Students

1

STRUCTURE, RHEOLOGY AND APPLICATIONS OF THERMALLY-GELLING NANOEMULSIONS

by

Li-Chiun Cheng

B.S. in Chemical Engineering, National Taiwan University

M.S. in Chemical Engineering Practice, Massachusetts Institute of Technology

Submitted to the Department of Chemical Engineering
in partial fulfillment of the requirements for the degree of

Doctoral Philosophy in Chemical Engineering

at the

MASSACHUSETTS INSTITUTE OF TECHNOLOGY

February 2020

Author ....

Department of Chemical Engineering
January 10, 2020

Certified by ....

Patrick S. Doyle
Robert T. Haslam (1911) Professor of Chemical Engineering
Thesis Supervisor

Accepted by ....

Patrick S. Doyle
Robert T. Haslam (1911) Professor of Chemical Engineering
Chairman, Department Committee on Graduate Students

Structure, Rheology and Applications of Thermally-Gelling Nanoemulsions

by

Li-Chiun Cheng

Submitted to the Department of Chemical Engineering on February 10, 2020

in partial fulfillment of the requirements for the degree of

Doctor of Philosophy in Chemical Engineering

ABSTRACT

Colloidal gelation is an effective tool to engineer material properties. Nanoemulsions, liquid-liquid dispersions where the droplet size is on the order of 100 nm, have become an emerging model system for studying aspects of colloidal gel materials. In conventional approaches, the gelation of nanoemulsions relies on the addition of another component into the suspension. However, such strategies require adding or removing components, which can be challenging for material processing, manipulation and studies of the colloidal gel physics. Therefore, a simple external stimulus such as temperature that can induce gelation of the nanoemulsion is highly desired.

This thesis focuses on the design and property-structure relationship of novel nanoemulsion dispersions whose gelation is responsive to temperature. Armed with a molecular-scale understanding of the thermally-gelling nanoemulsion system, we design a gelling platform that can accommodate a wide range of colloidal formulations and gelling nanoemulsions that are responsive to different external stimuli such as pH and ionic strength. Moreover, by using the resulting thermally-gelling nanoemulsions, we study fundamental aspects of colloidal gel physics and develop applications for practical use.

First, we design a gelling colloidal system whose inter-droplet interaction is modulated through thermally-responsive repulsions. By including amphiphilic oligomers in colloidal suspensions, the ionic surfactants on the colloids are replaced by the nonionic oligomer surfactants at elevated temperatures, leading to a decrease in the electrostatic repulsion. The mechanism is examined by carefully characterizing the colloids, and subsequently allowing the construction of interparticle potentials to capture the material behaviors. With the thermally-triggered surfactant displacement, the dispersion assembles into a macroporous viscoelastic network, and the gelling mechanism is robust over a wide range of compositions, colloid sizes and component chemistries.

Second, with the molecular understanding of the thermally-gelling nanoemulsion system, nanoemulsions that are responsive to different stimuli are designed and studied. In one project, we report a gelling nanoemulsion system in which the material properties are responsive to changes in temperature and pH. The nanoemulsion is stabilized using a weak acid surfactant containing a poly(ethylene glycol), PEG, segment and a carboxyl group. We show that the interplay of the dissociated carboxyl group and the PEG segments greatly affects the nanoemulsion properties and gives rise to the thermally and pH-responsive gelation of the system. In the other project, we revisit

the original nanoemulsion that the Doyle group designed and investigate the previously-overlooked depletion interactions and screened electrostatic repulsions. We take advantage of these interactions and study the material behaviors by sequentially applying two different gelation routes – first screening the electrostatic repulsion and then inducing the droplet bridging. The results show a non-intuitive trend in the material, and we show that the screening of electrostatic repulsions at room temperature in the first step has a considerable influence on the nanoemulsion microstructures and the associated rheological properties.

Third, using thermally-gelling nanoemulsions, we investigate the effect of processing history on the material properties of colloidal gels. We provide new experimental evidence of path-dependent rheology and associated microstructures in colloidal gel systems. Moreover, we also show that material properties can be beyond the limit set by direct quenching and the gel strength can be greatly enhanced. On the other hand, we perform multiple particle tracking (MPT) to probe the nanoemulsion gels at a micrometer scale. We show that, by tailoring the surface chemistry of MPT probe beads, different domains of the gel microstructures are independently probed. The transportation modes of particles and the gel strength at different length scale are obtained.

Finally, the complex structure from the self-assembled nanoemulsions is utilized for practical applications. We show that we can synthesize hierarchical hydrogels using 3D-printing. By properly engineering the nanoemulsions, the gel serves as ink with good shear-thinning behavior and remarkable structural recovery. The bottom-up route via droplet self-assembly provides various internal structures, while the top-down route during printing shapes the hydrogel geometry. The resulting hydrogels can be used in applications such as membranes and tissue engineering.

Thesis Supervisor: Patrick S. Doyle

Title: Robert T. Haslam (1911) Professor of Chemical Engineering

Acknowledgement

I am grateful to so many people for the past couple of years. It has been challenging but fulfilling, but nothing would have been done without these people. First and foremost, I want to thank my advisor Prof. Patrick S. Doyle. I joined this group with basically zero knowledge and experience in research, but Prof. Doyle has been very patient and supportive teaching me the right way to be a good researcher. He taught me how to analyze the problems, how to design the experiments, how to treat the results and how to interpret physical meanings behind the data. I am always able to learn new things and get motivation from him in our meetings. He always encourages me to work on the projects that I am really excited about and allows me to do the things I am enthusiastic about, even though it means sometimes I change my directions two times in a week. Moreover, he has been very helpful when I am struggling with all kinds of different things. I am always able to sit down and talk to him personally, and he always listens and gives me his advice and help with patience. I am grateful and very lucky to have him as my advisor.

I would also like to thank my committee members Prof. James W. Swan and Prof. Gareth H. McKinley. Prof. Swan always helps me to think outside the experimental box and makes my research with more perspectives. For the past two years, I also had chances working with him on a few projects and it has been a great experience to learn more things from him. Prof. McKinley teaches me how to carefully interpret my data and to design experiments using rheometers. He always gives me useful thoughts with his creativity, and always lets me know the appropriate way to present my results. Committee meetings with Prof. Swan and Prof. McKinley (and of course Prof. Doyle) are not easy, but I always feel I become a better researcher after talking to them.

The next person I always cannot appreciate enough is Prof. Lilian C. Hsiao. Lilian has been not only a perfect mentor but also a very good friend since the day I stepped into the lab. Lilian has been teaching me everything about colloidal gels and nanoemulsions, and every other detail I should take care of in research and academia. Even though she left MIT and became a professor, Lilian always helps me when I have questions any time when I need her help and we can always have random conversations outside research. When I am in the conferences, she always takes me to meet other professors, which is difficult for people, especially junior graduate students, when they just attend these scientific conferences. I am truly grateful to have her as my mentor when I begin the Ph.D., and now as a good friend after school.

I also want to thank Doyle group members and people I have worked with at MIT. Special thanks to Dr. Lynna Chen, Dr. Jae Jung Kim, Dr. Ankur Gupta and Dr. Sarah Shapiro who always help me and listen to me with their kindness and patience every time I encounter difficulties. I would like to thank (soon-to-be-Dr.) Beatrice Soh for being a wonderful labmate who I can share everything, mostly complaints about everything, with her. I also want to thank people that I have worked with, Dr. Zachary Sherman, Dr. Doug Godfrin, Liang-Hsun Chen, Signe Lin Kuei Vehusheia, Dr. Paul Bisso, Dr. Carlos A. P. Siepermann, Dr. Nitesh Mittal and Dr. Meysam Hashemnejad, for many great projects and ideas that we have come up with. I also thank Dr. Alona Birjiniuk, Dr. Benjamin Renner, Dr. Gaelle Le Goff, Max Nagarajan, Nidhi Juthani, Dr. Alex

Table of Contents

List of Figures

consistent with our proposed mechanism where the surfactant displacement and the subsequent decrease in the repulsion are triggered by the dehydration of the functional end-group (Fig 2.2A). (b) T_{gel} and G_P for various surfactants. Gelation was observed for all ionic surfactants, while no sol-gel transition was observed for the non-ionic surfactant (Tween 20) across the experimental temperature window. (c) T_{gel} and G_P for two different nanoparticles. Gelation occurs for both liquid PDMS droplets and solid polystyrene (PS, D = 58nm and ϕ = 0.30) colloids. No gelation is observed with the absence of PEGMA. Additionally, no sol-gel transition was observed for the aqueous continuous phase, indicating the gelation does not result from the self-assembly or association of SDS and PEGMA. Inset: Transmittance of a pure PEGMA aqueous solution (P = 0.33) as a function of temperature using UV-Vis spectroscopy at a wavelength = 500 nm......... 57

List of Tables

Chapter 1
Introduction

1.1 Motivation

Colloidal gelation is an effective tool to engineer material properties. By properly inducing the gelation in colloidal suspensions, researchers can rationally modulate the rheological properties of the materials and create complex microstructures [1]. For example, colloidal suspensions that undergo gelation can be used as ingredients and rheology modifiers in food or cosmetic products [2], and the complex assembled microstructures can be used as scaffolds for tissue engineering [3,4] and porous material design [5]. Therefore, colloidal gels have been of great interest in both fundamental studies and practical applications.

Among a diverse set of colloidal systems, nanoemulsions, liquid-liquid dispersions where the droplet size is ~ 100 nm, have become an emerging model system studying aspects of colloid-based materials [6]. Their nanoscale droplet size leads to remarkable stability, large interfacial area and optical transparency, which have been utilized for various functional materials [7]. Additionally, due to their flexibility in the formulation, interdroplet interactions are easily tuned, making nanoemulsions a powerful model system to study aspects of soft matter physics such as self-assembly, gelation and suspension rheology [8].

In conventional approaches, the self-assembly and gelation of nanoemulsions rely on the addition of another component into the suspensions. For example, strategies such as introducing depletion interaction via the addition of the depletants [9] and screening electrostatic repulsions via the addition of electrolytes [10] have been widely exploited in the literature. However, such strategies require adding or removing another component, which can be challenging for material processing and manipulation and the study of colloidal gel physics. Moreover, to make nanoemulsions a more versatile material, it is also desirable to develop nanoemulsion systems that respond to external stimuli. Therefore, a simple external stimulus like temperature that can induce gelation of the nanoemulsion is highly desired.

1.2 Colloidal gels

A colloidal gel is a semi-solid system composed of a percolated, network-like structure of a dispersed phase within a continuous carrier fluid [11]. Colloids can be either solids such as polystyrene [12], silica [13] or poly(methyl methacrylate) [14], or liquids such as oils (i.e. emulsions) [15]. For colloidal gels, the colloidal loading can be as low as 0.1 % [8]. Despite such low loading, the structural integrity provided by the assembled spanning gel network gives rise to mechanical properties such as viscoelasticity and yield stress.

The concept of inducing colloidal self-assembly and gelation is quite straightforward: it is governed by the competition between attractive and repulsive interactions between colloids, as shown in Fig. 1.1. For a given common colloidal suspension with a canonical formulation, there must be attractions and repulsions. Under the condition of colloidal stability, the repulsion is greater than the attraction, and colloids homogeneous disperse in the system without self-assembly. On the other hand, if the attraction can overcome the repulsion, the colloids can undergo self-assembly and even gelation if the effective attraction is strong enough. Moreover, if the change of dominance is subjected to external stimuli (such as temperature), the gelation can be stimuli-responsive (such as thermally-responsive).

repulsion > attraction   attraction > repulsion
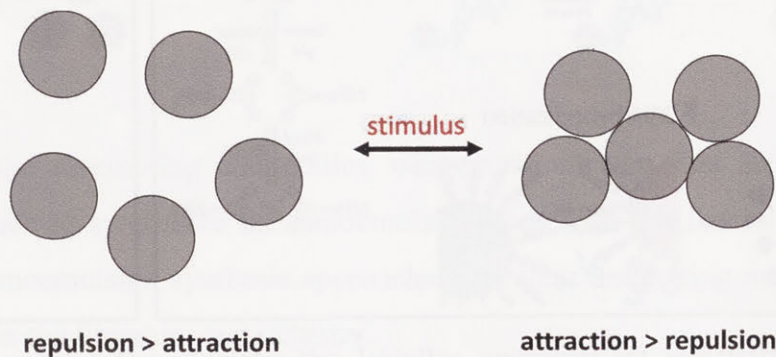
Figure 1.1 Colloidal self-assembly and gelation are governed by the competition between attractive and repulsive interactions.

As described, the colloidal gelation is the result of the competition between attractive and repulsive interactions. Gelation can take place when the attractions overcome repulsions. Therefore, to induce gelation, one can either increase the attractions or decrease the repulsions in the suspensions. Common strategies to trigger colloidal gelation are summarized in Fig. 1.2. To date in the literature, increasing attraction between colloids is still the major approach to induce self-assembly and gelation. Approaches including electrostatic attraction [4], dipole-dipole interaction [16], depletion

interaction [17], association between grafted polymers [18], photo-polymerization [19], DNA hybridization [20], polymer bridging [21] and hydrogen bond/metal-ion coordination [19] have been applied. On the other hand, despite much fewer studies that have been done, inducing colloidal gelation can be achieved by modulating (suppressing) repulsions. For example, if the colloids are charged stabilized, one can trigger the gelation by screening the electrostatic repulsion via the addition of electrolytes to the suspension [22]. On the other hand, if the charged species grafted on the colloids have an intermediate isoelectric point, one can control the charged state, and hence the electrostatic repulsion, of the colloids by changing the pH of the system [23].
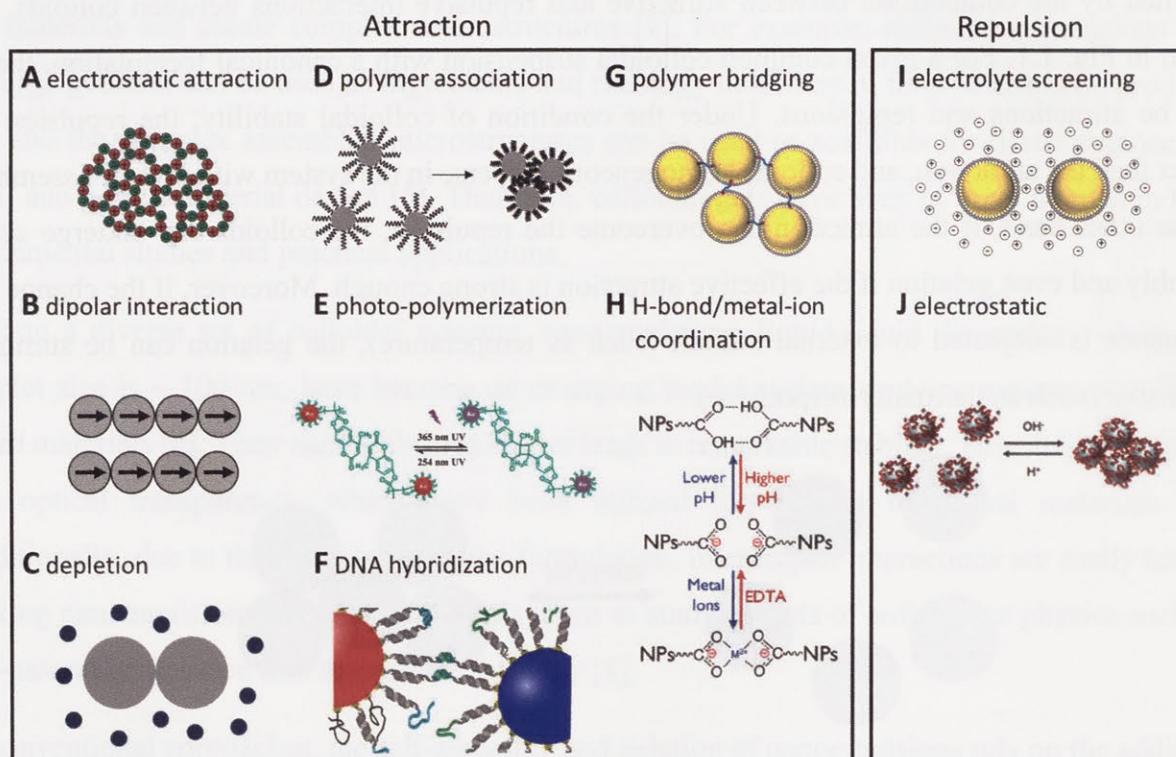
Figure 1.2 Common strategies for triggering colloidal self-assembly and gelation. (A) Electrostatic attraction [4,24]. (B) Dipolar interaction. (C) Depletion interaction. (D) Polymer association. (E) Photo-polymerization [19]. (F) DNA hybridization [20]. (G) Polymer bridging. (H) hydrogen bond/metal-ion coordination [19]. (I) Screening of electrostatic repulsion. (J) Electrostatic repulsion [23].

1.3 Nanoemulsions

Nanoemulsions are kinetically stable liquid-liquid dispersions where the droplet size is on the order of 100 nm [6]. A typical nanoemulsion is composed of two immiscible liquids (such as oil and water) and emulsifiers [7]. One of the commonly-used emulsifiers is surfactants. Surfactants are

amphiphilic molecules that are often pictured as molecules containing ionic heads and hydrophobic tails. The addition of surfactants significantly reduces the interfacial tensions between the two immiscible liquids, and further stabilized the resulting emulsion droplets by providing steric or electrostatic hindrance depends on the types of the surfactants that are used.

Because of the nano-sized droplet size, nanoemulsions have remarkable stability, large interfacial area and optical transparency, which have made nanoemulsions a versatile material not only for fundamental research [25] but also practical applications such as in cosmetics [26,27], food [28], pharmaceuticals [29] and sensors [30]. Moreover, due to their flexibility in the formulation, interdroplet interactions are easily tuned, making nanoemulsions a powerful model system to study aspects of soft matter physics such as self-assembly, gelation and suspension rheology [8]. Among all these topics, nanoemulsions that undergo gelation are of great interest due to their versatility in diverse fields. For fundamental studies, gelling nanoemulsions can be used as a model colloidal gel system to study the rheology-structure relationship under a large shear [31] or to investigate the dynamics during colloidal gelation [32]. On the other hand, gelling nanoemulsions can also be used in practical uses such as membranes [33] and skincare products [9]. Therefore, the design and the study of gelling nanoemulsion are of importance.

1.3.1 Synthesis

When designing the assembling and gelling nanoemulsions, the first step is to choose the appropriate approach to synthesize the nanoemulsions based on the formulations. This section summarizes the nanoemulsion synthesis approaches and their underlying mechanisms that have been widely used in the literature and industry.

To synthesize nanoemulsions from the separated phases, the energy required ΔG during the emulsification is considered as,

$$\Delta G = \gamma \Delta A - T \Delta S \tag{1.1}$$

where γ is the interfacial tension (or the energy required to form the interface per surface area), ΔA is the change in the interface area, T is the absolute temperature and ΔS is the increase in entropy due to the increase in the possible arrangement from the bulk separated phases to dispersed droplets. For nanoemulsions, the $\gamma \Delta A$ term is dominant [28]. Therefore, energy input $\geq \gamma \Delta A$ is

required during the emulsification process. Depending on the energy input, there are two primary approaches to produce nanoemulsions: high-energy methods and low-energy methods.

1.3.1.1 High-energy methods

High-energy methods use intensive mechanical force to overcome the surface energy. By applying mechanical force with power density $\approx 10^8$ to 10^{10} W/m^3, the mechanical energy is converted to the turbulent flow in the continuous phase and subsequently transformed into stresses on the droplets of the dispersed phase [34]. The stresses break down the larger droplets into smaller droplets and eventually the nanoemulsions can be obtained [7]. In the high-energy methods, a two-step synthesis is often used [6]. As shown in Fig. 1.3A, in the first step a pre-emulsion (macroemulsion) is prepared by simply mixing the continuous phase, surfactants and dispersed phase under a gentle stirring such as magnetic stirrer with a sufficient period of time. The preparation of pre-emulsions ensures the consistency of the initial condition of the emulsions being processed into the nanoemulsions and facilitates the synthesis. In the second step, the pre-emulsion is processed into the nanoemulsion with high-energy input. The two most widely used approaches are high-pressure homogenization (Fig. 1.3B) and ultrasonication (Fig. 1.3C).
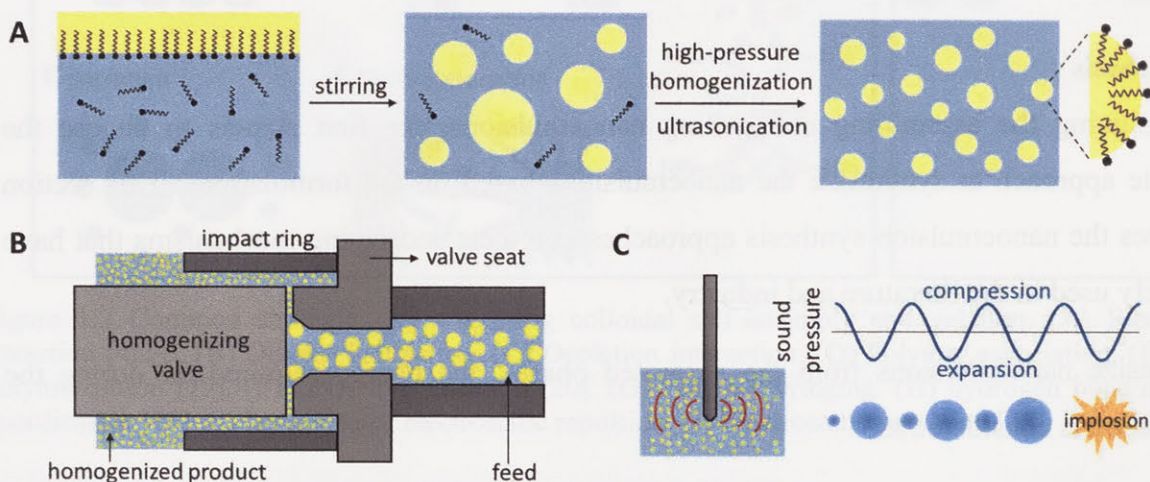
Figure 1.3 Schematic of the nanoemulsion synthesis using high-energy methods. (A) Preparation of pre-emulsion. (B) High-pressure homogenization (the schematic is adapted from https://www.substech.com/dokuwiki/). (C) Ultrasonication (the schematic is adapted from https://ultrawaves.de/technology/ultrasonic-disintegration).

In high-pressure homogenization, a homogenizing valve is used to pressurize the sample and forces the sample to flow through a very narrow gap with a spacing of several micrometers. During the homogenization, turbulent flow is created in the continuous phase which leads to strong shear and elongation stresses on the emulsion droplets. The droplets are therefore ruptured and broken down into smaller droplets. A similar mechanism is used in the ultrasonication but the turbulence is induced by the acoustic wave. In the ultrasonication, the high-intensity periodic acoustic wave induces implosions in the continuous phase due to cavitation. The implosion leads to the strong turbulence and therefore the droplets are ruptured [34,35].

Despite the intensive energy input and the instrumental requirements, the high-energy approaches have many advantages. For example, since the energy input is from external mechanical forces, the high-energy methods are relatively insensitive to the component physicochemical properties thus they allow greater flexibility to the nanoemulsion formulations, as compared to low-energy methods. Moreover, due to such insensitivity, nanoemulsions with droplet volume fraction up to 60% can be achieved [25]. Last but not least, various nanoemulsion droplet sizes with reasonable polydispersity and high-volume throughput can be easily obtained by controlling the number of passes and homogenizing pressure (for high-pressure homogenizer), or the ultrasonication time and wave amplitude (for ultrasonication) [34,35].

1.3.1.2 Low-energy methods

In low-energy methods, the system experiences an ultra-low interfacial tension ($\sim 10^{-5}$ to 10^{-4} N/m) at the phase inversion point [6]. The phase inversion point takes place during the synthesis process while the system is traversing the phase diagram, as shown in Fig 1.4. The phase inversion point can be obtained through either changes in composition (known as Phase Inversion Composition, PIC, Fig. 1.4 A) or in temperature (known as Phase Inversion Temperature, PIT, Fig. 1.4B).
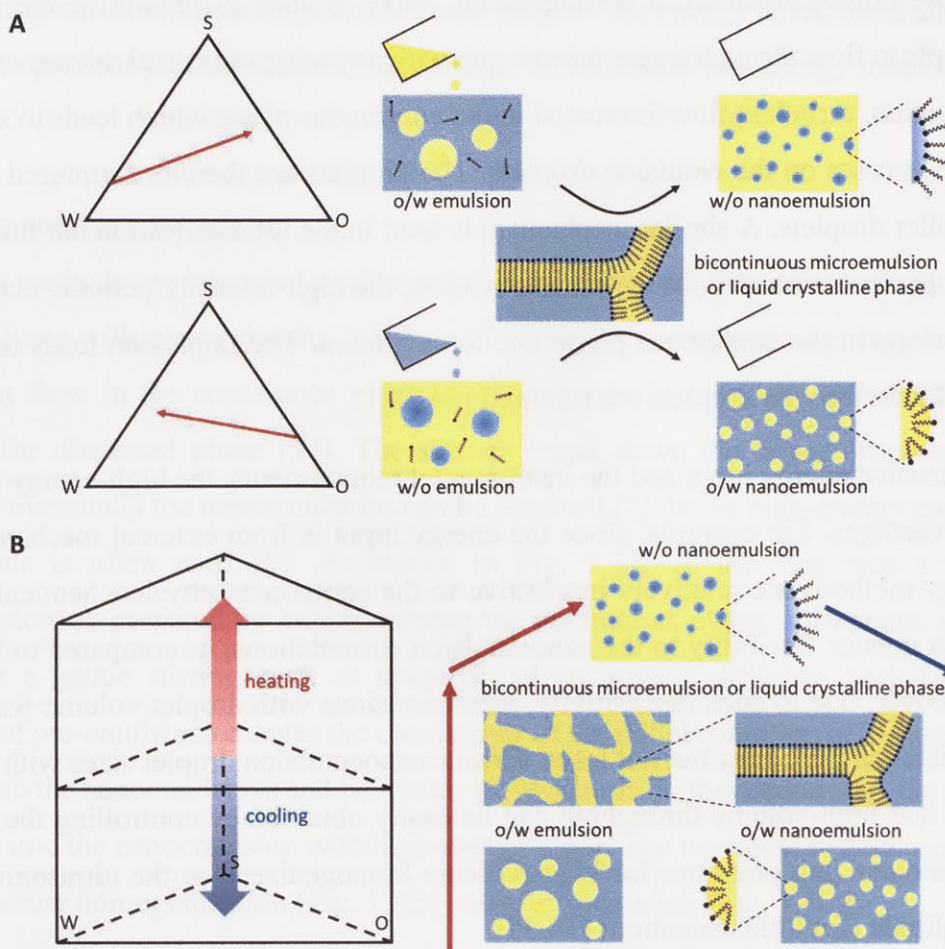
Figure 1.4 Schematic of the nanoemulsion synthesis using low-energy methods. (A) Phase Inversion Composition, PIC, method. (B) Phase Inversion Temperature, PIT, method. The schematic is adapted from figures in [28,36,37].

In PIC methods, the continuous phase is added dropwise into the homogeneous mixture composed of the dispersed phase and surfactants under stirring. As more continuous phase is added, the system reaches the phase inversion point at which the bicontinuous microemulsion or the liquid crystalline phase are formed due to the very low interfacial tension [28,37]. As more continuous phase is added, the bicontinuous microemulsion or the liquid crystalline phase are broken down into nano-sized droplets of the dispersed phase under the stirring, and the nanoemulsion is obtained. The same principle holds in the PIT method where the difference lies in the path to achieving the phase inversion point. As shown in Fig. 1.4, the phase inversion point is achieved through controlling the temperature of the mixture composed of the continuous phase, dispersed phase and surfactants. Using oil-in-water (O/W) nanoemulsion synthesis as an example, at the lower temperature, the surfactants are more hydrophilic and reside in the water (continuous) phase. As

30

the temperature increased, the surfactants become more lipophilic and migrate to the oil (dispersed) phase. At the phase inversion point, the hydrophilicity and lipophilicity reach a balance at which the surfactants evenly distribute in both phases, and the bicontinuous microemulsion or the liquid crystalline phase are formed. The subsequent cooling makes the surfactants more hydrophilic again and therefore the O/W nanoemulsion is formed. In PIT method, good control of temperature is critical. For example, if cooling speeds are not fast enough, the coalescence of droplets takes place [38], which may lead to the instability of the nanoemulsion suspension.

As can be expected, in the low-energy methods, the nanoemulsion synthesis is highly sensitive to the choice of the surfactants. One important and widely-used parameter is the hydrophilic-lipophilic balance (HLB) of the surfactants. In general, low HLB values ($\approx$ 1 to 10) correspond to lipophilic surfactants and W/O nanoemulsions are favored. On the other hand, high HLB values (>10) corresponds to hydrophilic surfactants and O/W nanoemulsions are favored [39,40]. The manipulation of HLB values is commonly achieved by mixing two types of surfactants with different HLB values. Another important parameter associated with the amount of the surfactants is the surfactant-to-emulsion ratio (SER). For O/W nanoemulsions, it is also known as surfactant-to-oil ratio (SOR). It has been reported that droplet sizes are highly dependent on SER values [36,41–43]. One should note that HLB and SER are not the only important parameters for the nanoemulsion formation in low-energy methods. Other parameters such as temperature, stirring speed, rate of the continuous phase addition and packing parameter of surfactants on droplets are also critical to the nanoemulsion synthesis [28].

In low-energy methods, it is critical to understand the physicochemical properties of the surfactants and how the surfactants partition between the continuous and dispersed phases. Depending on the types of nanoemulsions, surfactants must be carefully chosen. Therefore, compared to the high-energy methods, there are more limitations in the nanoemulsion formulations. However, the low-energy methods are preferred in industrial processes since only simple mechanical stirring is required, and PIC is often more favorable than PIT because good control of temperature is challenging. Moreover, since specialized equipment is not required, the production of nanoemulsion can be more easily scaled up.

1.3.2 Strategies for nanoemulsion gelation

As described in Section 1.3, there has been great interest in the design and the study of gelling nanoemulsions. This section briefly summarizes common strategies, shown in Fig. 1.5, that have been applied to induce the self-assembly and gelation of nanoemulsions (as well as sub-micron emulsions).

A Depletion interaction **B** Polymer bridging **C** Polymer-surfactant complex

depletant

D Grafted polymer interaction **E** Screening of electrostatic repulsion **F** Jamming
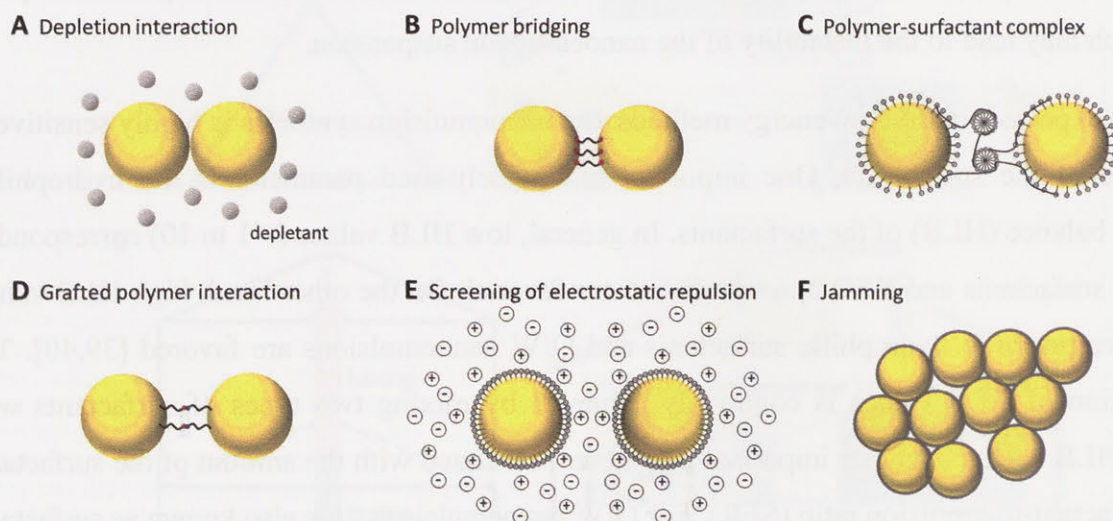
Figure 1.5 Common strategies to induce nanoemulsion gelation: (A) Depletion interaction, (B) polymer bridging, (C) polymer-surfactant complex, (D) grafted polymer association, (E) screening of electrostatic repulsion, and (F) jamming.

1.3.2.1 Depletion interaction

Depletion interaction is an entropically-driven attractive interaction that takes place when colloids are suspended in the continuous phase containing non-adsorbing molecules [17]. These non-adsorbing molecules, called depletants, are excluded from the vicinity of the colloids and therefore provide an osmotic pressure to the colloids, as shown in Fig. 1.5A. This osmotic pressure acts as an effective attractive force between the colloids, leading to the self-assembly and ultimately the gelation of the system. The strength of the depletion and the effective length scale are then determined by the concentration and the size of the depletants, respectively. For nanoemulsion systems, the depletants can be surfactant micelles [44–53], non-adsorbing polymers [54–56] or even smaller droplets [57].

1.3.2.2 Polymer bridging

Contrary to the depletion interaction where the added molecules are excluded from the nanoemulsion droplets, gelation via polymer bridging relies on the association between the molecules and the droplets. Recently, the Doyle group has designed a nanoemulsion gelation mechanism in which the droplets can be bridged by adding telechelic oligomers into the suspension [21]. Moreover, the droplet bridging (and hence the gelation) is triggered by an increase in temperature. In the canonical formulation, the nanoemulsion is composed of nano-sized polydimethylsiloxane (PDMS) droplets stabilized by sodium dodecyl sulfate (SDS) suspended in an aqueous continuous phase containing poly(ethylene glycol) diacrylate (PEGDA). As the temperature increased, the acrylate group on PEGDA becomes increasingly hydrophobic and partitions into the oil/water interface. Such partitioning leads to the droplet bridging which acts as an effective attraction that ultimately gives rise to gelation. It has been shown that the gelling mechanism also takes place over a wide of component chemistries and compositions.

1.3.2.3 Polymer surfactant complex

The droplet bridging can be also achieved by the polymer-surfactant complex where the bridging is mediated by surfactant micelles in the continuous phase. The surfactant micelles are usually from the excess of the surfactants that are used to stabilize the nanoemulsion droplets. The schematic is shown in Fig. 1.5C. In this mechanism, the polymers are uncharged molecules containing polar moieties such as poly(ethylene glycol) or poly(vinyl alcohol), and the surfactants are ionic surfactants such as SDS or cetyltrimethylammonium bromide [58–60]. The interaction responsible for the formation of the complex is from the ion-dipole interaction (ion-induced dipole interaction) in which the charged head of the ionic surfactant associates with the polar segments on the uncharged polymers. The ion-dipole interaction has been extensively studied in the literature [61]. Experimental techniques including rheometry [62], neutron scattering [63], isothermal titration calorimetry [64,65], NMR [65] and potentiometric titration [66], as well as thermodynamic models [67] and simulations [68].

In addition to the bridging of droplets, polymer surfactant complex can also lead to an increase in the effective volume fraction of the droplet, and the gelation can be induced through jamming

[69,70]. In this scenario, the complex does not bridge the droplet. Instead, a think adsorbed layer outside the droplet is formed. The gelation through jamming will be discussed in Section 1.3.2.6.

1.3.2.4 Grafted polymer interaction

In addition to the bridging of droplets mediated by free molecules in the continuous phase, self-assembly and gelation can also be achieved by the direct association or chemical bonding between the molecules adsorbed on the droplets. The mechanism is shown in Fig. 1.5D where the association provided by the grafted molecules makes the droplets 'sticky' and leads to an effective attraction. Strategies using polymerization of proteins via sulfhydryl−disulfide interchange [71] and DNA hybridization [72–74] have been performed.

1.3.2.5 Screening of electrostatic repulsion

In addition to enhancing the attractive interaction between the droplets, gelation of nanoemulsions can also be induced by suppressing repulsions. Perhaps the most widely seen approach is the screening of electrostatic repulsion by adding the electrolytes into charged-stabilized nanoemulsion suspensions. This is also a classic phenomenon that can be well-described by Deryaguin-Landau-Verwey-Overbeek (DLVO) theory [22,75]. The addition of electrolytes reduces the effective length scale of the electrostatic repulsion (i.e. Debye length), leading to the emergence of a secondary minimum in the interactive potential and eventually inducing the gelation [15,22,76–81].

1.3.2.6 Repulsive jamming and pure jamming

Overall, the aforementioned mechanisms describe that gelation can be effectively induced by either enhancing the attractions or suppressing the repulsions between droplets. However, modulating interactive potentials is not the only way to trigger the nanoemulsion gelation. Such method, so-called repulsive gelation [52], is through the increase of effective oil volume fraction in emulsion systems [8,25]. The effective oil volume fraction (ϕ_e) is calculated by considering the actual oil volume fraction (ϕ_a) and the excluded volume resulted from either the repulsive charge cloud that extends from the oil/water interface (i.e. Debye length) or the steric hindrance provided

by the bulky emulsifiers [6,7], and $\phi_e = \phi_a(1 + L/a)^3$ where a is the droplet radius and L is the Debye length or the steric length scale provided by the bulky emulsifiers. When ϕ_e is greater than the maximum random jamming limit, a viscoelastic nanoemulsion gel is obtained. Therefore, the increase in ϕ_e can be achieved by either decreasing the droplet size [7,8,15,25] or using bulkier emulsifier molecules such as proteins [82,83], copolymers [84,85] and particles [86].

1.4 Rheology

One of the most common ways to characterize properties of colloidal gels is to study their rheology. Rheology is a study of how complex fluids deform under stress [87], where a complex fluid is defined as a material composed of a liquid base and its supramolecular structure. Common complex fluids include suspensions [88], emulsions [89,90], colloidal gels [91,92] and polymer solutions [93]. When a complex fluid is strained, the microstructure simultaneously stores and dissipates the deformation energy, giving rise to rheological properties such as compliance and viscoelasticity. To study the (bulk) rheology of the material, geometries such as parallel plates, cone-and-plate, coaxial cylinders and capillary flow are widely used [2]. Among all these available approaches, in this thesis, parallel plates and cone-and-plate rheometry (Fig. 1.6) are heavily used. As shown, for the rheological measurement to proceed, the material is subjected between the upper plate (or cone) and the lower plate. The lower plate is often a Peltier plate to control the temperature of the sample. Then, an oscillatory shear is applied to the material by the upper geometry. The rheometer measures the response and properties such as viscoelastic moduli and yield stresses can be obtained.
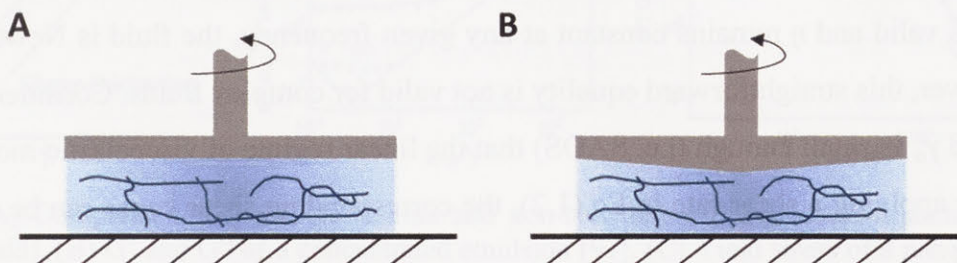
Figure 1.6 (A) Parallel plates. (B) Cone-and-plate. The top fixtures (gray parts) are rotated to induce shear strains in frequency-dependent manner.

Contrary to Newtonian fluids where the shear stress is always proportional to the shear rate when the fluid is deformed, complex fluids exhibit diverse behaviors deviating from this linear relation [94]. Properties of complex fluid include shear-thinning (viscosity decreases when shear rate increases), shear-thickening (viscosity increases when shear rate increases), yield stress (stress threshold that a material transforms from a liquid-like state to a solid-like state), and viscoelasticity (a material simultaneously exhibits viscous and elastic characteristics). In this thesis, the viscoelastic moduli are of great interest due to their ability to characterize diverse properties of gelling nanoemulsions such as the critical gelation points, gel dynamics and gel strengths.

Viscoelastic moduli (in the linear regime) are measured using small-amplitude oscillatory shear (SAOS) applied by either parallel plates or cone-and-plate rheometry. Assuming the material is now subjected to a shear strain, γ, with an amplitude, γ_o, in a sinusoidal manner with oscillatory frequency, ω. The time-dependent shear strain can be expressed as

$$\gamma = \gamma_o \sin(\omega t) \tag{1.2}$$

where t is the time. The rheometer then measures a corresponding shear stress, σ. γ and σ can be related by the following equation

$$\sigma = \eta \dot{\gamma} \tag{1.3}$$

where η is viscosity and $\dot{\gamma}$ is shear rate by taking time-derivative on γ. In Eq. (1.2) and Eq. (1.3), since the strain is first controlled and the corresponding stress is recorded, the above rheometer measurement is called 'strain-controlled', on the other hand, a 'stress-controlled' can be obtained vice versa.

If Eq. (1.3) is valid and η remains constant at any given frequency, the fluid is Newtonian (Fig. 1.7A). However, this straightforward equality is not valid for complex fluids. Considering a strain is applied and γ_o is small enough (i.e. SAOS) that the linear regime of viscoelastic moduli can be measured, by applying a shear rate in Eq.(1.2), the corresponding shear stress can be obtained as followed [95],

$$\sigma = \sigma_o \sin(\omega t + \delta) \tag{1.4}$$

where the output stress can be also expressed in a sinusoidal manner but with a phase shift, δ. If δ is zero, the material is an elastic solid obeying Hooke's law (immediate response between shear

stress and shear rate); and if δ is $\pi/2$, the material is a simple Newtonian fluid. The linear relation between $\sigma(t)$ and $\gamma(t)$ can be generalized as $\sigma = G\gamma$ and expanded in terms of trigonometric identities as followed,

$$\sigma(t) = \gamma_o[G' \sin(\omega t) + G'' \cos(\omega t)] \tag{1.5}$$

$$\sin(\omega t + \delta) = cos\delta \sin(\omega t) + sin\delta \cos(\omega t). \tag{1.6}$$

And two quantities are defined,

$$G'(\omega) \equiv \frac{\sigma_o}{\gamma_o} cos\delta \qquad G''(\omega) \equiv \frac{\sigma_o}{\gamma_o} sin\delta \tag{1.7}$$

where $G'(\omega)$ is called storage modulus (elastically, store deformation energy) and $G''(\omega)$ is called loss modulus (viscously, dissipate deformation energy). One example of the viscoelastic moduli of a concentrated emulsion is shown in Fig. 1.7B.

In addition to SAOS measurements in a linear manner, rheological properties in the nonlinear regime can be measured by applying a large-amplitude oscillatory shear (LAOS). In LAOS measurements, yield stresses are often of interest [96]. Yield stress is a threshold that a material transforms from a solid-like to a liquid-like state. By gradual increasing σ applied to the sample, yield stress σ_y can be obtained by observing the sudden decrease of the moduli. An example of the yield stress measurement of nanoemulsion gels is shown in Fig. 1.7C.
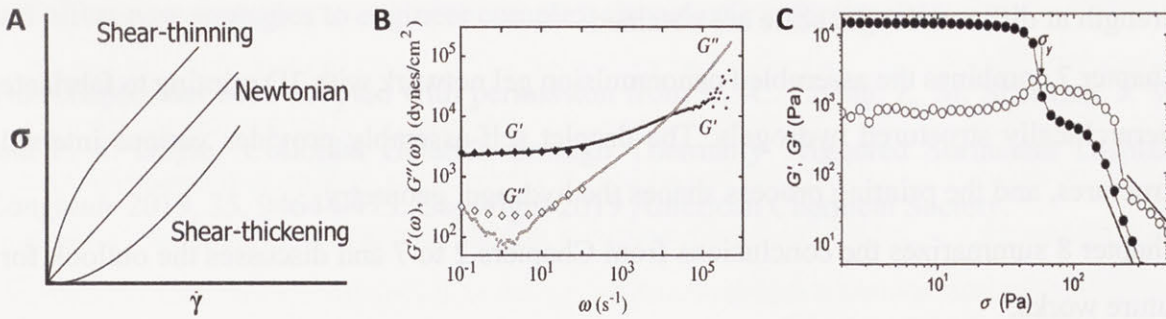
Figure 1.7 (A) Comparison between Newtonian and non-Newtonian fluids (shear-thinning and shear-thickening fluid). (B) G' and G" of a concentrated emulsion [97]. (C) Yield stress of a nanoemulsion gel [98].

1.5 Thesis organization

The following chapters of this thesis can be generally divided into two parts. Chapters 2 to 4

describe the design of gelling nanoemulsions with controllable material properties by understanding the gelation mechanism at a molecular scale. Chapters 5 to 7 describe how the gelling nanoemulsions can be used for both fundamental studies (Chapter 5 and 6) and practical applications (Chapter 7). Specifically,

- Chapter 2 describes a new colloidal gelling platform in which the repulsive interaction is modulated to induce the gelation. By understanding the molecular behavior of the constituents, the gelling platform can apply to a wide range of colloidal formulations.

- Chapter 3 describes a design of thermally and pH-responsive nanoemulsion gelation, and studies the gel properties by modulating both attractive and repulsive interactions through changes in temperature and pH.

- Chapter 4 revisits the thermally-gelling nanoemulsion that Doyle group designed and investigates the previously-overlooked interactions. Two-stage gelation is applied by sequentially tuning different inter-droplet interactions and a new gel state is achieved.

- Chapter 5 takes advantage of the thermally-gelling behavior and investigates the effect of processing history on the material properties of colloidal gels. New experimental evidence of path-dependent rheology and associated microstructures of a model colloidal gel is provided.

- Chapter 6 performs multiple particle tracking to probe the nanoemulsion gels. By tailoring the surface chemistry of the probe beads, the transportation modes of particles and the gel strength at different length scale are obtained.

- Chapter 7 combines the assembled nanoemulsion gel network with 3D printing to fabricate hierarchically structured hydrogels. The droplet self-assembly provides various internal structures, and the printing process shapes the hydrogel geometry.

- Chapter 8 summarizes the conclusions from Chapters 2 to 7 and discusses the outlook for future works.

Chapter 2

Colloidal Gelation through Thermally Triggered Surfactant Displacement

2.1 Overview

Colloidal systems that undergo gelation attract much attention in both fundamental studies and practical applications. Rational tuning of interparticle interactions allows researchers to precisely engineer colloidal material properties and microstructures. In this chapter, contrary to the traditional approaches where modulating attractive interactions is the major focus, we present a platform wherein colloidal gelation is controlled by tuning repulsive interactions. By including amphiphilic oligomers in colloidal suspensions, the ionic surfactants on the colloids are replaced by the nonionic oligomer surfactants at elevated temperatures, leading to a decrease in electrostatic repulsion. The mechanism is examined by carefully characterizing the colloids, and subsequently allowing the construction of interparticle potentials to capture the material behaviors. With the thermally-triggered surfactant displacement, the dispersion assembles into a macroporous viscoelastic network, and the gelling mechanism is robust over a wide range of compositions, colloid sizes and component chemistries. This stimulus-responsive gelation platform is general and offers new strategies to engineer complex viscoelastic soft materials.

This chapter has been adapted with permission from L. -C. Cheng, Z. M. Sherman, J. W. Swan and P. S. Doyle "Colloidal Gelation through Thermally Triggered Surfactant Displacement" *Langmuir* 2019, 35, 9464-9473. Copyright 2019 American Chemical Society.

2.2 Introduction

Colloidal suspensions that undergo gelation are widely used as scaffolds in tissue engineering [4], as carriers in drug delivery [24], as ingredients and products in the food industry [99,100] and as building blocks in porous material design [101]. In particular, colloidal gelation triggered by increasing temperatures has been used in various applications such as complex material design,

tissue engineering and drug delivery. For example, our group has previously demonstrated thermally-induced gelation as a bottom-up strategy for hierarchical hydrogel synthesis via 3D-printing [33]. Moreover, thermally-gelling colloidal suspensions are also useful for biomedical and pharmaceutical applications. At room temperature, the liquid-like behavior makes the suspension easily injectable. While at the body temperature (after injection), the colloidal self-assembly gives rise to in-situ gelation which has been utilized as scaffolds for cell culture [3] and site-specific controlled drug delivery [102].

Tuning inter-colloid interactions allows one to engineer macroscopic material properties and internal microstructures [1]. In conventional approaches, self-assembly and gelation are driven by manipulating attractions such as electrostatic attraction [4], depletion [100,103,104], polymer bridging [33,105] and dipole-dipole interaction [16,106]. On the other hand, modulating the repulsions between colloidal particles has been investigated [18,75,107] much less than manipulating attractions [4,16,33,100,103–106] as a means to drive self-assembly. One example is controlling steric repulsions to induce flocculation in dispersions of nanoparticles with grafted polymer brushes by changing the solvent quality with temperature [18,107]. Upon decreasing the temperature, stabilizing polymer brushes collapse, which leads to a decrease in the steric repulsion and an increase in affinity between polymers. Therefore, changes in interparticle repulsions are coupled to changes in attractions, making it difficult to independently control the attraction and the repulsion, and the analyses have primarily focused on the effective attraction by lumping the two interactions. Another classic example is inducing gelation by screening the electrostatic repulsion between like-charged colloids using electrolytes [75]. Adding electrolytes reduces the range of the repulsion, resulting in aggregation due to van der Waals or other attractions. However, this method to modulate interactions requires adding or removing salts, which can be challenging for material processing and manipulation. Therefore, a simple external stimulus like temperature that can modulate the interactions is highly desired.

In this chapter, we report a stimulus-responsive gelling platform where interparticle interactions are modulated through a thermally-responsive electrostatic repulsion. By including nonionic thermally-responsive oligomer surfactants in colloidal suspensions that are charge-stabilized by ionic surfactants, the ionic surfactants on the colloids are displaced by the nonionic oligomers at elevated temperatures. Such thermally-triggered surfactant displacement results in the decrease in

colloidal repulsion, and hence induces the colloidal self-assembly, which is contrary to most prior studies wherein the modulation of attractive interactions has been the major focus. Our system shows rich phase behaviors and mechanical properties. We demonstrate that this gelation platform is general and robust over a wide range of composition, colloid size and component chemistry. By carefully characterizing the colloids and obtaining a mechanistic understanding of their response, we construct the interparticle potential and explain trends in material behaviors. We also show that our gelling system is in good agreement with well-established theories in the literature and therefore can be predictably extended to other systems.

2.3 Materials and methods

2.3.1 Materials

Polydimethylsiloxane (PDMS, viscosity = 5 cSt), sodium dodecyl sulfate (SDS), sodium dodecylbenzenesulfonate (SDBS), cetrimonium bromide (CTAB), Tween 20, poly(ethylene glycol) methacrylate (PEGMA, $M_n \approx 360$ g mol^{-1}), poly(ethylene glycol) methyl ether (PEGME, $M_n \approx 350$ g mol^{-1}), poly(ethylene glycol) (PEG, $M_n \approx 300$ g mol^{-1}) and Nile Red were purchased from Sigma Aldrich. Poly(ethylene glycol) acrylate (PEGA, $M_n \approx 400$ g mol^{-1}) was purchased from Monomer-Polymer & Dajac Labs. Unmodified latex polystyrene (PS) nanoparticles with particle diameter D = 58 nm (aqueous suspension with the concentration of 10% w/v) was purchased from Magsphere Inc., and the water was removed by placing the solution in an oven at T = 50 °C. All chemicals were used without further purification.

2.3.2 Nanoemulsion synthesis

The oil-in-water nanoemulsions studied in this work contained PDMS droplets (with diameter D and volume fraction ϕ) suspended in an aqueous continuous phase of oligomers (with volume fractions P) and surfactants. The total concentration of surfactant was 0.175 M. The canonical system was composed of oil droplets (D = 50 nm and ϕ = 0.30) suspended in the continuous phase containing SDS and PEGMA with P = 0.33. To synthesize the nanoemulsion, a pre-emulsion was first prepared by adding PDMS to a pre-mixed continuous phase and agitating with magnetic stirring at a speed of 600 rpm for 15 minutes to ensure there was no visually-observed bulk phase

separation. The pre-mixed continuous phase consisted of deionized water, surfactants at a concentration of 0.175 M and oligomers with P. The pre-emulsion was passed through a high-pressure homogenizer (EmulsiFlex-C3, Avestin) at a homogenizing pressure of 18 kpsi to form the nanoemulsion. The homogenization was conducted for various numbers of passes, N, depending on the target droplet size (Appendix A1). For example, N = 12 for the canonical nanoemulsion with D = 50 nm. A heat exchanger was used at the outlet of the homogenizer with 4 °C water circulating, and the emulsion was subsequently cooled to 4 °C in the refrigerator between each pass to prevent thermally-induced gelation and oligomer adsorption during the homogenization. The droplet size and the polydispersity were measured using dynamic light scattering (90Plus PALS, Brookhaven Instruments) after diluting the sample to ϕ = 0.002. All nanoemulsions have a size polydispersity of 0.22 ± 0.02 in this chapter.

2.3.3 Rheological characterization

All rheological properties were measured by using a stress-controlled rheometer (DHR-3, TA instrument) equipped with a 1° 60 mm aluminum upper-cone and a temperature-controlled Peltier lower-plate. To minimize evaporation, a deionized water-wetted solvent trap was used, and a few drops of deionized water were added on top of the aluminum cone. For each measurement, a pre-shear step was performed by applying a constant rotation at a speed of 10 rad/s for 30 seconds, and the measurement started after a 60-second period where the nanoemulsion remained quiescent at 20.0 °C. Freshly loaded nanoemulsion was used for each measurement to avoid the effect of thermal history [105].

Small-amplitude oscillatory shear (SAOS) at a shear strain γ = 0.05% was performed to conduct the frequency-sweep measurements and temperature-jump experiments. The frequency-sweep measurements at various temperatures, T, were conducted with angular frequency ω = 1 to 200 rad s^{-1} and the dynamic linear viscoelasticity was obtained. Before each measurement, the temperature was kept at T for 10 minutes in order to reach the quasi-equilibrium (Appendix A2). For the nanoemulsion with P = 0.33 and ϕ = 0.10, γ = 0.03% was applied to stay in the linear regime. Temperature-jump experiments were performed by a three-stage time-sweep SAOS measurement at T = 20 or 55 °C with ω = 20 rad s^{-1}. The measurements started with T = 20 °C for 5 minutes, and the temperature was jumped to 55 °C for 10 minutes. The temperature was either maintained

at 55 °C or decreased to 20 °C in the third stage. Different yield stresses were performed at the beginning of the third stage for one minute (see Appendix A2 for more details).

Large-amplitude oscillatory shear (LAOS) was performed to determine the strain at the limit of linearity, γ_L. Before the measurement, the nanoemulsion was kept at $T = T_{gel} + 25$ °C for 10 minutes. LAOS was then carried out over a range of shear strain $\gamma = 0.001$ to 5% at an angular frequency of 20 rad s^{-1}. γ_L is then defined as the shear strain where the viscoelastic moduli start to deviate from the linear region. Following the method by Shih et al. [108], γ_L is experimentally chosen as the point where G' deviates more than 5% from the plateau in the linear regime.

2.3.4 Isothermal titration calorimetry (ITC)

ITC measurements were performed using a TA Instrument Nano ITC calorimetry. The experimental procedure and the data analysis followed a methodology similar to the work studying the adsorption of proteins onto nanoparticles [109] (see Appendix A3 for more data analysis details). Before each measurement, the reference cell was filled with fresh aqueous SDS solution at a concentration of 5.3 mM, and the sample cell was filled with the fresh nanoemulsion with $\phi = 0.001$ suspended in an aqueous continuous phase containing free SDS at a concentration of 5.3 mM. The SDS concentration was chosen to be well below the critical micelle concentrations across the experimental temperature window [110]. During the measurement, 25 injections of 10 μL PEGMA aqueous solution (P = 0.00748 and [SDS] = 5.3mM) were titrated from a syringe into the sample cell with a continuous stirring at a speed of 200 rpm. Each injection was separated with a 300-second interval to ensure equilibrium was reached (Appendix A3). The blank tests were conducted by titrating PEGMA aqueous solution into the sample cell filled with an aqueous solution of 5.3 mM SDS. The heat data was then subtracted from the data of blank test, and the background-corrected data was used for the subsequent analysis (Appendix A3).

2.3.5 Zeta potential

Zeta potentials of the nanoemulsion droplets were measured by a Brookhaven Instruments 90Plus PALS zetasizer. The sample nanoemulsion was with $\phi = 0.001$ suspended in an aqueous continuous phase containing free SDS at a concentration of 5.3 mM and PEGMA at a volume

fraction of 0.00187. Before each measurement, the temperature was raised to the target temperature for 10 minutes. Fresh nanoemulsion was loaded for each measurement.

2.3.6 Confocal microscopy

The microstructures of the nanoemulsion at T = 20.0 and 55.0 °C were captured using a confocal laser scanning microscope (LSM 700, Zeiss) equipped with a 20× air-immersion objective. The temperature was controlled using a heating stage (Heating Insert P S1, Zeiss) with a temperature controller (TempModule S1, Zeiss). Before the nanoemulsion synthesis, PDMS was fluorescently labeled by pre-dissolving the lipophilic dye, Nile Red (excitation/emission wavelength = 550/626 nm) at a concentration of 0.05 mg mL^{-1}. To image the microstructure, 150 µL of the fluorescently labeled nanoemulsion was loaded into a glass chamber (Lab-Tek^{TM} 155411, Thermo Fisher Scientific) with a coverlid. The chamber was mounted on the heating stage equipped on the microscope. Before the imaging, the temperature was increased to the target temperature and was kept for 10 minutes.

2.4 Results and discussion

2.4.1 Thermally-gelling nanoemulsions

In this work, we used nanoemulsions as a model colloidal system, although we will show the colloidal gelation can be applied to other colloidal suspensions. Nanoemulsions are liquid-liquid dispersions where the droplet size is ~ 100 nm. Because of their stability, large interfacial surface area and ease of synthesis, there is emerging interest for fundamental studies and practical applications of nanoemulsions in various fields [6]. Additionally, due to flexibility in the formulation, interdroplet interactions are easily tuned, making nanoemulsions a powerful model system to study aspects of soft matter physics such as self-assembly [8], gelation [105] and suspension rheology [7]. Here, the canonical system consists of polydimethylsiloxane (PDMS) droplets with a volume fraction $\phi = 0.30$ dispersed in an aqueous phase containing poly(ethylene glycol)methacrylate (PEGMA) with a volume fraction P = 0.33. The droplets have a diameter of D = 50 nm and are stabilized by the ionic surfactant sodium dodecyl sulfate (SDS). The nanoemulsion is liquid at room temperature, but transforms into a solid-like gel upon increasing

44

temperature. We studied this transition using small-amplitude oscillatory shear to measure the linear viscoelastic storage modulus G' and loss modulus G''. In Fig. 2.1A we show the viscoelastic response over a range of angular frequencies, ω. The material shows liquid-like behavior, where $G'(\omega) \sim \omega^2$ and $G''(\omega) \sim \omega$ at room temperature [18]. Upon heating, $G'(\omega)$ and $G''(\omega)$ grow, and their frequency-dependence changes. G' and G'' have the same scaling with ω, $G'(\omega) \approx G''(\omega) \sim \omega^{0.5}$, at the critical gelation temperature T_{gel} = 30 °C. According to the classic work by Chambon and Winter [111,112], at critical gelation point $G'(\omega)$ and $G''(\omega)$ have the same power law behavior where $G' \sim G'' \sim \omega^n$ and n is the relaxation exponent. At this critical gel point, the colloidal system forms a sample-spanning gel network. For our canonical formulation, T= 30 °C corresponds to the Chambon-Winter critical condition, and this criterion is used to define the gelation temperature (Fig. 2.1A). Moreover, in our system, n is $\approx$ 0.5, which indicates the formation of a percolated gel or a pretransitional glass phase [113,114].

Further heating the nanoemulsion leads to a dramatic increase in the elasticity, and the increase becomes limited above T_{gel} + 20 °C (Appendix A2). In this high-temperature regime, $G'(\omega) > G''(\omega)$ and $G'(\omega)$ is nearly independent of frequency with a plateau modulus, G_P. The nanoemulsion system shows a remarkable sol-gel transition as the elasticity increases by nearly four orders of magnitude, and the nanoemulsion transforms from a transparent liquid to a turbid, solid-like material shown in Fig. 2.1B. The turbidity indicates the formation of droplet aggregates. To further probe the gel microstructure, confocal microscopy was performed to visualize the gel network, as shown in Fig. 2.1C. The microstructure of our nanoemulsion gel is a spanning network of colloid-rich and colloid-lean domains, similar to networks observed from arrested phase separation of other attraction-driven colloidal gels [103,104]. Interestingly, the nanoemulsion gel can re-enter the liquid state with sufficient cooling and moderate shearing (see Appendix A2).
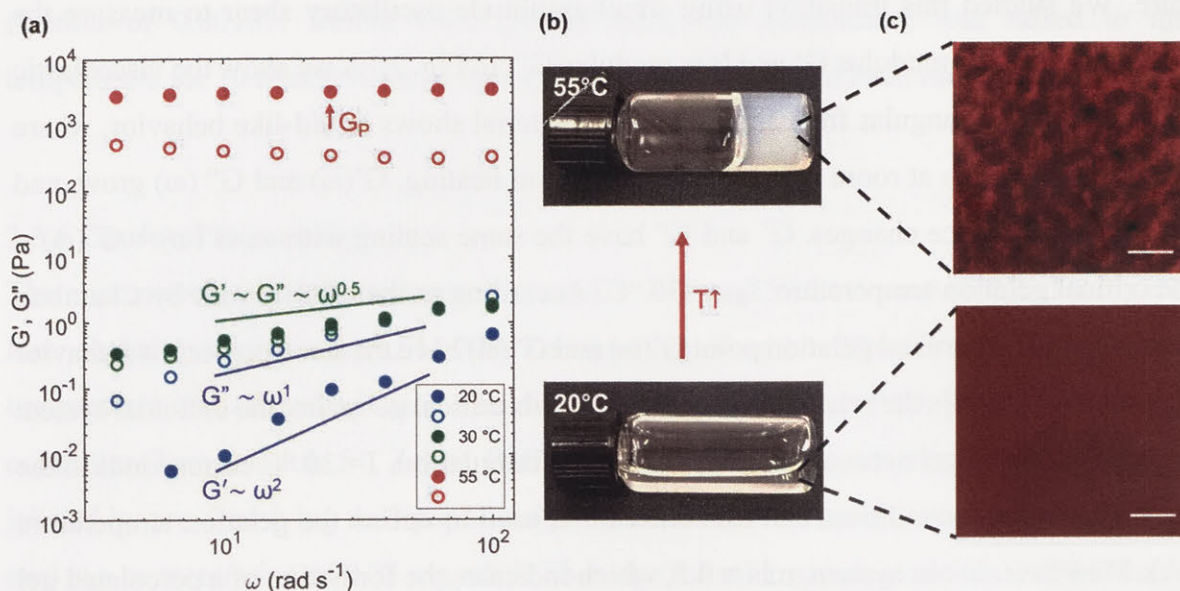
Figure 2.1 Thermally-triggered gelling behavior of the model nanoemulsion system. The canonical system contains PDMS droplets (diameter D = 50 nm, volume fraction ϕ = 0.30) suspended in an aqueous continuous phase containing PEGMA (volume fraction P = 0.33) and SDS. (a) Linear viscoelasticity, storage modulus G' (closed symbols) and loss modulus G" (open symbols), of the nanoemulsion at various temperatures. At T = 20 °C, the nanoemulsion is liquid-like. At T = 30 °C, the nanoemulsion undergoes a sol-gel transition where $G'(\omega) \sim G''(\omega) \sim \omega^{0.5}$ giving the gelation temperature T_{gel} = 30 °C. At T = 55 °C, the nanoemulsion is solid-like where $G'(\omega)$ is nearly independent of ω. (b) Photographs of the nanoemulsion taken after 10 minutes at T = 20 and 55 °C. (c) Microstructures of the nanoemulsion at T = 20 and 55 °C captured using confocal microscopy. Oil droplets were fluorescently labeled with a lipophilic dye, Nile Red, before the nanoemulsion synthesis. At T = 20 °C, the droplets are homogeneously suspended in the continuous phase. At T = 55 °C, the nanoemulsion droplets self-assemble into a spanning network of droplet-rich domains characteristic of arrested phase separation. Scale bars = 10 μm.

2.4.2 Mechanism of colloidal gelation

We then investigated the gelling mechanism, and a schematic of the proposed mechanism is presented in Fig. 2.2A. At room temperature, the SDS-stabilized droplets homogeneously disperse in the continuous phase containing PEGMA. However, PEGMA molecules provide a strong depletion interaction $\approx$ 30 kT (for P = 0.33 and D = 50 nm), and because the dispersion is homogeneous at room temperature, we assumed this attraction is overcome by a strong electrostatic repulsion from the charged SDS on the droplets. This hypothesis was confirmed by measuring the zeta potential of droplets, ζ, shown in Fig. 2.2B and by calculating the corresponding repulsion strength ($\approx$ 35 kT, details in later discussion). However, as temperature increased, the nanoemulsion suspension gels. We hypothesized that the gelation results from a decrease in repulsion through displacement of the ionic surfactant on the droplet surface and the strong

depletion force from the excess PEGMA molecules in solution. To validate the hypothesis, we measured ζ at elevated temperatures. We found that the magnitude of ζ decreases with temperature as shown in Fig. 2.2B while ζ is unchanged without PEGMA (Appendix A3), indicating desorption of SDS [22,75] in the presence of PEGMA. Isothermal titration calorimetry (ITC) was performed to further probe the adsorption of PEGMA. We obtained the quantitative adsorption behavior at elevated temperature by analyzing the heat associated with the adsorbing reaction (Appendix A3). As shown in Fig. 2.2B, the number of PEGMA adsorbed per droplet, n, increases with temperature. The trends of $\zeta(T)$ and $n(T)$ support the hypothesis of a thermally-triggered SDS replacement by PEGMA on the nanoemulsion surface. Upon heating, the methacrylate group on PEGMA becomes increasingly hydrophobic and partitions into the oil/water interface. The proposed mechanism is further supported by ITC results where the PEGMA adsorption is an entropy-driven process (endothermic adsorption): the dehydration of the methacrylate groups frees the water molecules and results in an increase in translational entropy [109]. Finally, we showed that ζ and n are quantitatively correlated using the Grahame equation [22] where the surface potential is estimated from the charge density (Appendix A3).

Figure 2.2 Thermally-triggered surfactant displacement mechanism. (a) Schematic of the proposed gelling mechanism. At elevated temperatures, the methacrylate groups of PEGMA partition into the oil/water interface and displace the SDS. The displacement of SDS decreases the repulsive interaction between colloids. The excess PEGMA in the continuous phase provides a significant depletion attraction, and together with the depletion from SDS micelles and the van der Waals interactions, the droplets self-assemble into gels. Contributions to the interaction potential as a function of distance are shown in the inset of (c). (b) Temperature-dependent zeta potential, ζ (blue symbols, left y-axis), and the number of PEGMA adsorbed per droplet, n (red symbols, right y-axis). As temperature increases, $|\zeta|$ decreases while n increases, supporting our hypothesis that PEGMA replaces SDS on the droplet which decreases the surface charge and electrostatic repulsion. (c) Interaction potential at rising temperatures, as a function of droplet center-to-center distance r scaled by the droplet radius a. The inset shows the contributions to the potential at T = 50.0 °C from depletion from PEGMA, depletion from SDS micelles, electrostatic repulsion and van der Waals interaction (VDW). As temperature increases, the repulsive barrier decreases, and the nanoemulsions can overcome the barrier to self-assemble into a gel.

48

2.4.3 Estimation of Interactive potentials

The overall pairwise interaction between droplets has contributions from depletion attraction arising from both PEGMA molecules and SDS micelles in solution, electrostatic repulsion and van der Waals interactions shown in Fig. 2.2C. The interactions from each contribution are depicted in Fig. 2.3. We can estimate each contribution to the pair potential to better understand the gelation. Note that in our system, the PEGMA has two roles: the non-adsorbing PEGMA molecules ($\sim 10^6$ per droplet) in the continuous phase provide the depletion interaction, and the adsorbed PEGMA molecules ($\sim 10^3$ per droplet) on the droplets lead to the decrease in electrostatic repulsion by displacing SDS.
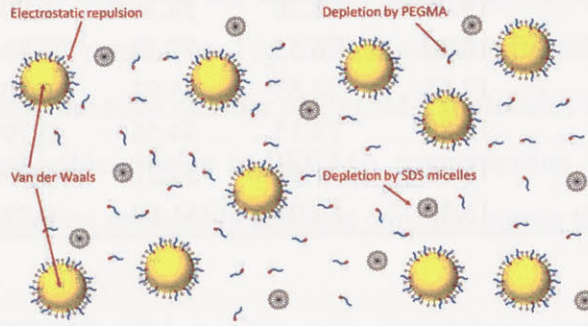
Figure 2.3 Schematic diagram of the system used for estimating the interactive potentials. A total of four interactions were considered: electrostatic repulsions, depletion by PEGMA, depletion by SDS micelles and van der Waals interaction.

2.4.3.1 Electrostatic repulsion

To estimate the electrostatic repulsion, U_{elec}, Yukawa repulsion is considered as followed [22,75],

$$U_{elec} = \varepsilon_{elec} \frac{2a}{r} e^{-\kappa(r-2a)} \qquad (2.1)$$

where a is the droplet radius and r is the droplet center-to-center distance. κ^{-1} is the Debye length and is estimated as followed,

$$\kappa^{-1} = \sqrt{\frac{\varepsilon_o \varepsilon_r kT}{1000 e^2 N_A \sum z_i^2 M_i}} \qquad (2.2)$$

where ε_o is the electric permeability of free space, k is Boltzmann constant, T is the absolute tempeature, e is the elementary charge, N_A is Avogadro's number, z is the charge number and M

is the molar concentration. ε_r is the dielectric constant of the continuous phase, which is calculated by considering the dielectic constants of water [115] and PEGMA. The dielectric constant of PEGMA is estimated from the dielectric constant of PEG backbone [116]. ε_r is then calculated using the mixing rule, which the deviation from the measured value has shown to be negligible at the high PEG concentration regime such as the case in our system [117]. Table 2.1 lists the ε_r of PEG, water and continuous phase using mixing rule, and the resulting κ^{-1} from Eq. 2.2.

Table 2.1 Dielectric constants of PEG, water and the continuous phase, and the corresponding Debye length.

T (°C)	$\varepsilon_{r,PEG}$	$\varepsilon_{r,water}$	ε_r	κ^{-1} (nm)
25	19.05	78.30	58.75	0.809
30	18.30	76.55	57.32	0.806
35	17.55	74.83	55.93	0.802
40	16.80	73.15	54.56	0.799
45	16.05	71.51	53.21	0.795
50	15.30	69.91	51.89	0.791

The strength of the electrostaic repulsion, ε_{elec}, is estimated from[22,75]

$$\varepsilon_{elec} = 32\pi\varepsilon_o\varepsilon_r \left(\frac{kT}{ze}\right)^2 \text{atanh}^2 \left(\frac{1}{4}\frac{ze\xi}{kT}\right) \tag{2.3}$$

which is obtained from Gouy-Chapman solution to Poisson-Boltzmann equation with the superposition assumption and Derjaguin approximation.

2.4.3.2 PEGMA depletion

The PEGMA depletion is the dominant attraction due to the high concentration. In fact, the depletion interaction between nano-sized colloids has been widely studied by both experiments [13,118,119] and simulations [120,121]. To estimate the depetion from non-asorbing PEGMA, Asakura-Oosawa potential is used [17,122]

$$U_{dep} = -\frac{\varepsilon_{dep}(a+\delta_P)^3}{\delta_p^2(\frac{3a}{2}+\delta_P)}\left[1-\frac{3}{4}\frac{r}{a+\delta_P}+\frac{1}{16}\left(\frac{r}{a+\delta_P}\right)^3\right] \tag{2.4}$$

when $2a \leq r \leq 2(a + \delta_p)$. Here we also assumed PEGMA is an ideal polymer. Therefore, an additional configurational entropy from the depletants contributes to the depletion strength, ε_{dep}, and the interaction range, δ_P [17]. ε_{dep} and δ_P are then calculated as

$$\varepsilon_{dep} = \phi_p \frac{a}{R_g} 3 ln 2 \tag{2.5}$$

$$\delta = \sqrt{2 ln 2} R_g \tag{2.6}$$

where ϕ_p is the depletant volume fraction and R_g is the radius of gyration of the depletant.

For the estimation, we simply assumed the morphology of the PEGMA is independent of the temperature. Moreover, the ITC result from Fig. 2.2B shows that the number of PEGMA adsorbed per droplet is $\sim O(10^3)$, while the total number of PEGMA molecules in the system per droplet is $\sim O(10^6)$, suggesting a negligible change in PEGMA concentration in solution as T increases. Therefore, the PEGMA depletion presumbly remains constant across the temperature window (25 to 50°C).

2.4.3.3 SDS micelle depletion

Depletion by SDS micelles is also estimated using Asakura-Oosawa potential. By assuming the micelles behave like hard-spheres, the micelle depletion is calculated as follows [17,52,123],

$$U_{dep} = -(\xi C_m kT) \left(\frac{\pi a}{2} \left(d_{m,eff} - (r - 2a) \right)^2 \right) \tag{2.7}$$

when $2a \leq r \leq 2a + d_{m,eff}$, and

$$\xi = \frac{1 + \phi_{m,eff} + \phi_{m,eff}^2 - \phi_{m,eff}^3}{\left(1 - \phi_{m,eff} \right)^3} \tag{2.8}$$

where $\phi_{m,eff}$ is the effective volume fraction of micelles by considering the Debye layer [7] and is calculated as

$$\phi_{m,eff} = \frac{4\pi}{3} \left(\frac{d_{m,eff}}{2} \right)^3 C_m = \frac{4\pi}{3} \left(\frac{d_m + 2\kappa^{-1}}{2} \right)^3 C_m \tag{2.9}$$

C_m is the concentration of the micelle and is calculated as

$$C_m = \frac{(C_o - C_{ads} - C_{CMC})N_A}{N_{agg}}$$

(2.10)

where C_o is the total concentration od SDS, C_{ads} is the concentration of SDS adsopbed on the droplets, C_{CMC} is the critical micelle concentration (≈ 8 mM) [110,124,125], and N_{agg} is the aggregation number of micelle (≈ 60) [110,124,125]. For the estimation, we assume the morphology of the micelles is independent of the temperature.

2.4.3.4 Van der Waals interaction

Van der Waals interaction is estimated as followed [22],

$$U_{VDW} = \frac{-Aa}{12(r - 2a)}$$

(2.11)

by assuming a uniform droplet size and Derjaguin approximation is used. Here, $A = 3.3 \times 10^{-22} J$ is the Hamaker constant of PDMS-water-PDMS [126,127].

2.4.3.5 Overall pairwise interaction

As shown in Fig. 2.2C, increasing temperature leads to a decrease in the repulsive barrier, and the system can more easily overcome this energetic barrier to self-assemble and undergo gelation. We acknowledge the quantitative behavior of the potentials may not be precisely captured, but the estimations provide mechanistic insight to explain trends in material microstructures and rheological properties (shown in Fig. 2.4 and Appendix A2).

2.4.4 Effect of material composition

Controlled gelation via this mechanism is general and robust over a wide range of composition, colloid size and component chemistry. We tested the gelling mechanism by investigating the material phase behavior (T_{gel}) and gel elasticity (G_P) over a wide range of formulations. First, we demonstrated that nanoemulsion gelation can be robustly controlled over a wide range of

composition, P shown in Fig. 2.4A and Fig. 2.4B and ϕ shown in Fig. 2.4C and Fig. 2.4D. We found that T_{gel} decreases significantly with P for $0.13 \leq P \leq 0.35$, indicating the gelation is more easily induced when more depletants are present. In contrast, T_{gel} increases mildly with ϕ for $0.1 \leq \phi \leq 0.35$, which is contrary to common colloidal systems where larger ϕ facilitates the gelation. We believe such trend with respect to ϕ results from a decrease in SDS micelles and electrostatic screening [52]. To validate this postulate, we studied the effect of [SDS] on the properties of the nanoemulsion gels (Appendix A2). The results are consistent with our predicted trend wherein a decrease in the total [SDS] leads to an increase in the gelation temperature and a decrease in the gel strength. For data in Fig. 2.4, we kept the total [SDS] = 0.175M constant, so more SDS remains in the continuous phase with smaller ϕ, leading to stronger micelle depletion and electrostatic screening.
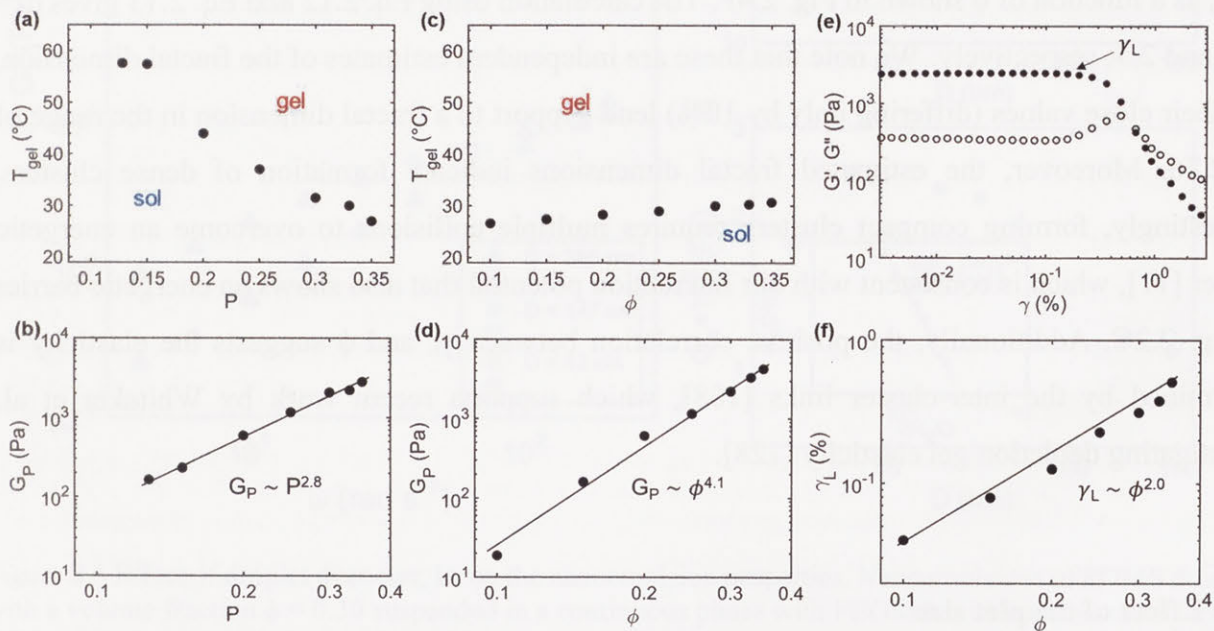
Figure 2.4 Gelling mechanism is robust over a wide range of compositions. (a) T_{gel} as a function of PEGMA volume fraction in the continuous phase, P. (b) G_P as a function of P showing a power-law dependence of $G_P \sim P^{2.8}$. Nanoemulsions in (a) and (b) are composed of PDMS droplet with $D = 50 \pm 1$ nm and a volume fraction $\phi = 0.30$. (c) T_{gel} as a function of ϕ. Because the bulk SDS concentration decreases with increasing ϕ, T_{gel} decreases slightly due to weaker micelle depletion attraction. (d) G_P as a function of ϕ, showing a power-law dependence of $G_P \sim \phi^{4.1}$. Nanoemulsions in (c) and (d) are composed of PDMS droplet with $D = 50 \pm 1$ nm dispersed in the continuous phase with P = 0.33. (e) G' and G" as a function of the shear strain, γ. The strain at the limit of linearity, γ_L, is the strain at which G' and G" begin to change with γ. The nanoemulsion used here is composed of PDMS droplet with $D = 50$ nm and $\phi = 0.30$ suspended in the continuous phase with P = 0.33. (f), γ_L as a function of ϕ, showing a power-law dependence of $G_P \sim \gamma^{2.0}$.

We also investigated G_P as a function of P and ϕ. With increasing P, G_P increases over one order of magnitude as a power-law $G_P \sim P^{2.8}$, which is quantitatively consistent with colloidal gels

assembled by depletion attractions alone [104]. As ϕ increases, G_P increases over two orders of magnitude as a power-law $G_P \sim \phi^{4.1}$. Shih et al. suggested a scaling behavior relating macroscopic rheological properties to microstructures [108]: by assuming the gel network is composed of aggregated clusters, the scaling behavior of G_P with ϕ provides the gel structural information in terms of the cluster fractal dimension [108], d_f:

$$G_P \sim \phi^x, \qquad x = \frac{1}{3 - d_f} \tag{2.12}$$

$$\gamma_L \sim \phi^y, \qquad y = \frac{1}{3 - d_f} \tag{2.13}$$

To conduct the scaling analysis, we measured the strain at the limit of linearity, γ_L as shown in Fig. 2.4E, as a function of ϕ shown in Fig. 2.4F. The calculation using Eq. 2.12 and Eq. 2.13 gives $d_f =$ 2.76 and 2.5, respectively. We note that these are independent estimates of the fractal dimension, and their close values (differing only by 10%) lend support to a fractal dimension in the range of 2.5-2.76. Moreover, the estimated fractal dimensions indicate formation of dense clusters. Interestingly, forming compact clusters requires multiple collisions to overcome an energetic barrier [11], which is consistent with our interaction potential that also shows an energetic barrier in Fig. 2.2C. Additionally, the positive correlation between γ_L and ϕ suggests the elasticity is determined by the inter-cluster links [108], which supports recent work by Whitaker et al. investigating depletion gel elasticity [128].

2.4.5 Effect of droplet size

The microstructure of our gel shown in Fig. 2.1C is consistent with the prediction from mode-coupling theory (MCT) where the attractive glass line penetrates into the spinodal regime and the gelation is through an arrested phase separation [129,130]. To further compare to MCT, we probed the system properties as a function of droplet size (Fig. 2.5). We found that gelation only occurs for droplets with D < 150 nm, and a stronger gel was obtained as D decreased as shown in Fig. 2.5A and 2.5C. We also observed a broad minimum in G" in Fig. 2.5A, which is a reminiscent of glassy dynamics [1,11]. Within the gelation regime, T_{gel} decreases with D as shown in Fig. 2.5B, which is consistent with MCT where gelation is more easily induced with larger D [130]. Inspired by MCT, we then expect a power law scaling of the normalize plateau modulus $G_P D^3 / kT$ with

$2R_g/D$ where $R_g = 0.55$ nm is the radius of gyration of PEGMA. The resulting figure in Fig. 2.5C shows that $G_P D^3/kT$ exhibits a power law behavior with $2R_g/D$ with an exponent of -2.2, which is in good agreement with the MCT prediction of -2.0 [130]. Overall, the analyses show that the properties of our model nanoemulsion are in good agreement with theoretical studies, and predictions can be made about the expected behavior of this platform system.
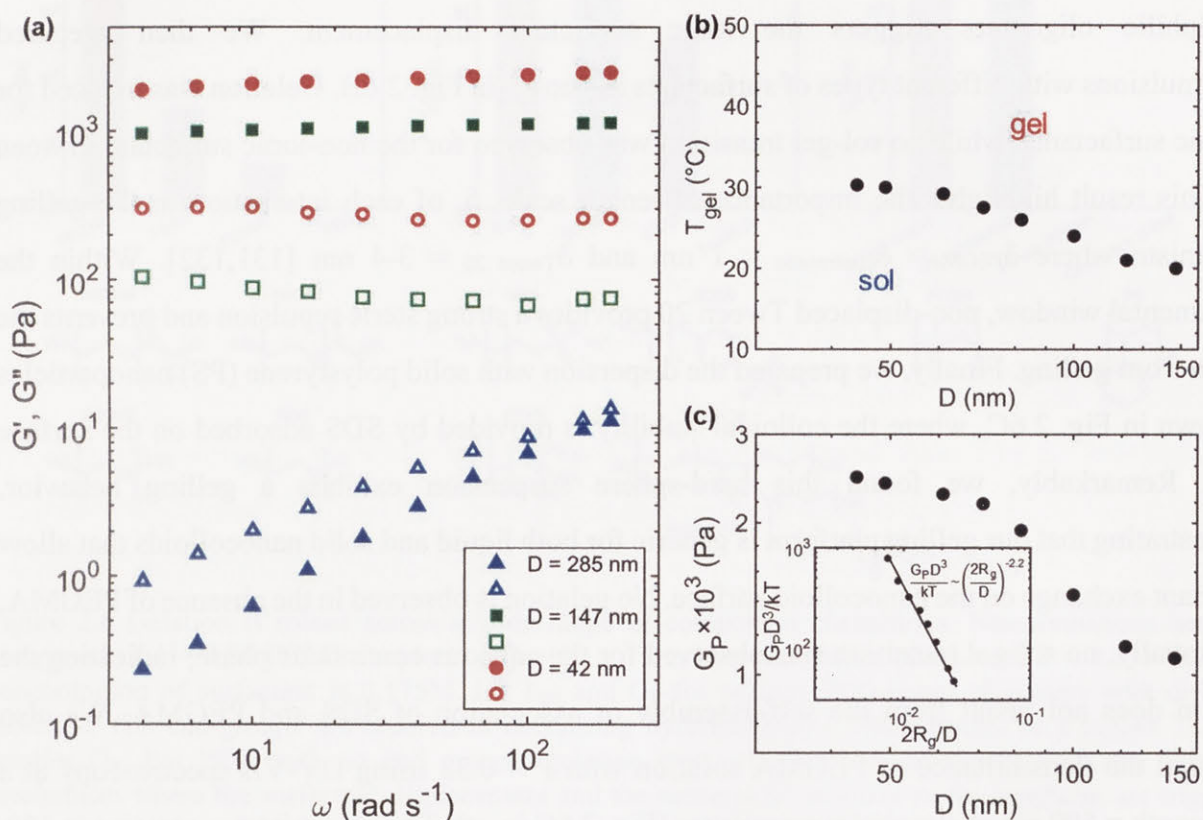
Figure 2.5 Effect of droplet diameter, D, on the nanoemulsion properties. Nanoemulsions of PDMS droplets with a volume fraction $\phi = 0.30$ suspended in a continuous phase with PEGMA with a volume fraction P = 0.33. (a) Linear viscoelasticity (G': closed symbols, G'': open symbols) of the nanoemulsion with different D at T = T_{gel} + 25 °C. No gelation was observed across the experimental temperature window for D > 150 nm. Within the gelation regime (D < 150 nm), stronger gels are obtained for smaller D. Additionally, G'' of the gel shows a broad minimum at moderate angular frequencies, which is reminiscent of glassy dynamics indicating a transition from α- to β-relaxation. (b) Gelation temperature, T_{gel}, as a function of D. For smaller D, a higher temperature is required to induce gelation. (c) Plateau modulus, G_P, as a function of D. The inset shows the normalized plateau modulus, $G_P D^3/kT$, as a function of normalized PEGMA depletion length scale, $2R_g/D$, where R_g is the radius of gyration of PEGMA. The result shows a power-law behavior with an exponent = -2.2, consistent with predictions of mode-coupling theory (MCT).

2.4.6 Robustness of the gelling platform

Finally, we investigated the gelling mechanism across a wide range of component chemistries (Fig. 2.6). We first prepared nanoemulsions with PEG-based oligomers of different moieties as shown in Fig. 2.6A. Gelation was induced with all amphiphilic oligomers, and the less hydrophobic PEG results in higher T_{gel} and smaller G_P. No gelation was observed with non-modified PEG. The observation from oligomer chemistry supports our proposed mechanism where the dehydration of amphiphilic oligomers triggers the ionic surfactant displacement. We then prepared nanoemulsions with different types of surfactants as shown in Fig. 2.6B. Gelation was induced for all ionic surfactants, while no sol-gel transition was observed for the non-ionic surfactant (Tween 20). This result highlights the importance of length scale, δ, of each interaction in the gelling mechanism where $\delta_{PEGMA} \approx \delta_{electrostatic} \approx 1$ nm and $\delta_{Tween\ 20} \approx 3\text{-}4$ nm [131,132]. Within the experimental window, non-displaced Tween 20 provides a strong steric repulsion and prevents the system from gelling. Finally, we prepared the dispersion with solid polystyrene (PS) nanoparticles as shown in Fig. 2.6C, where the colloidal stability is provided by SDS adsorbed on the surface [101]. Remarkably, we found this hard-sphere suspension exhibits a gelling behavior, demonstrating that our gelling platform is generic for both liquid and solid nanocolloids that allow surfactant exchange on the nanocolloid surface. No gelation is observed in the absence of PEGMA. Additionally, no sol-gel transition was observed for the aqueous continuous phase, indicating the gelation does not result from the self-assembly or association of SDS and PEGMA. We also measured the transmittance of PEGMA solution with P = 0.33 using UV-Vis spectroscopy at a wavelength = 500 nm at elevated temperatures (Fig. 2.6C inset). The transmittance remains at 100 % across the experimental temperature window and no phase separation is observed, suggesting PEGMA stably stays in the water. We note that the gelation mechanism presented here is different from our prior work where the gelation is through polymer bridging via di-functional gelators [21,33,101,105].
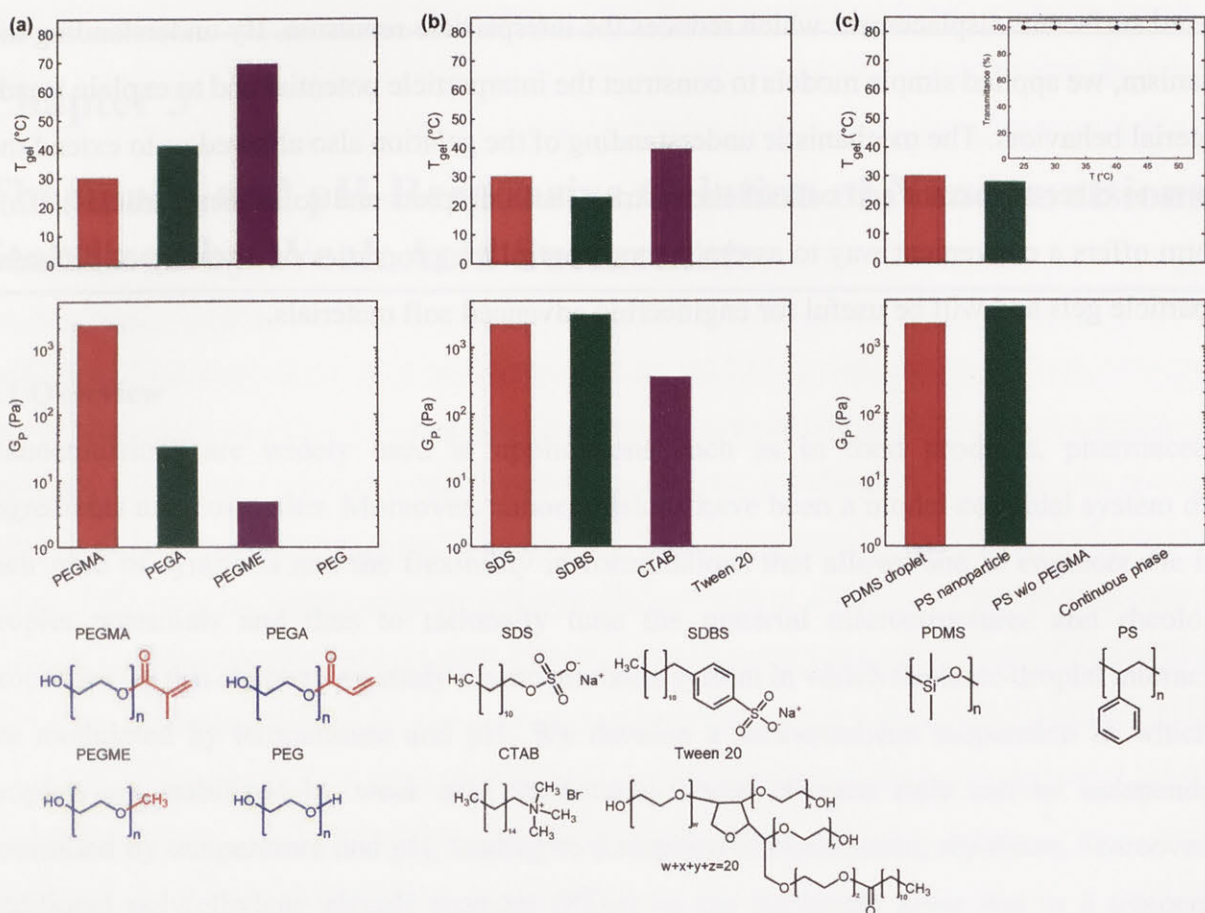
Figure 2.6 Gelation is robust across a wide range of component chemistries. Nanoemulsions here are composed of $\phi = 0.30$ PDMS droplets of $D = 50 \pm 1$ nm in a continuous phase with $P = 0.33$. The total concentration of surfactant is 0.175M. (a) T_{gel} and G_P for various PEG-based oligomers with different moieties. The end-groups are ordered in decreasing hydrophobicity which results in a higher T_{gel} and smaller G_P. For PEG with no end groups, gelation was not observed, consistent with our proposed mechanism where the surfactant displacement and the subsequent decrease in the repulsion are triggered by the dehydration of the functional end-group (Fig 2.2A). (b) T_{gel} and G_P for various surfactants. Gelation was observed for all ionic surfactants, while no sol-gel transition was observed for the non-ionic surfactant (Tween 20) across the experimental temperature window. (c) T_{gel} and G_P for two different nanoparticles. Gelation occurs for both liquid PDMS droplets and solid polystyrene (PS, $D = 58$nm and $\phi = 0.30$) colloids. No gelation is observed with the absence of PEGMA. Additionally, no sol-gel transition was observed for the aqueous continuous phase, indicating the gelation does not result from the self-assembly or association of SDS and PEGMA. Inset: Transmittance of a pure PEGMA aqueous solution ($P = 0.33$) as a function of temperature using UV-Vis spectroscopy at a wavelength = 500 nm.

2.5 Conclusion

Overall, we presented a colloidal gelation platform whose microstructure and mechanical properties can be controlled easily and reliably using an external temperature source. We systematically investigated the gelation mechanism and confirmed that it is due to thermally-

triggered surfactant displacement which reduces the interparticle repulsion. By understanding the mechanism, we applied simple models to construct the interparticle potential and to explain trends in material behaviors. The mechanistic understanding of the gelation also allowed us to extend the platform to other surfactant and colloid chemistries (both droplets and solid nanoparticles). This platform offers a convenient way to assemble and control the properties of a variety of different nanoparticle gels and will be useful for engineering advanced soft materials.

Chapter 3

Thermally and pH-Responsive Gelation of Nanoemulsions Stabilized by Weak Acid Surfactants

3.1 Overview

Nanoemulsions are widely used in applications such as in food products, pharmaceutical ingredients and cosmetics. Moreover, nanoemulsions have been a model colloidal system due to their ease of synthesis and the flexibility in formulations that allows one to engineer the inter-droplet potentials and thus to rationally tune the material microstructures and rheological properties. In this chapter, we study a nanoemulsion system in which the inter-droplet interactions are modulated by temperature and pH. We develop a nanoemulsion suspension in which the droplets are stabilized by weak acid surfactants whose charged state can be independently controlled by temperature and pH, leading to a responsive electrostatic repulsion. Moreover, the additional poly(ethylene glycol) segment (PEG) on the surfactant gives rise to a temperature responsive attraction between droplets via PEG-PEG association and ion-dipole interaction. The interplay of these three interactions gives rise to non-monotonic trends in material properties and structures as a function of temperature. The underlying mechanism resulting in these trends is obtained by carefully characterizing the nanoemulsion droplets and studying the molecular interactions. Such mechanistic understanding also provides guidance to modulate the inter-droplet potential using pH and ionic strength. Moreover, the molecular understanding of the weak acid surfactant also sheds light on the destabilization of the nanoemulsion droplets triggered by a switch in pH. The control of the competition of attractive and repulsive interactions using external stimuli opens up the possibility to design complex nanoemulsion-based soft materials with controllable structures and rheological properties.

This chapter has been adapted with permission from L. -C. Cheng, S. M. Hashemnejad, B. Zarket, S. Muthukrishnan and P. S. Doyle "Thermally and pH-Responsive Gelation of Nanoemulsions Stabilized by Weak Acid Surfactants" *Journal of Colloid and Interface Science* 2020, 563, 229-240. Copyright 2020 Elsevier Inc.

3.2 Introduction

Nanoemulsions are kinetically stable liquid-liquid suspensions where one immiscible liquid disperses in another with droplet size on the order of 10 to 100 nm. The nanoscale droplet size leads to robust stability, large interfacial area and optical transparency, which has made nanoemulsions a popular topic in the field of colloidal and interface science for the past two decades [6]. Moreover, the small lipophilic domains can be further utilized in applications such as nano-reactors for polymerizations [133,134] or nano-cargos in food products [28,38,135]. The other important feature of nanoemulsions is the ease of synthesis in which new formulations can be easily synthesized. Such flexibility allows researchers to modulate the interactions between droplets and hence the material properties, making nanoemulsion a versatile material in diverse fields such as in sensors [136,137], cosmetics [26], and the complex material design [86]; and a compelling model system for studying colloidal behavior such as suspension rheology [7], self-assembly [8] and gelation [10].

Nanoemulsions that undergo gelation have attracted much attention in both fundamental studies [10,32,60] and practical applications [9,33]. Gelation of nanoemulsions, or for general colloidal suspensions, is controlled by modulating the interactions between the droplets, and the gelation can be induced by manipulating either attractive or repulsive interactions. For attraction-driven gelling systems, one common way to induce gelation is via a depletion interaction. By adding depletants to the continuous phase, these non-adsorbing species are excluded from the vicinity of the droplets, leading to an imbalance in the osmotic pressure. This osmotic pressure acts as a net attractive force between the droplets, ultimately giving rise to the gelation [17,122]. Different depletants including surfactant micelles [51,52] and non-adsorbing polymers [9] have been used to obtain gelling nanoemulsions. On the other hand, gelation of nanoemulsions can also be induced by modulating repulsions. Perhaps the most widely seen approach is the screening of electrostatic repulsion by adding the electrolytes into charged-stabilized nanoemulsion suspensions. The addition of electrolytes reduces the effective length scale of the electrostatic repulsion, leading to the emergence of a secondary minimum in the interactive potential and eventually inducing the gelation [15,22]. Another example utilizing electrostatic repulsion, so-called repulsive gelation [52], to obtain nanoemulsion gels is through the increase of effective oil volume fraction in electrostatically-stabilized emulsion systems [8,25]. The effective oil volume fraction (ϕ_e) is calculated by considering the actual oil volume fraction (ϕ_a) and the excluded volume resulted

60

from the repulsive charge cloud that extends from the oil/water interface (i.e. Debye length, κ^{-1}), and $\phi_e = \phi_a(1 + \kappa^{-1}/a)^3$ where a is the droplet radius. As the droplet size decreases, ϕ_e increases. When ϕ_e is greater than the maximum random jamming limit, a viscoelastic nanoemulsion gel is obtained.

Our group has been designing and studying nanoemulsion systems in which gelation is triggered by an external stimulus — an increase in temperature [21,138,139]. By understanding the inter-droplet interactions at a molecular level, we have designed various thermally-gelling nanoemulsions in which the system experiences a sol-gel transition at elevated temperatures. For example, by adding telechelic oligomers where both ends of the hydrophilic backbone are functionalized with hydrophobic moieties to the continuous phase, the oligomers act to bridge droplets upon increasing the temperature and ultimately lead to gelation [21,98]. On the other hand, we also designed another thermally-gelling mechanism by including non-ionic amphiphilic oligomers in charged-stabilized oil-in-water nanoemulsions [138]. At elevated temperatures, the non-ionic oligomers replace the ionic surfactants on the droplets. Such displacement leads to a dramatic decrease in the electrostatic repulsion and gives rise to gelation. Finally, we also developed a gelling nanoemulsion by adding a small-amount of Pluronic copolymers to the continuous phase. We hypothesized that the gelation at elevated temperatures is induced through jamming via the formation of copolymer micelles and the increase of ϕ_e by the adsorption of copolymers onto the droplets [139]. Overall, these external-stimuli responsive systems enhance the ability for material processing and manipulation, which benefits not only the fundamental research such as studying the effect of processing history on the material behaviors [105] but also practical applications such as the design of hierarchical structured hydrogels [33]. However, for both fundamental studies and applications, it would be desirable to develop systems that respond to another stimulus in addition to temperature. For example, systems that are responsive to the change of pH can be utilized for skincare products [140,141] or enhanced oil recovery [142].

In this chapter, we report a gelling nanoemulsion system in which the material properties are responsive to temperature and pH. The nanoemulsion is synthesized through a low-energy route, and the droplets are stabilized using a weak acid surfactant containing a PEG segment and a carboxyl group. The deprotonation of the carboxyl group greatly influences the behavior of the nanoemulsion. The material behavior is characterized by rheometry and confocal microscopy

[14,128,143–146]. This new nanoemulsion system shows a non-intuitive behavior that is very different from all of the prior thermally-gelling systems our group has studied. At elevated temperatures, the viscoelastic moduli first increase, then decrease and finally increase again, and the microstructures of the assembled nanoemulsion also show the same non-monotonic trend. This non-intuitive trend is explained by the non-monotonic increase in the net attraction due to the competition between repulsive and attractive interactions, which are investigated by measuring the zeta potential of the nanoemulsion droplets and comparing our system with the studies in the literature. We hypothesize that the association between PEG segments and charged carboxylate groups are responsible for the changes in the inter-droplet interactions. Armed with this mechanistic understanding, we further show that the thermally-responsive rheological properties of the nanoemulsion can be modulated through the change of pH and ionic strength. Moreover, with the knowledge of the molecular geometry of the surfactants, we also demonstrate that the nanoemulsion droplets can be destabilized by changing the pH of the system. This work opens up the opportunity to design multi-stimuli responsive nanoemulsion systems by controlling the chemical moieties of the surfactants adsorbed on the droplets.

3.3 Materials and methods

3.3.1 Materials

Isopropyl myristate (IM, purity $\geq$ 98%), laureth-11 carboxylic acid ($M_n \approx$ 690 g/mol, impurities: NaCl $\leq$ 1.5%, water = 8-12%), lauric acid (purity $\geq$ 98%), sodium hydroxide (NaOH, purity $\geq$ 97%), sodium chloride (NaCl, purity $\geq$ 99%) and Nile Red (purity $\geq$ 98%) were purchased from Sigma Aldrich. Poly(ethylene glycol) (PEG400, M_n = 400 g/mol, purity $\geq$ 98%) was purchased from TCI Chemicals. All chemicals were used without further purification.

3.3.2 Nanoemulsion synthesis

The oil-in-water nanoemulsion contained IM droplets (weight fraction ϕ = 12.5 wt%) stabilized by a mixture of carboxylic acid-based surfactants composed of laureth-11 carboxylic acid (12.5 wt%) and lauric acid (3.13 wt%), and a co-surfactant PEG400 (9.38 wt%) [139] suspended in the de-ionized water. The hydrophilic-lipophilic balance (HLB) of the mixed surfactant is 13. We have

also demonstrated that it is important to use the co-surfactant to stabilize the nanoemulsion by measuring the size of the droplets over time at various PEG400 concentrations (Appendix B Fig. B1).

We used the Phase Inversion Composition (PIC) method to synthesize the nanoemulsions which provides a low-energy route to obtain nano-sized droplets [6]. For synthesis, a homogeneous oil mixture containing IM, surfactants and co-surfactants was first prepared. Next, the de-ionized water was added drop-wisely into the oil mixture under a constant stirring using a magnetic stirrer bar. The stirring speed was kept at 1100 rpm throughout the synthesis. This approach is called the PIC method since the continuous phase is added into the disperse phase. During the addition, at some critical point which is known as phase inversion point, the oil-water interface experiences an ultra-low interfacial tension which facilitates the formation of nano-sized droplets [36,147]. We measured the droplet size and the polydispersity by using dynamic light scattering (90Plus PALS, Brookhaven Instruments) after diluting the nanoemulsion to $\phi = 0.5$ wt% using de-ionized water. In our system, the resulting droplet diameter is 20 nm with a polydispersity ≈ 0.08.

3.3.3 pH measurement

The pH of nanoemulsions was measured using a pH meter (Orion Star™ A215, ThermoFisher Scientific) equipped with an Orion™ ROSS Ultra™ Refillable pH/ATC Triode™ electrode. All the measurements were performed at 20 °C. For the different pH values studied in this work, pH was adjusted using NaOH. The reported pH values were obtained by measuring the pH of the whole nanoemulsion suspension (both continuous phase and the droplets).

3.3.4 Rheological characterization

The rheological properties of the nanoemulsion were measured by using a stress-controlled rheometer (DHR-3, TA instrument) equipped with a 2° 40 mm upper-cone and a temperature-controlled Peltier lower-plate. To prevent evaporation of the sample, a solvent trap was used and a few drops of water were added on top of the cone. Before each measurement, a conditioning procedure was applied to the sample: a pre-shear step was applied by performing a constant rotation at a speed of 10 rad/s for 30 seconds, followed by a 60-second period where the sample

stayed quiescently on the rheometer. The whole conditioning step was kept at 20.0 °C in order to eliminate any possible thermal history effect [105]. In the pre-shear step, no gelation or self-assembly of the nanoemulsion suspension is obtained (as shown in Fig. 3.1 and Fig. 3.2 where the rheology is reported, and Fig. 3.3 where the confocal images are reported). Therefore, this pre-shear step has no influence on the gel structures and the associated rheological properties when the temperature is increased.

Frequency-sweep and temperature-ramp measurements were performed using small-amplitude oscillatory shear (SAOS) at a shear strain $\gamma = 0.05\%$. For frequency-sweep measurements, the storage modulus, G', and the loss modulus, G", at various temperatures, T, with angular frequency $\omega = 1$ to 100 rad/s were measured. Before each measurement, the temperature was kept at the target T for 30 min. For temperature-ramp measurements, G' and G" were measured as a function of temperature at a fixed angular frequency $\omega = 25$ rad/s. The nanoemulsion droplets stay stable over the experimental temperature window by monitoring the droplet size as a function of temperature (Appendix B Fig. B2). For each measurement, the fresh nanoemulsion was loaded on the rheometer.

3.3.5 Zeta potential

Zeta potentials of the nanoemulsion droplets with different temperatures and pH were measured by a Brookhaven Instruments 90Plus PALS zetasizer. Before each measurement, the mother nanoemulsion ($\phi = 12.5$ wt%) was freshly diluted to $\phi = 0.5$ wt%. For each measurement, the fresh nanoemulsion was loaded.

3.3.6 Confocal microscopy

The microstructures of the assembled nanoemulsion at various temperatures were captured using a confocal laser scanning microscope (LSM 700, Zeiss) equipped with a 63× oil-immersion objective. The temperature was controlled using an objective warmer (OW-1, Warner Instruments) and a microscope heating stage (Heating Insert P S1, Zeiss) equipped with a temperature controller (TempModule S1, Zeiss). The temperature was independently calibrated by an additional digital thermometer (#51 II, Fluke).

For visualization, IM was fluorescently labeled by dissolving Nile Red in IM at a concentration of 0.1 mg/g before the nanoemulsion synthesis. The spatial resolution of the confocal microscope is ≈ 200 nm. Therefore, the individual nanoemulsion droplets (size range from 20 to 110 nm) cannot be detected. To visualize the microstructures, the nanoemulsion was loaded in a homemade cylinder-shaped glass chamber using Secure-Seal™ spacers. The resulting chamber is with a height ≈ 500 μm and a diameter ≈ 9 mm. A small diameter ensures the thermal homogeneity throughout the sample [101]. Before the images were taken, the nanoemulsion-filled chamber was mounted on the heating plate at the target T for 30 minutes. Fresh samples were used for each rheological characterization and confocal imaging (i.e. the samples after rheological measurements were discarded and not reused for confocal imaging).

3.4 Results and discussion

3.4.1 Thermally-responsive nanoemulsions

Our nanoemulsion is a liquid at room temperature, but transitions into a viscoelastic gel upon heating. However, when the temperature (T) is further increased, the mechanical strength decreases and then increases again. We quantitatively studied this interesting phase behavior using the small-amplitude oscillatory shear rheometry. Fig. 3.1 shows the schematic of the nanoemulsion suspension and the dynamic viscoelastic moduli (storage modulus G' and loss modulus G") as a function of angular frequency (ω) at elevated temperatures. At T = 20 and 25 °C, the nanoemulsion shows a liquid behavior where $G''(\omega) \sim \omega^1$ [2]. When T is increased, $G'(\omega)$ and $G''(\omega)$ increase and the system undergoes a sol-gel transition. Eventually, $G'(\omega)$ is larger than $G''(\omega)$, suggesting the nanoemulsion has transitioned from a liquid at room temperature to a viscoelastic gel at T = 35 °C.

Surprisingly, G' and G" decrease as T is further increased, as shown in Fig. 3.1C. The trend in the viscoelastic moduli as a function of temperature can be more clearly seen in Fig. 3.2. The decrease in G' and G" remains until T reaches 45 °C. However, when T is further increased, G' and G" increase again, and such increase remains within our experimental temperature window, as shown in Fig. 3.1D and Fig. 3.2. We also noticed that the gel strength of this nanoemulsion (the largest G' is $\sim 10^0$ to 10^1 Pa) is significantly smaller than the prior thermally-gelling nanoemulsions our group has developed ($G' \sim 10^4$ to 10^5 Pa) [21,138,139]. The data reported in Fig. 3.2, as well as

Fig. 3.1, are all above the rheometer's torque limit. Data that cannot be measured are not presented (e.g. the storage modulus G' at T = 20 and 25 °C). We also show that the trend in Fig. 3.2 is statistically significant as the change in viscoelastic moduli is well above the standard errors (Appendix B Fig. B3).
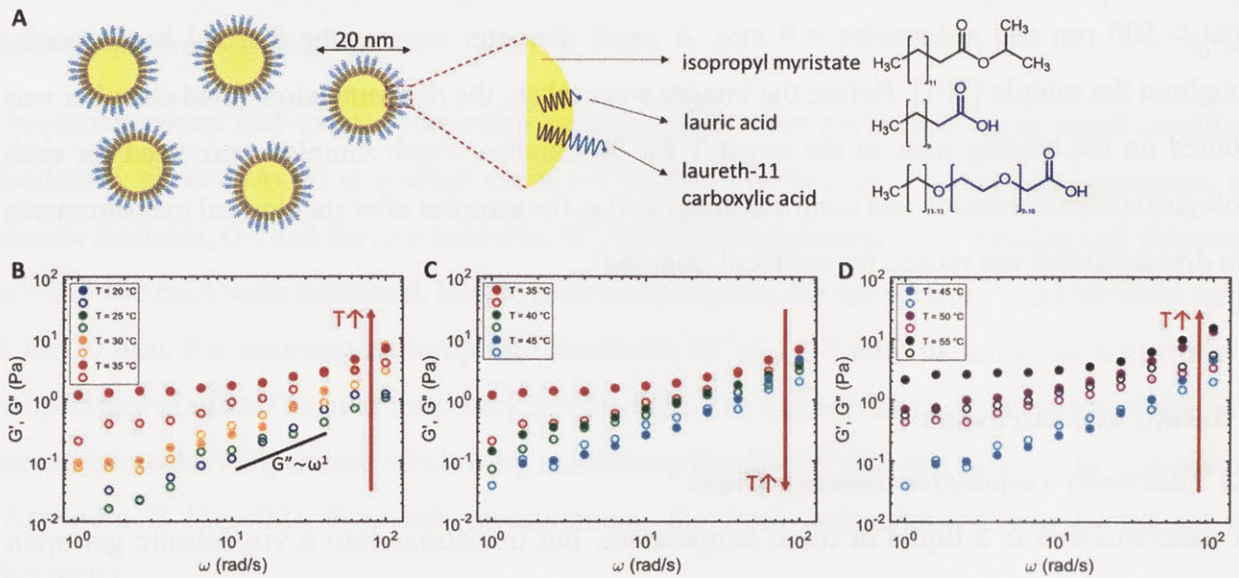
Figure 3.1 Schematic of the nanoemulsion suspension and the linear viscoelastic moduli (closed: G', open: G'') as a function of angular frequency (ω) at elevated temperatures. The pH of the nanoemulsion is 2.5. (A) The schematic of the nanoemulsion suspension. Upon increasing the temperature, viscoelastic moduli (B) first increase, (C) then decrease, and (D) finally increase again.
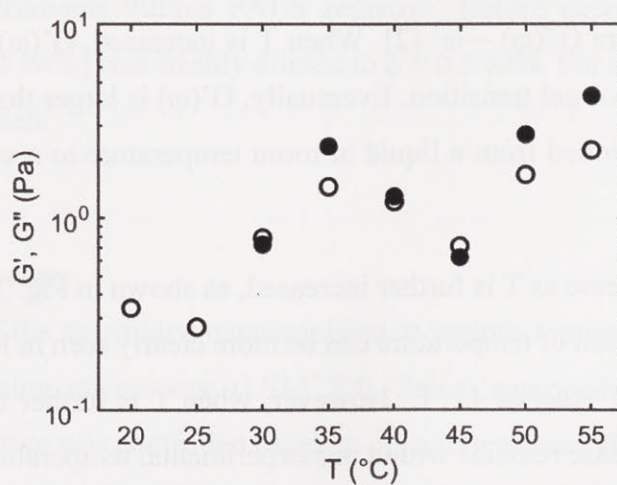
Figure 3.2 Linear viscoelastic moduli (closed: G', open: G'') as a function of temperature at an angular frequency ω = 25 rad/s from Fig. 3.1 (see Appendix B Fig. B3 with data with error bars).

3.4.2 Direct visualization of microstructures

Rheological properties of materials are dictated by their microstructures. Here, the microstructure of the nanoemulsion as a function of temperature was captured by confocal microscopy. Representative confocal images of self-assembled nanoemulsions are shown in Fig. 3.3. The oil droplets are fluorescently labeled using Nile Red. At room temperature, the image shows a red blur, suggesting that nanoemulsion droplets are homogeneously dispersed in the continuous phase. This is because the resolution limit of our confocal microscopy setup is ≈ 200 nm at which single droplets (diameter = 20 nm) cannot be visualized. When T is increased to 30 °C, a connected network begins to form, corresponding to the rheological sol-gel transition observed in Fig. 3.1B. While it is difficult to obtain 3D reconstructed images of the assembled microstructures by confocal microscopy due to turbidity, the 2D images suggest that the network is very sparse. This observation is similar to our prior work on a different thermally-gelling nanoemulsion which also shows a very sparse gel network in 2D confocal images near the gel point [101]. At T = 35 °C, a well-connected gel network is observed, which is again consistent with the viscoelastic gel from Fig. 3.1B.

When T is continuously increased to 40 and 45 °C, the gel network appears to break down into separate domains. The broken network is exhibited as cloud-like structures in Fig. 3.3 at T = 40 and 45 °C. This visual breakup of the network is consistent with the rheological response shown in Fig. 3.2 where the viscoelastic moduli decrease when T is increased from 35 to 45 °C. Finally, when T is further increased to 50 °C, remarkably, the nanoemulsion again assembles into a well-connected gel network, corresponding to the recovery of the viscoelastic moduli in Fig. 3.2 when T is increased to 50 °C and above.
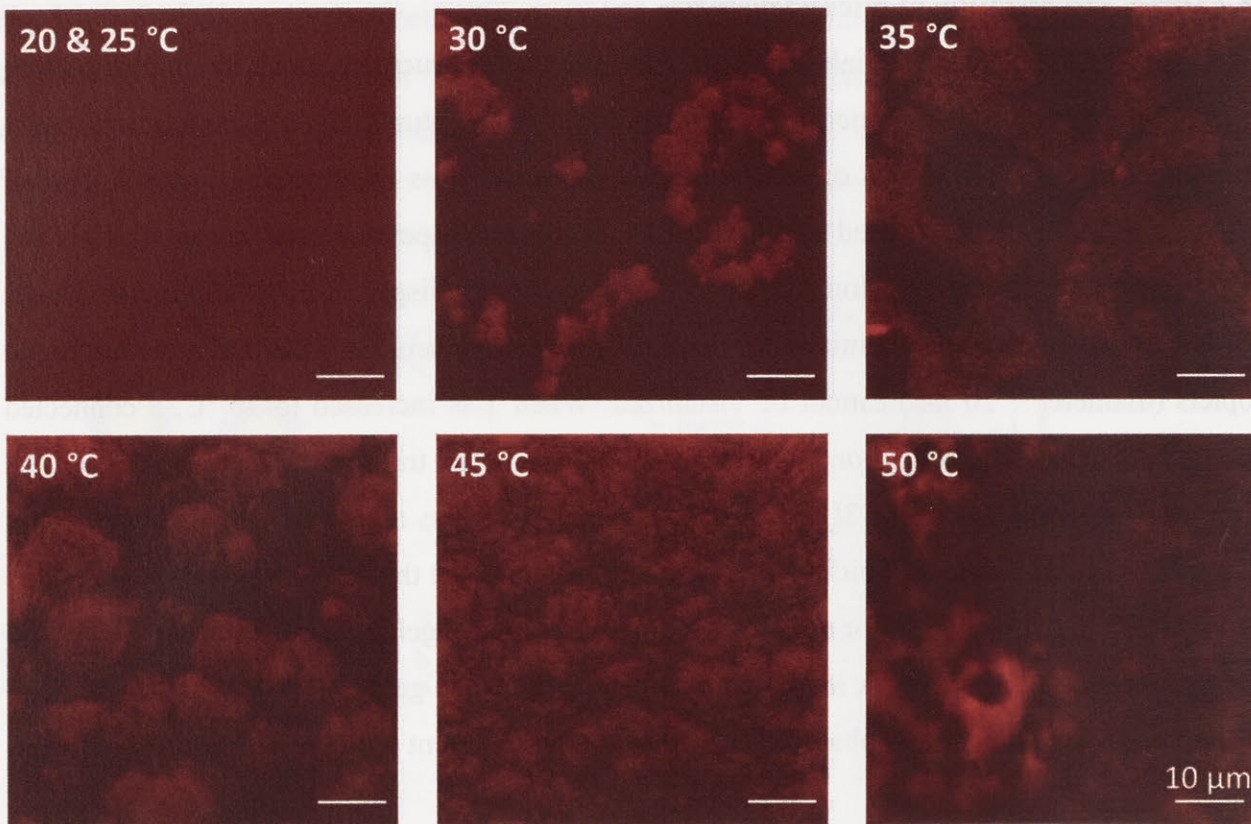
Figure 3.3 Microstructures of the nanoemulsion (pH = 2.5) at elevated temperatures using confocal microscopy. The oil droplets are fluorescently labeled using Nile Red. Scale bars = 10 μm.

3.4.3 Proposed mechanism of nanoemulsion gelation

Colloidal gelation is a result of the competition between attractive and repulsive interactions. Colloidal suspensions, as well as nanoemulsions, gel when the attractive interaction overcomes the repulsive interaction. Therefore, the non-intuitive trend in the viscoelastic moduli of our nanoemulsion (Fig. 3.1 and Fig. 3.2) suggests a non-monotonic increase in the net attraction due to the competition between attractive and repulsive interactions between nanoemulsion droplets as a function of temperature. In the following text, we will discuss the sources of both interactions.

3.4.4.1 Repulsive interaction

In our system, the nanoemulsion droplets are stabilized by carboxylic acid surfactants (12.5 wt% laureth-11 carboxylic acid and 3.13 wt% lauric acid). At room temperature, the weak acid surfactants are uncharged and the PEG segments on droplets provide the steric repulsion that gives

rise to the colloidal stability of the nanoemulsion. However, this steric repulsion is most likely not responsible for the increase in the repulsive interaction as a function of temperature as the number density of the surfactant is not modulated. Therefore, we hypothesized that the dissociation of the carboxylic acids leads to a temperature-dependent electrostatic repulsion between the droplets, as illustrated in Fig. 3.4A. To validate this hypothesis, we measured the zeta potential (ζ) of the nanoemulsion droplets as a function of temperature, and the result is shown in Fig. 3.5A. At room temperature, the droplets are nearly uncharged, suggesting the dissociation of the carboxyl group is negligible. However, as the temperature is increased to 35 °C, a decrease in ζ is observed. Such decrease indicates the dissociation of the carboxyl group is promoted when the temperature is increased, and the negative value of ζ strongly supports that it is the residual carboxylate group on the droplet that gives rise to the surface charge, and hence the increase in the magnitude of ζ, of the nanoemulsion droplets. Consistent with our results, it has been reported in the literature that the dissociation of carboxylic acids [148–151], as well as other weak acids [152], is enhanced at elevated temperatures.

The trend of decreasing ζ as a function of temperature is consistent with the trend of viscoelastic moduli. In Fig. 3.5A, ζ remains nearly zero from T = 20 to 30 °C, starts to decrease from T = 30 to 35 °C, experiences a large decrease from T = 35 to 45 °C and finally reaches a plateau when T $\geq$ 45 °C. This trend in ζ is consistent with the viscoelastic moduli in Fig. 3.2. Starting from room temperature, first, G' and G" experience an initial increase. During this initial period, the electrostatic repulsion should be negligible since ζ is nearly zero, and the increase in viscoelastic moduli and the formation of assembled gel network (Fig. 3.3) are presumably due to the increase in attractive interaction between droplets. The details of the attraction will be discussed later. Next, ζ undergoes a dramatic decrease, hence the increase in the electrostatic repulsion, when T is increased to 45 °C, and the viscoelastic moduli decrease within the same temperature range in Fig. 3.2. This decrease in G' and G" suggests the repulsion overcomes the attraction. Finally, as the temperature is further increased, ζ reaches a plateau, leading to a nearly constant electrostatic repulsion. In this regime, G' and G" meet their second increase and the gel network is again exhibited (Fig. 3.3), indicating the attractive interaction overcomes the electrostatic repulsion in the high-temperature regime, as in the initial period (T = 20 to 30 °C).
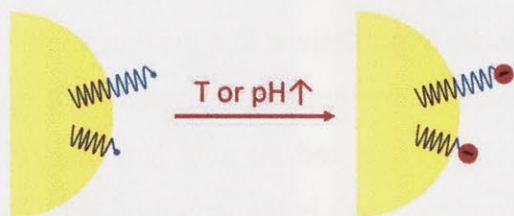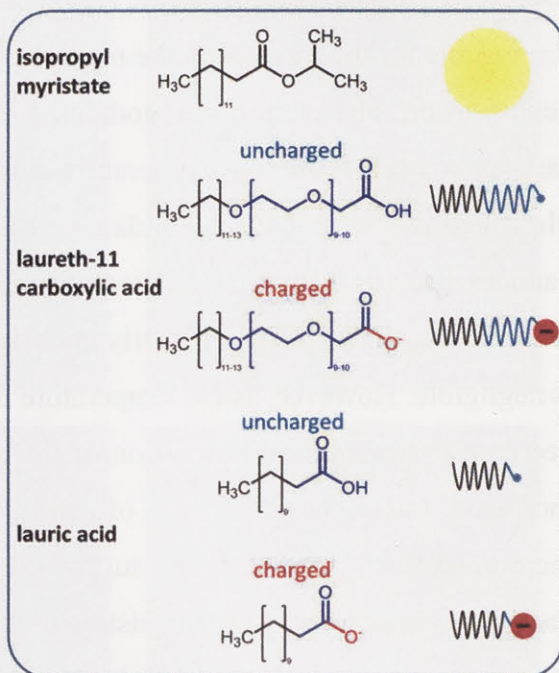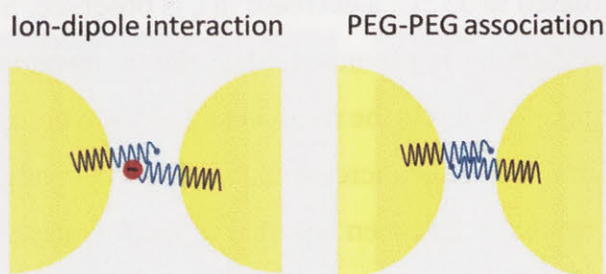
Figure 3.4 Schematic of the sources of repulsive and attractive interactions in the system. (A) Repulsive interaction is from the deprotonation of the carboxylic group on the surfactant molecules absorbed on the nanoemulsion droplets. (B) Attractive interactions are from 1) the ion-dipole interaction (ion-induced dipole interaction) from the carboxylate groups and PEG segments on the surfactants, and 2) PEG-PEG association from the PEG segments on laureth-11 carboxylic acids.
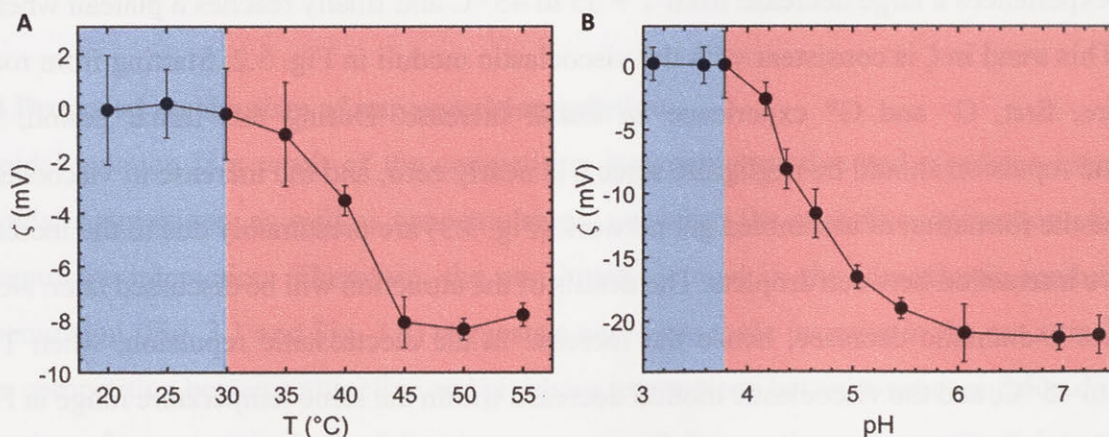
Figure 3.5 Zeta potential (ζ) of the nanoemulsion droplets as a function of (A) temperature, T and (B) pH at T = 20 °C. pH was adjusted using NaOH. The pH of the nanoemulsion in (A) is 3.1. The error bars are standard errors from 30 measurements.

Thus far, we have demonstrated that our nanoemulsion system has an electrostatic repulsion which is modulated by temperature. By comparing trends in the zeta potential to the trends observed in the rheological measurement, we propose that there must be competing attractive interactions. In the next section, we will discuss the origin of the attractive interactions in our system.

70

3.4.3.2 Attractive interaction

By considering the constituents of our nanoemulsion, we believe there are two sources that are responsible for the attractive interaction between the droplets: 1) the ion-dipole interaction between the charged carboxylate group and the poly(ethylene glycol) segment (PEG) on laureth-11 carboxylic acid, and 2) the association between PEGs on the laureth-11 carboxylic acids between droplets. A schematic diagram of both mechanisms is shown in Fig. 3.4B. For clarification, free PEG in the continuous phase (M_w = 400 g/mol) is denoted as PEG400, and the PEG on the weak-acid surfactant ($M_w \approx$ 400-440 g/mol) is denoted as PEG_w.

The ion-dipole interaction (ion-induced dipole interaction) results from the interaction between the ionic carboxylate group and PEG_w on the uncharged laureth-11 carboxylic acids. As shown in Fig. 3.5A, the increased temperature leads to the dissociation of the carboxyl group of the surfactant adsorbed on the droplet. However, as we will discuss the effect of pH on the system later, only a fraction of the carboxyl groups on the nanoemulsion droplets is deprotonated even at high temperatures. Therefore, the PEG_w on the undissociated laureth-11 carboxylic acids on one droplet can interact with the ionic carboxylate groups on the other droplet (Fig. 3.4B), giving rise to a net attraction between droplets. Indeed, the ion-dipole interaction between the charged headgroups of the surfactants and the uncharged hydrophilic moieties of polymers has been extensively studied in the literature [61]. Experimental techniques including rheometry [62], neutron scattering [63], isothermal titration calorimetry [64,65], NMR [65] and potentiometric titration [66], as well as thermodynamic models [67] and simulations [68], have strongly supported the concept of ion-dipole association.

To the best of our knowledge, the ion-dipole interaction between charged carboxylate groups and PEGs has not been systematically studied in the literature. However, it has been shown that the ion-dipole interaction not only takes place in the well-known SDS/PEG system [63–66,68], but also in other systems where uncharged polymers, such as PEG or poly(N-vinylpyrrolidone), are mixed with charged species such as free ions and cetyltrimethylammonium bromide (CTAB) [61,62,153,154]. These prior works demonstrate that the ion-dipole interaction is generic and should also take place in our case where the charged carboxylate groups coexist with uncharged PEGs.

The other proposed attractive interaction between nanoemulsion droplets is from the PEG_w-PEG_w association. It has been widely observed in the literature that PEG becomes more hydrophobic in aqueous solutions when the temperature is increased [155–158]. For such aqueous PEG solutions, when the temperature is elevated, the affinity between PEGs is increased and the phase separation can be induced (i.e. a lower critical solution temperature, LCST, can be defined) [159,160]. This affinity could give rise to a net attractive interaction between the nanoemulsion droplets via the PEG_w on laureth-11 carboxylic acid (Fig. 3.4B). Such attraction using the LCST behavior of polymers has been utilized to induce the gelation of block copolymer colloids [161]. On the other hand, the UCST behavior has also been utilized to induce colloidal gelation in polymer-grafted nanoparticle suspensions [18,107].

For linear PEGs (such as in our system), it has been found that the temperature to induce a cloud point is higher for shorter PEG molecules [156,158,159], as the affinity between PEGs is strengthened when the molecular weight is increased. Therefore, considering the short PEG_w backbone, our system will never achieve the LCST under our experimental conditions. However, it does not mean that PEG-PEG association does not take place when the temperature is below the LCST. It has been proposed that the enhanced PEG-PEG affinity at rising temperature in water is due to the conformational equilibrium in the segments [160]. The segments prefer the polar conformations (i.e. water is a good solvent) at lower temperatures and prefer the nonpolar conformations at higher temperatures (i.e. water is becoming a poor solvent). Importantly, it has been shown that such conformational change in the segments is gradual at elevated temperatures. Bjoerling et al. have studied the conformational adaption of the PEG chains using ^{13}C NMR [156]. They found out that even for the short PEG (M_w = 600 g/mol), the segment undergoes a gradual conformational change at T = 25 to 75 °C, which is consistent to our experimental temperature window (T = 25 to 55 °C) and supports our proposed mechanism that PEG-PEG association can give rise to an attractive interaction in our system.

Bridging interaction mediated by free PEG400 in the continuous could also take place. We speculate that PEG400 does not play a major role in inter-droplet interactions. In our proposed mechanism, the attraction is from the ion-dipole interaction and PEG_w-PEG_w association between surfactants on different droplets. However, based on this proposed mechanism, we do not want to

rule out the possibility that PEG400 can bridge the nanoemulsion droplets via these attractive interactions by chaining the molecules such as PEG_w-PEG400-PEG_w or COO⁻-PEG400- COO⁻.

Overall, in our system, we believe the competition of the temperature-dependent attraction and repulsion between the nanoemulsion droplets is responsible for the non-monotonic trend in the viscoelasticity moduli (the moduli first increase, then decrease and finally increase again as temperature increases). When the repulsion dominates in the system, the gelation is diminished and hence the decrease in the viscoelastic moduli. On the other hand, when the attraction dominates, the viscoelastic moduli increase. By carefully considering the constituents of the system, we propose the attraction comes from the PEG_w-PEG_w association and the ion-dipole interaction (COO⁻-PEG_w). Therefore, comparing with the rheological data in Fig. 3.2, we have concluded that the decrease in the moduli at T = 35 to 45 °C is due to the significant increase in the zeta potential (and hence the electrostatic repulsion). Based on the zeta potential data, it can be then concluded that the second increase in the viscoelastic moduli (T ≥ 45 °C) is primarily due to the increased PEG_w-PEG_w association. Since the zeta potential (and hence the charge density of the droplets) stays unchanged within this temperature window, we do not expect an increase in the ion-dipole interaction at T ≥ 45 °C as no significant evidence in the literature suggests this interaction is affected by temperature. Finally, in the first gelation regime (T = 20 to 35 °C), the gelation is due to both ion-dipole interaction (since the magnitude of the zeta potential increases) and PEG_w-PEG_w association.

As depicted in Fig. 3.4, the ion-dipole and PEG_w-PEG_w interactions rely on different regions of the surfactant molecules. Therefore, the interactions are highly coupled and it is very difficult to isolate the dominance between PEG_w-PEG_w association and the ion-dipole interaction (COO⁻-PEG_w). Although the two interactions are difficult to decouple and immediately unclear due to the lack of a well-developed model, we can gain some understanding of their combined strength by estimating the electrostatic repulsion which they must overcome to gel the suspension. Using the zeta potential data in Fig. 3.5, we can estimate the strength of the electrostatic repulsion, ε_{elec}, as [138]

$$\varepsilon_{elec} = 32\pi\varepsilon_o\varepsilon_r\left(\frac{kT}{ze}\right)^2 \operatorname{atanh}^2\left(\frac{1}{4}\frac{ze\xi}{kT}\right) \tag{3.1}$$

where ε_o is the electric permeability of free space, ε_r is the dielectric constant of the continuous

phase (here ε_r of water is used for estimation), k is Boltzmann constant, T is the absolute temperature, e is the elementary charge, z is the charge number and ξ is the zeta potential. The results are shown in Fig. 3.6, and reveal that the electrostatic repulsion in our system is quite weak. Even for the strongest electrostatic repulsion, ε_{elec} is only $\approx 0.6\ kT$ (T ≥ 45 °C). Moreover, as shown in Fig. 3.1 and 3.2, the mechanical strength of this nanoemulsion gel is very weak (G' is ~ 10^0 to 10^1 Pa), as compared to other nanoemulsion gels our group has developed (G'~ 10^4 to 10^5 Pa) where stronger attractive interactions were introduced to the nanoemulsion suspensions [21,138,139], suggesting the competing attractive interactions (PEG_w-PEG_w association and ion-dipole interaction) are also very weak.
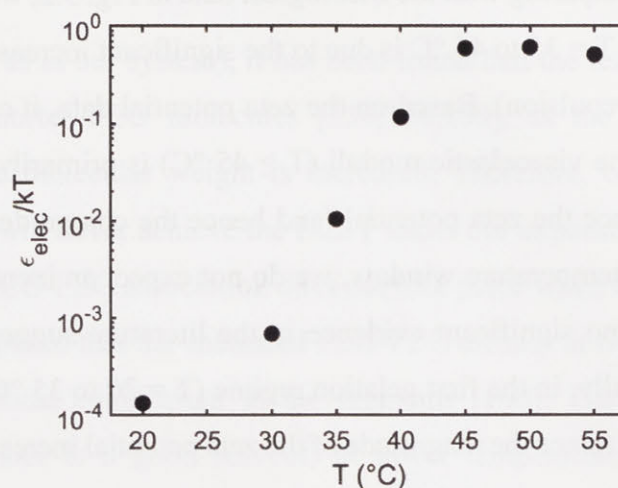
Figure 3.6 The strength of the electrostatic repulsion, ε_{elec}, as a function of temperature using zeta potential reported in Fig. 3.5A.

3.4.4 Effect of pH on the rheological properties

We have shown that temperature can be used to control protonation of the carboxyl group of the surfactant on the droplet (Fig. 3.5A), and the resulting change in the electrostatic repulsion significantly affects the rheological response of the nanoemulsion gel (Fig. 3.1 and 3.2). However, to control the protonation of weak acids, a more straightforward way is to adjust the pH of the system. In this section, we investigate the effect of pH on the nanoemulsion suspension by studying the zeta potential of the droplets, rheological response and the droplet stability as a function of pH.

The zeta potential (ζ) of the nanoemulsion droplets as a function pH is shown in Fig. 3.5B. As expected, ζ decreases ($|\zeta|$ increases) with increasing pH since the deprotonation of the carboxyl

group is facilitated at the basic condition. Starting from the pristine nanoemulsion (pH = 3.1), ζ stays nearly zero until the pH is elevated to 3.8, and then experiences a significant decrease when pH > 4. This change in ζ is consistent with the reported pKa of laureth-11 carboxylic acid in the literature where the apparent pKa is determined to be $\approx$ 4 using potentiometric titration [162], and laureth-11 carboxylic acid is the major surfactant in our system. As the pH is further increased (pH > 6), ζ reaches a plateau, suggesting the deprotonation of the carboxylic acid is complete. The magnitude of the final ζ from Fig. 3.5B ($\zeta \approx$ -23 mV, the effect of pH) also suggests that only partial deprotonation of the carboxylic acid is achieved by thermal energy ($\zeta \approx$ -8 mV) as shown in Fig. 3.5A.

We then investigated the effect of pH on the nanoemulsion rheology. The viscoelastic moduli during a temperature ramp are shown in Fig. 3.7. It should be noted that for the pristine nanoemulsion in Fig. 3.7, pH is 2.5, which is lower than the pH of the 'pristine' nanoemulsion for the zeta potential measurement in Fig. 3.5B where the pH is 3.1. This difference is due to the required dilution for the zeta potential measurement, in which the nanoemulsion is diluted from 12.5 wt% (Fig. 3.7) to 0.5 wt% (Fig. 3.5B). In Fig. 3.7, when pH is increased, the increase in the G' and G" takes place at higher temperatures, indicating a higher gelation temperature is required when the pH is higher. Moreover, when pH is $\geq$ 5, no gelation can be induced within the experimental temperature window. The increase in pH weakens the thermally-gelling behavior of the nanoemulsion system, and this is expected since the electrostatic repulsion from the dissociation of the carboxylic acids plays an important role in the rheological response, as discussed previously. Compared with temperature, pH is a more effective strategy to promote the deprotonation of the carboxylic acid as more negative ζ can be obtained (Fig. 3.5B). Therefore, it is not surprising that pH significantly suppresses the gelling behavior.
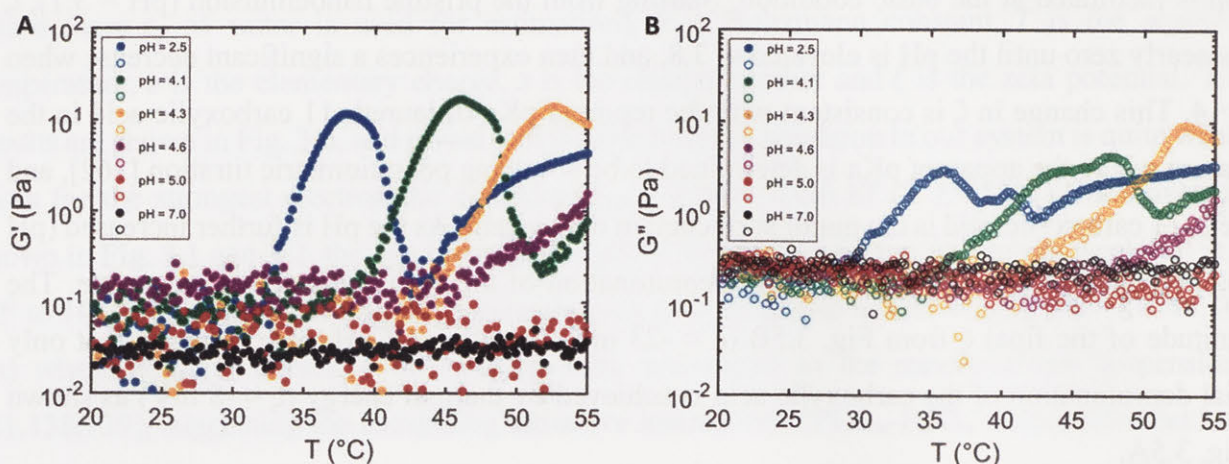
Figure 3.7 Effect of pH on the rheological properties of the nanoemulsion using SAOS at a fixed angular frequency = 25 rad/s. The figure shows (A) storage modulus, G' and (B) loss modulus, G" as a function of temperature, T, at various pH values. pH was adjusted using NaOH.

We have to emphasize that the temperature-ramp rheology shown in Fig. 3.7 is different from the data shown in Fig. 3.2 where the G' and G" are reported at a fixed angular frequency using frequency-sweep measurements at various temperatures (temperature-jump). Our group has previously studied the effect of the thermal history on the rheological properties of thermogelling nanoemulsions in great detail, in which the temperature-ramp route can effectively build up the strength of the gel [105]. Therefore, we did expect that there will be a difference in viscoelastic moduli between Fig. 3.2 and Fig. 3.7 of the pristine nanoemulsion (pH = 2.5). Here the rheological characterization using a temperature ramp is used as a strategy to conveniently obtain a quantitative understanding of the effect of pH on the nanoemulsion rheology over a wide range of temperatures.

Finally, we studied the effect of pH on the stability of the nanoemulsion by monitoring the size of droplets over a course of time. In this work, we used the phase inversion composition (PIC) method to synthesize the nanoemulsion. For the PIC method, or for any low-energy method to obtain nanoemulsions, the surfactant molecular geometry plays a crucial role in the formation of the droplet and the stability of the oil/water interface [28]. This molecular geometry is quantified by a quantity called packing parameter $p = a_T/a_H$, where a_T and a_H are the cross-sectional areas of the tail group and head group respectively. Different p values lead to different types of surfactant packing at the oil/water interface, and hence favor different curvature of the interface. The stability of the nanoemulsion at different pH is shown in Fig. 3.8. The pH was adjusted *after* the nanoemulsion synthesis. As shown, the increase in pH facilitates the instability of the nanoemulsion suspensions, whereas the pristine nanoemulsion stays stable throughout the

76

experimental time window. As shown in Fig. 3.5B, increasing pH leads to the deprotonation of the carboxyl group of the surfactant on the droplets. Such deprotonation transforms the surfactant from being non-ionic ($\zeta \approx 0$ at low pH) to anionic ($\zeta < 0$ at higher pH), and therefore changes p. This change in p ruptures the original packing of the surfactants at the oil/water interface, leading to an instability of the interface and therefore the increase in the droplet size. Such instability highlights the importance of the molecular geometry of the surfactant in stabilizing the oil/water interface, and also suggests that in our system the increase in pH can be used as a strategy to demulsify the nanoemulsion droplets, that can be applied in practical applications such as in cosmetics [163,164], food industry [135,165], enhanced oil recovery [166–168] and water treatment [169].
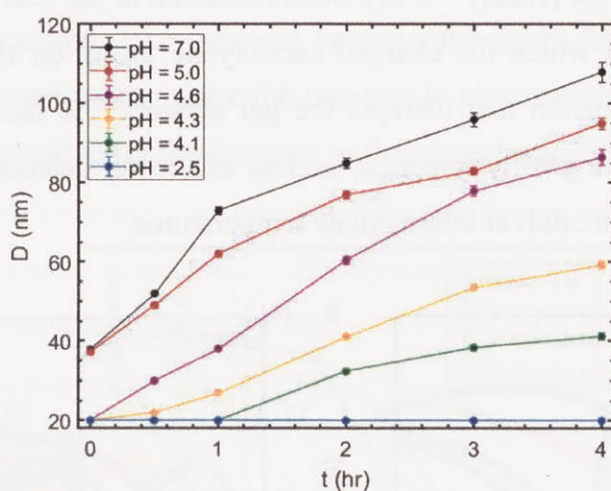
Figure 3.8 The stability of the nanoemulsion at room temperature as a function of pH by monitoring the nanoemulsion droplet size over time. pH was adjusted using NaOH. See Appendix B Fig. B4 for a long-time droplet size monitoring. The error bars are standard errors from 15 measurements.

From Fig. 3.8, we acknowledge that during the rheological characterization the size of the nanoemulsion droplets increases for pH values greater than 2.5. Thus, trends in the pH-responsive rheology in Fig. 3.7 are possibly convoluted with changes in droplet size. In order to decouple as much as possible pH changes in interactions from droplet size effects, we applied a fast temperature-ramp characterization (total measuring time $\approx$ 20 min in Fig 3.6). Given this short amount of time, the change of size is limited (almost negligible for pH up to 4.3) and the thermally-gelling behavior can still take place since the droplet size is still in the nanoemulsion regime. In prior work we have extensively studied the effect of droplet size on a different thermally-gelling nanoemulsion system [21,138].

3.4.5 Effect of ionic strength on the rheological properties

The charged nature of the nanoemulsion droplets suggests the possibility to tune the gel properties using ionic strength. By screening the electrostatic repulsion using electrolytes, we expected the gelation of the nanoemulsion can be more easily induced at elevated temperatures. We again used the temperature-ramp rheology to study the effect of the ionic strength using sodium chloride (NaCl), and the result is shown in Fig. 3.9. As expected, the addition of NaCl facilitates the thermal gelation of the nanoemulsion where the increase in G' and G" takes place at lower temperatures. Moreover, the magnitude of the decrease in the viscoelastic moduli at the intermediate temperature is significantly reduced as more NaCl is added (e.g. the G' value at 30 °C for [NaCl] = 1.0 M compared to that at $\approx$ 44 °C for [NaCl] = 0 M). Such reduction in the decline of moduli supports our proposed mechanism in which the charged carboxylate group on the droplet leads to an increase in electrostatic repulsion that disrupts the gel network. As more NaCl is added, the electrostatic repulsion is more greatly screened, leading to a lower gelation temperature and less reduction in the viscoelastic moduli at intermediate temperatures.
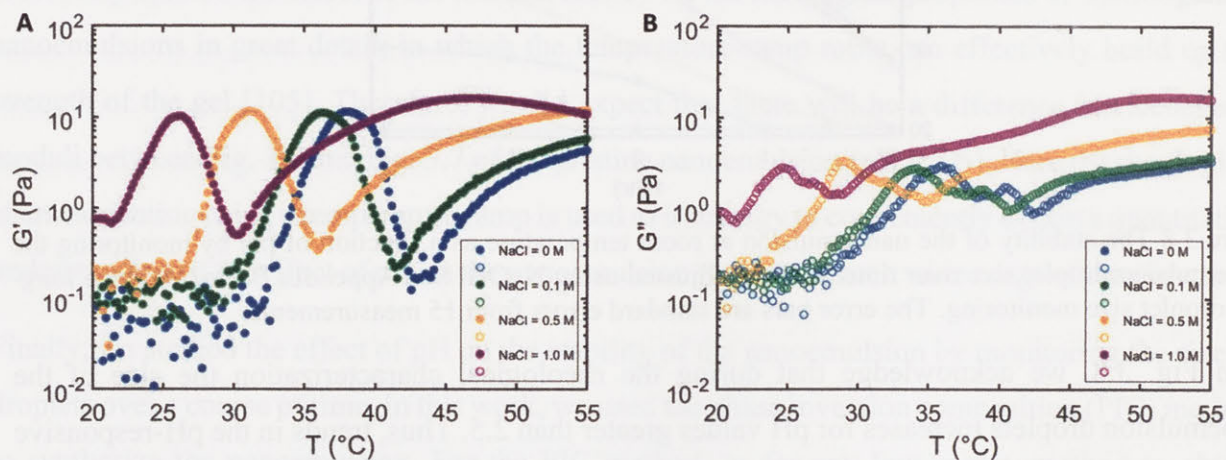
Figure 3.9 Effect of the ionic strength on the rheological properties of the nanoemulsion (pH = 2.5) using SAOS at a fixed angular frequency = 25 rad/s. The figure shows (A) storage modulus, G' and (B) loss modulus, G" as a function of temperature, T, with increasing ionic strengths. The ionic strength was adjusted using NaCl as indicated in the figure.

However, even for the highest ionic strength ([NaCl] = 1.0 M), the decrease in the viscoelastic moduli still exists. Moreover, the magnitude of the peak in the moduli is nearly the same across the [NaCl] window, suggesting repulsive interaction is still critical. As discussed earlier, the emergence of the electrostatic repulsion due to the thermally-triggered dissociation of the carboxyl group is responsible for the breakdown of the gel network (Fig. 3.1 to 3.3). Therefore, we

hypothesized the addition of NaCl also facilitates the deprotonation of the carboxylic acids. Indeed, the effect of ionic strength on the dissociation of weak acids has been already studied in the literature. It has been found out that the addition of electrolytes promotes the deprotonation of various weak acids since the activity coefficients of the ionic species are highly sensitive to the ionic strength [170–173]. This promoted dissociation due to NaCl is validated in Fig. 3.10 where the temperature-dependent zeta potential of the nanoemulsion droplets, ζ, at elevated [NaCl] is measured. As [NaCl] increases, the dissociation of carboxyl acids takes place at lower temperatures and $|\zeta|$ at higher temperatures is also increased, which is consistent with prior studies where the electrolytes facilitate the weak acid dissociation [170–173]. Moreover, at higher [NaCl], ζ reaches a plateau at lower temperatures. This is consistent with the rheological data in Fig. 3.9 where the minimum in moduli takes place at lower temperatures for higher [NaCl], which also supports the proposed mechanism where the increase in electrostatic repulsion due to the weak acid dissociation is responsible for the decrease in the viscoelastic moduli.
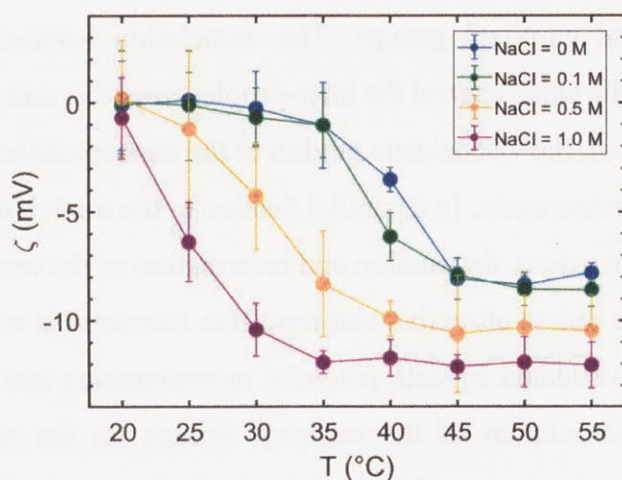
Figure 3.10 Zeta potential (ζ) of the nanoemulsion droplets as a function of temperature (T) at elevated ionic strength. Ionic strength was adjusted using NaCl. The pH of the nanoemulsion is 3.1. The error bars are standard errors from 30 measurements.

We also note that, as shown in Fig. 3.9, at high ionic strength (NaCl = 1.0 M), the nanoemulsion can gel near room temperature. This early gelation is not intuitive since it seems to disagree with the discussion on the promoted carboxylic acid dissociation. Therefore, the addition of electrolyte must also modify the attractive interaction to induce an early onset of gelation. Indeed, prior studies have shown that the addition of the salts facilitates the association between PEG molecules [174–177]. The phase separation, or the cloud point, takes place at a lower temperature when more

salts are added [174,176,177]. Therefore, in our system, the addition of NaCl enhances the attractive interaction resulting from the PEG-PEG association between the droplets, which also supports our proposed mechanism where the PEG_w-PEG_w association gives the inter-droplet attraction in our nanoemulsion suspension. We acknowledge that the effect of the ionic strength on the attraction and repulsion is interconnected. Future work will focus on the decoupling of the effect of the addition of electrolytes on the nanoemulsion gelation and the contribution to both attractive and repulsive interaction in a more quantitative fashion.

3.5 Conclusion

Building of a molecular-scale understanding of our prior thermally-gelling nanoemulsion systems [21,138,139], in this chapter we develop a new nanoemulsion system in which the properties can be modulated through both temperature and pH. The nanoemulsion is synthesized using a low energy method, and the droplets are stabilized with weak acid surfactants containing poly(ethylene glycol) segments (PEG) and carboxyl groups. The association between the PEGs and the deprotonation of the carboxylic acids control the inter-droplet attractive and repulsive interactions. As the temperature is increased, the viscoelastic moduli of the nanoemulsion system first increase, then decrease and finally increase again. In a parallel fashion to the moduli trends, the gel network also experiences an initial formation, destruction and reformation as the temperature is increased. Such non-intuitive trends are due to attractive and repulsive interactions which both change as a function of temperature, as validated by zeta potential measurements and comparisons to prior research [148–151]. The dissociation of the carboxyl groups on the surfactant was further leveraged as a strategy to tune the nanoemulsion gel rheological properties by changing the pH of the system. Moreover, with an understanding of surfactant packing at the interface, we can further destabilize the nanoemulsion droplets by changing the surfactant packing parameter via pH [28]. Finally, we showed that the ionic strength of the system can be used as another engineering handle to tune the gel properties.

The presented work shows that subtle competition between attractive and repulsive interactions determines the system's properties, allowing researchers to design more complex nanoemulsion-based soft matter materials. Moreover, the mechanistic understanding of the interactive potentials at the molecular level provides various engineering strategies to manipulate the material properties.

For example, the presented gelling nanoemulsions can be used in cosmetic products such as a skin cream – in the bottle the nanoemulsion system is a liquid at ambient temperature with good flowability, and the nanoemulsion can gel in contact with the skin due to a rise in temperature. Thereafter, a change of pH due to prolonged contact with the skin can disrupt the nanoemulsion gel network and the nano-sized droplets can then be easily absorbed into the skin [6,26]. Furthermore, the oil droplets are effective vehicles to encapsulate hydrophobic active ingredients [9,38]. In addition, a nanoemulsion system which responds to changes in both pH and temperature could find use in enhanced oil recovery applications where temperature and pH gradients can be found. Future work will focus on developing skincare products using the presented nanoemulsion system, and in developing a deeper quantitative understanding of the pairwise interactions between nanoemulsion droplets.

Chapter 4

Tuning Material Properties of Nanoemulsion Gels by Sequentially Screening Electrostatic Repulsions and then Thermally-Inducing Droplet Bridging

4.1 Overview

Nanoemulsions are widely used in applications such as food products, cosmetics, pharmaceuticals, and enhanced oil recovery for which the ability to engineer material properties is desirable. Moreover, nanoemulsions are emergent model colloidal systems due to the ease in synthesizing monodisperse samples, flexibility in formulations, and tunable material properties. In this work, we study a nanoemulsion system previously developed by our group in which gelation occurs through thermally-induced polymer bridging of droplets. We show here that the same system can undergo a sol-gel transition at room temperature through the addition of salt, which screens the electrostatic interaction and allows the system to assemble via depletion attraction. We systematically study how the addition of salt followed by a temperature jump can influence the resulting microstructures and rheological properties of the nanoemulsion system. We show that the salt-induced gel at room temperature can dramatically restructure when the temperature is suddenly increased, and achieves a different gelled state. Our results offer a route to control the material properties of an attractive colloidal system by carefully tuning the interparticle potentials and sequentially triggering the colloidal self-assembly. The control and understanding of the material properties can be used for designing hierarchically structured hydrogels and complex colloidal-based materials for advanced applications.

This chapter has been adapted with permission from L. -C. Cheng, S. L. K. Vehusheia and P. S. Doyle "Tuning Material Properties of Nanoemulsion Gels by Sequentially Screening Electrostatic Repulsions and then Thermally-Inducing Droplet Bridging" *under review*

4.2 Introduction

Colloidal gelation is an effective tool to engineer material properties. By properly inducing the gelation of colloidal suspensions, one can precisely modulate the macroscopic properties and create complex microstructures [1]. For example, colloidal suspensions that undergo gelation can be used as rheology modifiers [14] or ingredients in pharmaceutical [24,102,178] and food products [99,179], and the complex structures can be used as scaffolds in tissue engineering [3,4] or porous material design [5]. Among a diverse set of colloidal suspensions, nanoemulsions have been an emerging model colloidal system for studying aspects of colloidal gel systems [6]. Nanoemulsions are liquid-liquid suspensions (e.g. oil droplets suspended in water) where the droplet size is on the order of 100 nm. The ease of nanoemulsion synthesis and the great flexibility in their formulations allow one to engineer the inter-droplet potentials and thus to rationally tune the material microstructures and associated macroscopic properties [8]. Therefore, gelling nanoemulsions have attracted much attention in both fundamental studies [15,25,138] and practical applications [9,26,33].

Several strategies have been applied to induce the gelation of nanoemulsions. One common approach to trigger the gelation is by depletion interaction. By adding non-adsorbing molecules into the continuous phase of the nanoemulsions, the molecules are excluded from the vicinity of the droplets due to the increase of entropy [17,122,180]. Such exclusion gives rise to an imbalance in the osmotic pressure, leading to a net attractive interaction between the droplets and ultimately gelation of the system. Different types of non-adsorbing depletant molecules such as polymers [9,138] and surfactant micelles [51,52] have been employed to induce the self-assembly and gelation of nanoemulsions. Another well-known approach to obtain gelling nanoemulsions is to modulate the effective range of the inter-droplet electrostatic repulsion [10,15,31]. By adding electrolytes to the charged-stabilized nanoemulsions (e.g. stabilized by ionic surfactants), the ions from the dissociating electrolytes screen the electrostatic repulsion by decreasing the Debye length [22,75]. If enough electrolytes are added into the nanoemulsions, a secondary minimum can be obtained in the pairwise interactive potentials and the system can self-assemble and eventually gel [10,31]. Recently, our group has designed another gelling nanoemulsion mechanism in which the gelation is responsive to an increase in temperature [21,98]. In this approach, telechelic oligomers are added to the continuous phase and their hydrophobic end groups will preferentially partition into the oil domains upon an increase in temperature, resulting in inter-droplet bridging. The

polymer bridging acts as an effective attractive force between the droplets and ultimately gives rise to gelation at high enough temperatures.

Overall, for the works discussed above, the gelation is induced by a single gelation route (i.e. pure depletion, electrolyte screening or droplet bridging). To obtain more diverse material behaviors, a sequential application of different gelation routes to the nanoemulsion can be beneficial. Inspired by the aforementioned studies and associated gelling mechanisms, in this work we revisit our thermally-gelling nanoemulsions and study their material behaviors when sequentially tuning the droplet interactions – first screening the electrostatic repulsion and then inducing the droplet bridging. The nanoemulsion studied here consists of polydimethylsiloxane (PDMS) nano-droplets suspended in an aqueous continuous phase containing poly(ethylene glycol) diacrylate (PEGDA). PEGDA is then the thermally-triggered telechelic polymer bridging agent where the PEG segment is the hydrophilic backbone and the acrylate groups at the ends are the hydrophobic moieties. The PDMS nano-droplets are stabilized by an anionic surfactant sodium dodecyl sulfate (SDS), which provides a charged nature of the droplets that allows us to screen the electrostatic repulsion by adding electrolytes into the system.

To carry out the study, we first added the electrolyte (sodium chloride, NaCl) to the nanoemulsion system to induce the first-stage gelation by screening the electrostatic repulsion. We showed that the system can undergo a sol-gel transition at room temperature with a small amount of NaCl, similar to prior published studies [7,10,76]. We quantitatively investigated the system by calculating the inter-droplet pairwise interactions under the effect of the screened electrostatic repulsion. We discovered that the non-adsorbing PEGDA (since the bridging is not induced at room temperature) gives rise to a significant depletion attraction, and thus a slight increase in the ionic strength can result in gelation of the system. After pre-conditioning the nanoemulsion with NaCl at room temperature, we then increased the temperature to induce PEGDA droplet bridging. Our results show a non-intuitive trend in the material properties in which a stronger gel is not necessarily obtained with this 'two-stage' gelation. We also showed that the screening of electrostatic repulsions at room temperature in the first step has a considerable influence on the subsequent nanoemulsion microstructures and the associated rheological properties at elevated temperatures. We then used the established pairwise interactive potential and the dynamics of the thermal gelation to explain the trends in material behavior under the sequential application of

stimuli. Our results suggest that sequential droplet self-assembly can be an effective tool to engineer properties of colloid-based materials, and an understanding of the molecular behavior of the constituents is critical for designing self-assembling systems.

4.3 Materials and methods

4.3.1 Materials

Polydimethylsiloxane (PDMS, viscosity = 5 cSt), sodium dodecyl sulfate (SDS), poly(ethylene glycol) diacrylate (PEGDA, $M_n \approx 700$ g mol^{-1}), sodium chloride (NaCl), lipophilic dye PKH26 (excitation and emission wavelengths $\lambda_{ex}/\lambda_{em}$ = 551/567 nm) and photoinitiator 2-hydroxy-2-methylpropiophenone (Darocur 1173) were purchased from Sigma-Aldrich. All chemicals were used without further purification.

4.3.2 Nanoemulsion synthesis

The nanoemulsion studied in this work consists of a disperse phase PDMS of a volume fraction ϕ = 0.15 (droplet diameter = 36 nm with polydispersity = 0.18) suspended in a continuous phase composed of PEGDA of a volume fraction = 0.33 and SDS. The total concentration of SDS is 0.175 M. The concentration of NaCl is adjusted by adding NaCl into the nanoemulsion after the synthesis.

The nanoemulsion was synthesized using a high-pressure homogenizer (EmulsiFlex-C3, Avestin) [21,33,98,143]. Before the homogenization, a pre-emulsion was first prepared by adding PDMS into a pre-mixed continuous phase consisting of de-ionized water, SDS and PEGDA. The mixture was stirred using magnetic stirring with a speed of 700 rpm. Stirring was maintained for 15 min and no macroscopic phase separation was observed. The pre-emulsion was subsequently processed into nanoemulsions using high-pressure homogenization at a pressure of 18 kpsi for 16 passes. The emulsion was cooled to 4 °C between each pass and the final nanoemulsion (pure nanoemulsion without addition of NaCl) was stored at 4 °C until further use. NaCl with different target concentrations was then added to the pure nanoemulsion and mixed by vortexing immediately before the characterization. The small amount of NaCl added has a negligible effect on the volume fraction of the nanoemulsions.

The size of nanoemulsions was measured using dynamic light scattering (90Plus PALS, Brookhaven Instruments). Before the measurement, the nanoemulsion was diluted from $\phi = 0.15$ to $\phi = 0.002$ using an aqueous diluting agent composed of PEGDA of a volume fraction = 0.33.

4.3.3 Rheological measurements

All rheological measurements were conducted using a stress-controlled rheometer (DHR-3, TA instrument) equipped with a 1° 60mm aluminum upper-cone and a Peltier lower-plate to control the sample temperature. For each measurement, the nanoemulsion was loaded onto the lower plate at 20 °C. To minimize evaporation, a wetted solvent trap was used and a few drops of de-ionized water were added on the top of the upper-cone. Before each measurement, a rejuvenation step was performed by applying constant shear at a shear rate of 2500 s^{-1} for 60 seconds followed by a 10-minute period where the sample remained quiescent at T = 20.0 °C. By studying the flow curves of the nanoemulsions, we showed that at such a high shear rate the gel structure appears to be broken down, especially for nanoemulsions with added salt for which the gelation is induced by screening the electrostatic repulsion (Appendix C Fig. C1). The gel structure can then be recovered after 10 minutes by monitoring the viscoelastic moduli (Appendix C Fig. C2). Our rejuvenation protocol using high shear rates is consistent with prior work by Wilking et al. [31] who studied the rheology-structure relation of nanoemulsion gels.

The frequency sweep measurements were then performed after the rejuvenation step. Small-amplitude oscillatory shear (SAOS) was applied to measure the dynamic viscoelastic modulus at a shear strain = 0.05% with angular frequency ω = 1 to 200 rad s^{-1}. For the measurements at different temperatures, the sample was raised from T = 20.0 °C to the target temperature and then remained quiescent for 10 minutes before applying SAOS. Freshly loaded nanoemulsion was used for each measurement.

4.3.4 Confocal microscopy

Direct visualization of the nanoemulsion microstructures under different conditions was performed using a confocal microscope (LSM 700, Zeiss) equipped with a 63X oil-immersion objective (numerical aperture = 1.4). To prepare the sample for imaging, 1 vol% of fluorescent dye and 1

vol% of photo-initiator were mixed with the nanoemulsion sample by vortexing for 60 seconds. It has been shown in our previous work that the addition of these chemicals has a negligible effect on the microstructures [101,105]. Subsequently, 150 μL of the mixture was loaded into a glass chamber (Lab-Tek™ #155411, Thermo Fisher Scientific) and followed by a 10-minute period where the sample remained quiescent at T = 20.0 °C. For the samples at elevated temperatures, the mixture was placed in the oven at the target T for 10 minutes. The sample was subsequently exposed to UV light (λ = 365 nm) for 50 seconds in the oven. The crosslinking of the excess PEGDA in the continuous phase then locked the assembled microstructure in place, allowing for confocal imaging at room temperature [101,105,143].

4.4 Results and discussion

Fig. 4.1 summarizes the different routes to induce self-assembly and gelation of the nanoemulsion studied in this work. We start with the thermal gelation of the nanoemulsion via PEGDA bridging. Afterward, we study the effect of electrolyte screening on the material properties by adding NaCl into the nanoemulsion suspension. Finally, we study the material behavior by sequentially inducing the screening of electrostatic repulsion via the addition of NaCl and then the PEGDA bridging via the increase in temperature. The material behavior is characterized by rheometry and confocal microscopy.
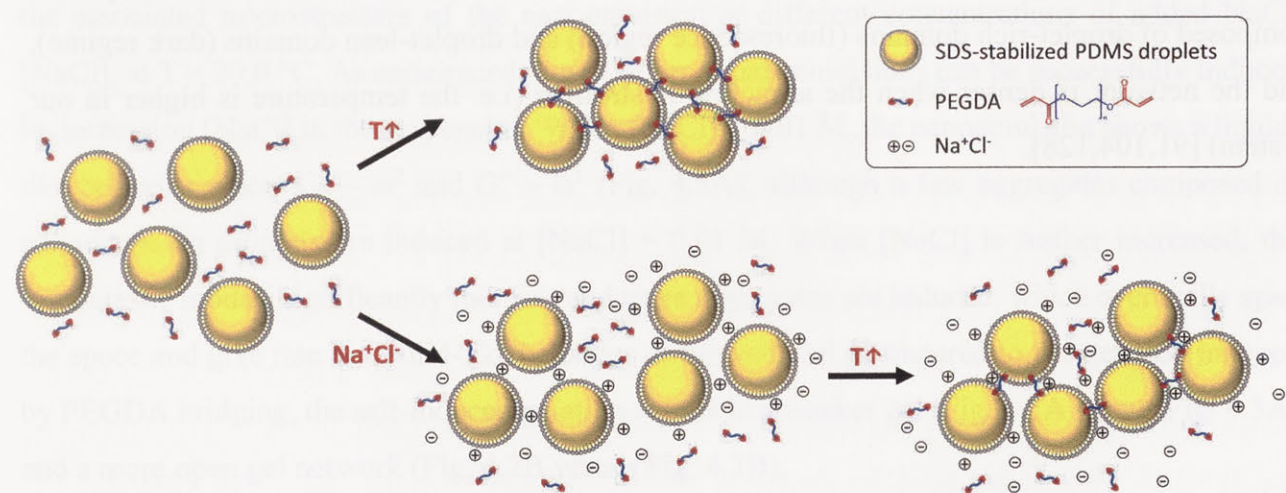
Figure 4.1 Schematic of the gelation routes studied in this work. Upper route: thermal gelation via PEGDA bridging at elevated temperatures. Lower route: sequentially screening of electrostatic repulsion by adding NaCl and then inducing thermal bridging with PEGDA bridging.

4.4.1 Thermally-gelling nanoemulsions via PEGDA droplet bridging

Here, we briefly introduce the thermally-triggered PEGDA droplet bridging, and the associated nanoemulsion rheology and microstructures. Readers interested in more detailed studies of this thermally-gelling nanoemulsion system are referred to the previous works by our group [21,98,101,105,143]. As depicted in Fig. 4.1, the thermally-gelling nanoemulsion is a result of the inter-droplet bridging via PEGDA molecules. At elevated temperatures, the acrylate groups at the termini of PEGDA become increasingly hydrophobic and partition into the oil/water interface, leading to droplet bridging [21]. The linear viscoelastic moduli (storage modulus G' and loss modulus G") and the associated microstructures of the nanoemulsions at elevated temperatures are shown in Fig. 4.2. At room temperature (T = 20.0 °C), the nanoemulsion shows a liquid-like behavior in which $G' \sim \omega^2$ and $G'' \sim \omega^1$ (Fig. 4.1A) [2], and no assembled structure is observed by confocal microscopy (Fig. 4.1B). Upon increasing the temperature, G' and G" increase, and the system undergoes a sol-gel transition between T = 30.0 °C and 32.5 °C, upon which G' is greater than G" and the system behaves as a viscoelastic solid. The increase in the mechanical strength results from the assembled gel network. As shown in Fig. 4.1B, at elevated temperatures, the nanoemulsion droplets first assemble into cluster aggregates (T = 30.0 °C) and then a sparse gel network is formed (T = 32.5 °C) [101,181]. When the temperature is further increased, a more well-connected and space-filling network is formed. The gelling nanoemulsion shows a classic arrested phase separation behavior in which the microstructure shows the bi-continuous phases composed of droplet-rich domains (fluorescence region) and droplet-lean domains (dark regime), and the network is denser when the attraction is stronger (i.e. the temperature is higher in our system) [91,104,128].
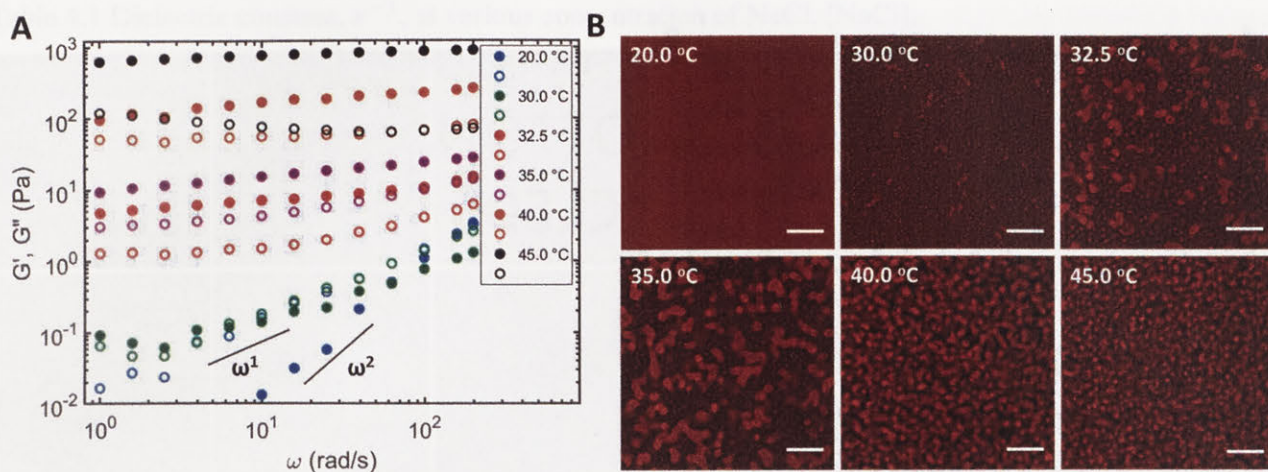
Figure 4.2 Rheological response and the associated microstructures of the nanoemulsion at elevated temperatures. [NaCl] = 0 M. (A) Linear viscoelastic moduli (closed symbols are storage moduli G', open symbols are loss moduli G") as a function of angular frequency ω. (B) The microstructure of the assembled nanoemulsions at elevated temperatures. The droplets are fluorescently labeled using a lipophilic dye and imaged using confocal microscopy. Scale bars = 10 μm.

4.4.2 Screening of electrostatic repulsion via NaCl

For charge-stabilized colloidal suspensions, it is widely known that one can induce colloidal assembly and gelation by addition of an electrolyte to screen the inter-particle electrostatic repulsion [22,75]. Since our nanoemulsion is stabilized by ionic surfactants (SDS), we expect the same screening effect can take place in our system. Fig. 4.3 shows the rheological response and the associated microstructure of the nanoemulsion at different concentrations of added NaCl, [NaCl], at T = 20.0 °C. As anticipated, the gelation of nanoemulsions can be successfully induced by increasing [NaCl] in the suspension. When [NaCl] ≤ 0.01 M, the nanoemulsion shows a liquid-like behavior where $G' \sim \omega^2$ and $G'' \sim \omega^1$ (Fig. 4.3A), although a few aggregates composed of nanoemulsion droplets are induced at [NaCl] = 0.01 M. When [NaCl] is further increased, the viscoelastic moduli significantly increase and more aggregates are induced, which eventually span the space and give rise to a solid-like behavior of the material. Compared to the gelation induced by PEGDA bridging, the salt-induced gelation results in a weaker gel (Fig. 4.2A versus Fig. 4.3A) and a more open gel network (Fig. 4.2B versus Fig. 4.3B).
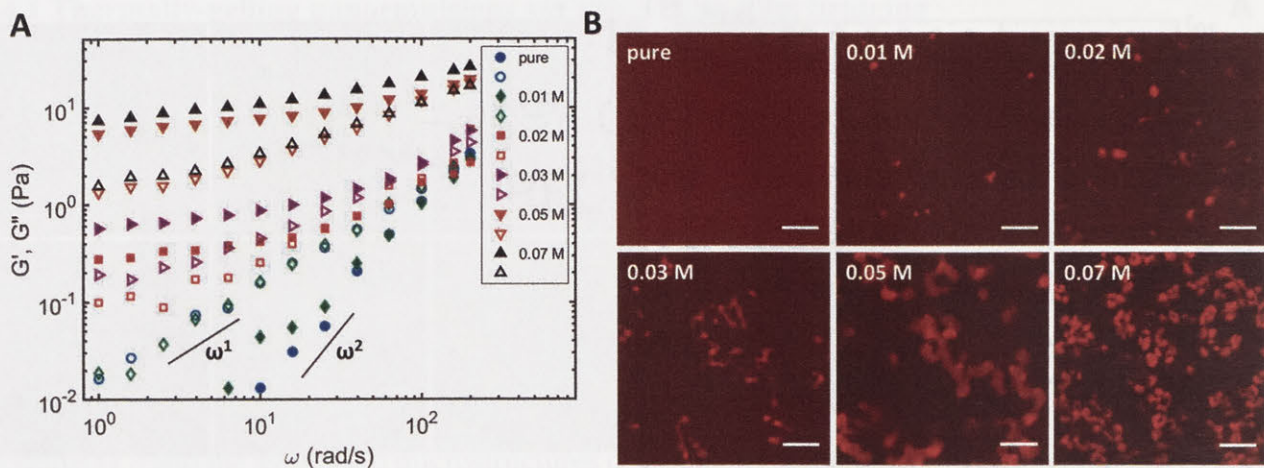
Figure 4.3 Rheological response and the associated microstructures of the nanoemulsion at various values of added salt [NaCl], at T = 20.0 °C. (A) Linear viscoelastic moduli (closed symbols are storage moduli G', open symbols are loss moduli G") as a function of angular frequency ω. (B) The microstructure of the assembled nanoemulsions at various values of added salt [NaCl]. Scale bars = 10 μm.

Interestingly, we note that the salt concentration needed to induce gelation is quite low in our system ([NaCl] ~ 0.01 to 0.1M), as compared to other investigations where SDS-stabilized PDMS nanoemulsions were also studied ([NaCl] ~ 0.1 to 1M) [15,31]. Moreover, even a slight variation in [NaCl] can give rise to a significant change in the suspension rheology and associated microstructures. We proposed two effects that are responsible for such sensitivity to added salts. First, at room temperature where PEGDA droplet bridging is not induced, the non-associating PEGDA acts as a depletant in the system that gives to an attractive interaction with a strength = 15.5 kT, where k is Boltzmann constant and T is the absolute temperature (the calculation will be discussed in detail in the next section). The addition of salt screens the electrostatic repulsion and then makes the strong depletion attraction easily dominate. Second, the length scales associated with the range of these interactions also play an important role. For electrostatic repulsion, the effective length scale is characterized by the Debye length [22,75], κ^{-1}, and the results are shown in Table 4.1. Details of the calculation will be discussed in the next section. Because an excess of SDS is added to facilitate the nanoemulsion synthesis, there is already a large concentration of charged species in the continuous phase even without added NaCl. Therefore, κ^{-1} is 0.71 nm for [NaCl] = 0 M. On the other hand, for depletion interaction the range of the interaction is determined by the size of the depletant [17] – here the radius gyration (R_g) of PEGDA is approximately 0.7 nm [132]. As can be seen, the range of the attractive and repulsive interactions are comparable, and a slight decrease in κ^{-1} can easily make the depletion attraction dominant in the system.

90

Table 4.1 Dielectric constant, κ^{-1}, at various concentration of NaCl, [NaCl].

[NaCl] (M)	κ^{-1} (nm)
0	0.71
0.01	0.68
0.02	0.66
0.03	0.64
0.05	0.60
0.07	0.57

4.4.3 Estimation of interactive potentials

To support the discussion in the last section, we present here a quantitative description of the interactions involved in the nanoemulsion system. We consider the scenario shown in Fig. 4.4A where the system is composed of charged-stabilized nanoemulsion droplets, non-adsorbing PEGDA, SDS micelles, sodium ions and chloride ions. The schematic diagram in Fig. 4.4A then describes the scenario of the salt-added nanoemulsion at room temperature and with no PEGDA droplet bridging. Estimation of the pairwise interactive potentials follows the methodology developed in our prior work [138] which has been shown to successfully describe the interactive potentials of a similar gelling nanoemulsion system. As shown in Fig. 4.4A, the overall pairwise interaction between droplets has contributions from screened electrostatic repulsion, depletion attraction arising from both PEGDA molecules and SDS micelles in the continuous phase, and van der Waals interaction. Next, we briefly summarize how to estimate each interaction.

4.4.3.1 Electrostatic repulsion

The electrostatic repulsion, U_{elec}, is estimated using the Yukawa potential [22,75],

$$U_{elec} = \varepsilon_{elec} \frac{2a}{r} e^{-\kappa(r-2a)} \tag{4.1}$$

where a and r are the radius and the center-to-center distance of nanoemulsion droplets respectively. κ^{-1} is the Debye length and is calculated as followed,

$$\kappa^{-1} = \sqrt{\frac{\varepsilon_0 \varepsilon_r kT}{1000 e^2 N_A \sum z_i^2 M_i}} \tag{4.2}$$

where ε_0 is the electric permeability of free space, k is Boltzmann constant, T is the absolute tempeature, e is the elementary charge, N_A is Avogadro's number, z_i is the charge number ($= 1$ since both NaCl and SDS are monovalent) and M_i is the molar concentration. M_i is determined by the molar concentration of added NaCl and the remaining free [SDS] in the continuous phase that is estimated by considering the area of SDS occupied on the oil droplet ($= 0.617$ nm^2/molecule) [182]. ε_r is the dielectric constant of the continuous phase, which is calculated by considering the dielectric constants of water [115] and PEGDA. The dielectric constant of PEGDA is estimated from the dielectric constant of PEG backbone ($\varepsilon_{r,PEG} = 14.5$) [116]. ε_r is then calculated using the mixing rule, for which the deviation from the measured value has shown to be negligible at the high PEG concentration regime such as the case in our system [117].

The strength of the electrostaic repulsion, ε_{elec}, is calcuated using the following equation [22,75],

$$\varepsilon_{elec} = 32\pi\varepsilon_0\varepsilon_r \left(\frac{kT}{ze}\right)^2 \text{atanh}^2 \left(\frac{1}{4}\frac{ze\xi}{kT}\right) \tag{4.3}$$

which is obtained from Gouy-Chapman solution to Poisson-Boltzmann equation with the superposition assumption and Derjaguin approximation. The zeta potential, ξ, of the nanoemulsion droplets is -44.3 mV and is measured using a Zetasizer (Brookhaven Instruments 90Plus PALS).

4.4.3.2 PEGDA depletion

The PEGDA depletion is estimated from Asakura-Oosawa potential [17,122],

$$U_{dep} = -\frac{\varepsilon_{dep}(a + \delta_P)^3}{\delta_p^2(\frac{3a}{2} + \delta_p)}\left[1 - \frac{3}{4}\frac{r}{a + \delta_P} + \frac{1}{16}\left(\frac{r}{a + \delta_P}\right)^3\right] \tag{4.4}$$

when $2a \leq r \leq 2(a + \delta_p)$. To consider the polymeric nature of PEGDA (instead of simple hard-shperes), we use the ideal polymer assumption. Therefore, an additional configurational entropy

from the polymeric depletants contributes to the depletion strength, ε_{dep}, and the interaction range, δ_P [17]. ε_{dep} and δ_P are then estimated as

$$\varepsilon_{dep} = \phi_p \frac{a}{R_g} 3ln2 \qquad (4.5)$$

$$\delta = \sqrt{2ln2}R_g \qquad (4.6)$$

where ϕ_p is the PEGDA volume fraction and R_g is the radius of gyration of PEGDA (≈ 0.7 nm) [132]. For the estimation of the potential, we assumed the morphology of the PEGDA is independent of the [NaCl], since not a large amount of NaCl is added into the system. Therefore, in our calculations we assume the PEGDA depletion remains constant for all values of [NaCl].
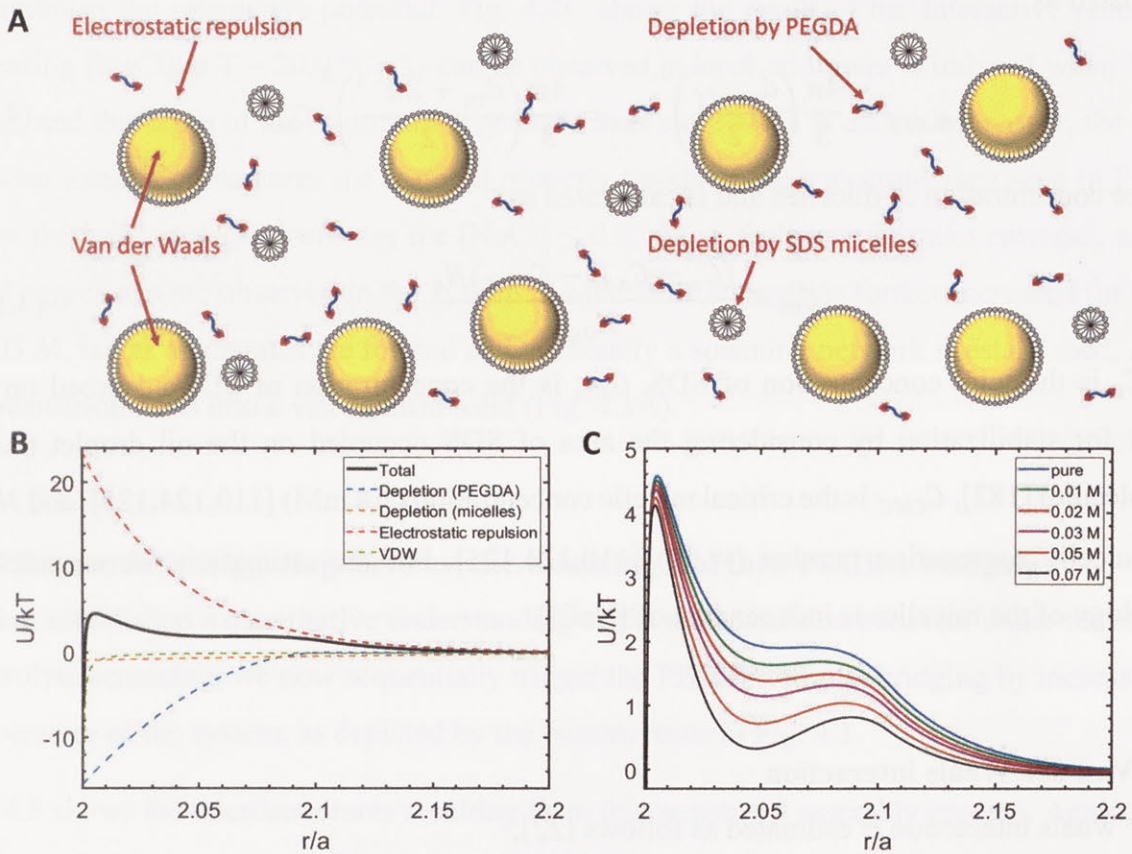
Figure 4.4 Estimates interaction potentials at various [NaCl] of the nanoemulsion at T = 20 °C. (A) Schematic of the system used for estimating the interaction potentials. A total of four interactions were considered: screened electrostatic repulsions, depletion by PEGDA, depletion by SDS micelles, and van der Waals interaction. (B) Contributions to the potential at [NaCl] = 0 M and T = 20 °C from depletion by PEGDA, depletion by SDS micelles, electrostatic repulsion, and van der Waals (VDW) interaction. (C) Overall interaction potential at various values of added [NaCl] at T = 20 °C.

4.4.3.3 SDS micelle depletion

Depletion by SDS micelles is also estimated by the Asakura-Oosawa potential. Assuming micelles behave like hard-spheres, the micelle depletion is calculated as follows [17,52,123],

$$U_{dep} = -(\xi C_m kT)\left(\frac{\pi a}{2}\left(d_{m,eff} - (r - 2a)\right)^2\right) \tag{4.7}$$

when $2a \leq r \leq 2a + d_{m,eff}$, and

$$\xi = \frac{1 + \phi_{m,eff} + \phi_{m,eff}^2 - \phi_{m,eff}^3}{\left(1 - \phi_{m,eff}\right)^3} \tag{4.8}$$

where $\phi_{m,eff}$ is the effective volume fraction of micelles by considering the Debye layer [7] and is calculated as

$$\phi_{m,eff} = \frac{4\pi}{3}\left(\frac{d_{m,eff}}{2}\right)^3 C_m = \frac{4\pi}{3}\left(\frac{d_m + 2\kappa^{-1}}{2}\right)^3 C_m. \tag{4.9}$$

C_m is the concentration of micelles and is calculated as

$$C_m = \frac{(C_o - C_{ads} - C_{CMC})N_A}{N_{agg}} \tag{4.10}$$

where C_o is the total concentration of SDS, C_{ads} is the concentration of SDS adsorbed on the droplets for stabilization by considering the area of SDS occupied on the oil droplet (0.617 nm^2/molecule) [182], C_{CMC} is the critical micelle concentration ($\approx$ 8 mM) [110,124,125], and N_{agg} is the micelle aggregation number ($\approx$ 60) [110,124,125]. For the estimation, we assume the morphology of the micelles is independent of [NaCl].

4.4.3.4 Van der Waals interaction

Van der Waals interaction is estimated as follows [22],

$$U_{VDW} = \frac{-Aa}{12(r - 2a)} \tag{4.11}$$

by assuming a uniform droplet size and Derjaguin approximation is used. Here, $A = 3.3 \times 10^{-22}$J is the Hamaker constant of PDMS-water-PDMS [126,127].

4.4.3.5 Overall pairwise interaction potentials

Fig. 4.4B shows the resulting contribution from each interaction to the overall interaction at T = 20.0 °C and [NaCl] = 0 M. In this system, the repulsion comes from the electrostatic repulsion provided by the charged SDS on the nanoemulsion droplets, and the major attraction comes from the PEGDA depletion via the free PEGDA in the continuous phase. Although PEGDA provides a significant depletion attraction with a strength = 15.5 kT, the even stronger electrostatic repulsion dominates the interaction. Therefore, no minimum in the overall pairwise interaction is observed and no self-assembly is induced. Although the electrostatic repulsion prevails in the system at T = 20.0 °C and [NaCl] = 0 M, the addition of electrolytes can effectively screen the electrostatic repulsion by decreasing its characteristic length scale (i.e. Debye length, κ^{-1}), leading to a local minimum in the interactive potential. Fig. 4.4C shows the result of the interactive potential at increasing [NaCl] at T = 20.0 °C. As can be observed, a local minimum is induced when NaCl is added, and the depth of the minimum is greater when more NaCl is added. Moreover, the overall pairwise interaction captures the material property trends of the nanoemulsions seen in Fig. 4.3. When the ionic strength increases for [NaCl] ≤ 0.02 M, a shallow minimum emerges, and few small aggregates are observed in the system. As the ionic strength is further increased for [NaCl] ≥ 0.03 M, larger aggregates are formed and eventually a spanning network is established, and the nanoemulsion turns into a viscoelastic solid (Fig. 4.3A).

4.4.4 Sequentially triggering electrostatic screening and then PEGDA bridging

Having established a quantitative understanding of the nanoemulsion behavior under the effect of electrolyte screening, we now sequentially trigger the PEGDA droplet bridging by increasing the temperature of the system, as depicted by the bottom route in Fig. 4.1.

Fig. 4.5 shows the microstructures resulting from this sequential assembly process. Again, in this work, we first increase the ionic strength of the system at T = 20.0 °C (as shown in the bottom row of Fig. 4.5) and then increase the temperature to induce the PEGDA droplet bridging (moving vertically upwards from the bottom of Fig. 4.5). We chose the temperatures for these studies to be 32.5 °C and 45.0 °C to represent the point near (right above) the gelation point of the pure system ([NaCl = 0 M) and the point where the gel network is well-established due to the thermal PEGDA droplet bridging, respectively. Generally, as more NaCl is added, at elevated temperatures there

are more remnants from the salt-induced structure at T = 20.0 °C, even though stronger PEGDA droplet bridging is induced at T = 45.0 °C. In other words, when [NaCl] is higher at T = 20.0 °C, the nanoemulsion is more difficult to rearrange its assembled structures at this low temperature via subsequent thermally-induced PEGDA bridging.
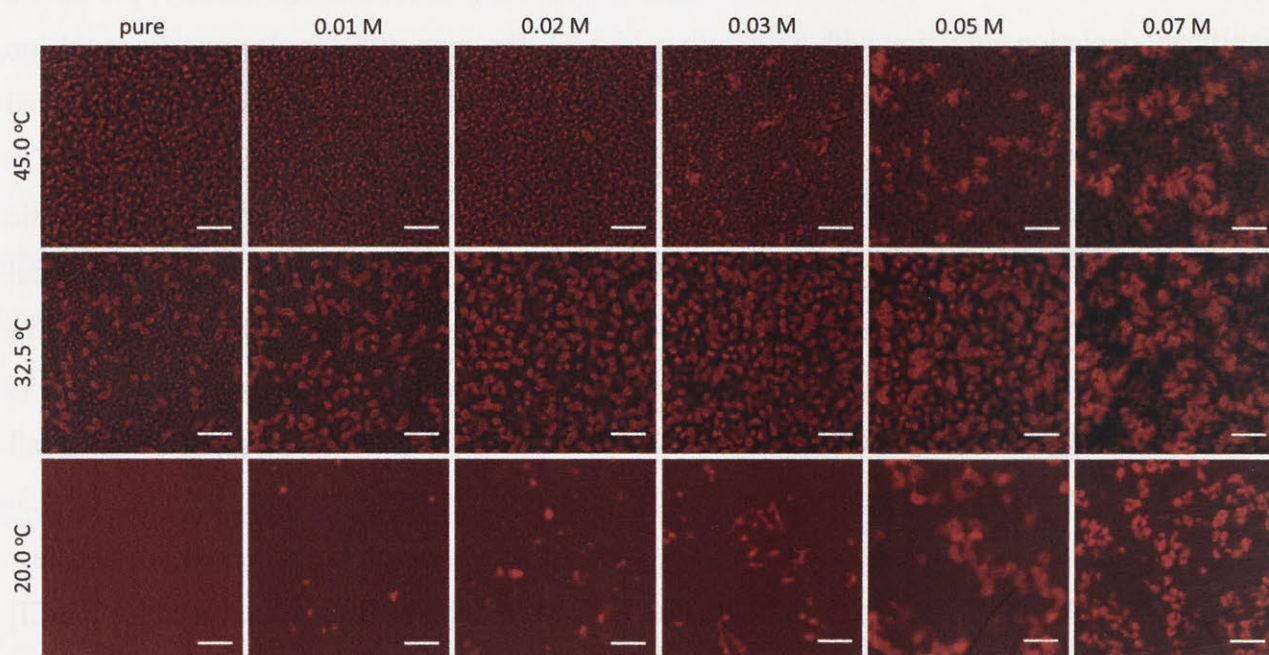
Figure 4.5 Microstructures of the nanoemulsion observed after sequentially screening the electrostatic repulsion, and then inducing PEGDA thermal bridging of droplets. Scale bars = 10 μm.

For [NaCl] ≤ 0.02 M, the microstructures across the experimental [NaCl] window are similar at T = 45.0 °C regardless of [NaCl]. However, the nanoemulsions with added salt display a more established network of thick strands at T = 32.5 °C. Trends in the microstructures can be quantitatively analyzed by calculating the characteristic length, L_C, of the structure by applying a fast Fourier transform to the confocal images and then calculating the correlation length from the scattering spectrum [32,91,101,105,143]. The results for the calculated L_C are shown in Fig. 4.6. For [NaCl] ≤ 0.02 M, L_C at T = 32.5 °C decreases with increasing [NaCl], corresponding to the increase in the number of thick strands seen in the confocal images. On the other hand, at T = 45.0 °C L_C stays nearly constant over this [NaCl] window, suggesting a similar gel network is obtained. However, for [NaCl] ≥ 0.03 M, more remnants from the salt-induced structure at T = 20.0 °C are observed at elevated temperatures. At T = 32.5 °C and 45.0 °C, it can be easily observed that there are large aggregates incorporated into the gel network, and the number and the size of the aggregates are larger when [NaCl] is higher. These trends are also observed in Fig. 4.6

for [NaCl] ≥ 0.03 M where L_C increases as [NaCl] is increased at T = 32.5 °C and 45.0 °C.
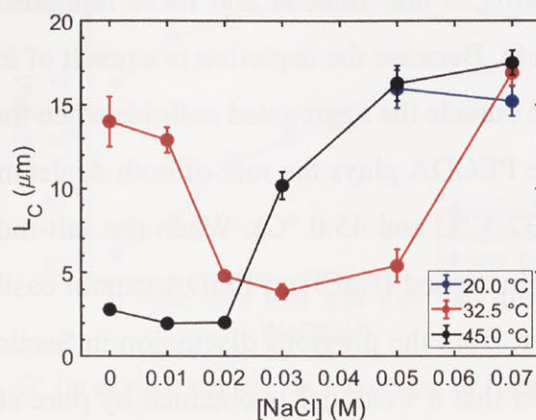
Figure 4.6 Correlation length, L_C, calculated from images in Fig. 5 as a function of [NaCl] for three different temperatures. L_C of images for [NaCl] ≤ 0.03 M at T = 20 °C cannot be characterized. Error bars are standard errors from 20 images.

The viscoelastic moduli under each condition are also measured, and the results are shown in Fig. 4.7. Interestingly, the rheological data shows the trend that a stronger gel is not necessarily obtained with added NaCl even though the gelation is 'pre-induced' with the addition of NaCl at room temperature. This non-intuitive trend can be more clearly seen in Fig. 4.8 where the G' at an intermediate angular frequency ($\omega = 10$ rad s^{-1}) from Fig. 4.7 is plotted as a function of [NaCl] for the three temperatures. For T = 20.0 °C (no PEGDA droplet bridging is induced), the gel is stronger when more NaCl is added. However, when the temperature is increased to T = 45.0 °C, the gel is weaker when more NaCl is added at T = 20.0 °C, even though the system starts with a 'pre-gel' state with non-negligible mechanical strength. For T = 32.5 °C, the gel strength increases first when the nanoemulsion starts with a low concentration of NaCl for [NaCl] ≤ 0.03 M, and G' decreases when [NaCl] is further increased.

We believe two reasons are responsible for this non-intuitive trend in the microstructures and the rheological response. The first reason is related to the depth of the secondary minimum induced by the increased [NaCl] at T = 20.0 °C (Fig. 4.4C). When [NaCl] is higher, the secondary minimum is deeper. For the structure to be rearranged as the temperature is increased, the system needs to escape from this minimum and undergo the PEGDA droplet bridging. Therefore, it is reasonable that with increasing [NaCl] there are more remnants of the salt-induced structures at T = 20.0 °C observed at the higher temperatures (Fig. 4.5). The same mechanism applies to the rheological behavior in Fig. 4.8. In the analysis in Section 4.4.3 and Fig. 4.4 where the effect of NaCl screening

at T = 20.0 °C is discussed, it is shown that the PEGDA depletion plays an important role. At T = 20.0 °C, PEGDA droplet bridging is not induced and these non-adsorbing PEGDA polymers behave as depletants in the system. Because the depletion is a result of increased osmotic pressure [17], the depletants are excluded outside the aggregated colloids when the clusters and gel network are formed [1]. In our study, the PEGDA plays the role of both depletant and thermally-triggered droplet bridging agent (at T = 32.5 °C and 45.0 °C). When the salt-induced structures are more difficult to be reconstructed (at increased [NaCl]), PEGDA cannot easily enter between droplets and undergo bridging. Moreover, from the previous discussion in Section 4.4.1 and 4.4.2 as well as in Fig. 4.8, it can be observed that a weak gel is obtained by pure electrolyte screening (blue data in Fig. 4.8 at T = 20.0 °C) compared to the pure thermally bridging (red and black data in Fig. 4.8 at [NaCl] = 0 M). Therefore, when [NaCl] is high, the salt-induced aggregation is strong enough to stay intact when the temperature is increased. Under these conditions, the system has difficulty rearranging, the effect of PEGDA bridging is diminished, and hence a weaker gel results (black data in Fig. 4.8).
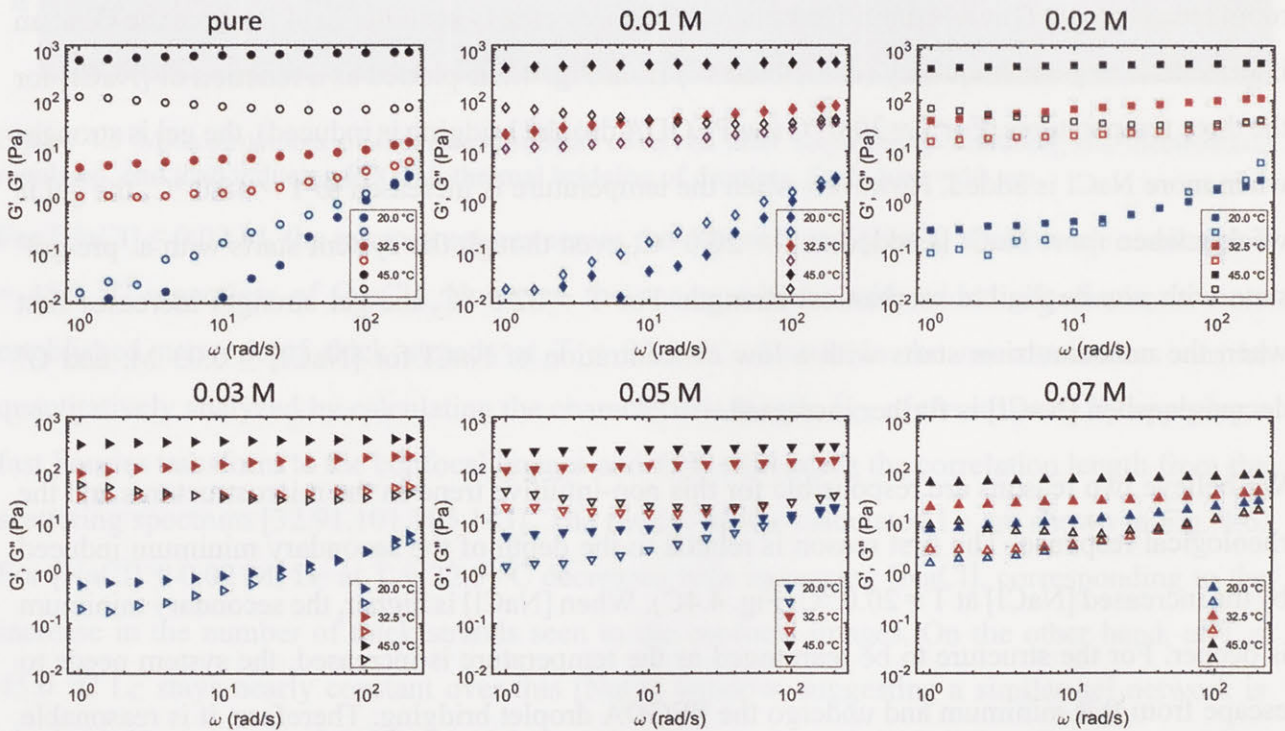
Figure 4.7 Linear viscoelastic moduli (closed symbols = G', open symbols = G") as a function of angular frequency, ω, of the nanoemulsion after sequentially screening the electrostatic repulsion via added salt, and then thermally induced bridging of droplet by PEGDA.
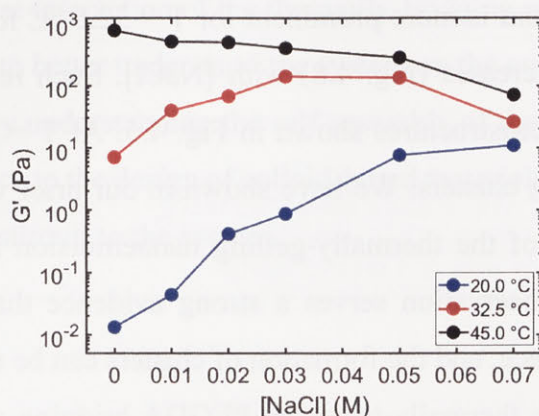
Figure 4.8 Storage modulus, G' (at $\omega = 10$ rad s^{-1}), as a function of [NaCl] for three temperatures. Data is from Fig. 4.7.

The second reason explaining the trends in microstructures and rheology relates to the dynamics of the PEGDA bridging-induced gelation. It can be noticed that the first reason as just discussed (the depth of the minimum in the pairwise interactive potentials and the mechanism of PEGDA depletion and bridging) describes well the material behavior at T = 45.0 °C (and at T = 32.5 °C for [NaCl] > 0.03 M) where both microstructure and rheology have a monotonic trend — L_C monotonically increases (Fig. 4.6) and G' monotonically decreases (Fig. 4.8) when the nanoemulsion is preconditioned with higher [NaCl]. However, for T = 32.5 °C, a non-monotonic trend is observed, L_C first decreases then increases and G' first increases then decreases when the nanoemulsion is preconditioned with higher [NaCl]. We believe this is due to the dynamics of the gelation via PEGDA bridging. In our prior works, we have shown that under the thermally-triggered PEGDA bridging, the gelation of nanoemulsions undergoes a spinodal decomposition and then the structure is dynamically arrested [105,143]. Under this gelation route, a stronger attraction (i.e. PEGDA bridging at higher temperatures) gives rise to an earlier arrest and stops the network coarsening [11,129,183]. This behavior can be characterized by measuring the viscoelastic moduli with time at different temperatures (Appendix C Fig. C3) where at T = 45.0 °C the moduli reach a plateau after t ≈ 400 seconds, while at T = 32.5 °C the moduli still increase with time over the experimental window (t = 600 sec). In other words, the large-scale structural reconstruction of the salt-induced structure is suppressed at high temperatures, as the strong PEGDA bridging can more effectively dynamically arrest the gel network, while at lower temperatures the system can more effectively take advantage of the 'pre-gel' structures induced by added salt and undergo the structural reconstruction. Therefore, compared to the nanoemulsion

at T = 45.0 °C, the rearrangement is more prominent for T = 32.5 °C for [NaCl] ≤ 0.03 M as L_C decreases (Fig. 4.6) and G' increases (Fig. 4.8) with [NaCl]. Such rearrangement can be also visually observed from the microstructures shown in Fig. 4.5. At T = 32.5 °C, the gel network coexists with freely-suspending clusters. We have shown in our prior work that such coexistent structures are a characteristic of the thermally-gelling nanoemulsion near the critical gelation temperature [101,105]. This observation serves a strong evidence that the PEGDA bridging-induced reconstruction takes place, and the formation of clusters can be used as a qualitative scale to evaluate how effectively the thermally-triggered PEGDA bridging rearranges the assembled network. As more [NaCl] is added at T = 20.0 °C, fewer clusters are observed and a more well-connected gel network is formed. When [NaCl] is above 0.03 M, the coexisting clusters at T = 32.5 °C cannot be observed, and the trend of material properties at T = 32.5 °C follows the trend of those at T = 45.0 °C, and again we believe it is due to the depth of the minimum is too deep for the system to reconstruct itself, as we described above.

4.5 Conclusion

In this work, we introduce an approach to modulate the microstructures and the rheological properties of a nanoemulsion suspension by sequentially screening the electrostatic repulsion and then thermally triggering the droplet bridging. We revisited the nanoemulsion system developed in our group previously and carefully studied the inter-droplet interaction from each constituent in the system. By calculating the pairwise interactions, we found that the non-associating PEGDA contributes to a significant depletion interaction, and the nanoemulsion system can undergo a sol-gel transition at room temperature by screening the electrostatic repulsion with the addition of NaCl. By subsequently inducing the PEGDA droplet bridging via an increase in temperature, we show that the system can restructure and reach a different gelled state. We then used the established pairwise interactive potential and the dynamics of the thermal gelation to explain the trend in material behavior under the sequential application of stimuli. Our results suggest that the first screening of the electrostatic repulsion can be used as an effective strategy to template the structure of the nanoemulsion system and the second thermally bridging can then consolidate the gel network. Moreover, our discussion highlights that a quantitative understanding of the inter-droplet interaction is required to understand the behavior of the system. The future work will then focus

on establishing the pairwise interaction of the thermally-bridging mechanism from first principles and applying simulations to better understand the system on the colloidal scale and the associated dynamics. Overall, here by understanding the self-assembly of the system at the molecular level, this work provides guidance to the design of colloid-based materials with complex microstructures by carefully applying the stimuli to the system.

Chapter 5

Thermal Processing of Thermogelling Nanoemulsions as a Route to Tune Material Properties

5.1 Overview

Many soft matter systems have properties which depend on their processing history. It is generally accepted that material properties can be finely tuned by carefully directing self-assembly. However, for gelling colloidal systems, it is difficult to characterize such path-dependent effects since the colloidal attraction is often provided by adding another component to the system such as salts or depletants. Therefore, studies of and an understanding of the role of processing on the material properties of attractive colloidal systems are largely lacking. In this chapter, we systematically studied how processing greatly influences the properties and the microstructures of model attractive colloidal systems. We perform experiments using a thermogelling nanoemulsion as a model system where the isotropic attraction can be precisely tuned via the temperature. The effects of processing conditions on gel formation and properties is tested by performing well-designed sequential temperature jumps. By properly controlling the thermal history, we demonstrate that properties of colloidal gels can be beyond the limit set by direct quenching, which has been a major focus in literature, and that otherwise slow aging of the system associated with a decrease in elasticity can be prevented. Our results provide new experimental evidence of path-dependent rheology and associated microstructures in attractive colloidal systems and provide guidance to future applications in manufacturing complex colloid-based materials.

This chapter has been adapted with permission from L. -C. Cheng, P. D. Godfrin, J. W. Swan and P. S. Doyle "Thermal Processing of Thermogelling Nanoemulsions as a Route to Tune Material Properties" *Soft Matter* 2018, **14**, 5604-5614. Copyright 2018 Royal Society of Chemistry.

5.2 Introduction

Properties of many materials are affected by how they are processed. Perhaps the oldest and most

common example is metal forging: after the metal is shaped into the desired geometry, it is subsequently heated and maintained at an elevated temperature, and then cooled (quenched) to achieve the final state. This intermediate step, known as thermal annealing, allows the metallic atoms to relocate themselves and form specific microstructures. By manipulating time and temperature, annealing can effectively alter mechanical properties of the metallic materials, such as ductility and toughness [184,185]. Such thermal treatments can be also used in glasses or ceramic materials to remove internal stresses and prevent material failure [184]. In modern technology, thermal annealing is also important in semiconductor manufacturing. Thermal treatment significantly improves the electric [186], optical [187,188], magnetic [189] and mechanical properties [190]. Annealing can be also applied to graphene-based materials to improve mechanical strength and electric conductivity due to improved atomic ordering [191].

In addition to hard condensed matter, (thermal) processing can also be applied to soft matter. Kim *et al.* found that poly(isoprene)-b-poly(lactide) copolymer melts can form aperiodic quasicrystalline states that are commonly found in metal alloys [192]. By rapidly quenching the copolymer melt from the disordered state using liquid nitrogen, then reheating it to $T < T_{ODT}$ (where T_{ODT} is the order-disorder transition temperature), the self-assembled polymer micelles can form hexagonal C14 and cubic C15 Laves phases. She *et al.* studied the self-assembly of polystyrene-b-poly(L-lactide) copolymer thin films grafted on silicon wafers [193]. By thermally annealing the polymer film, large-scale perpendicular cylinder structures could be obtained. Moreover, such alignment of block copolymer films can also be controlled *via* an electric field. Olszowka *et al.* applied an in-plane electric field to process a triblock copolymer thin film composed of polystyrene-b-poly(2-hydroxyethyl methacrylate)-b-poly(methyl methacrylate) copolymer [194]. A highly ordered stripe pattern perpendicular to the film plane could be achieved. Lu *et al.* studied how thermal processing controls polyamide 66/clay nanocomposite crystals [195]. By carefully controlling the thermal history (melt, slow cooling, annealing), high crystallinity could be obtained.

There have been relatively few experimental studies examining how processing via temporal modulation of inter-particle interactions affects the material properties of gelling colloidal suspensions. A promising approach is to use electric [196] and magnetic fields [16,197] to direct self-assembly. In such systems, the external fields induce polarization that results in anisotropic

inter-particle dipole-dipole interactions. The advantage of using such fields is that the interaction can be temporally modulated and is reversible, such that annealing strategies (e.g. AC electric fields or toggled magnetic fields) can be implemented to achieve equilibrium crystalline structures. However, the induced dipole-dipole interaction scales with the particle volume and becomes weak when the particles approach the nanoscale [19]. Wagner and coworkers studied the properties of octadecyl-coated silica nanoparticles (which gel when the system is cooled) subject to different thermal histories [18,198]. However, they found the rheological response of the system was independent of its thermal history. Sherman et al. employed simulations to study the self-assembly of nanoparticles under a toggled depletion attraction [120,199]. Interestingly, by using time-dependent, periodically toggled attractions, particles could self-assemble into well-ordered crystalline structures without kinetic trapping in a disordered state. However, it is difficult to experimentally implement time varying colloidal interactions in gelling systems which rely on the addition of a third component (such as depletants or salts) as a means to vary inter-particle interactions. Recently, our group has developed a thermally gelling oil-in-water nanoemulsion consisting of surfactant stabilized, nano-sized polydimethylsiloxane droplets suspended in a poly(ethylene glycol) diacrylate (PEGDA) aqueous continuous phase [21]. At elevated temperatures, the hydrophobic end groups of the PEGDA partition into the oil/water interface and bridge droplets, which results in isotropic attractive interactions that can be temporally tuned "at will" without adding another component. Initial work [143] has shown that different heating rates result in different rheological responses, though thermal processing as a means to tune microstructure and mechanics has not been studied. We have also developed a technique that enables us to directly visualize the gel microstructure at any state using confocal microscopy [33,101,143], allowing us to study how processing controls the gel structures. Additionally, the major changes in the macroscopic (rheological) properties and microstructure of the nanoemulsion can be captured within $\Delta T = 30$ to 40 °C (from room temperature to T = 50-60 °C) [98,101]. Such advantages make this nanoemulsion a suitable model system to understand how thermal processing affects the behavior of colloidal gels with quantifiable experimental evidence.

In this chapter, we experimentally investigate sequential thermal processing of thermogelling nanoemulsions as a means to control material properties. We use rheological properties and real-space microstructural correlations as our canonical metrics to characterize the material behaviors. By changing thermal processing routes, we show that properties of colloidal gels can be beyond

the limit set by direct quenching. For example, under certain thermal processing conditions, the gel strength of the nanoemulsion can increase by 47% compared to a step-jump in temperature, and the thermal processing can effectively prevent a decrease in gel strength due to slow relaxation resulting from directly quenching the system at high temperatures. The path-dependent properties of our attractive colloidal systems motivate the concept that one should think beyond just varying chemical composition as a means to control material properties and should expand to consider processing as an equally important parameter. Indeed, several works have shown that even a single material system shows diverse structures and complex properties by carefully directing the self-assembly [200–202]. In addition to being model colloidal systems, nanoemulsions are widely used in applications such as food products, cosmetics, pharmaceuticals, and enhanced oil recovery for which the ability to engineer material properties through processing conditions is desirable [6].

5.3 Materials and methods

5.3.1 Materials

Sodium dodecyl sulfate (SDS), poly(ethylene glycol) diacrylate (PEGDA, M_n = 700 g/mol), silicone oil (polydimethylsiloxane, PDMS, viscosity = 5cSt at 25 °C), lipophilic dye PKH26 (excitation and emission wavelengths $\lambda_{ex}/\lambda_{em}$ = 551/567 nm) and photoinitiator 2-hydroxy-2-methylpropiophenone (Darocur 1173) were purchased from Sigma-Aldrich. All chemicals were used without further purification.

5.3.2 Synthesis of nanoemulsions

The nanoemulsion system studied in this chapter was composed of a disperse phase PDMS of volume fraction = 0.15, an aqueous continuous phase consisting of PEGDA of volume fraction = 0.33, SDS of concentration = 0.175M and deionized water.

The nanoemulsions were synthesized by the following procedure. First, a pre-emulsion was prepared by adding PDMS to the aqueous continuous phase composed of PEGDA and SDS using magnetic stirring with a speed of 700 rpm. Stirring was maintained for 20 min or until no macroscopic phase separation was observed. A high-pressure homogenizer (EmulsiFlex-C3, Avestin) was used to process the pre-emulsion into the corresponding nanoemulsion. The

homogenization was conducted at a pressure of 18 kpsi for 14 passes. The emulsion was cooled to 4 °C between each pass and the final nanoemulsion was stored at 4 °C until further use.

The size of PDMS droplets was monitored using dynamic light scattering (90Plus PALS, Brookhaven Instruments). Fig. D1 (Appendix D) shows the evolution of droplet size after each pass. The droplet size was measured by diluting the oil volume fraction of the emulsion from 0.15 to 0.002 using an aqueous diluting agent consisting of PEGDA with volume fraction = 0.33. It has been reported previously that dilution using this diluent does not affect the droplet size and polydispersity [21]. The nanoemulsion suspension used in this work has a droplet size equal to 37 nm with polydispersity equal to 0.187.

5.3.3 Rheology

Rheological characterization was performed by using a stress-controlled rheometer (ARG2, TA instrument) equipped with a 2° 60mm aluminum upper-cone and a temperature-controlled Peltier lower-plate. For each measurement, the nanoemulsion was loaded onto the Peltier plate at 20 °C. A wetted solvent trap was used and a few drops of deionized water were added on top of the cone to control the evaporation. Before each measurement, a preshear step with a constant rotation at a rate of 20 rad/s for 30 seconds followed by a 90 seconds period where the sample remained quiescent at T = 20 °C, was performed. Thermal processing measurements (one-step and two-step jumping) were carried out at an oscillatory frequency = 20 rad/s with strain = 0.1 %. The speed of temperature increase was set to be the maximum rate that the rheometer was able to achieve. Fig. D2B (Appendix D) shows the actual temperature history during the measurement. Large amplitude oscillatory shear (LAOS) at an oscillatory frequency = 20 rad/s with strain = 15 % was performed to yield the nanoemulsion at 50 °C for the gel aging (Fig. 5.5). LAOS was applied at t = 600 s for 30 seconds. Freshly loaded nanoemulsions were used for each measurement.

5.3.4 Confocal microscopy

Direct visualization of the gel microstructures was carried out by using a confocal laser scanning microscope (LSM 700, Zeiss) quipped with a 63X oil-immersion objective (numerical aperture = 1.4). Samples for imaging were prepared as follows. First, the nanoemulsion was mixed with 1

vol% fluorescent dye and 1 vol% photoinitiator. It has been shown previously that the addition of this small amount of chemicals does not affect the microstructures [143]. Subsequently, 150 μL of the mixture was loaded into a glass chamber (Lab-Tek™ #155411, Thermo Fisher Scientific). Pipetting samples into glass chambers for microscopy mimics the preshear step on the rheometer. Then, the sample-loaded glass chamber was put onto the Peltier plate on the rheometer at 20 °C for 90 seconds, and the sample underwent the same thermal history as during the rheological characterization. The time scale of the heat transfer from the Peltier plate to the sample through the glass is negligible. The thickness of the glass microscope slide is 0.15 mm according to the vendor. The thermal diffusivity of the glass slide is about 0.55 mm^2/s [203]. Therefore, the diffusive time scale is 0.152/0.55 = 0.04 s, which is negligible compared to the experimental time scale. After thermal processing, the sample was exposed to UV-light (λ = 365 nm) for 50 seconds. The crosslinking of the PEGDA in the continuous phase locks the pristine microstructure in place, which allows one to directly visualize the gel structure at room temperature using confocal microscopy.

5.4 Results and discussion

5.4.1 Thermally responsive nanoemulsions

Self-assembly of the nano-sized polydimethylsiloxane (PDMS) droplets is driven by molecular-scale poly(ethylene glycol) diacrylate (PEGDA) bridging at elevated temperatures, as shown in Fig. 5.1A. The oil-in-water nanoemulsions were prepared using high-pressure homogenization, which allows easy preparation of large quantities of emulsions with a range of droplet sizes (Appendix D Fig. D1). The canonical nanoemulsion formulation used in this work contains PDMS droplets (droplet diameter 2a = 37nm) of volume fraction = 0.15 suspended in the aqueous continuous phase consisting of PEGDA of volume fraction 0.33 and sodium dodecyl sulfate (SDS) of concentration 0.175M. For this formulation, the changes in rheology and microstructure of the nanoemulsion throughout the gelation process can be captured within ΔT = 30 °C (Fig. 5.1C and 5.1D, from T = 20.0 to 50.0 °C).

At room temperature (20.0 °C), the droplets are well dispersed in the continuous phase due to the electrostatic repulsion provided by SDS on the droplet surface and small Peclet number (Pe = $\pi D^4 \Delta \rho g / 12 k_B T \sim 10^{-7}$, where D is the droplet diameter, $\Delta \rho$ is the density difference between the

oil and continuous phase, g is gravitational acceleration, k_B is the Boltzmann constant and T is absolute temperature) of the nano-sized droplets [6]. Accordingly, the nanoemulsion has a liquid-like behavior, which can be seen from direct observation (Fig. 5.1B) and the rheological response (Fig. 5.1C). As temperature rises, the hydrophobic end groups of PEGDA partition into the oil/water interface and form inter-droplet bridging. The gelation results in the increase of viscoelastic moduli (Fig. 5.1C), and ultimately gives a sample-spanning gel network and solid-like behavior of the sample.

5.4.2 One-step temperature jump rheology

We first investigated the sample with a single temperature jump (from T = 20.0 °C to a higher temperature). The one-step temperature jump can be viewed as directly quenching the nanoemulsion to a certain state, which is analogous to the formation of depletion gels by addition of small molecule depletants into a colloidal suspension. Although this simple quenching mechanism (i.e. one-step temperature jump) has been studied in our prior work [101,143], we will describe new insights in the following section which will guide our subsequent thermal processing.

Fig. 5.1C shows the results of small amplitude oscillatory shear (SAOS) rheological responses of the nanoemulsion at various temperatures throughout gelation from T = 20.0 to 50.0 °C. The figure records the measurements just after the samples reach the target temperature (see Appendix D Fig. D2 for complete response including the initial temperature increasing stage). The length of measurement was chosen to be 20 minutes which is long enough to capture the major changes in rheology and microstructure at the selected temperatures (Fig. 5.1C and 5.1D). At T = 20 °C, both moduli remain nearly constant and the loss modulus G" (measuring viscous dissipation) is larger than storage modulus G' (measuring elasticity) throughout the measurement. This liquid-like behavior holds when the temperature is increased up to 30.0 °C (Appendix D Fig. D2).
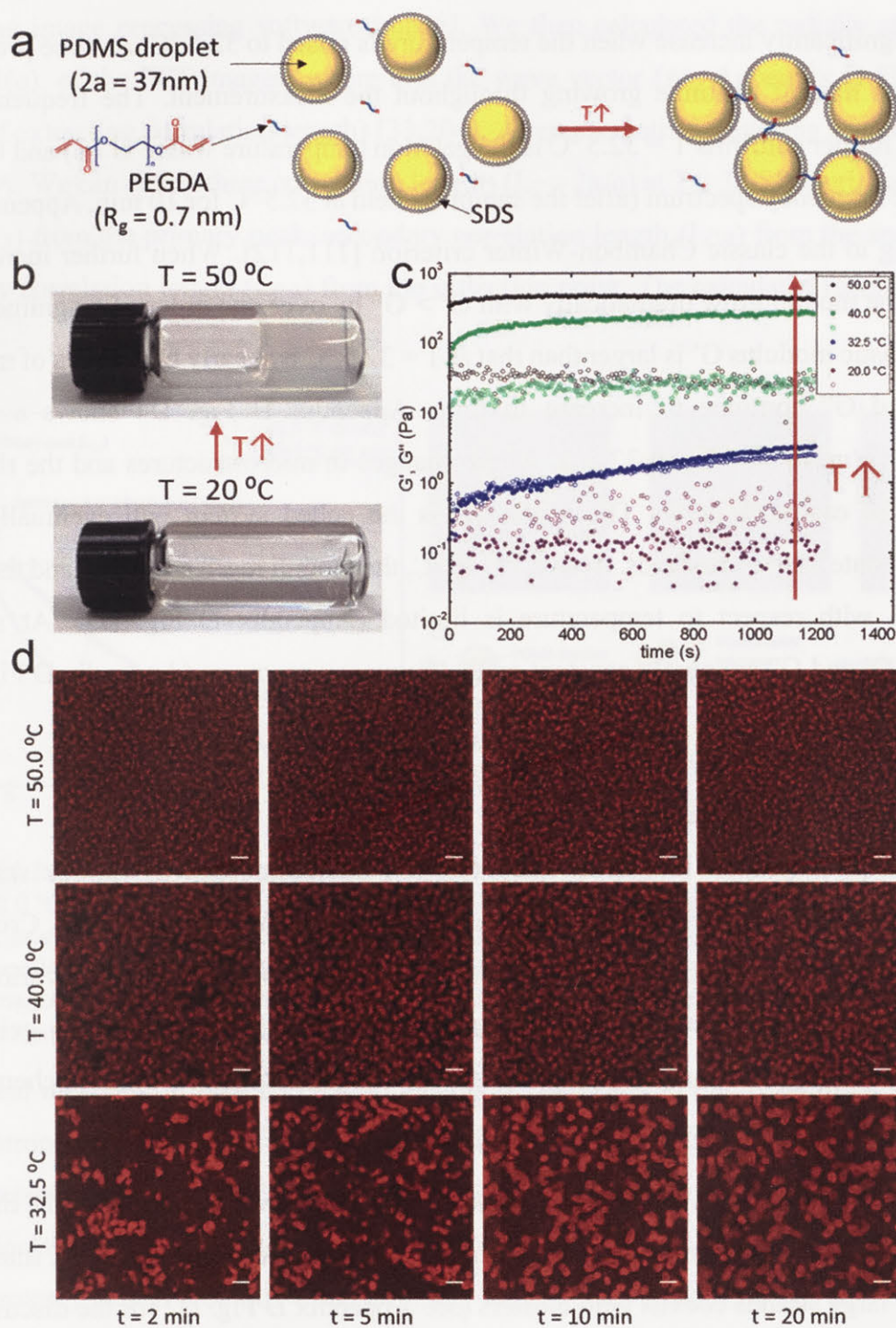
Figure 5.1(a) Schematic of thermally responsive self-assembly. At rising temperatures, the hydrophobic groups of PEGDA partition into the oil/water interface and form droplet bridging. (b) Direct observation of the thermogelling nanoemulsion at T = 20 and T = 50 °C. (c) Rheological responses of the nanoemulsion through one-step temperature jumping from T = 20.0 °C. The measurement records the moduli right after T reaches the target temperature at an oscillatory frequency of 20 rad/s. Closed symbols: G' (elastic modulus). Open symbols: G" (viscous modulus). (d) Direct visualization of the nanoemulsion microstructures using confocal microscopy at various times, t, at T = 32.5, 40.0 and 50.0 °C. Scale bars = 5μm.

The moduli significantly increase when the temperature is raised to 32.5 °C. As time proceeds, G' ≈ G" and both moduli continue growing throughout the measurement. The frequency sweep measurement further confirms T = 32.5 °C is the gelation temperature where $G'(\omega)$ and $G''(\omega)$ are parallel on the frequency spectrum (after the sample is held at 32.5 °C for 10 min, Appendix D Fig. D3), according to the classic Chambon-Winter criterion [111,112]. When further increasing the temperature, the moduli grow dramatically with G' > G" by over one order of magnitude. At T = 40.0 °C, the elastic modulus G' is larger than that at T = 32.5 °C by nearly two orders of magnitude, though G' and G" continue to increase in time. Appendix D Fig. D4 shows a long-time characterization (up to 50 min) at 32.5 °C where changes in microstructures and the rheological response can be easily observed. The result shows the gelled system will eventually reach a pseudo-steady state as time proceeds. Above T = 40 °C, the moduli reach a plateau, and the increase in the moduli with respect to temperature is limited (Appendix D Fig. D3). At such high temperatures, G' and G" are nearly constant on the frequency spectrum (Appendix D Fig. D3).

5.4.3 Hierarchal microstructures

We captured high-resolution images of nanoemulsion microstructures at various states using confocal microscopy. We labeled the oil droplets with a red, lipophilic dye (PKH26). Crosslinking the PEGDA in the continuous phase locks the self-assembled droplets in place at various states, and allows us to directly visualize the internal structures of the nanoemulsion gel at room temperature. Previous work has shown that the addition of small amounts of these chemicals has negligible influence on the nanoemulsion rheology and microstructure [143].

Fig. 5.1D shows the microstructures at different temperatures and various times, t. The times were chosen to be 2, 5, 10 and 20 minutes in order to capture the major rheological changes. Interestingly, at T = 32.5 °C large strands coexist with clusters (see Appendix D Fig. D2 for the discussion that these clusters are not stress-bearing structures.). As time proceeds, strands increase in number and size, and fewer clusters are present (see Appendix D Fig. D4 for long-time characterization). These microstructural trends are consistent with the rheology in Fig. 5.1C, where G' and G" increase in time, since the larger strands are believed to be responsible for the viscoelastic response [101].

In order to quantitatively study the microstructures in Fig. 5.1D, we measured correlation lengths from scattering plots. The raw confocal images were first processed *via* fast Fourier transform

(FFT) using image processing software ImageJ. We then calculated the radially averaged light intensity, $I(q)$, of the FFT images, where q is the wave vector (see Appendix D Fig. D5 for an example of extracting correlation length) [33,204]. A representative scattering spectrum is shown in Fig. 5.2A. We can define three correlation lengths ($L_C = 2\pi/q$) at $T = 32.5$ °C: primary correlation length ($L_{C,1}$) from the primary peak, secondary correlation length ($L_{C,2}$) from the secondary peak and tertiary correlation length ($L_{C,3}$) from the inflection point. The calculated results are listed in Table 5.1.
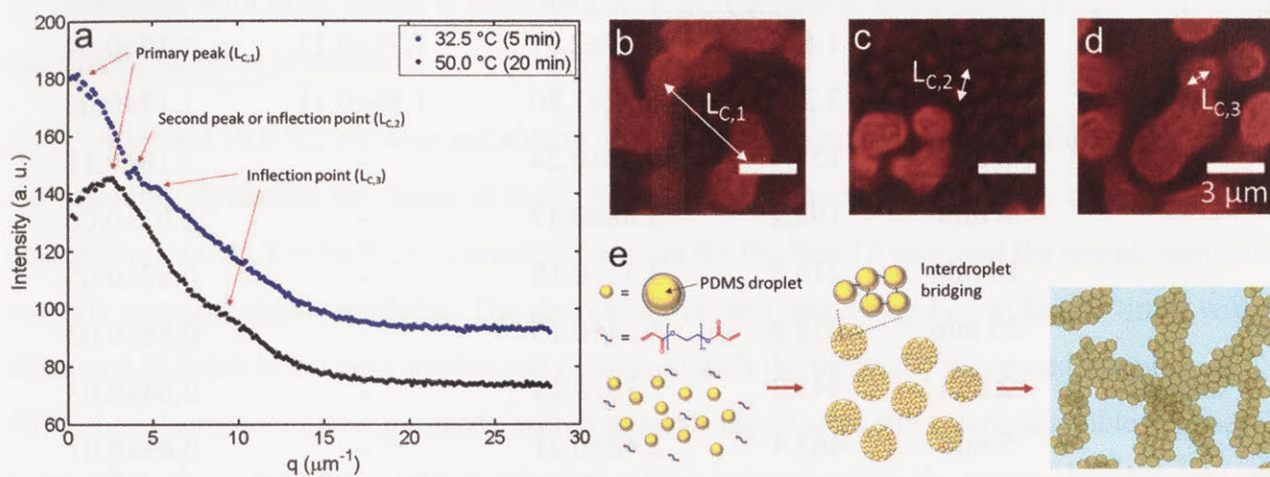
Figure 5.2 (a) Representative scattered intensity as a function of the wave vector, q, at $T = 32.5$ °C ($t = 5$ min) and 50.0 °C ($t = 20$ min) from FFT images. The I-q data is then used to quantify the correlation lengths, L_C, as shown in (b) correlation length of droplet-rich domains separated by droplet-poor domains, (c) correlation length of freely suspended clusters and (d) correlation length inside the droplet-rich domains. Images (b) to (d) are nanoemulsions at $T = 32.5$ °C at $t = 20$ min. (e) Schematic of the hierarchical microstructures formed by the nanoemulsion droplets.

The physical meaning of three correlation lengths is elucidated in Fig. 5.2B to D. $L_{C,1}$ extracted from the strongest scattering intensity corresponds to the averaged distance of the droplet-rich domains separated by the droplet-poor domains, shown as Fig. 5.2B. This primary correlation length (calculated as $2\pi/q_{max}$, where q_{max} is the wave vector corresponding to the strongest intensity) has been investigated in previous work [32,143]. On the other hand, $L_{C,2}$ and $L_{C,3}$ have not been reported before. $L_{C,2}$ corresponds to the correlation length of the clusters suspended in the continuous phase, as shown in the Fig. 5.2C, which is further confirmed by calculating the L_C of cropped images where only the freely suspended clusters are considered (Appendix D Fig. D6). Therefore, it is not surprising that $L_{C,2}$ is absent at $T = 40.0$ and 50.0 °C since no coexisting clusters are observed (Fig. 5.1D). The tertiary correlation length ($L_{C,3}$) is at a smaller length scale (i.e. larger q), suggesting a 'secondary' structure inside the droplet-rich domains, as represented in Fig.

5.2D. This is also validated by analyzing the intensity profile just within the droplet-rich domain shown in Appendix D Fig. D6.

Table 5.1 Correlation lengths (L_C) and the elastic moduli (G') of the nanoemulsions with a one-step temperature jump at various timestamps. Error bars = 1 standard deviation from 9-15 images.

Temperature	Time	G' (Pa)	$L_{C,1}$ (µm)	$L_{C,2}$ (µm)	$L_{C,3}$ (µm)
32.5 °C	2 min	0.635	23.3±10.1	1.38±0.07	1.15±0.05
	5 min	0.895	15.9±11.6	1.46±0.08	1.17±0.09
	10 min	1.628	8.49±2.01	1.71±0.12	1.18±0.04
	20 min	3.254	6.42±1.80	1.86±0.11	1.17±0.05
40.0 °C	2 min	151.9	3.90±0.24	-	1.10±0.11
	5 min	192.2	3.88±0.47	-	1.01±0.06
	10 min	216.8	3.32±0.19	-	0.87±0.05
	20 min	258.9	3.34±0.15	-	0.86±0.03
50.0 °C	2 min	445.3	2.30±0.14	-	0.64±0.03
	5 min	463.4	2.42±0.21	-	0.63±0.01
	10 min	461.4	2.50±0.19	-	0.65±0.01
	20 min	428.8	2.44±0.10	-	0.73±0.03

These secondary length scales ($L_{C,1}$ and $L_{C,3}$) are a manifestation of a hierarchical structure (see Appendix D Fig. D7 for two-stage yielding which also suggests a hierarchical network), which was not analyzed in our earlier publication. Such hierarchy has been found in a depletion gel by Lu *et al.*[103] where they found that after introducing depletants into a colloidal suspension, the colloids first form clusters, then form a spanning gel network, which is then arrested. Moreover, Schurtenberger and coworkers also found 'multiple steps' in depletion gel formation using simulations and showed that the higher order gel structures are built on 'meta-particles' composed of few particles [100]. Interestingly, in their work, a scattering spectrum showing multi-stages was also reported, similar to Fig. 5.2A here.

At T = 32.5 °C, $L_{C,3}$ remains nearly constant as time proceeds as shown in Table 5.1, and $L_{C,3} \approx$ 1.17 µm is consistent with the micron-sized clusters seen in Fig. 5.1D and Appendix D Fig. D6A. Additionally, at later times, more and thicker strands are formed while fewer freely suspended

clusters are present (see Appendix D Fig. D8 for the changes in the scattered intensity spectrum). Therefore, it is reasonable to postulate that the strands are formed from the aggregation of clusters (as supported by data in Appendix D Fig. D4), which is consistent with what has been described in the literature for other systems [100,103,205]. The proposed mechanism is shown in Fig. 5.2E. Upon increasing the temperature, droplets aggregate and form clusters, and the clusters serve as 'building blocks' which then self-assemble and span the macroscopic sample. The decrease in $L_{C,1}$ correlates with an increase in strands as time proceeds. As reported in Table 5.1, at $T = 32.5$ °C $L_{C,1}$ decreases with time, which is consistent with the qualitative observation in Fig. 5.1D where the strands increase in number.

At $T = 40.0$ and 50.0 °C, we were not able to capture the aggregation of such building blocks since the assembly dynamics are faster at these higher temperatures. However, we can still observe changes in $L_{C,3}$. At $T = 50$ °C, $L_{C,3}$ remains constant for the first 10 min, and the sample maintains a nearly constant elastic modulus. The decreasing G' and increasing $L_{C,3}$ at longer times will be discussed in detail in the next section and compared with the thermally processed samples. At $T = 40$ °C, $L_{C,3}$ decreases as time proceeds, which suggests the clusters still can re-assemble themselves even after they aggregate into a network. This reconstruction is reasonable because the characteristic diffusion time for 1 μm clusters is roughly 5 seconds, which suggests rearrangement over the rheological timescale is likely even after the bridging is formed. At such moderate temperature, the attraction is also weak enough not to induce strong dynamical arrest, such as what is seen at $T = 50$ °C.

5.4.4 Two-step thermal processing

The thermal processing demonstration in this chapter was conducted at $T = 32.5$, 40.0 and 50.0 °C. After the pre-shear (conditioning step) at $T = 20.0$ °C, the sample was first brought to $T_1 = 32.5$ or 40.0 °C. After holding at T_1 for $t_{hold} = 2$, 5 or 10 min, the temperature was then jumped to $T_2 = 40.0$ or 50.0 °C. Therefore, a total of nine processing histories were explored: three sets of progressive temperature jumps (T_1 to T_2: 32.5 to 40.0 °C, 32.5 to 50.0 °C and 40.0 to 50.0 °C) with three different t_{hold} at each corresponding T_1. The total measurement time was kept constant at 20 min for consistency with the one-step temperature jump experiments.

Fig. 5.3 shows the results of the rheological responses of the thermally processed samples (see

Appendix D Fig. D9 for the temperature history). Both moduli, G' and G", show the same trend under thermal processing, and only G' is plotted here for discussion (G" can be found in Appendix D Fig. D10). The results from the one-step temperature jump are also plotted for comparison. Fig. 5.3A shows the rheology of thermal processing between T = 32.5 to 40.0 °C. Comparing with one-step jump at T = 40.0 °C, holding at 32.5 °C hinders the development of the gel strength, and a smaller modulus is obtained when remaining at 32.5 °C longer. Additionally, similar to the one-step jump at T = 40.0 °C, the moduli of processed samples are still increasing at the end of the measurement, suggesting that the gel is not fully arrested. The shape and the trend of the curves suggest the possibility of a master curve by rescaling the time. The rescaled data is shown in Fig. 5.3B, in which time has been rescaled to be zero when the temperature reaches T_2. All processed samples collapse onto a master curve, suggesting the microstructures are self-similar, while the one-step jump sample is slightly above the master curve.

To investigate the microstructure of the processed sample as well as the structural self-similarity, we also performed confocal microscopy to visualize the microstructures. We used the Peltier plate equipped on the rheometer to make sure the imaging samples underwent exactly the same temperature history as the samples used for rheological measurements. We then focused on the microstructures after the thermal processing was complete (i.e. the microstructures at t = 20 min). The imaging results and the corresponding analyses for all thermal processed samples are shown in Fig. 5.4 and Table 5.2, respectively. The elastic moduli are also listed in Fig. 5.4. For convenience in later discussion, the correlation length of a one-step jump to temperature T will be denoted as L_c^T.
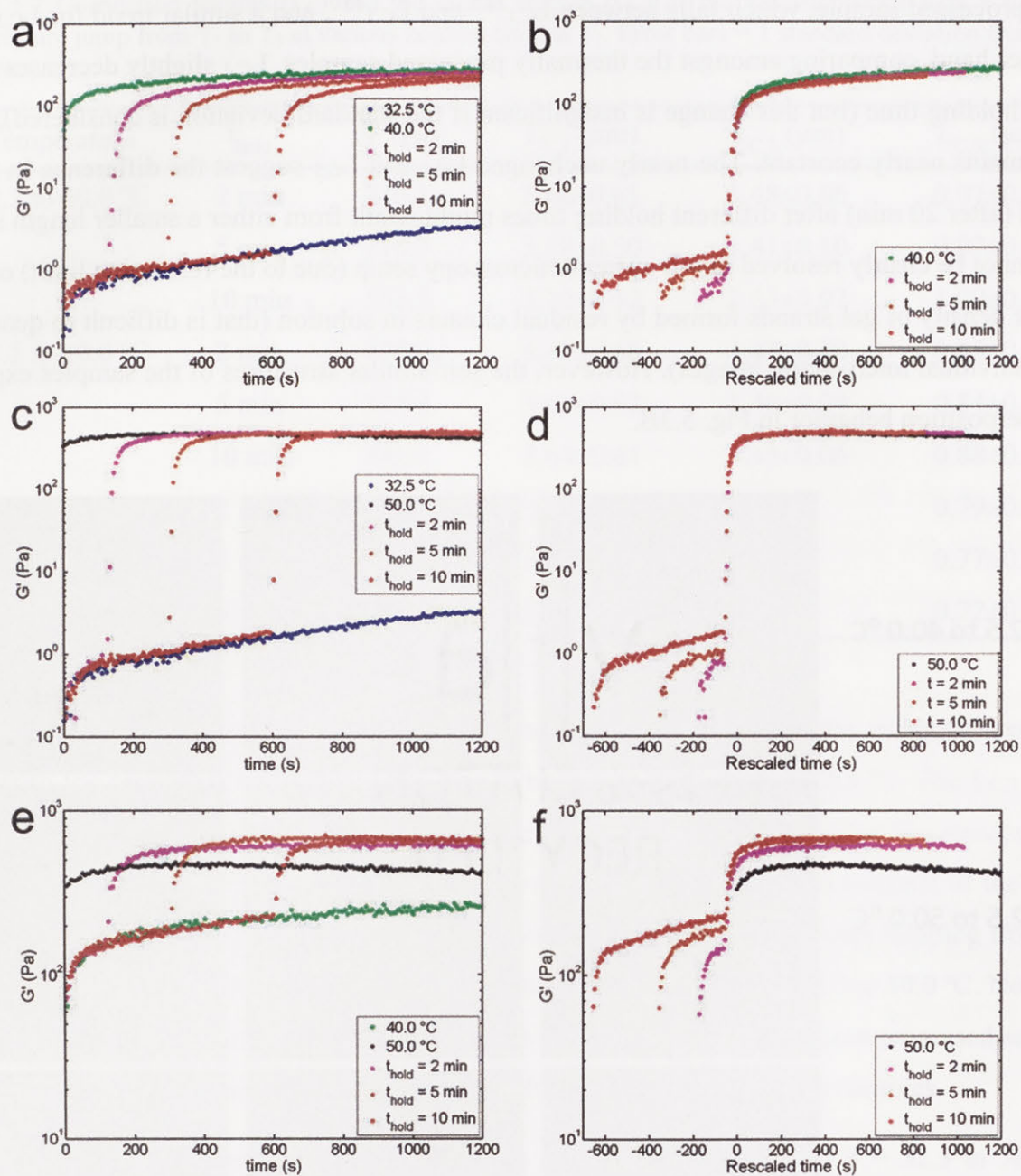
Figure 5.3 Temporal elastic modulus, G', of the nanoemulsion undergoing two-step temperature jump with (a) to (b) 32.5 to 40.0 °C, (c) to (d) 32.5 to 50.0 °C and (e) to (f) 40.0 to 50.0 °C. (a), (c) and (e) record the raw measurements. (b), (d) and (f) plot the G' versus rescaled time. Rescaled time is equal to $t - t_{hold} - t_{ramp}$ where t_{ramp} is the time needed for the temperature to adjust from T_1 to T_2 (limited by the Peltier plate). Typical values of t_{ramp} are 45-55 seconds (see Appendix D Fig. D6 for details).

Fig. 5.4A to 4C show the microstructures of the processed samples from T = 32.5 to 40.0 °C with different holding times. Surprisingly, the microstructures are significantly different from both nanoemulsions with direct holding at T = 32.5 °C and T = 40.0 °C. For the processed samples, the internal structures fall between T = 32.5 °C and T = 40.0 °C, which is further confirmed by the $L_{C,1}$

of the processed sample, which falls between $L_{C,1}^{32.5}$ and $L_{C,1}^{40.0}$, and a similar trend for $L_{C,3}$. On the other hand, comparing amongst the thermally processed samples, $L_{C,1}$ slightly decreases with longer holding time (but this change is insignificant if the standard deviation is considered), and $L_{C,3}$ remains nearly constant. The nearly unchanged $L_{C,1}$ and $L_{C,3}$ suggest the difference in final moduli (after 20 min) after different holding times might result from either a smaller length scale that cannot be clearly resolved in our current microscopy setup (due to the resolution limit) or the number density of gel strands formed by residual clusters in solution (that is difficult to quantify from individual microscopy images). However, the self-similar structures of the samples explain the superposition behavior in Fig. 5.3B.
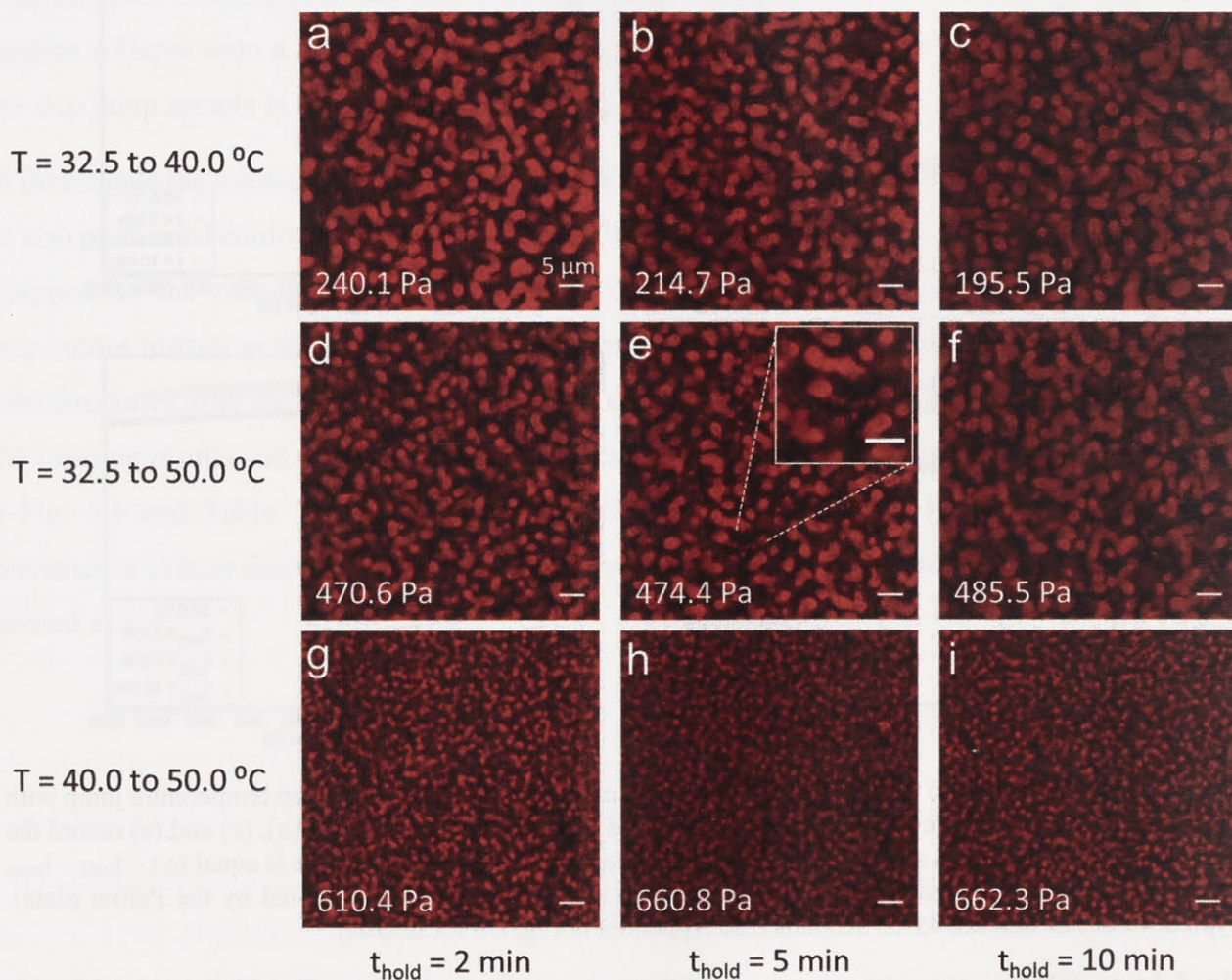
Figure 5.4 Microstructures of the nanoemulsion processed with a two-step temperature jump with t_{hold} = 2, 5 and 10 min. All images were taken at the end of thermal processing at t = 20 min. The elastic modulus at each condition is listed at the bottom left corner of each image. All scale bars = 5 μm.

Table 5.2 Correlation lengths (L_C) and the elastic moduli (G') of the nanoemulsions with a two-step temperature jump from T_1 to T_2 at various holding time at T_1. Error bars = 1 standard deviation from 9-15 images.

Temperature	t_{hold}	G' (Pa)	$L_{C,1}$ (µm)	$L_{C,2}$ (µm)	$L_{C,3}$ (µm)
32.5 to 40.0 °C	2 min	240.1	5.46±0.61	1.48±0.06	0.97±0.04
	5 min	214.7	5.19±0.50	1.41±0.10	0.97±0.04
	10 min	195.5	5.17±0.52	1.53±0.07	1.00±0.05
32.5 to 50.0 °C	2 min	470.6	5.42±0.68	1.41±0.10	0.85±0.02
	5 min	474.4	5.65±0.92	1.40±0.09	0.84±0.02
	10 min	485.5	5.64±0.61	1.45±0.06	0.88±0.05
40.0 to 50.0 °C	2 min	610.4	3.06±0.18	-	0.79±0.04
	5 min	660.8	3.01±0.21	-	0.77±0.01
	10 min	662.3	3.08±0.34	-	0.72±0.02

Interestingly, here we also observed an additional inflection point from the intensity spectrum, similar to the secondary peak in the one-step temperature jump at T = 32.5 °C. The $L_{C,2}$ in the processed samples results from the microstructure associated with finer, cluster-like structures, as highlighted in the inset of Fig. 5.4E. We believe this smaller structure is a remnant of the freely suspended clusters from 32.5 °C, which can be found in the processed samples jumping from T = 32.5 to 40.0 °C and T = 32.5 to 50.0 °C, while no signal is found for T = 40.0 to 50.0 °C. Note that even though there are only two correlation lengths that can be determined from processed samples from T = 40.0 to 50 °C, we still use $L_{C,1}$ and $L_{C,3}$ for consistency with other samples.

Fig. 5.3C shows the rheological response of the processed samples from T = 32.5 to 50.0 °C. Interestingly, the processed samples possess similar moduli as the sample with one-step temperature jump at T = 50.0 °C, while they have significantly different microstructures, as shown in Fig. 5.4D to 5.4F and Table 5.2. Again, the processed samples show intermediate values of $L_{C,1}$ and $L_{C,3}$ (i.e. $L_{C,1}^{T1} < L_{C,1} < L_{C,1}^{T2}$ and $L_{C,3}^{T1} < L_{C,3} < L_{C,3}^{T2}$), and the moduli collapse onto a master curve shown in Fig. 5.3D. By comparing among the processed samples, $L_{C,1}$ and $L_{C,3}$ still remain nearly constant, and the moduli are also relatively insensitive to the holding time, as observed when processing from T = 32.5 to 40.0 °C. The relative insensitivity is reasonable since a stronger attraction is induced at T = 50.0 °C, where the structure is dynamically arrested. Readers interested

in an estimation of attractive potential energy are referred to the previous work by our group [21]. This stronger attraction can be also qualitatively observed in Fig. 5.4 where the cluster associated microstructures ($L_{C,2}$, signifying the remanence of the clusters from 32.5 °C) can be more easily seen in the T = 32.5 to 50.0 °C sample due to dynamic arrest, compared to the T = 32.5 to 40.0 °C. Additionally, by observing $L_{C,3}$ (manifestation of the aggregated cluster with the droplet-rich domains), $L_{C,3}$ of the T = 32.5 to 50.0 °C sample is smaller than that of T = 32.5 to 40.0 °C. Indeed, $L_{C,3}$ is gradually reduced from the one-step jump at 32.5 °C ($L_{C,3} \approx 1.2$ µm) to the two-step jump ($L_{C,3} \approx 1.0$ µm for 32.5 to 40.0 °C and $L_{C,3} \approx 0.85$ µm for 32.5 to 50.0 °C). The decrease in $L_{C,3}$ suggests the aggregated clusters become tighter during the temperature jump.

Fig. 5.3E shows the rheological response of the processed samples from T = 40.0 to 50.0 °C. Interestingly, the modulus can be increased by 36 to 47 %, depending on the holding time. The processed samples again have intermediate values of $L_{C,1}$ and $L_{C,3}$ (i.e. $L_{C,1}^{T1} < L_{C,1} < L_{C,1}^{T2}$ and $L_{C,3}^{T1} < L_{C,3} < L_{C,3}^{T2}$), while $L_{C,2}$ is absent since there are no freely suspended clusters at T = 40.0 °C. However, from Table 5.2, G' with t_{hold} = 2 min is unexpectedly smaller than G' with t_{hold} = 5 and 10 min, since $L_{C,1}$ and $L_{C,3}$ remain nearly constant across different holding times. This difference in G' is reproducible when repeating the measurement (Appendix D Fig. D11). We hypothesize the difference in moduli might result from a smaller length scale that cannot be captured in our current microscopy setup. However, despite the slight difference, the processed samples do show the same trend that G' is larger than that of the one-step jump sample at T = 50.0 °C.

In addition to the increase in moduli (see Appendix D Fig. D10 for G''), we also note that thermal processing can prevent the gel from aging, which can be seen for the one-step jump to T = 50.0 °C. As shown in Fig. 5.3E, G' starts to decrease after t ≈ 10 min (black dots). We hypothesize that such aging is due to a slow structural relaxation because the nanoemulsion is directly and deeply quenched to a non-equilibrium state.[206] This age-dependent viscoelasticity associated with an internal stress relaxation in out-of-equilibrium systems has also been observed in depletion gels [207] and actin/fascin bundle networks [208]. To test our hypothesis, we performed a SAOS + LAOS measurement. If the relaxation is responsible for aging and the associated decrease in G', yielding (by using LAOS) the gel should facilitate such relaxation and achieve the same final state. The results are shown in Fig. 5.5. The blue data shows the aging behavior of the nanoemulsion gel

and the modulus eventually reached a plateau after ≈ 6000 s using only SAOS. On the other hand, in the black data we used LAOS to yield the gel for 30 s at t = 600s and the modulus still reached the same plateau as seen in the long time SAOS experiment, but the entire process only took ≈ 1000s. It thus takes approximately one-sixth the amount of time for the measurement with yielding to reach the final state. Additionally, similar to T = 40.0 to 50.0 °C processing (Fig. 5.3E), the samples processed from T = 32.5 to 50.0 °C also show that the decrease in G' can be effectively reduced by thermal processing, which is highlighted by the inset in Fig. 5.5 (this is not easily observed in Fig. 5.3C due to the scale of the y-axis).
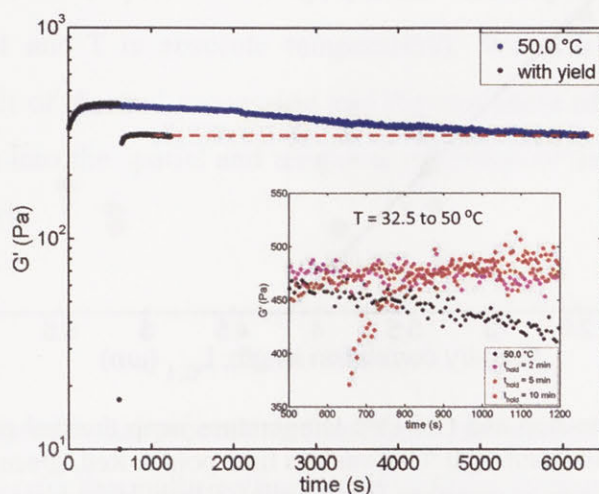
Figure 5.5 Temporal decrease in G' due to the slow relaxation when the nanoemulsion is directly quenched at T = 50.0 °C (blue). Yielding the nanoemulsion can effectively reduce the time needed to reach the final state (black). The yielding step is performed using LAOS with a strain = 15 % at a frequency = 20 rad/s. Inset plot highlights the thermal processing sample from T = 32.5 to 50.0 °C (which is difficult to notice in Fig. 5.3 due to the scale of the y-axis) can also prevent the decrease in modulus as processing from T = 40.0 to 50.0 °C.

Fig. 5.6 summarizes how the gel strength (G') and the microstructure ($L_{C,1}$) can be controlled *via* thermal processing. The black dots are the results of the traditional direct quenching (single temperature jump) of the nanoemulsion gel — G' increases as $L_{C,1}$ decreases. This inverse relation of G' to $L_{C,1}$ has been reported in prior studies [32,91]. On the other hand, with more complex thermal processing, properties beyond the limit set by direct quenching (indicated by the black dashed line) can be accessed. For example, with two-step processing we can maintain the same gel strength (e.g. G' ≈ 450 Pa), but create much more open microstructures (more than doubling of $L_{C,1}$ to ≈ 5.5 μm). We can also have gels with the same $L_{C,1}$ (≈ 5.5 μm) but with different G' (≈ 200 to 480 Pa). Additionally, two-step thermal processing can increase the gel strength beyond

that attainable by directly quenching the system with a strong attraction potential. Overall, we find that thermal processing allows us to access states above the dashed line depicted for the one-step temperature jumps.
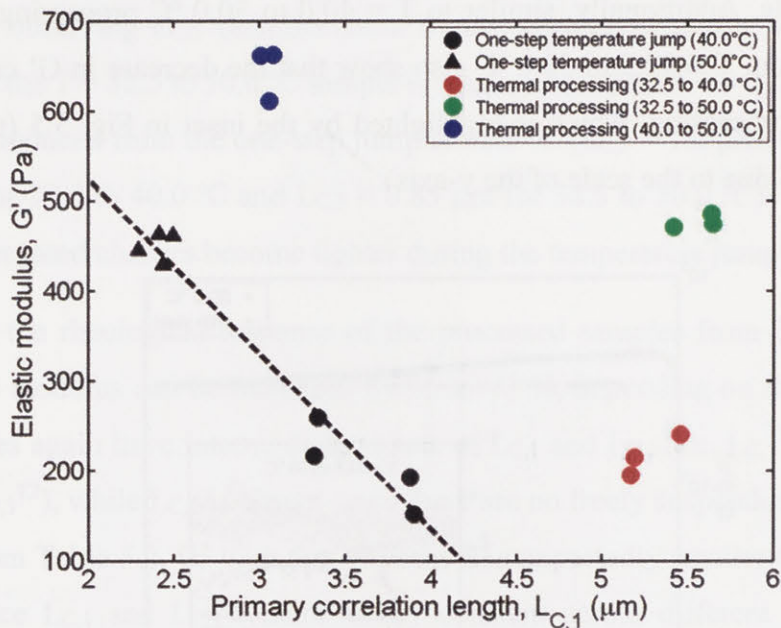
Figure 5.6 G' versus $L_{C,1}$ of one-step and two-step temperature jump thermal processing. Black dots are from the one-step jump at T = 40.0 and 50.0 °C at various time points. Red, green and blue symbols are the data after two-step jump processing is complete (t = 20 min). Black dashed line is drawn to guide the eye and denotes the limit set by direct quenching.

The properties of the nanoemulsion gels are highly dependent on how they reach the final state, even though the same final temperature is reached. The gels have significantly different rheology and microstructures depending on their thermal history, and these properties can be beyond the limit set by direct quenching, which has been a major focus in literature. We postulate that when undergoing thermal processing from T_1 to T_2, the system has a memory of the structures at T_1 and reconstructs these intermediate structures when switched to T_2. This postulate is consistent with the observation that the cluster-associated structures ($L_{C,2}$) are found in processed samples from T = 32.5 to 40.0 °C and from T = 32.5 to 50.0 °C, which indicates the remanence of the clusters from 32.5 °C. A holding step at T_1 seems to be similar to thermal annealing. Thermal annealing is often used as an additional step in material manufacturing processes that allows a system to reach the global free energy minimum without being kinetically trapped. It is therefore often used in order to create a regular order on a molecular scale and to improve and control the macroscopic properties [184]. However, contrary to the results of thermal annealing, colloidal gel systems are

often associated with a kinetically arrested disordered state, such as percolation [18] or spinodal decomposition [103], whereas the global energy minimum corresponds to the bulk phase separation [6,8]. Moreover, our thermal processing results are relatively insensitive to the length of time holding at T_1, and the thermal processing does not facilitate a regular pattern of colloidal order. Both behaviors are contrary to what has been reported in the literature, where the properties of the material are strongly dependent on the annealing time [193,194]. Future work using simulations will help elucidate the mechanism on the nanometer scale (i.e. single droplet) and the droplet diffusive time scale (droplet diffusive time $\approx a^2/D = 6\pi\eta a^3/k_BT \sim 10^{-4}$ sec, where a is the droplet diameter, D is the droplet diffusivity, η is the viscosity of the continuous phase k_B is the Boltzmann constant and T is absolute temperature). We will study both dynamics and mechanisms of the effect of thermal processing and the evolution of the microstructures, which will bring more insights into the spatial and temporal evolution of the system, as experimentally demonstrated in this work.

5.5 Conclusion

We have demonstrated that thermal processing conditions can be used to tune both the mechanical and structural properties of a thermally gelling nanoemulsion suspension. Under certain thermal processing conditions, the gel strength can be increased up to 47% compared to a single temperature jump. Additionally, the thermal processing can effectively prevent a decrease in gel strength due to a slow relaxation. By combining the results from one-step and two-step temperature jumps, properties of gels can be beyond the limit set by direct quenching, which has been a major focus in literature. We have also shown that the nanoemulsion gel is a hierarchical structure comprised of multiple length scales which are in turn related to the rheological properties. Our results suggest that the mechanistic reason for such control is that the system sequentially forms hierarchical microstructures and dynamic tuning of the droplet interactions through temperature can influence the trajectory taken through phase-space. Our work also provides new experimental evidence which relates the path-dependent rheological properties to associated microstructures in attractive colloidal systems. Future work using simulations will help validate the postulated mechanisms and role of hierarchical assembly. Concepts from our work could be applied to other attractive colloidal systems which can improve the understanding of such systems, and can be

utilized in colloid-based material design. Translation of model systems to products requires the development of industrial processes. Here we demonstrated that the process itself is an important tool to be leveraged to tune material properties.

Chapter 6

Multiple Particle Tracking Study of Thermally-Gelling Nanoemulsions

6.1 Overview

We perform multiple particle tracking (MPT) on a thermally-gelling oil-in-water nanoemulsion system. Carboxylated and plain polystyrene probes are used to investigate the role of colloidal probe size and surface chemistry on MPT in the nanoemulsion system. As temperature increases, hydrophobic groups of PEG-based gelators (PEGDA) partition into oil/water interface and bridge droplets. This intercolloidal attraction generates a wide variety of microstructures consisting of droplet-rich and droplet-poor phases. By tailoring the MPT colloidal probe surface chemistry, we can control the residence of probes in each domain, thus allowing us to independently probe each phase. Our results show stark differences in probe dynamics in each domain. For certain conditions, the mean squared displacement (MSD) can differ by over four orders of magnitude for the same probe size but different surface chemistry. Carboxylated probe surface chemistries result in "slippery" probes while plain polystyrene probes appear to tether to the nanoemulsion gel network. We also observe probes hopping between pores in the gel for carboxylated probes. Our approach demonstrates that probes with different surface chemistries are useful in probing the local regions of a colloidal gel and allows the measurement of local properties within structurally heterogeneous hydrogels.

This chapter has been adapted with permission from L. -C. Cheng, L. C. Hsiao and P. S. Doyle "Multiple Particle Tracking Study of Thermally-Gelling Nanoemulsions" *Soft Matter* 2017, **13**, 6606-6619. Copyright 2017 Royal Society of Chemistry.

6.2 Introduction

Colloidal gels are formed when sufficient colloid-colloid attractive interactions are introduced into colloidal suspensions [1]. At low to moderate particle loadings, colloids aggregate and give rise to

fractal clusters and chains, ultimately resulting in a space-filling interconnected network [92]. Such types of attraction are commonly provided by depletion [183,209,210], colloid surface charge [4,88] or polymer bridging [211] that can be controlled by external stimuli such as temperature, depleting agents, ionic strength, and pH values. By changing the colloid volume fraction and attractive potential, colloidal gels show diverse microstructures and mechanical properties [1]. Due to their viscoelastic properties, colloidal gels are used in various fields such as the food industry [99], drug delivery [211], tissue engineering [4], membranes [33] and drilling fluids [88].

Recently, our group has developed a thermally-gelling nanoemulsion system in which nano-sized polydimethylsiloxane droplets are dispersed in a continuous phase composed of water, sodium dodecyl sulfate and poly(ethylene glycol) diacrylate [21]. At high temperatures, the hydrophobic groups of the PEG-based gelators partition into the oil/water interfaces and form interdroplet bridging, giving rise to a thermally-responsive gel. It has been shown that the temperature-dependent properties such as gel point, shear modulus and yield stress can be tuned via droplet size, oil volume fraction (ϕ), gelator concentration (P) and gelator chemistry [21,98]. This system provides a wide parameter space and allows one to engineer the nanoemulsions' properties for specific practical applications [6]. For instance, our group has recently shown the application of these nanoemulsions in 3D printing to obtain hierarchical mesostructured hydrogels with potential utility in drug delivery, tissue engineering and membranes [33]. In addition, the interdroplet attractive potential can be finely modulated by adjusting temperature. This ability to tune the attractive potential without adding another component to the solution (e.g. depleting agent, salt, acid, etc.) allows ones to precisely control assembly conditions and the resulting microstructures.

In this chapter, we use multiple particle tracking to study the changes in microenvironment of the thermally-gelling nanoemulsion during gelation. Previously, we studied the mechanism of gelation by using rheological characterization, neutron scattering and cryo-transmission electron microscopy [98]. For nanoemulsions with $\phi < \phi_c$, where ϕ_c is a critical oil volume fraction, gelation is induced by homogenous percolation with a broad gel transition in which the droplet-droplet cluster formed and subsequently percolated. On the other hand, when $\phi > \phi_c$, gelation occurs through phase separation with a sharp sol-gel transition. In this regime, the strong interdroplet attraction can dynamically arrest the phase separation, and the nanoemulsions show bi-continuous microstructures consisting of droplet-rich and droplet-poor domains.

Microstructures of the nanoemulsions spanning a wide range of ϕ (0.1 to 0.33) and T (22 to 65 °C) were further studied using confocal microscopy [143]. We developed a technique where we labeled oil droplets by a lipophilic dye and locked the microstructures in place by photo-crosslinking the telechelic polymers at target temperatures, thus enabling direct visualization of the internal structures at room temperature. Using confocal microscopy and bulk rheological characterization, it was determined that the nanoemulsions undergo a two-stage gelation at rising temperatures: homogenous percolation followed by phase separation. This is contrary to what had been found previously, where the gelation is induced by single mechanism depending on ϕ [98]. However, we also showed that the thermal response of the nanoemulsion was sensitive to oil droplet size and temperature history, which could explain the difference in observations.

Although there are some differences in the results due to slight differences in composition, both works [98,143] showed that at sufficiently high ϕ and relatively high T, the nanoemulsions undergo phase separation and become dynamically arrested. Using inverted optical microscope with the texture analysis microscopy [32], Gao *et al.* captured the microscopic dynamic process of coarsening through spinodal decomposition to the arrested state. As expected, the nanoemulsion forms heterogeneous, bi-continuous networks consisting of droplet-rich and droplet-poor domains, consistent with the results by using confocal microscopy [143]. The microstructures were further studied by analyzing the large amplitude oscillatory shear (LAOS) rheology with simultaneous neutron scattering [96]. Interestingly, Kim *et al.* found out that the nanoemulsion gel shows two-step yielding. This nonlinear mechanical response is due to the initial compression and rupture of dense fractal domains, followed by clusters breakage into a homogeneous dispersion.

Although the work of the LAOS study focused more on the evolution of the heterogeneous nanoemulsion gel microstructures under yielding, it also suggests that the internal structures are of a hierarchical nature, and that it may be possible to obtain more information by locally probing the networks. However, there are few direct microscopic studies on thermogelling nanoemulsions. Moreover, the characterization of the nanoemulsion is primarily performed with bulk rheology. Although it has been shown that such studies can be aided by microscopy, direct probing without compromising the microstructures would be beneficial.

Here, we performed video microscopy multiple particle tracking (MPT) to study the thermally-gelling nanoemulsion at various temperatures. For this study, we chose a nanoemulsion with ϕ =

0.15. At this oil loading, the nanoemulsion microstructure shows a correlation length that spans 0.1 to 10 μm at different temperatures [143]. For such a highly heterogeneous system, MPT is a useful tool for quantitative analysis because the probes embedded in the sample can reveal the local rheological properties of the material on a microscopic scale [87,88,93,212–225]. We show that by tailoring the colloidal probe surface chemistry we can control the residence of the probes to be either in the droplet-rich or droplet-poor phase, thus allowing us to investigate each domain independently. Our results show stark differences in probe dynamics in each domain, and the dynamics also show significant probe-size dependency. Unmodified polystyrene beads appear to tether strongly to the nanoemulsion gel at elevated temperatures, whereas carboxylate-modified polystyrene beads appear to be "slippery" and explore the large pores in the nanoemulsion gel. This work introduces a method to target specific regions in a nanoemulsion gel for characterization via MPT, and has implications for the design of new nanoemulsion-based composite materials.

6.3 Materials and methods

6.3.1 Materials

Nanoemulsion and confocal imaging: Poly(ethylene glycol) diacrylate (PEGDA, $M_n = 700$ g/mol), sodium dodecyl sulfate (SDS), silicone oil (PDMS, viscosity = 5cSt at 25 °C), lipophilic dye PKH26 (excitation and emission wavelengths $\lambda_{ex}/\lambda_{em} = 551/567$ nm) and photoinitiator 2-hydroxy-2-methylpropiophenone (Darocur 1173) were purchased from Sigma-Aldrich and used without further purification.

Particle tracking: Fluorescent polystyrene beads were purchased from Polysciences (Fluoresbrite® YG, $\lambda_{ex}/\lambda_{em} = 441/486$ nm). Two types of probes with selected sizes were used in this work: polystyrene beads with no surface modification (diameter $2a = 1$ and 2 μm) and polystyrene beads surface modified with carboxylate groups ($2a = 1$, 1.5 and 2 μm).

6.3.2 Synthesis of nanoemulsion

The oil-in-water (O/W) nanoemulsion in this work consisted of PDMS droplets (D = 36 nm with polydispersity = 20%) dispersed in a continuous phase of PEGDA with volume fraction = 0.33, SDS at a concentration of 0.175M and de-ionized water. The oil volume fraction (ϕ) of the

nanoemulsion was 0.15. To generate the nanoemulsion, a pre-emulsion was first prepared by adding the silicone oil into the aqueous mixture of PEGDA and SDS under magnetic stirring with a speed of 700 rpm. Stirring was maintained for at least 15 min to ensure there was no macroscopic phase separation. This pre-emulsion was processed into the nanoemulsion by using a high-pressure homogenizer (EmulsiFlex-C3, Avestin). The homogenization was conducted at a pressure of 18,000 psi for 15 passes, and the emulsion was cooled to 4 °C between each pass. The diameter of the droplets was measured using dynamic light scattering (90Plus PALS, Brookhaven Instruments) after diluting the oil phase from $\phi = 0.15$ to $\phi = 0.002$ by using an aqueous diluting agent consisting of PEGDA in de-ionized water (P = 0.33). Dilution using this solution was shown to have negligible influence on the oil droplet size and polydispersity [21]. The final nanoemulsion was stored at 4 °C until further use.

6.3.3 Multiple particle tracking

Before adding the fluorescent probes into the nanoemulsion, the beads were washed in a solution with the same composition as the continuous phase of the nanoemulsion by centrifugation and redispersed by vortexing. This process was repeated three times for all beads to remove potential chemical residuals in the stock bead solutions. After the washing step, the beads were added into the nanoemulsion with a volume fraction $\approx 0.02\%$. Depending on the probe size, 50-100 randomly dispersed beads were tracked within the microscope field of view.

The nanoemulsion containing the colloidal probes was then sealed in a custom-built chamber that was designed to maintain thermal homogeneity when mounted on a microscope heating stage ($\Delta T \leq 0.2$ °C across the chamber). A schematic of the device is shown in Appendix E Fig. E1. The slides were fixed in place using UV-curing glue. After the sample was loaded into the chamber, both ends were sealed by epoxy glue.

Particle tracking was performed using an inverted fluorescence microscope (Axiovert 40 CFL, Zeiss) equipped with a 40x objective (N.A. = 0.75). A filter set (XF404, Omega Optical) was used which allowed only fluorescent beads to be excited and imaged. The temperature of the sample was controlled by a heating stage (TSA02i, Instec) mounted on the microscope stage. An objective warmer (OW-1, Warner Instruments) was used to minimize the potential thermal fluctuation due to the air between the objective and the sample [32]. The temperature was calibrated by an

additional digital thermometer (#51 II, Fluke).

The sample was placed on the stage when the heating stage reached the target temperature. Images were taken after 10 minutes by using a charged couple device (CCD) camera (Manta G-145, Allied Vision) at a speed of 30 frames per second with a shutter speed of 8 ms. A total of 900 frames were collected for each movie. The time for the largest beads to settle due to gravity in the chamber is $\approx$ 120 min in our system [94], which is much larger than the experimental time scale $\approx$ 10min. Moreover, although the Peclet number $\approx$ 0.5 indicates the gravitational settling is not negligible compared to Brownian motion for largest beads [6], we will show that the settling effect does not perturb the native microstructure of the gelling nanoemulsions in Section 6.3. For each type of bead at the target temperature, 5-8 movies were recorded to ensure a large ensemble of bead trajectories. The experiments were performed separately for beads with different surface chemistry and sizes suspended in freshly prepared nanoemulsions.

6.3.4 Microrheology

Probe dynamics from the movies were then analyzed by publicly available Matlab codes (http://people.umass.edu/kilfoil/downloads.html), which are based on IDL codes originally developed by Crocker and Grier [226], The mean squared displacement (MSD) is calculated by analyzing the bead trajectories:

$$MSD = \langle \Delta r^2(\tau) \rangle = \langle [r(t + \tau) - r(t)]^2 \rangle \qquad (6.1)$$

where r is the position of the bead, t is time, τ is lag time and the bracket represents the time and/or ensemble average. However, Eq. (6.1) needs to be corrected for a static error caused by the inherent noise in particle tracking [227,228]. An additional experiment was performed to determine the static error – the probes were immobilized in a 3 wt% agarose gel and the apparent MSD (so-called static error) was calculated (See Appendix E Table E1 for the static errors of all beads). The static error was then subtracted from Eq. (6.1).

The measured MSD was used to calculate the sample viscoelasticity via the generalized Stokes-Einstein relation (GSER) [87,97]. The complex shear modulus, G^* is described as,

$$G^* = \frac{k_B T}{\pi a i \omega F_u\{\langle \Delta r^2(\tau) \rangle\}} \qquad (6.2)$$

where $\omega = 1/\tau$ is the frequency, k_B is the Boltzmann constant, T is the absolute temperature, a is the bead radius, i is the imaginary unit and F_u is the Fourier transform function. In order to use GSER to calculate the shear moduli, Eq. (6.2) needs to be modified [97]. By assuming the local power law applies at the frequency of interest, Eq. (6.2) can be transformed to:

$$|G^*| \approx \frac{k_B T}{\pi a \langle \Delta r^2(1/\omega) \rangle \Gamma[1 + \alpha(\omega)]} \qquad (6.3)$$

where Γ is the gamma function and $\alpha(w) = \left. \frac{\partial \ln \langle \Delta r^2(t) \rangle}{\partial \ln t} \right|_{t=1/\omega}$.

Finally, the elastic modulus, G'(ω) and the viscous modulus, G''(ω) are calculated as,

$$G' = |G^*| \cos\left(\frac{\pi a(\omega)}{2}\right), \qquad (6.4)$$

$$G' = |G^*| \sin\left(\frac{\pi a(\omega)}{2}\right). \qquad (6.5)$$

6.3.5 Bulk rheology

Bulk rheology was measured using a stress-controlled rheometer (ARG2, TA Instruments) equipped with a Peltier plate to control temperature. A stainless steel 2° cone with a diameter of 60 mm was used to perform small amplitude oscillatory shear (SAOS) measurements at a strain of $\gamma = 0.05\%$ [21]. A solvent trap was used to reduce potential evaporation of the sample during the measurement and a few drops of de-ionized water were added on top of the cone. For both temperature ramp and frequency ramp characterizations, a preshear was applied by constant rotation at a rate of 20 rad/s for 30 seconds, followed by a one-minute period where the sample remained quiescent at T = 20 °C. For frequency sweep measurements, after the preshear was finished, the nanoemulsion was raised to the target temperature and then remained quiescent for 10 minutes. Freshly loaded nanoemulsion was used for each target temperature. For temperature ramp measurements, the temperature was raised at a speed of 2 °C/min with a fixed angular frequency $\omega = 20$ rad/s. The moduli were measured at a lag time of 5 seconds.

129

6.3.6 Confocal microscopy

The microstructures of the nanoemulsions with and without beads were captured by a laser scanning confocal microscope (LSM 700, Zeiss) equipped with a 63x oil-immersion objective (N.A. = 1.4). To prepare samples for imaging, the nanoemulsion was first mixed with 1 vol% of fluorescent dye PKH26 and 1 vol% of the photoinitiator Darocur. The addition of these chemicals has been shown to have negligible effect on the nanoemulsion microstructure [143]. For the samples containing probe beads, the beads were also added at this stage at the same volume fraction as used for particle tracking (beads were also washed as stated previously). Then, 150 μL of the mixture was loaded in a glass chamber (Lab-Tek™ #155411, Thermo Fisher Scientific). The sample was placed in a preheated oven at the target temperature for 10 minutes. Subsequently, the sample was exposed to UV light (λ = 365 nm) for one minute in the oven. The crosslinking of PEGDA locks the nanoemulsion microstructure in place to allow for direct visualization of the structure at room temperature on the confocal microscope.

6.4 Results and discussion

6.4.1 Thermally-gelling nanoemulsion system

The thermally-gelling oil-in-water (O/W) nanoemulsion is composed of silicone oil (poly(dimethyl siloxane), PDMS, 5 cSt) droplets (diameter $\langle D \rangle$ = 36 nm) dispersed in a continuous phase consisting of a telechelic polymer, poly(ethylene glycol) diacrylate (PEGDA, M_n = 700 g/mol), at a volume fraction P = 0.33, and a surfactant, sodium dodecyl sulfate (SDS), at a concentration of 0.175 M. The oil volume fraction ϕ was chosen to be 0.15. At ϕ = 0.15, the nanoemulsion microstructure shows a wide span of characteristic lengths ($\approx$ 1 to 20 μm) at different temperatures [143]. For such a highly heterogeneous system, multiple particle tracking (MPT) is a useful tool for quantitative analysis because the probes embedded in the sample can reveal the local rheological properties of the material [87,88,93,212–215,219–225]. In addition, at ϕ = 0.15, the viscoelastic moduli of the nanoemulsion above the gel temperature ranges from about 10 to 400 Pa [21,143]. With our experimental setup, the static error [227] is $\approx 2 \times 10^{-5}$ μm^2 which sets the limit of the largest measurable elastic modulus to $\approx$ 150 Pa, as calculated by the generalized Stokes-Einstein relation (GSER) [229]. We acknowledge the inherent limit of the video microscopy

130

particle tracking in our setup where materials with large elasticity cannot be well characterized. However, within the limit of 150 Pa, MPT is capable of capturing the local microenvironment in the gelling nanoemulsion. The focus of our work is to demonstrate one of the first studies in utilizing tracers of different surface chemistry to probe the local dynamics of spatially heterogeneous gelled nanoemulsions.

The thermal gelation of the nanoemulsions occurs due to interdroplet bridging via telechelic polymer gelators containing hydrophobic end groups [21]. When the temperature increases, the hydrophobic end groups of PEGDA partition into the oil/water interface which results in interdroplet bridging (Fig. 6.1A). This attractive interaction eventually results in an interconnected gel networks that span the system, transforming the nanoemulsion from a liquid-like material to a viscoelastic solid, as shown in Fig. 6.1B. At room temperature, the nano-sized droplets are well dispersed because of a large Laplace pressure and electrostatic repulsion provided by the surfactant [6–8]. Above the gel temperature, the droplets self-assemble and form a space-filling network, turning the nanoemulsion dispersion into a gel state. This increase in the apparent size of the droplet-rich phase also results in increased turbidity, consistent with what has been reported previously [60].
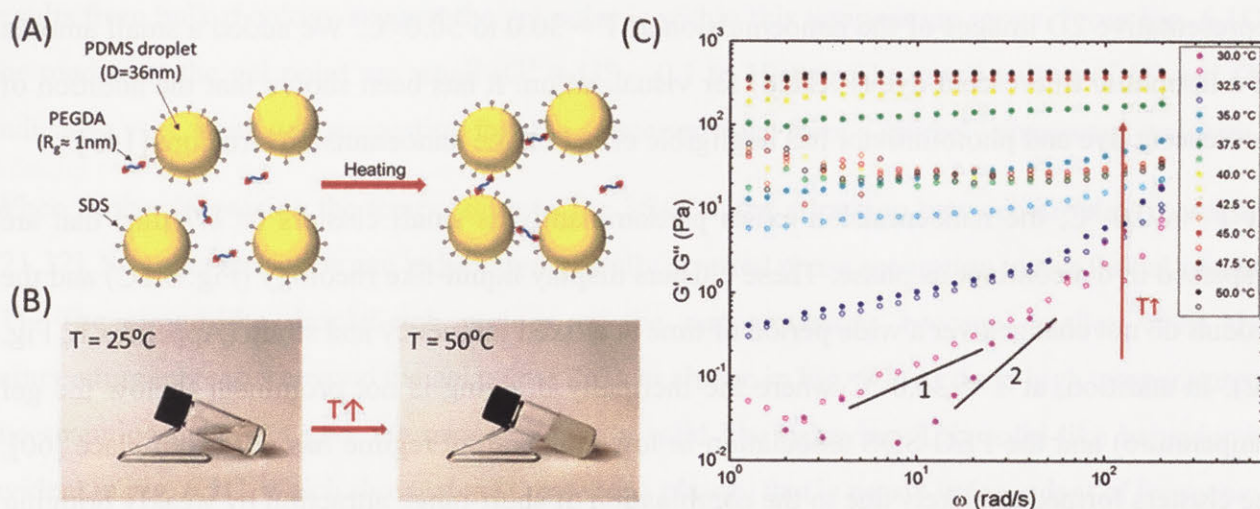
Figure 6.1 Thermally-gelling nanoemulsion (P = 0.33, ϕ = 0.15) and its viscoelasticity. (A) Schematic of the thermally-gelling mechanism. (B) Photographs of the nanoemulsion at T = 25 °C (transparent liquid) and T = 50 °C (turbid gel). (C) Frequency sweep of viscoelastic moduli from T = 30.0 to 50.0 °C (γ = 0.05%) from bulk rheology. Filled symbol = G'; open symbol = G".

Bulk small-amplitude oscillatory shear experiments were performed to measure the viscoelastic moduli (G' and G") over a range of temperatures spanning the gel point (Fig. 6.1C). At T = 30.0

131

°C, the storage module scales as $G' \sim \omega^2$ and the loss modulus scales as $G'' \sim \omega^1$, representing a liquid-like behavior [21,143]. At T = 32.5 °C, $G' \approx G'' \sim \omega^n$ over a wide span of frequencies, where n is the relaxation exponent [112]. Winter and Chambon suggested that the critical gel point is found when $G'(\omega)$ and $G''(\omega)$ show the same power law exponents on a log-log plot [111]. We find that n $\approx$ 0.5 (Fig. 6.1C), which indicates stoichiometrically balanced end-linking networks [113]. At the critical gel point, the colloidal system forms a sample-spanning gel network [113]. Above the gel point, the elastic modulus G' is larger than the viscous modulus G'' for all frequencies and both moduli become nearly independent of frequency.

6.4.2 Direct visualization of microstructures

The macroscopic viscoelasticity of a material is determined by its microstructure [2,230]. We used confocal microscopy to directly visualize the microstructure of the nanoemulsions at various temperatures. By taking advantage of the abundance of telechelic polymers (PEGDA) in the continuous phase, we locked the microstructure in place at target temperatures by photo-crosslinking the PEGDA with UV light for 1 minute. This approach enabled us to study the various microstructures at room temperature using fluorescence confocal microscopy. Fig. 6.2 shows representative 2D images of the nanoemulsion at T = 30.0 to 50.0 °C. We added a small amount of a lipophilic fluorescent dye (PKH26) for visualization. It has been shown that the addition of fluorescent dye and photoinitiator has negligible effect on the nanoemulsion structure [143].

At T = 30.0 °C, the nanoemulsion exists predominantly as small clusters ($\approx$ 0.7 μm) that are dispersed in the continuous phase. These clusters display liquid-like rheology (Fig. 6.1C) and the moduli do not change over a wide period of time at a fixed frequency and strain (Appendix E, Fig. E2). In addition, at T = 30.0 °C where the thermally bridging is not prominent (below the gel temperature) and the PEG-SDS association in low temperature regime has not taken place [60], the clusters formed are likely due to the combination of short-range attraction by weakly bridging and perhaps PEGDA depletion, and electrostatic repulsion by ionic groups of SDS on the droplets. These observations suggest the likelihood of forming a clustered fluid, which is consistent with weak droplet interactions at this moderate temperature [8,103,231,232]. Future studies are needed to fully characterize the nature of these clusters below the gel temperature.
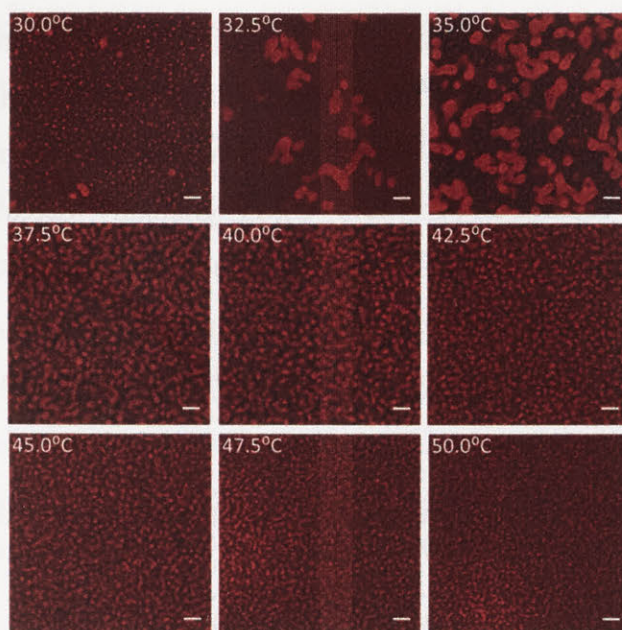
Figure 6.2 Representative 2D images of nanoemulsion microstructures by confocal microscopy at T = 30.0 to 50.0 °C. The red fluorescent regions are the droplet-rich phase and the dark regions are the droplet-poor phase. Scale bars = 5 μm.

At T = 32.5 °C, the droplets begin to form droplet-rich and droplet-poor regions which become more distinctive at T = 35.0 °C. In this temperature regime, thick droplet strands co-exist with small clusters [143]. Although it is difficult to discern a spanning network from the 2D images, results from bulk rheology suggest the gel point is within this temperature range. From Fig. 6.1C, the moduli at the gel point are small (G' ≈ G'' ~ 0.1 to 10 Pa). The small values of G' and G'' indicate a very weak gel, suggesting that the nanoemulsions form a sparsely connected structure.

When further increasing the temperature to T > 35.0 °C, the attraction between droplets increases [21,32]. Stronger attraction can induce dynamically arrested phase separation in a colloidal system [1]. The strand-like droplet-rich regions of the nanoemulsions become smaller when the temperature increases beyond the gel point [233], as shown in Fig. 6.2. At these high temperatures, the spanning networks give the nanoemulsion a solid-like behavior. This solid-like behavior is evident in Fig. 6.1C, which shows that G' reaches a plateau that is nearly independent of frequency and has a value that is an order of magnitude larger than G''.

Quantitative analysis of microstructures can be obtained by calculating correlation lengths of droplet-rich domains, L_C [143,204,234]. Using the image processing software ImageJ, we first applied a fast Fourier transform to the image and obtained the scattered light intensity. Then, we calculated the radially averaged light intensity I(q) of the processed image, where q is the wave

133

vector. Finally, we computed the correlation length as $L_C = 2\pi/q_{max}$, where q_{max} is the wave vector of the maximum averaged light intensity (Appendix E, Fig. E3 for an example). Table 6.1 lists L_C from T = 30.0 to 50.0 °C. The results are consistent to what has been reported in prior work [143]. Before the onset of phase separation (T = 35.0 °C), L_C gradually increases as temperature rises, and shows a sharp increase at T = 35.0 °C. After the phase transition, L_C decreases as temperature continues to rise. The results are consistent with the images in Fig. 6.2. Readers interested in a systematic study relating L_C to rheological properties of this nanoemulsion are referred to previous work by our group [143].

Table 6.1 Correlation lengths of droplet-rich domains (L_C), sizes of droplet-rich domains (L_{rich}) and sizes of droplet-poor domains (L_{poor}) from T = 30.0 to 50.0 °C. Error bars = 1 standard deviation from 5-8 images.

T (°C)	L_C (μm)	L_{rich} (μm)	L_{poor} (μm)
30.0	1.66 ± 0.08	0.67 ± 0.34	0.40 ± 0.16
32.5	17.3 ± 14.2	5.01 ± 2.68 0.55 ± 0.21	0.62 ± 0.55
35.0	32.9 ± 12.4	5.98 ± 4.01 0.49 ± 0.26	0.95 ± 0.54
37.5	3.46 ± 0.26	2.12 ± 2.28	2.90 ± 3.82
40.0	3.38 ± 0.29	1.95 ± 1.51	2.46 ± 3.54
42.5	2.54 ± 0.21	1.74 ± 1.42	2.10 ± 3.75
45.0	2.35 ± 0.23	1.69 ± 1.40	1.87 ± 1.88
47.5	2.08 ± 0.14	1.32 ± 1.40	1.52 ± 1.24
50.0	1.82 ± 0.31	1.24 ± 0.97	1.45 ± 1.94

In addition to L_C, we also computed the size of droplet-rich and droplet-poor domains, denoted as L_{rich} and L_{poor} respectively. By using ImageJ, we applied a built-in function "Analyze Particles" to the images after performing the "Threshold" function. For L_{poor}, the white/black values of images were first inverted before "Threshold". We set the average minimum Feret diameter to be L_{rich} or L_{poor}, where the Feret diameter is defined as the distance between two parallel lines that are tangential to the outline of a 2D object (Appendix E Fig. E4 for detailed description). For example, L_{rich} would be the diameter of sphere-like clusters at low temperatures and the width of the strand-like aggregates at high temperatures. An additional step is performed for computing L_{rich} at T = 32.5 and 35.0 °C. At these two temperatures, the histogram of sizes of droplet-rich domains shows a bimodal distribution with a local minimum in the probability distribution at 2 μm, distinguishing the two populations. This bimodal distribution is qualitatively seen in Fig. 6.2. Therefore, for these

two temperatures we calculate and report two averaged minimum Feret diameters. Moreover, At T = 30.0 to 35.0 °C, due to the lack of isolated droplet-poor domains, L_{poor} was computed by measuring the separation distance between two near droplet-rich domains (Appendix E Fig. E5 for an example). At least 50 measurements were obtained at each temperature. Table 6.1 lists L_{rich} and L_{poor} from T = 30.0 to 50.0 °C.

Here we acknowledge the large standard deviation listed in Table 6.1. The major reason for the large variation is because the droplet-rich and droplet-poor domains are spatially heterogeneous. Additionally, the concave surfaces of the objects might contribute to the deviation [235,236]. For example, the minimum Feret diameter of a concave droplet-rich strand would be larger than the width of the strand.

The results from Fig. 6.2 show that the nanoemulsion forms different interconnecting droplet-rich and droplet-poor phases at various temperatures. Next, we probe each domain by controlling the surface chemistry of MPT beads, and study how these two domains exhibit probe-size dependent dynamics.

6.4.3 Microstructures with particle tracking probes embedded

Fig. 6.3 shows representative images of the nanoemulsions mixed with green fluorescent polystyrene colloidal probes containing two different surface chemistries at selected temperatures. The top row is the samples mixed with carboxylate-modified polystyrene beads (hereafter denoted as carboxylate beads), and the bottom row is mixed with bare polystyrene beads (no surface modification, hereafter denoted as plain beads). The continuous phase of the nanoemulsions consists of excess SDS surfactant that adsorbs to the bare polystyrene beads and stabilizes them. The bead volume fraction is 0.02%, which is the same concentration used for the MPT experiments. Interestingly, all the carboxylate beads reside in the droplet-poor phase and nearly all the plain beads reside in the droplet-rich phase across all temperatures. This is confirmed by the fluorescent color of the beads – the carboxylate beads remain green in each image (their native emission color), but the plain beads appear yellow, due to the addition of red fluorescence (from the PKH26 dye in the droplets) and green fluorescence from the beads. To further validate the light spectrum addition argument, we mixed 1 μm plain beads in a nanoemulsion suspension of P = 0.33 and ϕ = 0.05 at T = 40 °C. At this low volume fraction, the nanoemulsion forms a microstructure that allows only

part of the plain beads to reside in the droplet-rich domains. Representative images are shown in Fig. 6.4. As expected, only the region of a bead in the droplet-rich phase becomes yellow, while the other part remains green. Fig. 6.4 also indicates that the yellow color is not a result of the adsorption of lipophilic dye to the entire bead surface. Fig. 6.3 and 6.4 illustrate that, by properly tailoring the surface chemistries of the beads, we can independently probe droplet-rich and droplet-poor domains via MPT. Further images from experiments with higher bead loadings are shown in Appendix E Fig. E6.
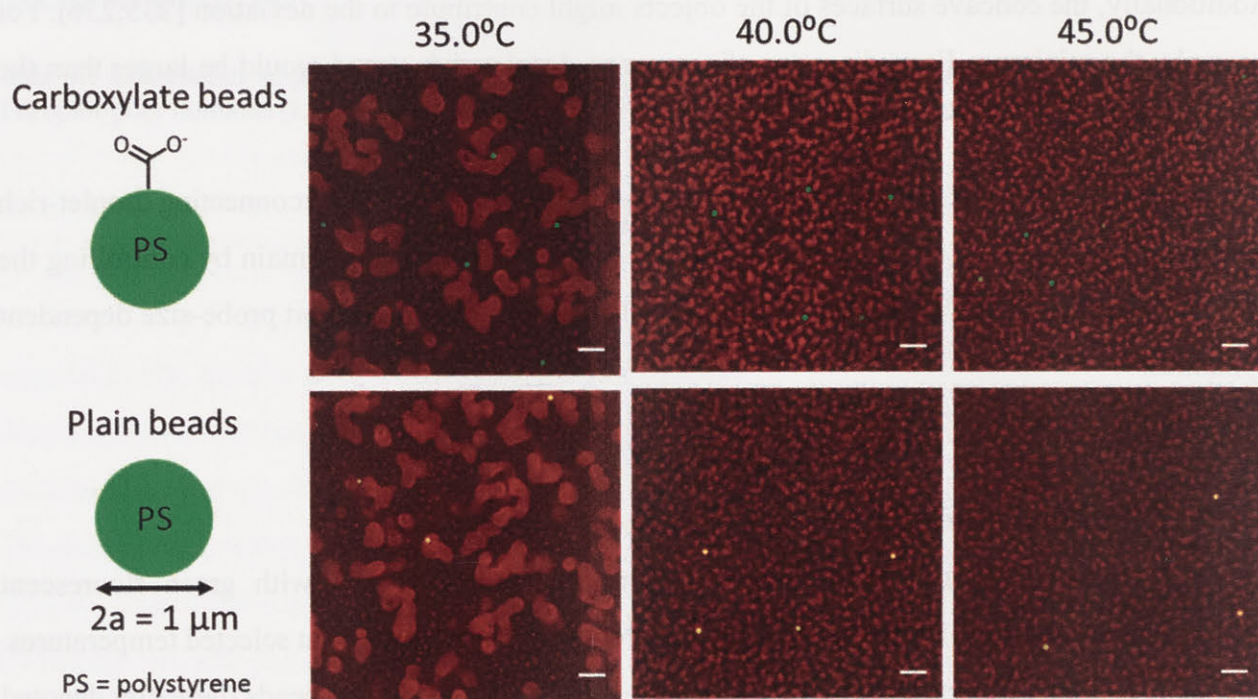
Figure 6.3 Representative confocal images of the nanoemulsion mixed with particle tracking probes at T = 35.0, 40.0 and 45.0 °C. Upper row: nanoemulsion mixed with carboxylate-modified polystyrene beads (carboxylate beads); bottom row: nanoemulsion mixed with bare polystyrene beads (plain beads). Carboxylate beads reside in the droplet-poor phase (dark region) and plain beads reside in the droplet-rich phase (red fluorescent region). Scale bars = 5 μm.

Qualitatively, the addition of the beads does not affect the microstructures formed by the nanoemulsions, as seen in Fig. 6.3. Quantitatively, we compare L_C of the pure nanoemulsion and the nanoemulsion mixed with carboxylate beads and plain beads at T = 35.0, 40.0 and 45.0 °C (Appendix E Table E2). The microstructures are not influenced by the addition of the beads as L_C of all systems are nearly the same at each temperature. We also performed a temperature-ramp rheology measurement to show that the addition of beads has negligible effect on the bulk linear viscoelasticity of the nanoemulsion (Appendix E Fig. E7). In addition, although plain beads reside

in the droplet-rich phase, we show that plain beads do not induce droplet aggregation (Appendix E Fig. E8).
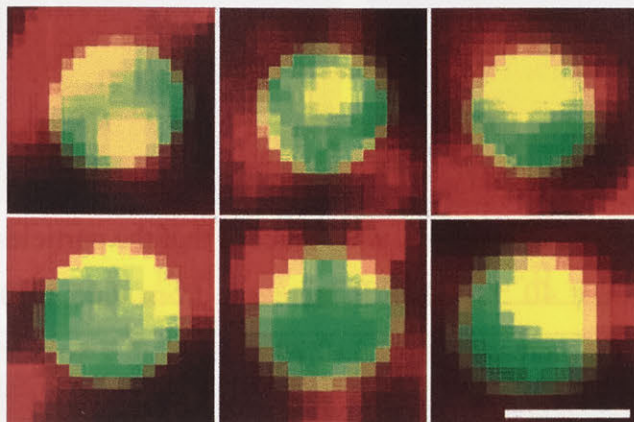
Figure 6.4 Confocal images of 1 μm plain beads embedded in the nanoemulsion with P = 0.33 and ϕ = 0.05 at T = 40.0 °C. Only the part of bead partitioning into the droplet-rich phase is yellow, while other parts remain green. This images support the hypothesis that the change in color observed for colloidal probes is correlated with their residence in the droplet-rich phase. Scale bar = 1 μm.

6.4.4 Bead-nanoemulsion droplet interaction

We hypothesize that the telechelic PEGDA polymer can thermally bridge the plain beads to the nanoemulsions, leading to the strong association of plain beads with droplet-rich regions. This hypothesis assumes that the hydrophobic end group of PEGDA associates with the plain bead surface. If such a polymer-bead association takes place, then plain beads should thermally cluster in the presence of PEGDA without nanoemulsions.

To test our hypothesis, we designed a bead-aggregation experiment. We mixed carboxylate and plain beads of diameter = 1 μm in a solution having the same composition as the continuous phase of the nanoemulsion and added 1 vol% of photoinitiator. The bead volume fraction was ≈ 0.2 %, and we performed the experiment at two different temperatures. For samples at T = 25 °C, the mixtures were directly exposed to UV light after sitting at room temperature for 10 minutes. For T = 40 °C, the samples were placed in the oven for 10 minutes and then immediately exposed to UV light. We also repeated the same experiment with a lower PEGDA volume fraction P = 0.05 (this was the lowest PEGDA concentration that could be used for photopolymerization). A total of eight samples (2 types of beads, 2 PEGDA concentrations, 2 temperatures) were investigated. The microstructures of the samples were observed by confocal microscopy.

Results are shown in Fig. 6.5. Under all conditions, carboxylate beads do not aggregate. On the other hand, plain beads aggregate at T = 40 °C, and the beads form larger clusters when more PEGDA is introduced. For a quantitative characterization, we define two quantities N_c and N_a. N_c is the average coordination number, which is defined as the average number of beads surrounding a central bead (center-to-center distance less than 1 μm in 2D images). N_a is the average aggregation size, which is defined as the average number of beads within a single aggregate. For all samples at T = 25 °C, N_c and N_a are zero, which means that the particles are well dispersed. For the plain bead groups at T = 40 °C, when P increases from 0.05 to 0.33, N_c increases from 0.84±0.94 to 1.1±0.91 and N_a increase from 2.3±0.79 to 2.9±2.0. Two other quantities, N_x and N_y, are also defined to signify the changes in the aggregation, where N_x is the fraction of beads in the aggregates (dimer, trimers, etc.) and N_y is the fraction of beads in the aggregates excluding dimers. At T = 40 °C, N_x and N_y increase from 0.50 to 0.78 and 0.13 to 0.44 respectively, as P increases from 0.05 to 0.33. This experiment shows that the plain bead-PEGDA mixture forms particle aggregates at high temperatures. In addition, stronger aggregation is induced when the PEGDA concentration is increased. In fact, telechelic polymer bridging via hydrophobic end-functionalized groups has been already found between solid particle surfaces [237–240], as well as in microemulsions [241–243] and micelles [244,245]. In Fig. 6.6, we propose a schematic of how nanoemulsion droplets associate with plain beads. On the other hand, we believe the absence of bridging in the carboxylate beads is because of the charged carboxylated group present on the polystyrene surface. Although the surfaces of carboxylate beads and nanoemulsion droplets can provide strong electrostatic repulsion (having zeta potentials of -45 and -42 mV respectively), the telechelic polymer bridging is stronger for the droplets presumably due to the more favorable chemical environment for the hydrophobic end group of PEGDA as it resides at the droplet surface.
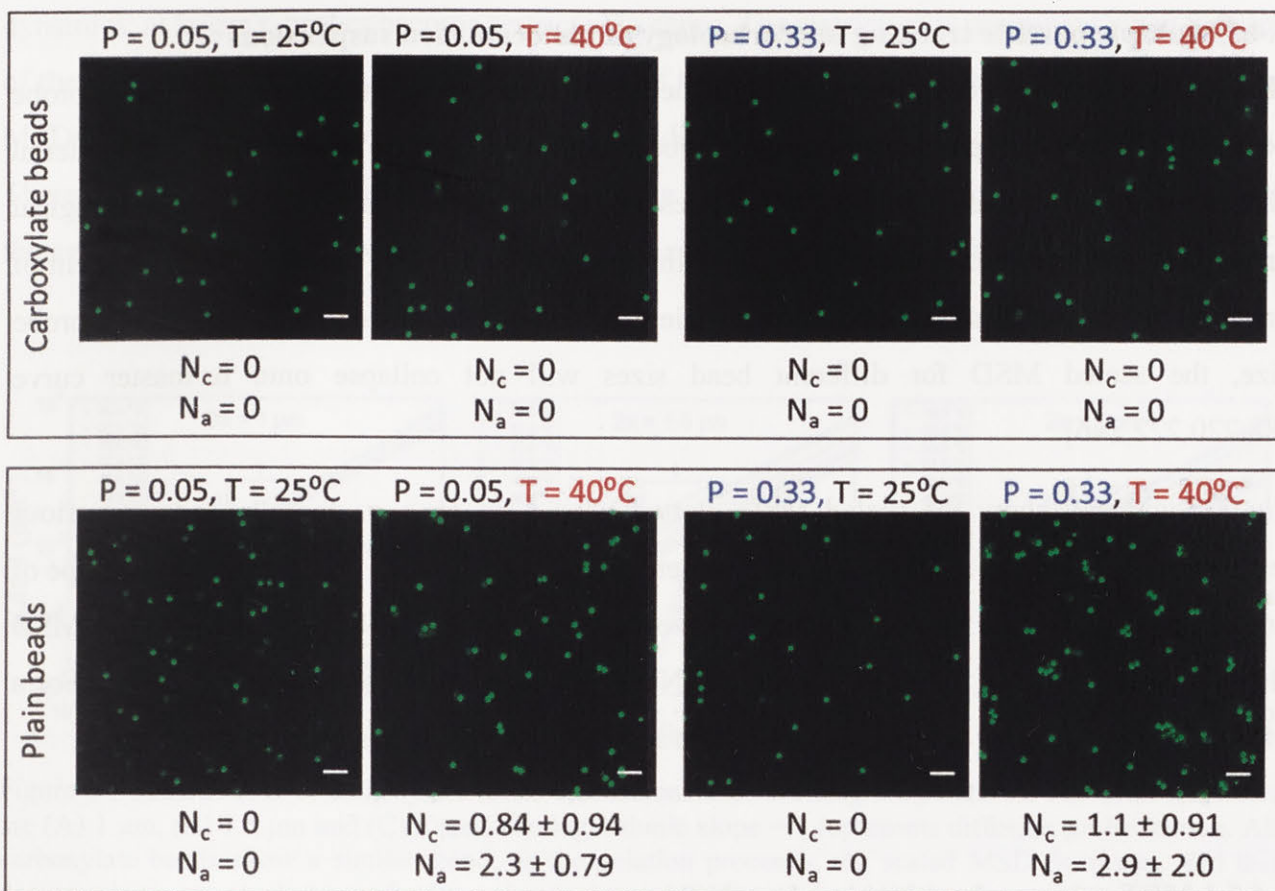
Figure 6.5 Representative confocal images to validate that plain beads share the same thermally-gelling mechanism as the nanoemulsion via PEGDA bridging. N_c is the averaged coordination number and N_a is the averaged size of an aggregate (number of beads). For all carboxylate bead groups and plain bead groups at T = 25 °C, $N_c = N_a = 0$, indicating beads are well dispersed in the solution. For the plain bead group at T = 40 °C, N_c and N_a increase from 0.84±0.94 to 1.1±0.91 and from 2.3±0.79 to 2.9±2.0, respectively, as P is increased from 0.05 to 0.33, indicating that clusters are induced by PEGDA, and that more PEGDA induces stronger aggregation. Scale bars = 5 μm. Error bars = 1 standard deviation.
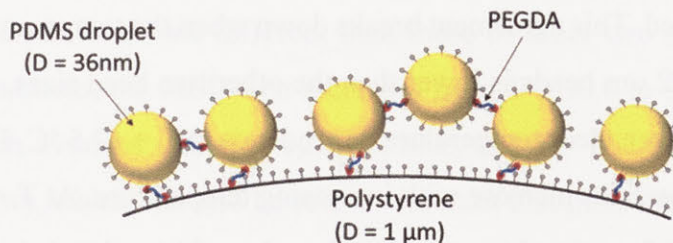
Figure 6.6 Schematic of the postulated correlation between plain polystyrene beads and nanoemulsion droplets.

6.4.5 Multiple particle tracking microrheology of nanoemulsion suspensions

Having shown that we can control whether the probe beads are in the droplet-rich (plain probe beads) or droplet-poor phase (carboxylate probe beads), we now use MPT to probe the material properties in each domain and compare the results. If the material has homogenous rheological properties across the probe length scale, then the scaled MSD, $a\langle \Delta r^2(\tau)\rangle$, will be independent of probe size. If the material is heterogeneous on length scales comparable to or larger than the probe size, the scaled MSD for different bead sizes will not collapse onto a master curve [88,220,222,246].

Fig. 6.7 and 6.9 show the scaled MSD plotted versus lag time, τ, for all beads at various temperatures. All of the scaled MSDs shown here have been corrected for static errors. A slope of one on the log-log MSD plot represents diffusive probe dynamics in a Newtonian fluid. For a MSD slope between zero and one, the fluid is non-Newtonian and shows viscoelastic behavior. For a MSD slope that is equal to zero, the material is solid-like and the beads are locally trapped.

6.4.5.1 MPT using carboxylate bead probes

Fig. 6.7 shows the results for carboxylate beads with diameter 2a = 1, 1.5 and 2 μm in the nanoemulsions at various temperatures. All of the carboxylate beads show a similar trend: as the gelation proceeds, the scaled MSD decreases, and this decrease is progressively larger for larger beads. This trend is consistent with the shrinking droplet-poor domains as nanoemulsions cluster via polymer bridging. At low temperatures (T = 30.0 to 35.0 °C), for all beads the scaled MSDs are diffusive and in good agreement, which suggests the nanoemulsion is homogeneous at these length scales being probed. This agreement breaks down when the temperature is increased to 37.5 °C, where $a\langle \Delta r^2(\tau)\rangle$ of 2 μm beads is lower than the other two bead sizes, and $a\langle \Delta r^2(\tau)\rangle$ for 1.5 μm probes begins to show a clear temperature dependence at T = 42.5 °C. Differences among the MSDs for the three probe sizes increase with increasing temperature. At T = 50.0 °C and $\tau = 10$ s, $a\langle \Delta r^2(\tau)\rangle$ of the 1.5 and 2 μm beads are smaller than that of 1 μm beads by half and one order of magnitude respectively. In addition, $a\langle \Delta r^2(\tau)\rangle$ of 2 μm beads has a slope which decreases with increasing lag time. While not reaching a plateau per se, the MSD suggests restricted probe dynamics consistent with beads being partially trapped in droplet-poor domain cages in the nanoemulsion gel. At smaller τ, probes are undergoing Brownian motion and show diffusive

dynamics; at larger τ, probes become restricted in cages. The restriction is prominent when the size of the droplet-poor domains is closer to the size of the beads, which also explains why the scaled MSDs do not collapse onto a master curve for different sizes of beads at high temperatures. Therefore, it is not surprising the 2 μm carboxylate beads are more sensitive to the gelation since the gel pore size, represented by L_{poor}, is ≈ 1 to 2 μm at elevated temperatures (Table 6.1).
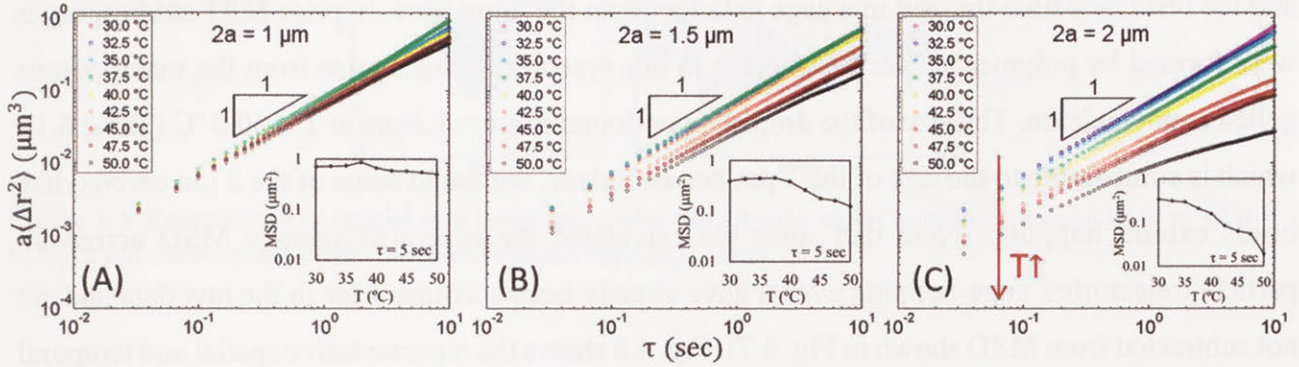
Figure 6.7 Scaled MSD of carboxylate beads of different sizes at rising temperatures. The bead diameters are (A) 1 μm, (B) 1.5 μm and (C) 2 μm. The logarithmic slope = 1 represents diffusive probe motion. All carboxylate beads show a similar trend: as the gelation proceeds, the scaled MSD decreases, and this decrease is progressively larger for larger beads. Inset: MSD at $\tau = 5$ s plotted versus temperature.

In Fig. 6.7A, 1 μm carboxylate beads show an interesting behavior. First, despite the fact that the nanoemulsion forms a strong gel, the MSD remains diffusive and does not decrease significantly at rising temperatures. In fact, for the probes which do not associate with the network, they show viscoelastic MSD only when they are trapped by the materials [225]. Even at T = 50.0 °C, the size of the droplet-poor domain is still larger than the 1 μm beads (Table 6.1), which indicates the 1 μm beads can still diffuse through this domain without much restriction compared to larger beads. Second, the MSDs of 1 μm beads are different than those of other two sizes of beads at rising temperatures. For 1 μm beads, the MSD first increases from T = 30.0 to 37.5 °C (Fig. 6.7A, T = 30.0 °C, magenta, which overlaps with T = 32.5 °C, blue, and T = 35.0 °C, cyan) and decreases after T = 40.0 °C (yellow), which can also be seen in the inset that plots the MSD at a lag time $\tau = 5$ s. This initial increase in MSD with temperature is less obvious for 1.5 μm beads and is almost absent for 2 μm beads. We believe that the higher mobility in this temperature range is due to the decrease in viscosity in the continuous phase (see Appendix E Fig. E9 for continuous phase viscosity as a function of temperature). At temperatures above T = 37.5 °C, the droplet-poor domain cages are well established (Fig. 6.2), and the decrease in MSD results from the steric

restriction of the cages and the hydrodynamic interaction from the surrounding droplet-rich phases [247]. Appendix E Fig. E10 shows the plot of MSD versus dimensionless lag time for carboxylate beads and includes an extended discussion in the increase and subsequent decrease of MSD at rising temperatures.

As the size of beads approaches to the size the droplet-poor domains, bead hopping can occur [247–249]. Hopping is a phenomenon when beads jump from one confinement cage to another, and the residence time trapped in a cage is longer than the jump time. In prior MPT studies, cages were formed by polymer networks, whereas in our system the cages arise from the macroporous gelled nanoemulsion. The size of the droplet-poor domains are ≈ 1.5 µm at T = 50.0 °C (Table 6.1), which is comparable to the size of the 2 µm beads. Indeed, we found some of the 2 µm carboxylate beads exhibit hopping. (Note that since we calculated the ensemble-average MSD across all particle trajectories, cage-hopping events have already been accounted for in the raw data and are not subtracted from MSD shown in Fig. 6.7). Fig. 6.8 shows the representative spatial and temporal probe trajectories for hopping beads. After constrained motions for a relatively long time, hopping happens at a very short time scale wherein the probe jumps from one droplet-poor phase cage to another. In addition, the trajectories shown in Fig. 6.8 are consistent with the size of the droplet-poor phase in Fig. 6.2 and Table 6.1. From Fig. 6.8, the movement is ~ 0.1 µm, along with size of the 2 µm beads, the size of the droplet-poor domain is about 2.1 µm, which is consistent to the results in Table 6.1 and Fig. 6.2 (Note that L_{poor} is defined as the minimum Feret diameter, which is the size of the domain in the smallest dimension.).
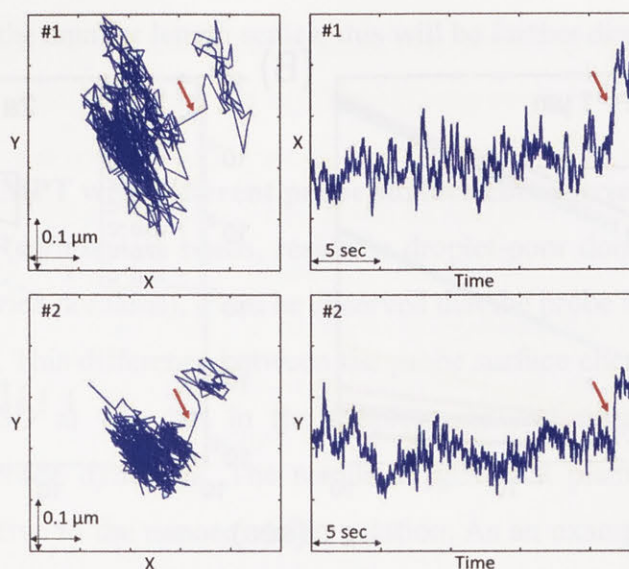
Figure 6.8 Representative spatial and temporal probe trajectories when hopping happens at T = 50.0 °C using 2 μm carboxylate beads. Arrows indicate hopping events.

6.4.5.2 MPT using plain bead probes

Fig. 6.9 shows the behavior of plain beads with 2a = 1 and 2 μm in the nanoemulsions at various temperatures. Overall, the plain beads are sensitive to the nanoemulsion gelation and have dynamics which range from simple diffusion in a Newtonian fluid at low temperatures to nearly flat MSDs at high temperatures, indicative of a solid-like material.

The MSDs of plain beads are probe-size dependent. At low temperatures, although the scaled MSDs $\sim \tau^1$ for both sizes, 2 μm beads have smaller $a\langle \Delta r^2(\tau) \rangle$. We believe this is due to the larger beads having a larger surface area to interact with the droplets or clusters in the nanoemulsion (See Appendix E Table E3 for the discussion on viscosity of the nanoemulsion obtained by bulk rheology and MPT at T = 30.0 °C). This association also affects the probe dynamics as the temperature increases. At T = 35.0 °C, $a\langle \Delta r^2(\tau) \rangle$ of 2 μm beads shows a clear decrease from T = 30.0 and 32.5 °C; while for 1 μm beads, this decrease happens at T = 37.5 °C. At T = 35.0 °C, the size of the droplet-rich domain ($\approx$ 6 μm from Table 6.1) is larger than both sizes of plain beads, which means that beads of both sizes can be entirely engulfed in the droplet-rich domain. Larger beads interact with more droplets. Such interaction can effectively limit bead motion and cause the observed decrease in the scaled MSD, which is more obvious at higher temperatures where beads show a flat MSD.
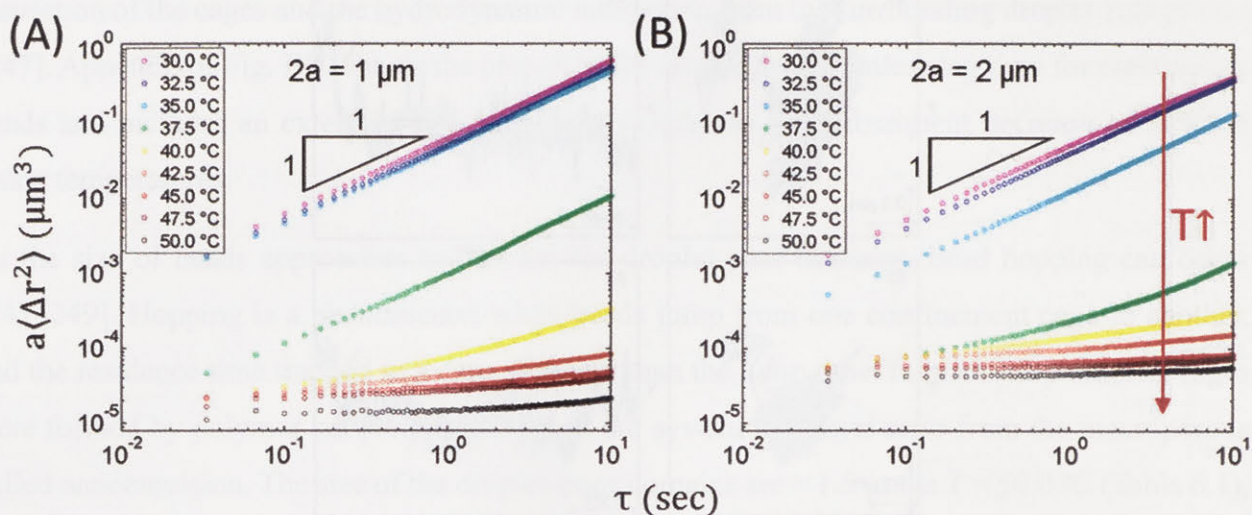
Figure 6.9 Scaled MSD of plain beads for different sizes at rising temperatures. The diameters are (A) 1 μm and (B) 2 μm. As temperature increases, the scaled MSD decreases and becomes flat. Both sizes of plain beads are sensitive to the temperature change, suggesting that measurements of material stiffness are dependent on the correlation between the probes and the network.

However, the smaller $a\langle\Delta r^2(\tau)\rangle$ for 2 μm beads at the same T does not hold when further increasing the temperature. When T is above 40.0 °C, the scaled MSD of 1 μm beads decreases faster than 2 μm beads and eventually has smaller $a\langle\Delta r^2(\tau)\rangle$, indicating that the smaller beads are more tightly trapped within the networks at high temperature. The more restricted probe dynamics of the smaller beads are explained by the size of the droplet-rich domains in Table 6.1. At temperatures above 40.0 °C, L_{rich} decreases from 1.95 to 1.24 μm, which means that 2 μm beads cannot be entirely enveloped in the droplet-rich phase. Instead, the beads partially enter the droplet-poor phase, which leads to less bridging to the nanoemulsion-rich gelled region and more mobile beads, as shown in Fig. 6.9.

The beads at T = 35.0 °C (cyan) show counter-intuitive scaled MSDs: although T = 35.0 °C is beyond the gel point from rheometer measurement (Fig. 6.1C), the probes exhibit diffusive behavior in which $a\langle\Delta r^2(\tau)\rangle \sim \tau^1$. It has been estimated the interdroplet attractive potential energy via PEGDA bridging is $\approx 0.89k_BT$ at 35.0 °C [21,32]. Compared to the attraction at higher temperatures, this weaker attraction might result in voids within the droplet-rich domains, which allows probes to easily move even in the denser phases, and the probe-size dependent scaled MSD implies spatial heterogeneity within the droplet-rich phase across the different length scales being probed. In addition, the rheometer measures rheological response from the cumulating interdroplet interaction across a bulk scale while MPT probes the local microenvironment, suggesting that a

144

weaker gel is probed at the smaller length scales, this will be further discussed later.

6.4.5.3 Comparison of MPT with different probe surface chemistries

By comparing Fig. 6.7 (carboxylate beads, reside in droplet-poor domains) and Fig. 6.9 (plain beads, reside in droplet-rich domains), it can be observed that the probe surface chemistry strongly affects the MPT results. This difference between the probe surface chemistry is also seen in Fig. 6.10, which shows MSD at $\tau = 10s$ in the droplet-poor and droplet-rich domains having dramatically different probe dynamics. The results suggest that plain beads that tether to the network are more sensitive to the nanoemulsion gelation. As an example, at T = 50.0 °C (black dots) the MSD of the plain beads is smaller than that of the carboxylate beads by over 4 orders of magnitude. Similar differences are also observed for beads with diameter of 2 μm. Therefore, along with the data shown in Fig. 6.7 and 6.9, the MPT of the nanoemulsion is strongly dependent on the probe surface chemistry, and each of them shows probe-size dependency, which correlates the results from Fig. 6.3.
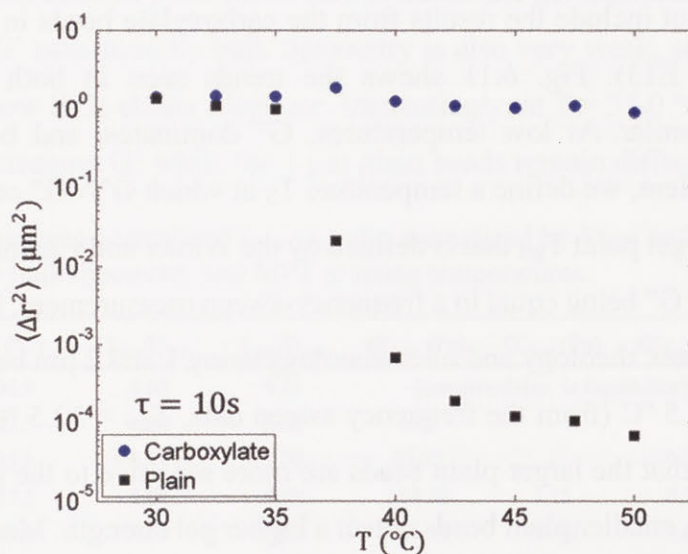
Figure 6.10 MSD at a lag time of 10s versus T for 1 μm carboxylate and plain beads at rising temperatures.

Our results are consistent with other works studying the effect of probe surface chemistry in microrheology, even though different systems were investigated [213,220,224,225,249–251]. One of the most well-studied systems is solutions of the semiflexible polymer F-actin (filamentous actin) [220,224,225,249,250]. Prior work showed that probe surface chemistry can be modified such that probes adhered to the F-actin networks. For example, the binding of the beads to the

networks is enhanced by using carboxylate polystyrene beads and is reduced by grafting bovine serum album (BSA) or polyethylene glycol (PEG) to the surface of the polystyrene beads [249]. Beads bound to the polymer networks are more sensitive to the material's changes in viscoelasticity as compared to those that do not adhere to the polymers. In addition, for beads that are strongly correlated with the network, also known as 'sticky beads' [249], the viscoelasticity of the material obtained by microrheology is closer to the bulk rheology characterization. On the other hand, the dynamics of probes having weak or no interaction with the networks depend on the ratio of the probe to mesh size a/ξ, as discussed above.

6.4.5.4 Viscoelasticity on the macroscopic and microscopic scales

We calculate the viscoelastic moduli of the nanoemulsion suspensions from the MPT results using Eq. (6.3) to (6.5). The results from MPT are compared with bulk rheology measurements (Fig. 6.1C) at a frequency $\omega \approx 20$ rad/s, shown in Fig. 6.11 (Appendix E Fig. E11 and E12 contain the frequency dependent viscoelastic moduli from MPT). Because the plain beads are more sensitive to the gelation, we do not include the results from the carboxylate beads in the comparison here (see Appendix E Fig. E13). Fig. 6.11 shows the trends seen in both micro- and macro-characterizations are similar. At low temperatures, G" dominates, and both moduli grow as temperature increases. Here, we define a temperature T_S at which G' $\approx$ G" on Fig. 6.11. Note that T_S is not necessarily the gel point T_{gel} that is defined by the Winter and Chambon criterion (power-law exponents of G' and G" being equal in a frequency-sweep measurement, Fig. 6.1C). From Fig. 6.11, T_S obtained from bulk rheology and microrheology using 1 and 2 μm beads is approximately 32.5 °C, 40.0 °C and 37.5 °C (from the frequency sweep data, $T_{gel} \approx 32.5$ °C, 37.5 °C and 35 °C respectively). It is seen that the larger plain beads are more sensitive to the gelation; however, in the G'-dominant regime, smaller plain beads detect a higher gel strength. Moreover, for both sizes of the plain beads, the viscoelastic moduli are smaller than that measured by bulk rheology. While the MSDs at elevated temperatures are small, they are still larger than the static error which sets the maximum measureable G' by MPT to approximately 150 Pa.

146
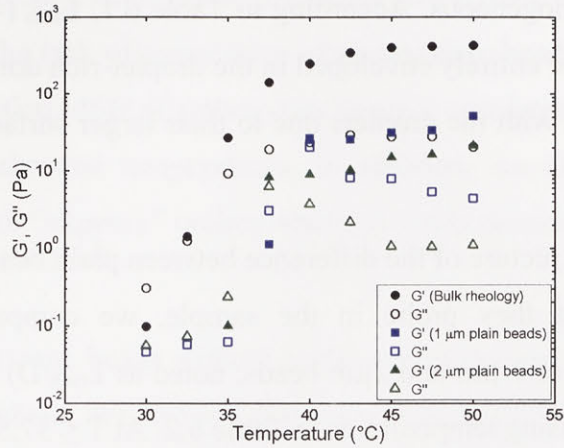
Figure 6.11 Comparison of the viscoelastic moduli from bulk rheology and microrheology using plain beads at frequency $\omega \approx 20$ rad/s. Filled symbol = G'; open symbol = G".

We believe the discrepancy in modulus between the macro- and microrheology is a result of measuring bead dynamics across different length scales in the gels. The rheometer measures the bulk rheological response from the entire gel. On the other hand, in MPT the plain beads probe the droplet-rich phase with a length scale on the order of 1 μm. As seen in our data (Fig. 6.9 and Table 6.2), at T = 32.5 °C, both sizes of plain beads cannot detect the gelling nanoemulsion. However, at this temperature, the G' measured by bulk rheometry is also very weak, so it is not unreasonable that the plain beads show little elastic response. Interestingly, at T = 35.0 °C, the 2 μm plain beads start to measure an increasing G' while the 1 μm plain beads remain diffusive in the sample.

Table 6.2 Comparison between normalized L_{rich} (L_{rich}/D, normalized by 1 μm or 2μm beads) and the G' ($\omega \approx 20$ rad/s) measured by bulk rheometry and MPT at rising temperatures.

T (°C)	$L_{rich}/D_{1\mu m}$	$L_{rich}/D_{2\mu m}$	G'_{bulk} (Pa)	$G'_{1\mu m}$ (Pa)	$G'_{2\mu m}$ (Pa)
30.0	0.65	0.31	(nanoemulsion is liquid-like)		
32.5	4.84	2.32	1.43	-	-
35.0	5.77	2.77	27.35	-	0.10
37.5	2.05	0.98	140.70	1.15	8.34
40.0	1.88	0.90	246.00	26.74	9.09
42.5	1.68	0.81	342.30	26.04	10.40
45.0	1.64	0.78	399.80	31.70	14.98
47.5	1.27	0.61	413.20	33.56	16.40
50.0	1.20	0.58	421.90	51.34	21.17

Our data at T = 35.0 °C suggests two points: first, because the droplet attraction is not strong, it is likely that small voids exist in the droplet-rich phase, although they cannot be clearly visualized with confocal microscopy due to the resolution limits. Second, the droplet distribution in the

droplet-rich phase is not homogeneous. According to Table 6.1, L_{rich} (≈ 30 µm) is large enough that both sizes of beads can be entirely enveloped in the droplet-rich domain. Therefore, the 2 µm beads have more association with the droplets due to their larger surface area and thus show an increased value of G'.

To provide a clearer physical picture of the difference between plain beads of varying size and the local microenvironment that they probe in the sample, we compare the normalized L_{rich} (normalized by the diameter of 1 µm and 2µm beads, noted as L_{rich}/D) with the G' measured by bulk rheometry and MPT at rising temperatures in Table 6.2. At $T \leq 37.5$ °C, droplet-rich domains are larger than both sizes of plain beads ($L_{rich}/D > 1$). The 2 µm plain beads measure a stronger gel since they can associate with more droplets. However, when $T > 37.5$ °C where only 1 µm plain beads can be completely enveloped in the droplet-rich domain, the 1 µm plain beads measure a stronger gel than the 2 µm plain beads. We believe it is because the 2 µm plain beads cannot be entirely trapped in the droplet-rich phase that generates the elastic properties of the nanoemulsion system ($L_{rich}/D < 1$). Future work is needed to expand the sizes of beads, especially using beads smaller than 1 µm.

MPT hence detects a weaker gel than bulk rheometry. This trend is consistent with prior work studying the effect of probe-size on microrheology in a Laponite solution [88] and associative poly(ethylene oxide) solutions [222], as well as the microrheology studies in a microgel particle suspension [212].

6.5 Conclusion
We carried out a systematic multiple particle tracking (MPT) study on thermally-gelling O/W nanoemulsions. In this work, we investigated the role of the colloidal probe size and surface chemistry on MPT in the nanoemulsion system. As temperature increases, hydrophobic groups of PEG-based gelators (PEGDA) partition into oil/water interfaces and bridge droplets. This inter-colloidal attraction generates a wide variety of microstructures consisting of droplet-rich and droplet-poor phases. By tailoring the MPT colloidal probe surface chemistry, we control the residence of probes and independently measure the probe dynamics within each phase. Our results show stark differences in the probe dynamics within each domain. At $T = 50.0$ °C, the mean squared displacement (MSD) can differ by over four orders of magnitude for the 1 µm beads but

with different surface chemistry. Carboxylate-modified polystyrene beads predominantly reside in the droplet-poor phase. The lack of association of carboxylate beads with the network results in "slippery" motion. The scaled MSD of carboxylate beads is consistent with a decreased size of the droplet-poor domain at elevated temperatures. In addition, we also observed probe hopping between pores in the gel for "slippery" probes when the beads become comparable in size to pores in the gel.

On the other hand, polystyrene beads without surface modification (plain beads) predominantly reside in the droplet-rich phase. We showed that the telechelic PEGDA polymer can bridge plain beads to each other at elevated temperatures, which suggests that PEGDA can also thermally bridge the plain beads to the nanoemulsion droplets. This bridging interaction with the network makes plain beads more sensitive to the viscoelastic changes of the nanoemulsion as temperature rises. The microrheological properties are also dependent on the size of the plain beads: larger beads are more sensitive to the gelation transitions while smaller beads detect larger moduli at higher temperatures.

Our approach allows for the unique ability to probe different regions of a colloidal gel and is useful for measuring local properties in these mesostructured hydrogels. Our quantitative results obtained from systematic studies shed light on the microstructures of thermally-gelling nanoemulsions. From our study, the probe-hopping phenomenon provides direct evidence that the droplet-poor phase is interconnected, and the results from plain beads suggest the presence of inhomogeneity within the droplet-rich phase. Furthermore, the selectivity of bead residence in different phases serves as a potential synthesis method for nanoemulsion-based composite materials. A novel aspect to these materials is that the added solid colloids with manipulated surface chemistry allows one to precisely control the residence of colloids in different phases within nanoemulsion gels. Based on the results presented here, we would expect different composite structures depending on the surface chemistry of the added colloids. Future work will look at structures formed at higher particle loadings. For instance, Janus particles with heterogeneous surface modification could provide the fine control of the particle position at the interface between droplet-rich and droplet-poor domains.

Chapter 7

3D Printing of Self-Assembling Thermoresponsive Nanoemulsions into Hierarchical Mesostructured Hydrogels

7.1 Overview

Spinodal decomposition and phase transitions have recently emerged as viable methods to generate a variety of bicontinuous materials. Here, we show that when arrested phase separation is coupled to the time scales involved in three-dimensional (3D) printing processes, hydrogels with multiple length scales spanning nanometers to millimeters can be printed with high fidelity. We use an oil-in-water nanoemulsion-based ink with rheological and photoreactive properties that satisfy the requirements of stereolithographic 3D printing. This ink is thermoresponsive and consists of poly(dimethyl siloxane) droplets suspended in an aqueous phase containing the surfactant sodium dodecyl sulfate and the cross-linker poly(ethylene glycol) dimethacrylate. Control of the hydrogel microstructure can be achieved in the printing process due to the rapid structural recovery of the nanoemulsions after large strain-rate yielding, as well as the shear thinning behavior that allows the ink to conform to the build platform of the printer. Wiper operations are used to ensure even spreading of the yield stress ink on the optical window between successive printing steps. Post-processing of the printed samples is used to generate mesoporous hydrogels that serve as size-selective membranes. Our work demonstrates that nanoemulsions, which belong to a class of solution-based materials with flexible functionalities, can be printed into prototypes with complex shapes using a commercially available 3D printer with minimal modifications.

This chapter has been adapted with permission from L. C. Hsiao, A. Z. M. Badruddoza, L. -C. Cheng and P. S. Doyle "3D Printing of Self-Assembling Thermoresponsive Nanoemulsions into Hierarchical Mesostructured Hydrogels" *Soft Matter* 2017, **13**, 921-929. Copyright 2017 Royal Society of Chemistry.

7.2 Introduction

Self-assembly is a popular method to engineer hierarchical microstructure in many types of soft materials including polymeric hydrogels [252]. Hydrogels can be formed through chemical or physical crosslinking methods, and are particularly attractive because they provide a hydrated environment with tunable diffusion profiles and mechanical properties [253–258]. Existing strategies to prepare structured hydrogels include the use of freeze drying [259,260] and sacrificial templating [261–263]. These methods only provide a coarse level of control over the resultant porous microstructure. Spinodal decomposition and phase transitions in situ have recently emerged as viable methods to generate a variety of bicontinuous materials including bijels [264], demixing polymers [265], and nematic liquid crystals [266]. These multiphase systems display a rich variety of microstructure due to the non-equilibrium thermodynamic instability of the constituent building blocks. Temperature responsiveness is inherent to many of these systems and represents a simple and effective tuning parameter to access porous microstructure in the micron length scale. Responsive colloids that form gel networks represent a particularly effective method of self-assembling such types of structure. Their characteristic domain size depends on the thermodynamics and kinetics of the highly non-equilibrium process [233,267]. Large, heterogeneous voids with strands that range from hundreds of nanometers to tens of microns are commonly observed in colloidal gels [103].

In this chapter, we show that when the dynamics of gelation are coupled to the time scales involved in three-dimensional (3D) printing processes, a new type of advanced hydrogel material with multiple length scales spanning nanometers to millimeters can be printed rapidly. 3D printing has gained popularity in recent years as an additive manufacturing platform that offers unparalleled flexibility in creating structures with arbitrary shapes and material properties [268,269]. Compared to ink jetting and extrusion-based methods, stereolithographic (SLA) printing is a layer-by-layer prototyping technique that shows excellent compatibility with liquid polymeric materials. A traditional SLA 3D printer operates by photopolymerization at the surface of a resin reservoir, in which the constructed model is progressively built by moving downwards into the ink [270]. Modern SLA 3D printers utilize an inverse setup and a layer-by-layer process to improve the printing resolution of each printed layer. First, a build platform is immersed into the resin tank containing the precursor ink. The microstructure is then photopolymerized using a 405 nm laser and actuated micromirrors, which patterns the desired motif through an optically transparent

window. Finally, the platform is withdrawn and re-immersed again to print the next layer, with automated wiper actions between each print step to remove remnant debris on the optical window (Fig. 7.1). Oxygen inhibition of the free radical polymerization is an important parameter to monitor as it controls the overall printing speed [271]. An oxygen permeable poly(dimethyl siloxane) (PDMS) layer is typically placed above the optical window to ensure a thin lubrication layer between the printed model and the resin tank, which prevents the model from adhering permanently to the window [269,272,273].

In order to leverage SLA printing for the fabrication of self-assembled hydrogels, the rheological properties of the ink should be compatible with the movement of the build platform. High strain rate deformations are applied to the ink as the platform is repeatedly immersed and retracted over the duration of the printing process. Many viscoelastic self-assembled materials can exhibit fluid instabilities [274] and yield irreversibly under these types of large stresses [2]. Thus, in order to print 3D mesoporous hydrogels with high speed and fidelity, the ink must be able to recover its original microstructure rapidly after yielding. In addition, the material should shear thin and exhibit liquid-like response [275] during platform movement such that it conforms to the base of the printed motif. Here, we demonstrate that thermoresponsive nanoemulsions, which belong to a class of multiphase materials, can be printed into hierarchical structures using a modern 3D SLA printer when the rheology of the complex fluid during the printing process is properly accounted for.

7.3 Materials and methods

7.3.1 Materials

We present an oil-in-water nanoemulsion-based ink with rheological and photoreactive properties that satisfy the requirements of SLA 3D printing. Chemicals are purchased from Sigma-Aldrich and used without further purification unless otherwise noted. A continuous phase with 33 vol% poly(ethylene glycol) dimethacrylate (PEGDMA, molecular weight $M_n = 750$ g/mol) and 200 mM sodium dodecyl sulfate (SDS) dissolved in deionized (DI) water, as well as an oil phase consisting of poly(dimethyl siloxane) (PDMS) droplets (viscosity, $\eta = 5$ cP) suspended at a volume fraction of $\phi = 0.25$. The hydrophobic fluorescent dye Nile Red (excitation wavelength = 550 nm, emission wavelength = 626 nm) is dissolved in the PDMS at a concentration of 0.05 mg/mL to enable confocal microscopy imaging of the nanoemulsions.

To prepare the nanoemulsions, a crude emulsion is first prepared by adding the oil phase into the continuous phase under stirring. The crude emulsions are then passed through a high pressure homogenizer (Emulsiflex-C3, AVESTIN) at a pressure of 15,000 psi for 20 passes. A heat exchanger is used to chill the sample to 5°C between each pass. After homogenization, the nanoemulsions are placed in a centrifuge at 5,000 rpm to remove any large impurities and the supernatant is stored at 4°C until further use. The final diameter of the droplets is measured using dynamic light scattering (90Plus PALS, Brookhaven Instruments) after dilution to $\phi = 0.002$ with a solvent of 33 vol% PEGDA in DI water ($\eta = 5.8$ cP). The diameter of the nanoemulsion droplets synthesized using this homogenizing method is $2a = (40 \pm 8)$ nm.

In order to synthesize 3D SLA printer ink, we require a photoinitiator mixture that is compatible with the nanoemulsions and that is tailored to the wavelength of the laser source. The photoinitiator 2-hydroxy-2-methylpropiophenone (Darocur) is typically used in photocuring applications. However, we find that the nanoemulsion droplet size becomes unstable and increases significantly when Darocur is incorporated (Fig. 7.2). An alternative photoinitiator is phenylbis(2,4,6-trimethylbenzoyl) phosphine oxide (TPO), which exhibits significant absorbance in the $\lambda = 385$ to 420 nm wavelength range and high molar extinction coefficients [276]. TPO is commonly used in photocurable resins because of the overlap between its absorbance spectrum and the emission wavelength of the near-UV light sources in 3D printing. We find that adding 0.1 g/mL of TPO in a 2 vol% co-solvent of butyl acetate provides the best balance between solubility, nanoemulsion stability and photocurability. The droplet sizes remain stable over a period of 2 h, which is comparable to the total print time. The TPO mixture is added to the nanoemulsion suspension at 2 vol% to generate fresh samples prior to each 3D printing experiment.

7.3.2 SLA printer modifications and setup

During the polymerization step in the chemical crosslinking of PEGDMA, the presence of oxygen slows the reaction by scavenging reactive photoinitiator radicals [271]. While this is normally undesirable, having a sufficiently thick oxygen inhibition layer below the cure zone is necessary to avoid scaffold adhesion to the optical window [269,272,273]. We modify the resin tank of a commercially available desktop SLA printer (Form 2, FormLabs) by replacing the PDMS layer above the optical window with a thin, optically transparent Teflon coating to ensure a sufficient

lubrication layer from the unpolymerized ink [269]. Teflon is effective because it has one of the highest oxygen permeabilites in polymeric materials (1600 barrers = 1.2×10^{-14} $m^2s^{-1}Pa^{-1}$ [277]) that is nearly double that of PDMS (800 barrers = 0.6×10^{-14} $m2s^{-1}Pa^{-1}$ [278]). The procedure to modify the resin tank is as follows. After removal of the PDMS layer, the surface of the window is treated with a high frequency electrode gun (BD-10AS, Electro-Technic Products). The plasma-treated window is evenly coated with 1H,1H,2H,2H-perfluorooctyltrimethoxysilane (Matrix Scientific) and baked in an oven (T = 80°C) for at least 8 h. The window is then cleaned with pure ethanol, dried, and coated with a layer of 1 wt% poly(4,5-difluoro-2,2-bis-trifluoromethyl-1,3-dioxole-co-tetrafluoroethylene) (Teflon AF 2400) in tetradecafluorohexane (FC-72). After the Teflon coating is completely dried, the edges of the optical window are reinforced with a UV adhesive (NOA 65, Norland Optics) to prevent nanoemulsion ink leakage into the optical chamber of the 3D printer.

To print hierarchical materials using the thermoresponsive nanoemulsions, the 3D printer is placed in an environmental incubator (Model 3110, Thermo Forma) set to six different temperatures (T = 22.0°C, 28.5°C, 31.5°C, 34.0°C, 38.0°C, 39.5°C). The setup is allowed to equilibrate for at least 2 hours prior to starting the printing experiment. Freshly prepared nanoemulsion inks are loaded into the resin tank and allowed to rest quiescently for 10 min to induce thermogelation. Samples used for confocal microscopy and scanning electron microscopy imaging are printed as slabs (20 mm × 80 mm × 1.5 mm) with 15 layers (thickness = 100 μm/layer). The total print time for each slab is 32 min.

7.3.3 Rheological characterization

Rheological measurements on the nanoemulsions are carried out using a stress-controlled rheometer (AR-G2, TA Instruments) equipped with an aluminum 2° cone-and-plate geometry (diameter = 60 mm, truncation gap = 58 μm). Small amplitude oscillatory measurements (strain γ = 5×10^{-4}, angular frequency ω = 20 rad/s) are used in the temperature ramp (ramp rate = 0.5°C/min) and temperature jump studies (T = 22.0°C, 30.0°C, 35.0°C, 40.0°C, 45.0°C). The linear viscoelastic moduli, G' and G", are monitored over the duration of the oscillatory measurements. In order to avoid slip, ultrafine sandpaper (320 grit) is adhered to the top geometry and the bottom Peltier plate for stress sweep experiments (γ = 1×10^{-4} to 15, ω = 20 rad/s), repeated

yielding/recovery experiments ($\gamma = 10$, $\omega = 20$ rad/s and $\Delta t = 20$ s for yield step; $\gamma = 5 \times 10^{-4}$, $\omega = 20$ rad/s and $\Delta t = 80$ s for recovery step), as well as steady shear experiments (shear stress $\sigma = 0.01$ to 100 Pa) that measure the change in nanoemulsion viscosity as a function of shear rate. We use pure nanoemulsions that has been passed through a 1.5 μm nylon filter in the rheological studies. A temperature ramp oscillatory experiment on nanoemulsions containing 2 vol% of the photoinitiator mixture is conducted to check for consistency in the gelation temperature T_{gel}.

7.3.4 Sacrificial templating and bead infusion studies

The nanoemulsions are removed from the printed hydrogels using a gradual solvent transfer process. Briefly, samples are rinsed with pure ethanol, transferred into a 1:1 v/v isopropanol/ethanol mixture for 30 min, then followed by a first soak in pure toluene for 2 h. The toluene bath is replaced with fresh solvent and samples are allowed to sit for at least 12 h to ensure complete removal of the PDMS, which is verified by a loss in fluorescence. To re-hydrate the samples, a reverse solvent transfer into 1:1 v/v isopropanol/ethanol, 1:1 v/v ethanol/DI water, and finally pure DI water is used. Samples are kept in DI water for at least 24 h to swell to their equilibrium state.

Fluorescent carboxylated polystyrene beads (5 wt%, diameters = 50 nm, 200 nm, and 1.0 μm, excitation/emission wavelengths = 505/515 nm) are purchased from Invitrogen and used without further purification. We place the porous hydrogel samples in 200 μL of the bead suspension for 4 h. After rinsing with DI water, the samples are ready for confocal microscopy imaging.

7.3.5 Microscopy imaging

We use confocal laser scanning microscopy (CLSM) to visualize the internal structure of the printed samples containing nanoemulsions and fluorescent beads after sacrificial templating. Imaging is performed on a Nikon A1R CLSM equipped with a resonant scanner head, diode lasers emitting at 488 and 561 nm, and a 60× oil immersion objective (NA = 1.4, working distance = 13 mm). Samples with dimensions of 5 mm × 5 mm × 1 mm are directly cut from the printed hydrogels and placed on a #1.5 coverslip for imaging in the xy- and xz-planes. The xy-plane images used for structural analysis have dimensions of 60.9 μm × 60.9 μm with a pixel size of 119 nm. A fast

Fourier Transform (FFT) is applied to the raw images using the image processing software ImageJ (NIH). The radially averaged scattered light intensity of the FFT images, I(q), is obtained using a radial profile plugin to ImageJ.

Porous hydrogel samples (T = 22°C, 34.0°C) are also imaged with a high resolution scanning electron microscope (HRSEM, Zeiss) at 5 kV accelerating voltage. Samples are cut into thin (~1 mm) sections, dried for at least 48 h at room temperature, and then adhered with carbon tape onto SEM stubs. All samples are sputter coated with approximately 10 nm of a Au-Pd alloy prior to imaging.

7.3.6 Mechanical characterization of filled and porous hydrogels

Nanoemulsion inks are photopolymerized into a traditional dogbone shape (cross sectional area, $A_o = 1.00 \times 10^{-5} \, m^2$, testing area length, $L_o = 15$ mm, thickness = 2 mm) for stress-strain mechanical testing. Briefly, 800 μL of nanoemulsions is added into a dogbone-shaped mold made out of a transparent polycarbonate sheet. A microscope coverslip is used to cover the top of the mold. The filled mold is placed in a vacuum oven (heated to the various temperatures used in the 3D printing) purged with nitrogen gas in order to remove oxygen from the samples. This permits even curing during the photopolymerization and reduces the formation of air bubbles. After an hour, the mold is placed under a UV lamp for 5 minutes to fully photopolymerize the hydrogels. To generate porous hydrogels for mechanical testing, we further treat the dogbones with toluene and rehydrate using the procedure that is described in the experimental section under sacrificial templating.

Both ends of the hydrogel dogbones are attached to cardboard scaffold using UV glue (NOA 65, Norland Optics). The cardboard pieces are clamped directly onto a set of 10N load cells on an Instron 8840 MicroTester. The testing procedure involves the application of an uniaxial extensional strain at a rate of 0.01 mm/s until rupture occurs. Young's modulus is obtained using the relation, $E = \sigma_e/\varepsilon = (FL_o)/(A_o\Delta L)$, where σ_e is the tensile stress, ε is the applied strain, F is the applied load, L_o and A_o are the dimensions of the hydrogel dogbone, and ΔL is the deformation length measured by the Instron tester. The engineering rupture stress is obtained using the relation $\sigma_{rup} = F_{rup}/A_o$, where F_{rup} is the measured force at which the sample fractures. A minimum of six independently prepared samples are used to generate each data point.

7.4 Results and discussion

7.4.1 Printing of self-assembled nanoemulsion hydrogels

The schematic in Fig. 7.1A and 7.1B shows the dynamical process used to print nanoemulsion-filled hydrogels with macroscopic features (honeycomb and multi-tier woodpile hydrogels are shown in Fig. 7.1D). Using temperature as a tuning parameter, we are able to print hydrogels that have internal microstructure that range from nanometer-sized droplets to mesoscopic structures. At $T < T_{gel}$, the nanoemulsions are photo-crosslinked into a homogeneous matrix. When the temperature is raised beyond a critical gelation point T_{gel}, the hydrophobic end groups on the PEGDMA molecules partition into the oil phase and serve as interdroplet bridges [21] (Fig. 7.1C), leading to the formation of a viscoelastic colloidal gel with different microstructures (Fig. 7.1E, F). Depending on application needs, these domains can either serve as pathways for the transport of hydrophobic molecules or be extracted to leave behind interconnected pores.
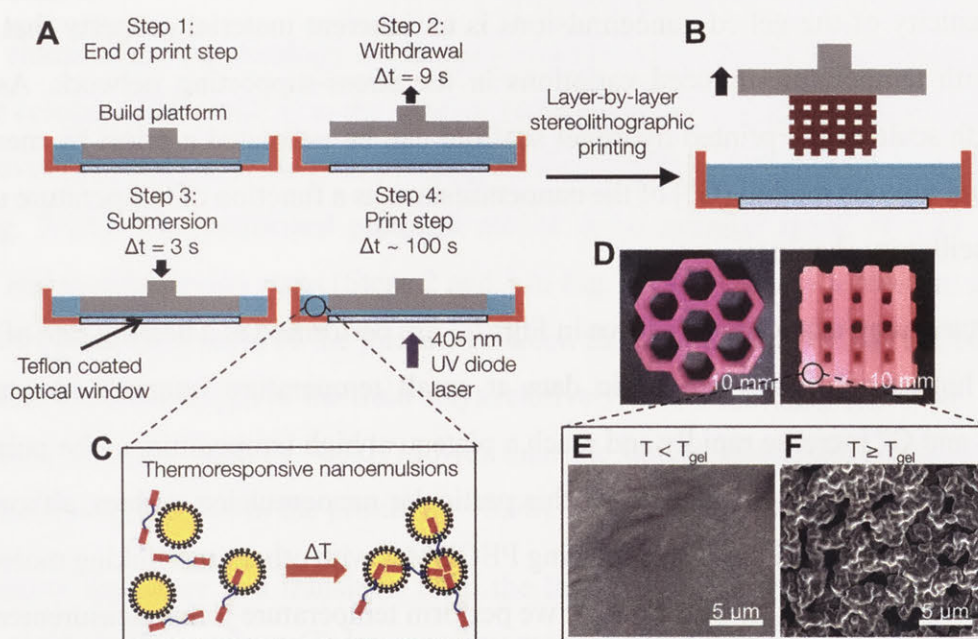
Figure 7.1 3D printing of self-assembled thermoresponsive nanoemulsion inks. A, B) Schematic of commercially available stereolithographic (SLA) printer with a custom-modified Teflon window to enhance oxygen permeability. Layer-by-layer SLA printing consists of four steps in which the desired motif is photocrosslinked, followed by high strain-rate withdrawal and submersion steps. The process repeats at a z-step size of 100 μm. C) Nanoemulsions (yellow) stabilized by surfactants in the resin tank are heated to induce self-assembly through interdroplet bridging of PEGDMA gelators (red are dimethacrylate groups). D) 3D honeycomb and woodpile structured hydrogels formed by using the nanoemulsion inks. E, F) The internal morphologies of the 3D printed scaffold that is either homogeneous at $T < T_{gel}$, or interconnected when $T \geq T_{gel}$.
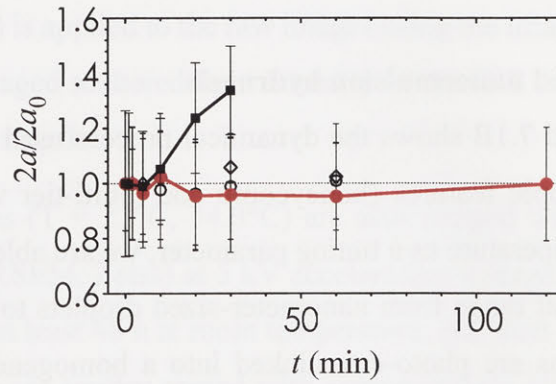
Figure 7.2 Change in PDMS droplet size as a function of time for various photoinitiator additives. Error bars represent the polydispersity of the droplets computed from fitting the raw autocorrelation data from dynamic light scattering with a log-normal distribution.

7.4.2 Rheological properties of the nanoemulsion inks

The viscoelasticity of the gelled nanoemulsions is an inherent material property that is directly correlated with temperature-induced variations in the stress-supporting network. As such, the internal length scale of the printed hydrogel scaffold can be estimated a priori by measuring the elastic (G') and viscous moduli (G") of the nanoemulsions as a function of temperature using small amplitude oscillatory rheology.

The temperature ramp experiments shown in Fig. 7.3 are performed at a heating rate of 0.5°C/min to generate high resolution viscoelastic data at small temperature intervals. As temperature increases, G' and G" increase rapidly and reach a plateau at high temperatures. The point at which G' = G" sets the value of T_{gel} = 29.2°C for this particular nanoemulsion system, although the gel temperature can be easily adjusted by replacing PEGDMA with other crosslinking molecules [21]. To account for the effect of the heating rate, we perform temperature jump measurements that are representative of print conditions. Fig. 7.3A indicates that G' and G" follow the same trend as the temperature ramp experiments, and that T_{gel} is found within a similar range. The rheology data shown in Fig. 7.3A and Fig. 7.4B-D are generated using pure nanoemulsions. Addition of the photoinitiator mixture results in a minor reduction in T_{gel} to 27.6°C (Fig. 7.3B), although the overall rheological behavior remains similar.

158
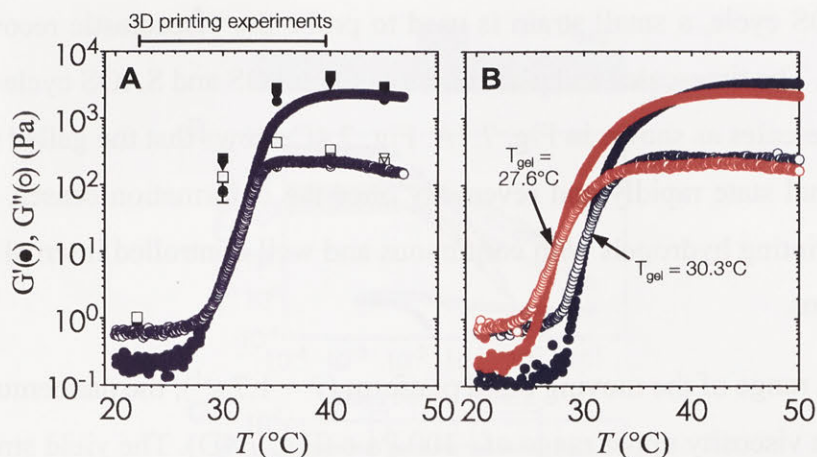
Figure 7.3 Temperature responsiveness of the nanoemulsion inks. A) Temperature ramp experiments captured at a heating rate of 0.5°C/min (purple) are overlaid with viscoelasticity data from the linear regime in the stress sweep measurements (squares), fully recovered samples in the yielding/recovery measurements (circles), and discrete temperature jump experiments (down triangles). B) Comparison of the values of T_{gel} for samples with (red) and without the photoinitiator mixtures (blue). Solid symbols represent G' and open symbols represent G".

In order to characterize the rheology of the nanoemulsion inks during the printing process, we estimate the compressive strain, γ, as the relative vertical displacement of the fluid induced by the platform movement, and the strain rate, $\dot{\gamma}$, using the linear velocity of the motorized stage through the ink (Fig. 7.4A). The motorized platform moves at an average speed of 1.27 cm/s in the withdrawal and re-submersion steps (Steps 2 and 3 in Fig. 7.1A). There is a constant gap of $h_{gap} = 100$ μm, set by the z-resolution of the printer, between the optical window and the bottom of the printed model. The total height of the fluid stays relatively constant at $h_{total} \sim 7.5$ mm. Yielding of the gels occurs at strain units ($\gamma < 0.01$) lower than the deformation imposed during the print process by the build platform in the printer ($\gamma = 0.98$).

Fig. 7.4B shows that there is a transition from the linear G'_{lin} at low γ to the nonlinear regime beyond the yield strain γ_y, where G' decreases by more than three orders of magnitude. We note here that the angular frequency (ω) of the oscillatory rheology is set to 20 rad/s to generate high resolution data on the rheometer. This value of ω provides the correct values G' and G" particularly when they become insensitive to differences in ω above the gel point of a viscoelastic suspension [111]. We use repeated cycles of large amplitude oscillatory shear (LAOS) and small amplitude oscillatory shear (SAOS) to investigate the structural recovery of the inks under the deformation imposed during the printing process. In the LAOS cycle, a strain amplitude much larger than the yield strain of the nanoemulsion is applied to simulate the withdrawal and submersion steps of

159

printing. In the SAOS cycle, a small strain is used to probe the viscoelastic recovery of the ink during the print step. The timescales and parameters of the LAOS and SAOS cycle are matched to the printing step timescales as shown in Fig. 7.1A. Fig. 7.4C shows that the gelled nanoemulsions recovers to its original state rapidly and reversibly once the deformation ceases. This structural recovery is key to printing hydrogels with continuous and well-controlled internal microstructure in all three dimensions.

Within the operation range of the moving build platform ($\dot{\gamma}$ = 1.7 s^{-1}), the nanoemulsions undergo shear thinning with a viscosity upper range of ~100 Pa·s (Fig. 7.4D). The yield stress, σ_y, and the power law exponent, n, can be obtained from fitting the Herschel-Bulkley model $\sigma = \sigma_y + k\dot{\gamma}^n$ to the viscosity data, where k is a consistency parameter and the steady shear viscosity is $\eta = \sigma/\dot{\gamma}$ [2]. A purely Newtonian liquid has constant viscosity at all shear rates (n = 1), whereas $0 \leq n < 1$ for a shear thinning fluid. These material properties are shown in Table 7.1 for nanoemulsions at different temperatures. In addition, we perform steady state characterization of the thermoresponsive nanoemulsions at T = 22°C and 40°C, which encompasses the full range of conditions tested in our study. We observe some viscosity hysteresis of the nanoemulsions at T = 22°C, but none at T = 40°C (Fig. 7.5). This gradual increase in viscosity at low temperatures could be explained by the formation of flow-induced clusters from the Brownian relaxation of the nanoemulsions and structural relaxation of the PEGDMA matrix with respect to viscous forces [279]. Nevertheless, the printed microstructure is unlikely to be affected by the shear imposed by the build platform given the long equilibration time during the print step. The yield stress of the material does present issues if the print area is not properly refilled after the withdrawal of the build platform. Classical Saffman-Taylor instabilities can also lead to viscous fingering that are comparable to the length scale of the self-assembled gel network within the nanoemulsions [280]. Thus, wiper operations are necessary to spread the ink out evenly between each layer-by-layer cycle in the printing process.
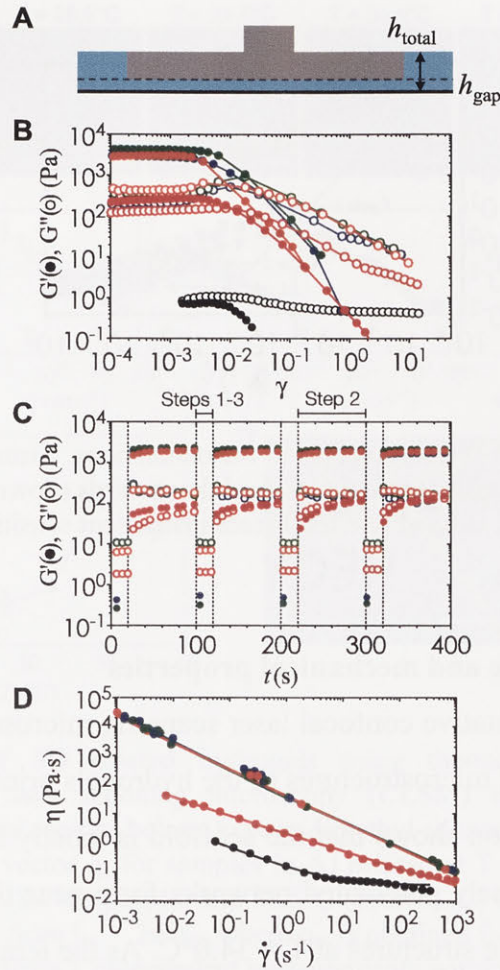
Figure 7.4 Rheology of thermoresponsive nanoemulsions. A) Schematic of the motorized build platform imposing a compressive strain at a known shear rate on the nanoemulsion ink. For our printing setup, γ = 0.98 and $\dot{\gamma}$ = 1.7 s^{-1}. B) Stress sweep experiments determines the linear regime and the yield strain at T = 22°C (black), 30°C (red), 35°C (orange), 40°C (green) and 45°C (blue). Solid lines guide the eye. C) Repeated large amplitude and small amplitude oscillatory experiments show that nanoemulsions recover rapidly and reversibly. Dashed lines mark the boundaries between yielding and recovery steps. The time scales and applied deformations are chosen to match the print and retraction steps in the 3D printer. Solid symbols represent G' and open symbols represent G". D) Steady shear rheology show yield stress behavior and shear thinning over the range of shear rates probed. Solid lines are Herschel-Bulkley fits.

Table 7.1 Rheological properties of nanoemulsion inks

T (°C)	σ_y (Pa)	n	G'$_{lin}$ (Pa)
22.0	0.06	0.75	0.17
30.0	0.08	0.41	3.24
35.0	22	0.25	899.4
40.0	25	0.30	2224
45.0	28	0.28	2210
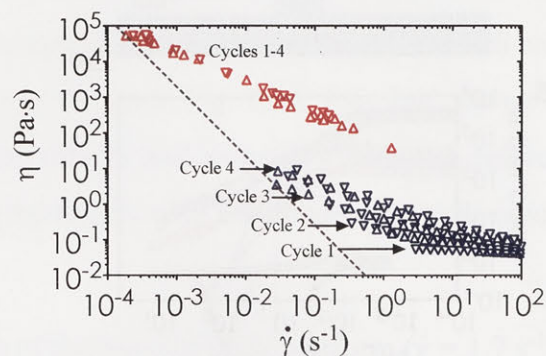
Figure 7.5 Viscosity hysteresis in thermoresponsive nanoemulsions. Steady state viscosity plotted as a function of shear rate for four upwards (up triangles) and downwards (down triangles) stress sweep cycles at T = 22°C (red) and 40°C (blue). Dashed line represents instrument sensitivity limits.

7.4.3 Hydrogel microstructure and mechanical properties

Fig. 7.6A is a panel of representative confocal laser scanning microscopy (CLSM) images in the xy-plane that show the range of microstructures of the hydrogels printed with the self-assembling nanoemulsions. Visual inspection shows that the scaffold is mostly homogeneous below the gel temperature at T = 22.0°C. Finely percolated networks form near the gel point at T = 28.5°C, which develop into spinodal-like structures at T = 34.0°C. As the temperature is further increased to T = 39.5°C, arrested phase separation results in a decrease in the length scale of the colloid-rich regions. We compute the scattered intensity I(q) from a fast Fourier Transform (FFT) applied to the raw 2D images (Fig. 7.6B), where q represents the wave vector or inverse length in real space. The characteristic gel length scale, $L_c = 2\pi/q_m$, is defined by the local peak q_m in the I(q) plots where possible and is plotted in Fig. 7.6C. The value of L_c increases gradually to a maximum at T = 34.0°C, followed by a decrease that is brought on by kinetic arrest at higher temperatures [233]. These results are in agreement with our earlier work on a similar system of thermoresponsive nanoemulsions in which samples were cast into molds [143]. In addition, we verify that the connective mesoscale structure is preserved between each printed layer. A zoomed out CLSM image of the hydrogel scaffold in the direction perpendicular to the printing (xz-plane) is shown in Fig. 7.6D, where a dashed line indicates the boundary of the two layers as observed in HRSEM images in Fig. 7.8A.

162
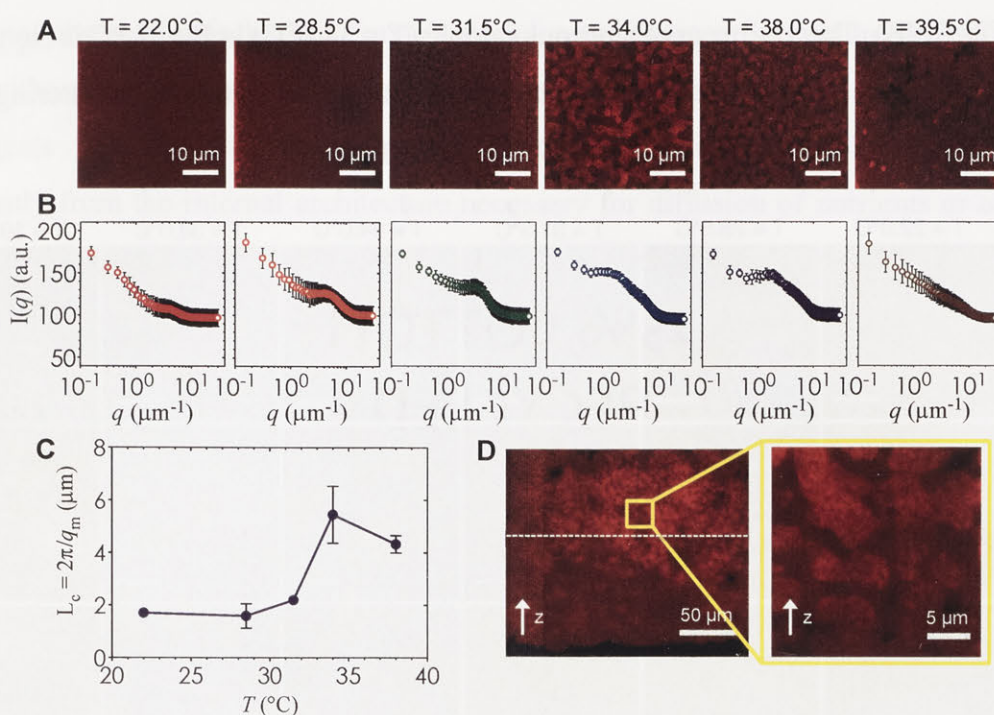
Figure 7.6 Microstructure of 3D printed hydrogels using thermoresponsive nanoemulsions. A) Representative 2D confocal laser scanning microscopy (CLSM) images of the scaffold internal microstructure, where fluorescent regions belong to poly(dimethyl siloxane) (PDMS) droplets. B). Intensity $I(q)$ as a function of the wave vector q, for samples in A) printed at $T = 22.0°C$ (red), $28.5°C$ (orange), $31.5°C$ (green), $34.0°C$ (blue), $38.0°C$ (purple) and $39.5°C$ (brown). C) Characteristic length scales of the self-assembled PDMS droplets from $L_c = 2\pi/q_m$, where q_m is obtained from peaks in $I(q)$. Error bars in B) and C) are standard deviations from 3 independent measurements within a sample. D) Zoomed out image in the xz-plane of a hydrogel scaffold printed at $T = 34.0°C$. Dashed line indicates boundary between two printed layers. Inset: Zoomed in image of the same sample.

The interconnectivity of the gel networks formed by the self-assembled thermoresponsive nanoemulsions allows for the transport of molecules and mesoscopic objects. We demonstrate this capability by using the nanoemulsions as a sacrificial template that is extracted from the 3D printed objects through solvent transfer with pure toluene. After rehydration, we immerse the samples in aqueous solutions containing fluorescent, carboxylated polystyrene beads with diameters of 50 nm, 200 nm, and 1.0 μm. Fig. 7.7 illustrates the capability of the printed porous hydrogels to serve as size-selective membranes. Beads of all sizes are able to diffuse into hydrogels having comparatively larger pore size ($T = 34.0°C$ and $38.0°C$) but not those with smaller pores ($T = 28.5°C$, $31.5°C$, $39.5°C$). The control scaffold sample printed at $T = 22.0°C$ ($T < T_{gel}$) does not permit the passage of the smallest bead size (50 nm) because of the isolated pore structure within it. A representative 3D CLSM image of a porous sample printed at $T = 34.0°C$ and treated with 200 nm beads shows that the fluorescent beads are able to diffuse into the channels in x, y, and z-

directions (Fig. 7.7B). The xz-image of a porous sample (T = 34.0°C) in Fig. 7.8C is captured from an xyz-stack; here, the imaging height is limited to 24 μm due to significant scattering from the remainder of the sample.
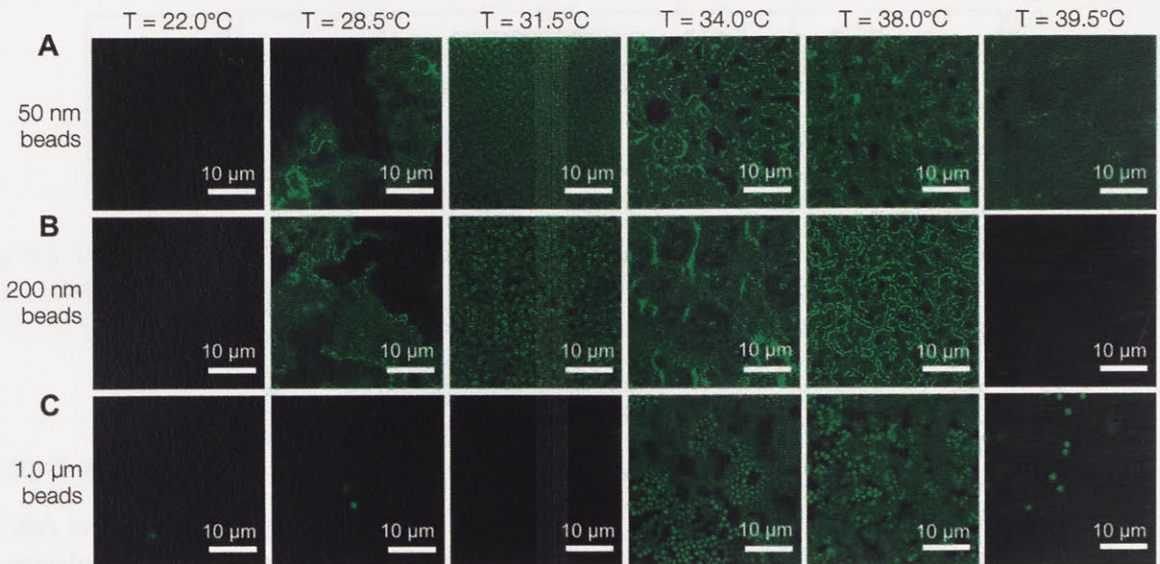
Figure 7.7 Printed porous hydrogels as size-selective membranes. Representative CLSM images of mesoporous hydrogel samples in which fluorescent polystyrene beads have been introduced. Beads of diameters A) 50 nm, B) 200 nm and C) 1.0 μm are allowed to diffuse into the interconnected porous network. Fluorescence here indicates the passage of beads into the sample. All images are captured at z = 10 μm above the bottom of the sample.
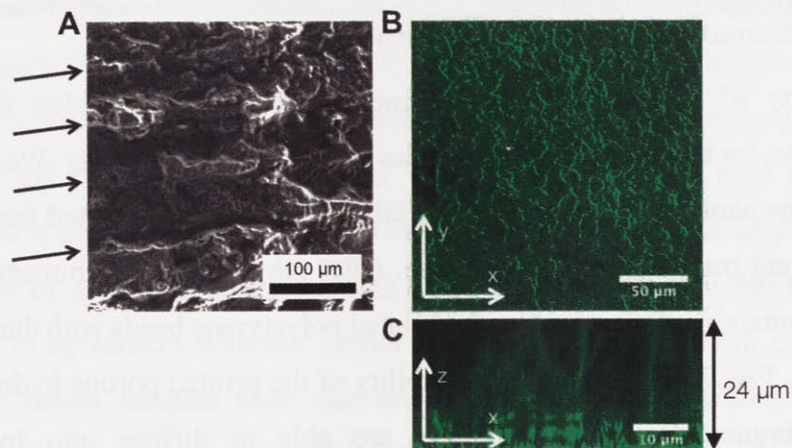
Figure 7.8 Images of printed hydrogels in three dimensions. A) HRSEM of porous hydrogel scaffold (T = 34.0°C) in the xz-plane, showing layered structure from SLA printing. Arrows indicate approximate location of boundaries spaced 100 μm apart. B, C) CLSM images of the same scaffold treated with fluorescent polystyrene beads (2a = 200 nm) in the B) xy-plane and C) xz-plane. The images in B) and C) are captured as an xyz-stack, where the z-dimension is limited to 24 μm because of significant backscatter from the rest of the sample.

An additional observation is that the Young's modulus and engineering rupture stress for hydrogels with and without nanoemulsions remain similar to within the experimental uncertainty (Fig. 7.9). This suggests that the mechanical properties of the hydrogel can be tuned completely independently from the internal architecture necessary for diffusion of nutrients or cell passage, which could be important in future applications of this material towards synthetic microvasculature and 3D cellular scaffolds.
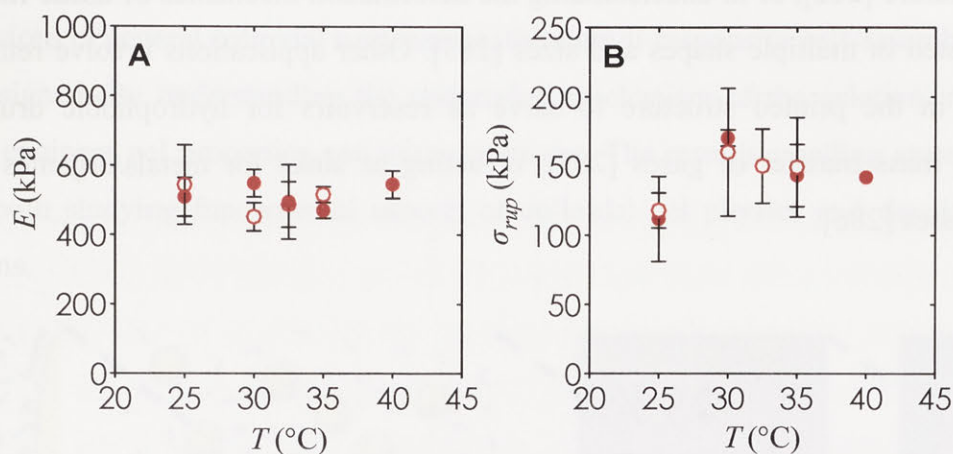
Figure 7.9 Mechanical properties of filled and porous hydrogel scaffolds. A) Young's modulus and B) engineering rupture stress of the filled (solid) and porous (open) as a function of T. Error bars are standard deviations from 6 independent samples.

7.5 Conclusion

Thermoresponsive nanoemulsions belong to a class of stimuli-responsive materials that are compatible with 3D SLA printing to generate hierarchical materials with tunable mesoscale porosity. The PEGDMA molecules in the nanoemulsion ink serve two important functions: 1) they induce colloidal gelation in which the characteristic length scale can be tuned based on the temperature, and 2) they provide photochemically crosslinked hydrogel materials on demand. Using a commercially available 3D printer with modifications to the resin tray to enhance oxygen permeability, we demonstrate that these nanoemulsions can serve as self-assembling precursor inks to be rapidly photopolymerized into macroscale structures with the desired features. Correct selection of photoinitiator is critical to maintain the stability of the nanoemulsions over the course of the printing process and to provide photoreactive response with the near-UV ($\lambda = 405$ nm) light sources that are commonly used in commercial 3D SLA printers. In addition, the rapid structural

recovery and shear thinning rheological properties of the ink is necessary for generating hierarchical materials with an interconnected morphology that allows the mass transport of mesoscopic objects into the hydrogels. However, due to the yield stress behavior of these inks, wiper operations between successive print steps are needed to spread the ink out evenly.

Future possibilities for these mesoporous materials include the crystallization of hydrophobic molecules in nanoemulsion-carrying channels for controlled or triggered drug delivery [281], synthetic vasculature [282], or in understanding the deformation mechanics of tissue-like models that can be printed in multiple shapes and sizes [283]. Other applications involve retaining the nanoemulsions in the printed structure to serve as reservoirs for hydrophobic drugs [284], modulating the mass transfer of gases [285], or acting as sinks for metals/organics in water treatment processes [286].

Chapter 8
Conclusion and outlook

A central message that this thesis tries to convey can be simply summarized as a cascade of length scales in Fig. 8.1. By understanding the molecular behavior of the constituents in the nanoemulsions or general colloidal suspensions, the stimuli-responsive self-assembly and gelation can be designed. By understanding the underlying mechanism of the gelation, researchers can rationally engineer gel properties and microstructures. The resulting gelling system can then be used for both studying fundamental aspects of colloidal gel physics and developing practical applications.
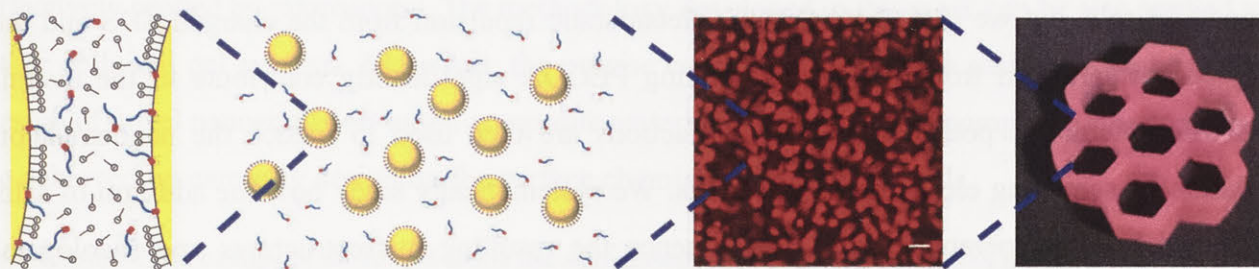
Figure 8.1 The 'Central Dogma' of this thesis.

In Chapter 2, a new thermally-responsive colloidal gelling platform is designed, and this platform is shown to be robust over a wide range of colloidal formulations. The colloidal interaction is modulated through the repulsive interaction, which results from the thermally-triggered surfactant displacement mechanism. By understanding the mechanism, we applied simple models to construct the interparticle potential and to explain trends in material behaviors. In the future, the estimation of interparticle potential can be applied to the Doyle group's previously-designed thermally-gelling nanoemulsion via polymer bridging (Section 1.3.2.2). Moreover, we also show that such platform can be applied to solid, hard-sphere nanoparticles. This suggests that one can easily design functional or multi-stimuli responsive materials by correctly functionalizing the nanoparticles. Overall, this platform offers a convenient way to assemble and control the properties of a variety of different nanoparticle gels and will be useful for engineering advanced soft materials.

In Chapter 3, we present a design of dual-responsive nanoemulsion gels where the gel properties

are responsive to changes in temperature and pH. The responsiveness comes from the weak acid surfactants containing poly(ethylene glycol) segments (PEG) and carboxyl groups. The association between the PEGs and the deprotonation of the carboxylic acids controls the inter-droplet attractive and repulsive interactions. This work opens up the opportunity to design multi-stimuli responsive nanoemulsion systems by just controlling the chemical moieties of the surfactants adsorbed on the droplets, and shows that subtle competition between attractive and repulsive interactions can determine the system's properties. Future work should focus on decoupling the convoluted interactions to better understand the system. For applications, the idea presented in this work can be applied to cosmetic products or enhanced oil recovery where temperature and pH gradients can be found.

In Chapter 4, we revisit Doyle's group previously-designed thermally-gelling nanoemulsions and reconsider the interactions that were overlooked. Not only does the PEGDA bridging play an important role, but we also show that the electrostatic repulsion from the charged SDS and the depletion interaction from the non-associating PEGDA significantly contribute to the overall pairwise interactive potentials. These interactions are then used to induce the nanoemulsion gelation by screening electrostatic repulsions. We systematically study how the addition of salts followed by a temperature jump can influence the resulting microstructures and rheological properties of the nanoemulsion system. We show that the pre-condition step with salts at room temperature has a considerable influence on the subsequent nanoemulsion microstructures and the rheological properties at elevated temperatures. For future work, the presented strategy can be used for designing hierarchically structured hydrogels and complex colloidal-based materials.

In Chapter 5, using thermally-gelling nanoemulsions, we investigate how thermal processing history affects the material properties of colloidal gel systems. By carefully designing the thermal processing route via a sequential temperature jump, we show that properties of colloidal gels can be beyond the limit set by direct quenching. Moreover, we show that the gel strength can be increased by nearly 50% under a proper thermal history. The path-dependent properties of our attractive colloidal systems motivate the concept that one should think beyond just varying chemical composition as a means to control material properties and should expand to consider processing as an equally important parameter. Future work using simulations or super-resolution microscopy will help validate the postulated mechanisms and role of hierarchical assembly.

Concepts from this work can be applied to other attractive colloidal systems which can improve the understanding of such systems, and can be utilized in colloid-based material design with richer material behaviors. Translation of model systems to products requires the development of industrial processes. Here we demonstrate that the process itself is an important tool to be leveraged to tune material properties.

In Chapter 6 we use multiple particle tracking (MPT) to probe the nanoemulsion gels at a micrometer scale. We show that, by tailoring the surface chemistry of MPT probe beads, different domains of the gel microstructures are independently probed. Plain polystyrene beads without any surface functionalization reside in the droplet-rich domains, while the charged polystyrene beads with functionalized carboxylate groups reside in the droplet-lean domains. The transportation modes of particles and the gel strength at different length scale are obtained. For future work, the calculation of spatial heterogeneity can help the understanding of the gel structure that cannot be effectively probed by microscopy. The methodology developed in this work can be also applied to other colloidal gel systems. Moreover, the precise control of the particle residence suggests the design of novel nanoemulsion-based composite materials where different composite structures can be achieved by carefully designing the surface chemistry of added colloids.

In Chapter 7 the complex structure from the self-assembled nanoemulsions is utilized for practical applications. We show that we can synthesize hierarchical hydrogels using 3D-printing. By properly engineering the nanoemulsions, the gel serves as ink with good shear-thinning behavior and remarkable structural recovery. The bottom-up route via droplet self-assembly provides various internal structures, while the top-down route during printing shapes the hydrogel geometry. For future possibilities, these composite hydrogel materials can be used for the crystallization of hydrophobic molecules in nanoemulsion-carrying channels for controlled or triggered drug delivery, synthetic vasculature, or in understanding the deformation mechanics of tissue-like models that can be printed in multiple shapes and sizes.

Appendix A

A1 Nanoemulsion synthesis and stability

A1.1 Control of nanoemulsion droplet size

The nanoemulsions were made using high pressure homogenization, which allows easy preparation of large quantities of emulsions with a range of droplet sizes [6]. In Chapter 2, the nanoemulsion droplet diameter (D) was controlled by the number of homogenizing passes (N) at a fixed homogenizing pressure $\Delta P = 18$ kpsi. Nanoemulsions discussed here consist of PDMS droplets (volume fraction $\phi = 0.30$) dispersed in an aqueous continuous phase containing PEGMA (volume fraction P = 0.33) and SDS with a total concentration = 175 mM in the system. The droplet size was determined using dynamic light scattering after diluting the nanoemulsion to $\phi = 0.002$ using an aqueous diluting agent with P = 0.33.

To synthesize the nanoemulsion, a pre-emulsion was first obtained by adding PDMS into a pre-mix aqueous continuous phase with P = 0.33 and [SDS] = 175 mM, and the mixture was then agitated using magnetic stirring for 15 minutes. The pre-emulsion was processed into the nanoemulsion with high pressure homogenization. Fig. A1 shows the droplet size as a function of N at $\Delta P = 18$ kpsi. The variation of droplet size follows an empirical exponential decay with N, as shown by the solid line in Fig. A1[6,7].
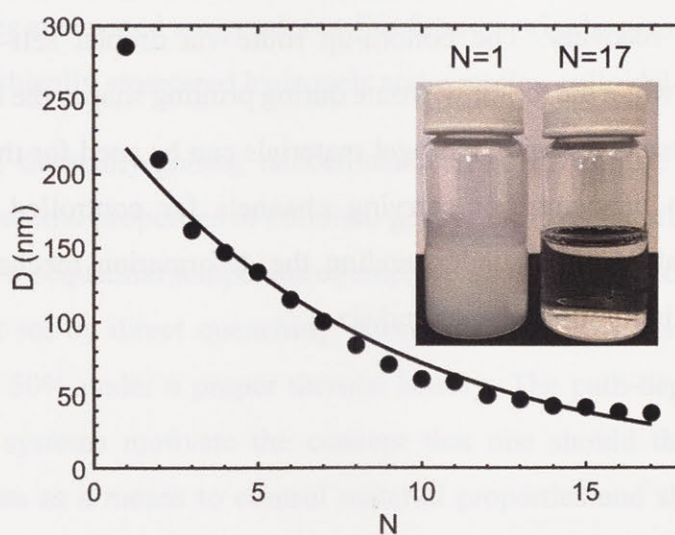
Figure A1 Evolution of nanoemulsion droplet diameter, D, with the number of homogenization passes, N. The size variation is fitted with an exponentially-decay function as shows by the solid line. The inset photograph shows the appearance of the nanoemulsion after N = 1 (opaque) and N = 17 (transparent).

A1.2 Nanoemulsion stability

The droplet stability was tested by investigating the effect of thermal gelation. The experiment was conducted by a series of temperature-jump steps. First, the nanoemulsion ($P = 0.33$, $\phi = 0.3$ and D = 53 nm) was placed in an oven where the temperature was kept at 55.0 °C for 10 minutes. After the gelation is induced (Fig. 2.1B), the nanoemulsion was cooled to 4 °C for 15 minute to ensure sufficient cooling. By applying a gentle shear, the nanoemulsion was able to re-enter to liquid-state (see A2 for a more detailed discussion on the recovery of the nanoemulsion system using rheometry). The droplet size was then measured using DLS, and the diameter was only slightly increased to D = 55nm. Such increase in droplet size might result from 1) the rate of Oswald ripening is increased at elevated temperatures [6], and 2) the oil/water interface is less stabilized during the surfactant displacement. However, the result still suggests the process of gelation does not significantly (less than 5%) affect the size of the droplets.

Another droplet stability test was also applied to monitor the size of nanoemulsion droplets in the PEGMA solution as a function of temperature using DLS. The data is shown in Fig. A2 below. Before each DLS measurement, the nanoemulsion is diluted by a PEGMA aqueous solution ($P = 0.33$) and the resulting oil volume fraction is 0.1%. As shown, the droplet size stays stable across the experimental temperature window, suggesting PEGMA does not dissolve in the oil droplets.
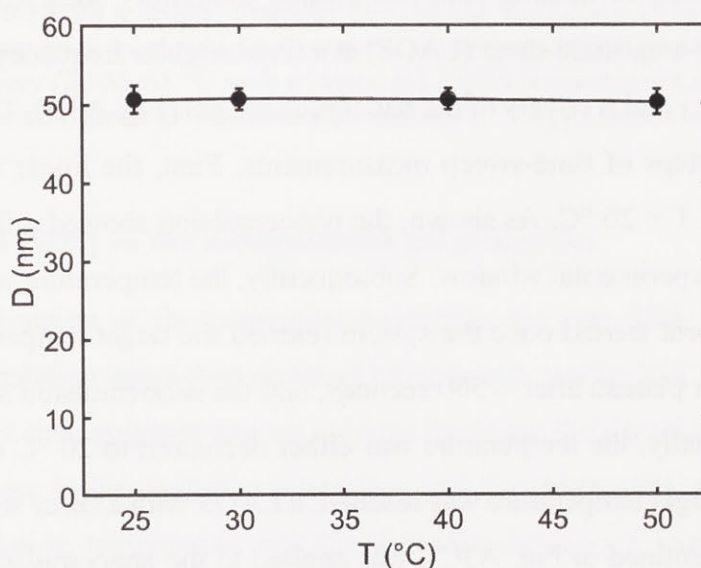
Figure A2 Nanoemulsion droplet size as a function of temperature. The error bars are standard errors from 3-5 independent measurements.

A2 Rheological characterization of the model nanoemulsion system

A2.1 Linear viscoelasticity and the plateau modulus of the canonical nanoemulsion

To determine the gelation temperature (T_{gel}) and the plateau modulus (G_P) of the nanoemulsion gels, we measured the linear viscoelasticity, storage modulus $G'(\omega)$ and loss modulus $G''(\omega)$, at rising temperatures. The results of the canonical nanoemulsion ($D = 50$ nm, $P = 0.33$ and $\phi = 0.3$) are shown in Fig. A3A (and Fig. 2.1A). At the room temperature, the nanoemulsion shows a liquid-like behavior. A critical sol-gel transition is found at $T = 30.0$ °C where $G'(\omega) \sim G''(\omega) \sim \omega^n$ using the classic Chambon-Winter criterion [111,112], and a gelation temperature, T_{gel}, is determined. As further increasing the temperature, G' and G'' grow, and G' becomes nearly independent of the applied frequency. In this high temperature regime, we found that the viscoelastic moduli do not appreciably change when $T \geq T_{gel} + 20$ °C (i.e. $T \geq 50$ °C in Fig. A3A). Therefore, in this work we determined the plateau modulus of all nanoemulsions with different formulations at a temperature of $T_{gel} + 25$ °C (Fig. 2.1A and Fig. 2.4 to 2.6), and the T_{gel} of each sample was determined using the Chambon-Winter criterion [111,112].

A2.2 Reversibility and recovery of the nanoemulsion gel

Rheological characterization combining small-amplitude oscillatory shear (SAOS, shear strain equal to 0.05%) and large-amplitude shear (LAOS) at a fixed angular frequency $\omega = 20$ rad s^{-1} was used to test the reversibility and recovery of the nanoemulsion gel (Fig. A3B). The characterization was composed of three steps of time-sweep measurements. First, the linear viscoelasticity was measured using SAOS at $T = 20$ °C. As shown, the nanoemulsion showed a liquid-like behavior with $G'' \gg G'$ over the experimental window. Subsequently, the temperature was raised to 55 °C, and the SAOS measurement started once the system reached the target temperature. The storage and loss moduli reached a plateau after ≈ 500 seconds, and the nanoemulsion showed a solid-like behavior as expected. Finally, the temperature was either decreased to 20 °C or kept at 55 °C in the third step. Once the target temperature was reached, a LAOS with a shear stress, $\sigma > \sigma_y$ (where σ_y is the yield stress determined in Fig. A3C), was applied to the nanoemulsion for 60 seconds, and the SAOS was then performed to measure the linear viscoelasticity.

The reversibility test (20-55-20 °C route) supports the existence of an energetic barrier in the estimated interactive potential (Fig. 2.2C). When the temperature is decrease from 55 to 20 °C, the system is still trapped in the energy minimum, and the nanoemulsion still shows significant elasticity over the experimental window (Fig. A3B). When larger σ is applied, the system can more easily escape from the energy minimum and re-enter the liquid state, supporting our estimated interactive potentials and the proposed gelling mechanism where the system needs to overcome an energetic barrier to undergo gelation. On the other hand, the recovery test (20-55-55 °C route) shows that storage and loss moduli decrease after a shear stress is applied. Such decrease is possibly due to a slow structural relaxation that has been found in similar colloidal gel systems [105] when the system is directly quenched to a state far from equilibrium [206]. It has been found that applying a large shear can facilitate such structural relaxation [105].
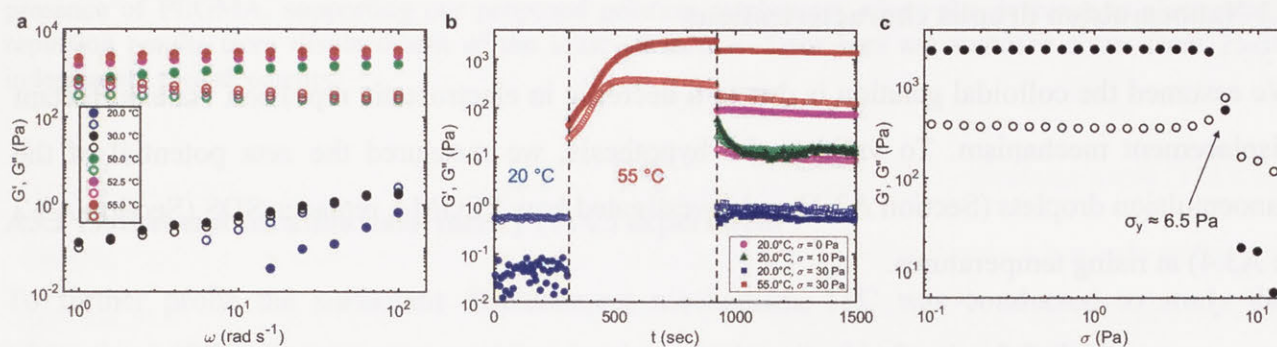
Figure A3 Rheological characterization of the model nanoemulsion system. The nanoemulsion is composed of P = 0.33 and φ = 0.3 with a droplet diameter D = 50 nm. (a) Linear viscoelasticity, G' and G", as a function of angular frequency, ω, at rising temperatures. (b) Reversibility (20-55-20 °C with different shear stresses, σ) and recovery (20-55-55 °C with σ) tests. (c) LAOS measurement at 55 °C to determine yield stress, $\sigma_y \approx 6.5$ Pa. For all figures: G' = closed symbols and G" = open symbols.

A2.3 Effect of total [SDS] on the nanoemulsion gel properties

In our *a priori* estimation of the interactive potentials, the free SDS in the continuous phase contributes to the depletion interaction and the Debye length, κ (Fig. 2.2C and Fig. 2.3). Therefore, for the same droplet size, polymer and oil volume fractions, the decrease in the total [SDS] will give rise to a decrease in the depletion interaction and the electrostatic screening, leading to the increase in the gelation temperature and the decrease in the gel strength. To validate these predictions, we studied the effect of the total [SDS] on the gel properties. The results are shown in Fig. A4. As expected, the T_{gel} increases and G_P decreases as the less SDS is added.
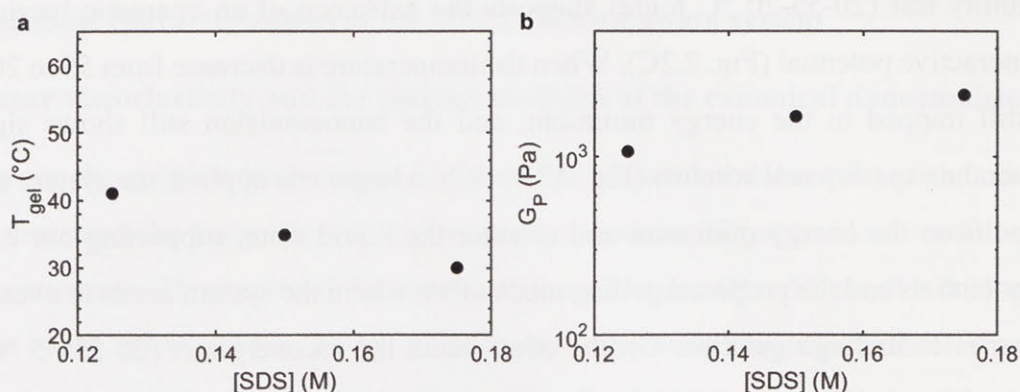
Figure A4 Gelling mechanism as a function of total [SDS] in the nanoemulsion. The PEGMA and oil volume fractions are 0.33 and 0.3 respectively. The droplet diameter is 50 nm. The figure shows (a) T_{gel} and (b) G_P as a function of [SDS].

A3 Nanoemulsion droplet characterizations

We assumed the colloidal gelation is due to a decrease in electrostatic repulsion via a surfactant displacement mechanism. To validate the hypothesis, we measured the zeta potential of the nanoemulsion droplets (Section A3.1) and investigated how PEGMA replaces SDS (Section A3.2 to A3.4) at rising temperatures.

A3.1 Zeta potential, ξ, of the nanoemulsion droplets

Fig. A5 shows the results of ξ as a function of temperature. As expected, ξ decreases with temperature (red) in the presence of PEGMA, and the changes in the zeta potential are much larger than measurement error bars, suggesting SDS desorbs from the droplets which leads to the decreases in the electrostatic repulsion (the desorption will be analyzed quantitatively in Section A3.4). On the other hand, ξ remains unchanged when no PEGMA is added to the system (blue). The observation in Fig. A5 supports our gelling mechanism in which the surfactant displacement of the ionic surfactants (SDS) only takes place when the amphiphilic oligomers (PEGMA) are added to the nanoemulsion system.
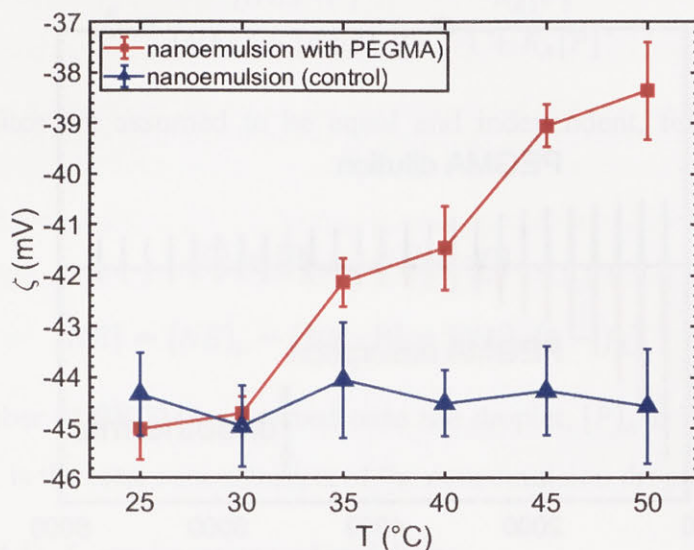
Figure A5 Zeta potential, ξ, of the nanoemulsion as a function of temperature, T. ξ only decreases in the presence of PEGMA, supporting our proposed gelation mechanism where the decrease in electrostatic repulsion results from displacement of the ionic surfactant. Error bars are standard errors from 25-30 independent measurements.

A3.2 Isothermal titration calorimetry (ITC) experiment

To further probe the surfactant displacement mechanism, ITC was conducted to study the adsorption of PEGMA onto nanoemulsion droplets. As described in Section 2.3, the measurements were performed by titrating PEGMA solution into the nanoemulsion (PDMS droplets suspended in an aqueous solution of [SDS] = 5.3 mM) at various temperatures. The ITC instrument measures the heat associated with the mixing, including the heat of PEGMA adsorption and the heat of PEGMA dilution. The heat of dilution can be measured using a blank test by titrating PEGMA into the SDS solution ([SDS] = 5.3 mM), which was served as the background signal to correct the raw adsorption data.

Fig. A6 shows an example of the result from an ITC measurement (red curve) and the corresponding blank test (blue curve) at T = 45.0 °C. Note that the result is not yet corrected by the background. The direction of the PEGMA adsorption data suggests the adsorption is an endothermic process, which supports our proposed mechanism (Fig. 2.2A) and rheological data that the gelation and the surfactant displacement take place at elevated temperatures. The data shown in Fig. A6 were then analyzed to obtain the detailed adsorption information in Section A3.3.
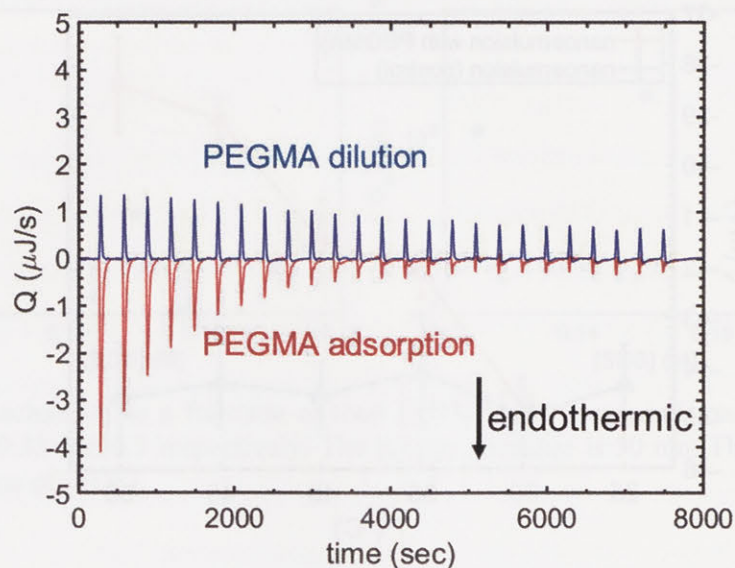
Figure A6 Results of an ITC measurement (red curve) and the corresponding blank test (blue) at T = 45.0 °C. The direction of the arrow indicates the endothermic process.

A3.3 ITC Data analysis

To further obtain the quantitative information of PEGMA adsorption behavior, the background-corrected data (Fig. A7) were fitted to an independent binding model using the data analysis software NanoAnalyze (TA Instruments). The independent binding model assumes all sites are equal in affinity and independent, and has been widely used in studies of small molecule binding [287], macromolecule-ligand interactions [288], adsorption of small molecules onto nanoparticles [289] and even adsorption of proteins onto nanoparticles [109,290].

To establish the adsorption isotherm from the independent binding model, we performed the equations that have been well-developed and widely-used in the literature [109,288]. First, the binding reaction with an equilibrium constant, K_A, is considered and shown as followed

$$NEs + P \rightleftharpoons NEs \cdot P \qquad K_A = \frac{[NEs \cdot P]}{[NEs][P]} \tag{A1}$$
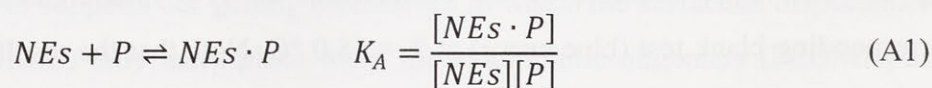
where NEs is the binding site on the nanoemulsion droplet and P is PEGMA.

The degree of saturation, f_A, is then defined as

176

$$f_A = \frac{[NEs \cdot P]}{[NEs] + [NEs \cdot P]} = \frac{K_A[P]}{1 + K_A[P]} \tag{A2}$$

Since all binding sites are assumed to be equal and independent, following relations can be established,

$$[P] = [P]_o - N[NE \cdot P] \tag{A3}$$

$$[NE] = [NE]_o - [NE \cdot P] = [NE]_o(1 - f_A) \tag{A4}$$

where N is the number of PEGMA adsorbed onto the droplet, $[P]_o$ is the total concentration of PEGMA and $[NE]_o$ is the total concentration of the nanoemulsion droplets.

Using Eq. (A2) to (A4), f_A can be expressed as follows,

$$f_A = \frac{1 + \dfrac{[P]_o}{N[NE]_o} + \dfrac{1}{NK_A[NE]_o}}{2} - \frac{1}{2}\sqrt{\left(1 + \dfrac{[P]_o}{N[NE]_o} + \dfrac{1}{NK_A[NE]_o}\right)^2 - \dfrac{4[P]_o}{N[NE]_o}} \tag{A5}$$

The heat measured from the ITC experiment, Q, is then calculated as,

$$Q = \Delta H V_{cell} N[NE]_o f_A \tag{A6}$$

where ΔH is PEGMA adsorption heat and V_{cell} is volume of sample cell. Therefore,

$$Q = \Delta H V_{cell} N[NE]_o \left[\frac{1 + \dfrac{[P]_o}{N[NE]_o} + \dfrac{1}{NK_A[NE]_o}}{2} \right.$$
$$\left. - \frac{1}{2}\sqrt{\left(1 + \dfrac{[P]_o}{N[NE]_o} + \dfrac{1}{NK_A[NE]_o}\right)^2 - \dfrac{4[P]_o}{N[NE]_o}} \right] \tag{A7}$$

Eq. (A7) is the adsorption isotherm associated with the heat and can be used in data analysis. Alternatively, consider the ITC measurement is done by discretely injecting certain amount of PEGMA solution into the nanoemulsion, the change in heat, ΔQ, from injections can be expressed as,

$$\Delta Q = Q(i) - Q(i-1) + \frac{V_{inj}}{V_o}\left(\frac{Q(i) + Q(i-1)}{2}\right) \tag{A8}$$

where V_{inj} is the injection volume each time and V_o is the initial cell volume.

Fig. A7 shows an example of the data analysis at T = 45.0 °C. The data (closed symbols) has been corrected from the blank test and is shown as a function of number of injections. The solid line indicates the result of model fitting using Eq. (A7) and (A8).
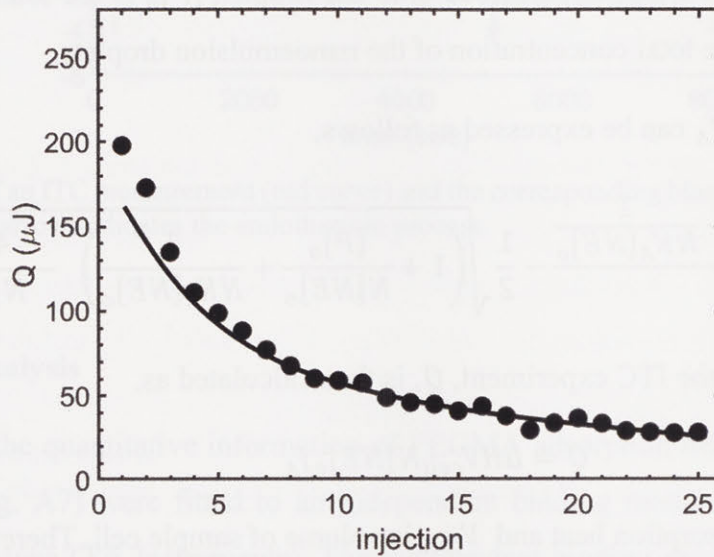
Figure A7 Example of ITC data analysis at T = 45.0 °C. Closed symbols: background-corrected data. Solid line: model fitting using Eq. (A7) and (A8).

Fig. A8 concludes the results from ITC measurements at elevated temperatures. Fig. A8A shows that the number of PEGMA adsorbed per droplet increases at the elevated temperatures. Along with the zeta potential shown in Fig. A5 where the magnitude decreases with T, the results are the direct evidence of the thermally-triggered surfactant displacement mechanism. Moreover, the resulting values in Fig. A8A can be further used to estimate the surface potential of nanoemulsion droplets and we show that the resulting values are consistent with the measured zeta potentials in Section A3.4.

Fig. A8B shows that the heat of PEGMA adsorption is a function of temperature. First, the result shows the adsorption process is an endothermic reaction across the temperature window, suggesting the entropy of the system increases during the adsorption [109,291]. Such increase in the entropy results from the increase in the translational entropy of the water molecules during the

dehydration of the PEGMA hydrophobic groups [109,291]. Therefore, the endothermic behavior supports our proposed mechanism where the dehydration of the hydrophobic groups of the oligomers drives the adsorption. Second, the magnitude of the adsorption heat decreases as the temperature increased. The decreasing heat suggests PEGMA is less stabilized in the continuous phase at elevated temperatures and to validate this hypothesis we compared the blank tests at different temperatures. As shown in Fig. A9, as expected, the dilution is an exothermic reaction across the temperature window, and the magnitude of the heat flow decreases at elevated temperatures. The result suggests that PEGMA is more stabilized in the continuous phase at lower temperatures, supporting the observation that less adsorption heat is required at higher temperatures.
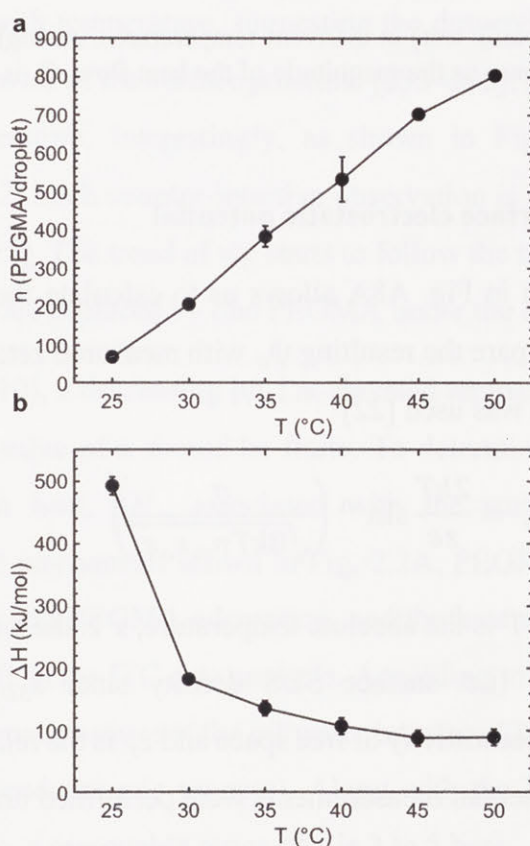
Figure A8 ITC results as a function of temperature. (a) The number of PEGMA adsorbed per droplets, n. (b) The heat of PEGMA adsorption onto the nanoemulsion droplets, ΔH. For both figures, the solid lines are drawn to guide the eye. Error bars are one standard deviation from 3 to 4 independent measurements.
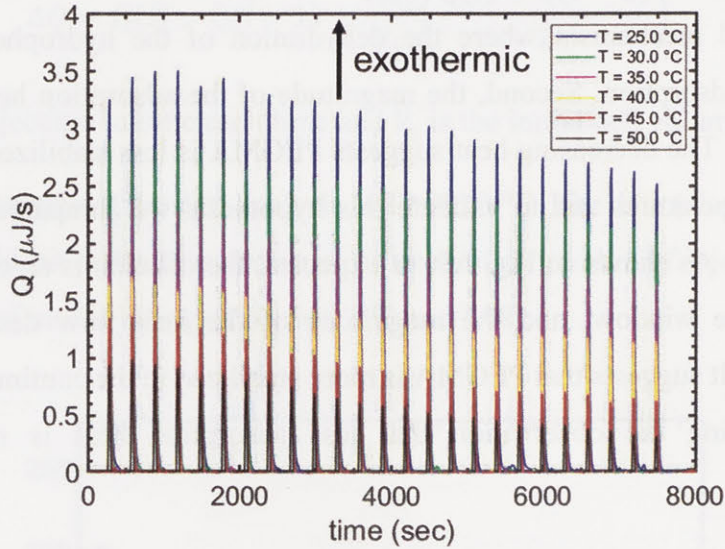
Figure A9 Dilution of PEGMA (blank test) at different temperatures. At higher temperature, PEGMA is less stabilized in the continuous phase as the magnitude of the heat flow, Q, is smaller.

A3.4 Estimation of droplet surface electrostatic potential

The PEGMA adsorption shown in Fig. A8A allows us to calculate the surface potential, ψ_o, of nanoemulsion droplets and compare the resulting ψ_o with measured zeta potentials in Fig. A5. To estimate ψ_o, Grahame equation was used [22]

$$\psi_o = \frac{2kT}{ze}\sin^{-1}\left(\frac{\sigma}{\sqrt{8kTn_\infty \varepsilon_o \varepsilon_r}}\right) \tag{A9}$$

where k is Boltzmann constant, T is the absolute temperature, z is the valence (charge number), σ is the surface charge density (i.e. surface SDS density since $z_{SDS} = 1$), n_∞ is the bulk concentration of ions, ε_o is the permittivity of free space and ε_r is the relative permittivity of water [115] since the ITC and zeta potential measurements were performed under a diluted condition. The Grahame equation has been used to estimate the surface potential of colloids [292] by considering the surface charge density, σ, estimated as

$$\sigma = \frac{(n_{SDS} - xn_{PEGMA})e}{A} \tag{A10}$$

where n_{SDS} is number of SDS on a droplet and is estimated by considering the area of SDS occupied on the oil droplet (= 0.617 nm^2/molecule [182]), n_{PEGMA} is the number of PEGMA adsorbed onto droplet from ITC measurements, A is the surface area of a droplet and x is the number of SDS replaced by PEGMA, which is not necessarily equal to unity as will be discussed shortly. To simplify the calculation, here we assume the number of replaced SDS molecules is the same across the temperature window, i.e. x is assumed to be a constant and independent of temperature.

By using Eq. (A9), (A10) and the values listed in Fig. A8A, the resulting estimated surface potentials at elevated temperatures are shown in Fig. A10B. Fig. A10A lists the temperature-dependent zeta potentials from Fig. A5 for comparison. Again, the magnitude of the measured ξ decreases (less negative) with temperature, suggesting the desorption of SDS, and the trend of ξ should also reflect the behavior of the surface potential [293–295], i.e. the magnitude of ψ_o should also decrease with temperature. Interestingly, as shown in Fig. A10B, $|\psi_o|$ increases with temperature for $x = 1$ and 2. Such counter-intuitive observation is possible since ε_r (Table 2.1) is temperature-dependent [115]. The trend of ψ_o starts to follow the trend of ξ as $x \geq 3$, indicating at least three SDS molecules are replaced by one PEGMA under the adsorption process.

Based on Eq. (A9) and (A10), a decreasing $|\psi_o|$ at elevated temperatures can be always obtained when $x \geq 3$, although the value of x should be finite. To determine a reasonable range of x, we considered the adsorption heat, ΔH, associated with the surfactant displacement process. According to the proposed mechanism shown in Fig. 2.2A, PEGMA adsorption in fact includes two steps: SDS desorption and PEGMA adsorption, and the heat associated with these two steps are lumped into a single ΔH in the ITC data analysis. According to prior work which studied SDS adsorption/desorption thermodynamics at the oil/water interface [296–298], the desorption heat of SDS is ≈ 15-20 kJ/mole (endothermic process). Along with the ITC results listed in Fig. A8B where ΔH is ≈ 100 kJ/mole, a reasonable range of x is 3 to 5 here.
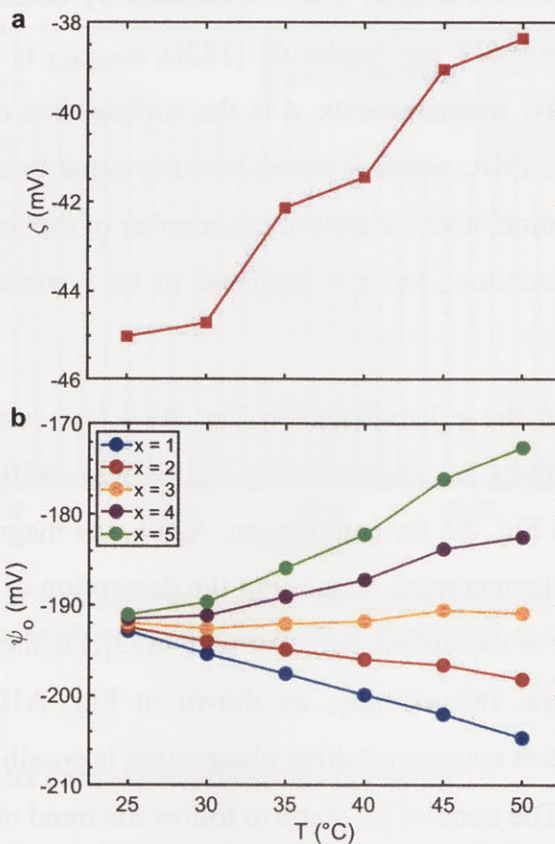
Figure A10 Comparison of the masured zeta potential, ξ, and the estimated surface potential, ψ_o, of the nanoemulsion droplets. (a) Measured ξ from Fig. A5. (b) Estimated ψ_o using Eq. (A9), (A10) and the values listed in Fig. A8A. The solid lines are drawn to guide the eye.

Appendix B

Length scale analysis

Although the packing and the exact conformation of the surfactants on the droplets are not known, we have estimated the length scales of PEGs in the nanoemulsion system. For clarification, free PEG in the continuous phase (M_w = 400 g/mol) is denoted as PEG400, and the PEG on the weak-acid surfactant ($M_w \approx$ 400-440 g/mol) is denoted as PEG$_w$. For both PEG400 and PEG$_w$, the radius of gyration is $\approx$ 0.68 nm [132], and the contour length of the extended chain is 5.3 nm (assuming both PEGs behave like an ideal polymer) [95]. The length scale of the repulsion can be obtained by estimating the Debye length, κ^{-1},

$$\kappa^{-1} = \sqrt{\frac{\varepsilon_0 \varepsilon_r kT}{1000 e^2 N_A \sum z_i^2 M_i}}$$

where ε_0 is the electric permeability of free space, ε_r is the dielectric constant of the continuous phase (here ε_r of water is used for estimation), k is Boltzmann constant, T is the absolute tempeature, e is the elementary charge, N_A is Avogadro's number z is the charge number and M is the molar concentration. For the system, κ^{-1} is $\approx$ 7 nm.
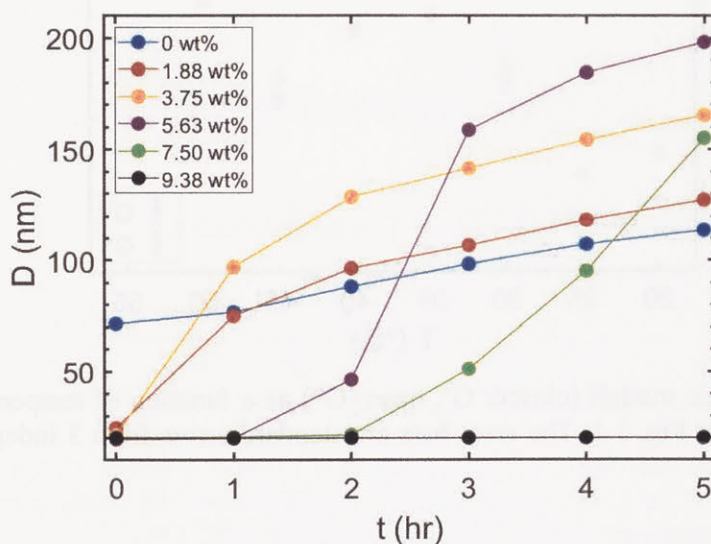
Figure B1 Nanoemulsion (pH = 2.5 at room temperature) stability as a function of concentration of co-surfactant PEG400. The data shows that a sufficient amount of PEG400 is needed to stabilize the nanoemulsion droplets.
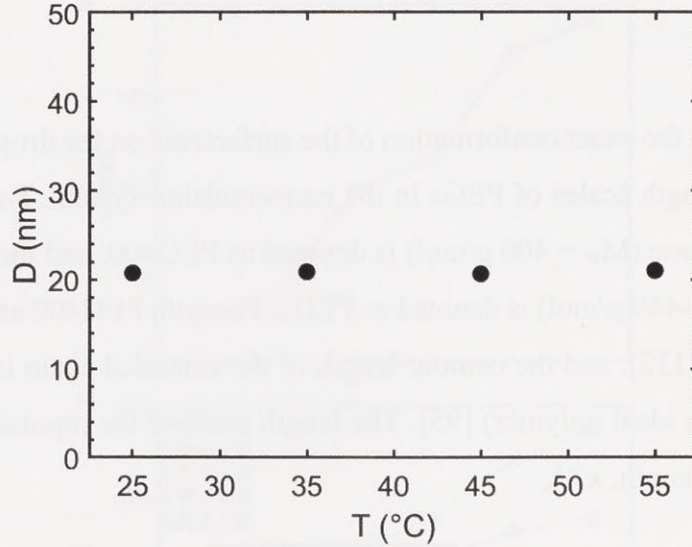
Figure B2 Size of nanoemulsion droplets as a function of temperature (pH = 2.5). For each temperature, the nanoemulsion (ϕ = 12.5 wt%) was heated to the target temperature for 30 min in the oven and diluted to ϕ = 0.5 wt% for the DLS measurements.
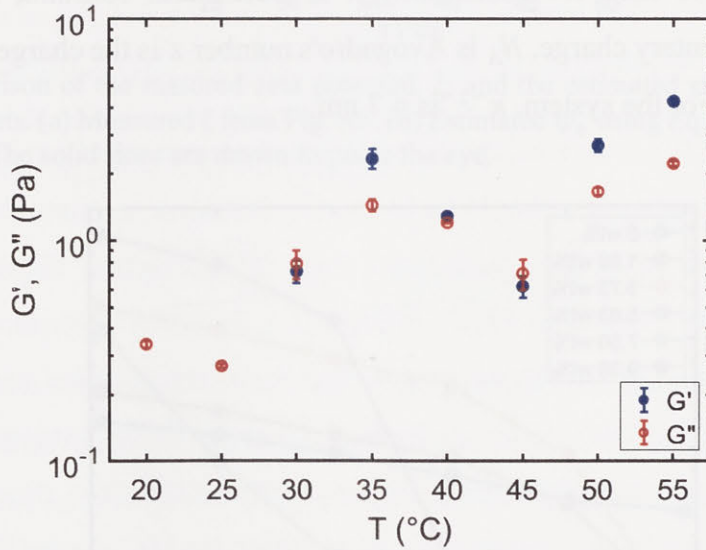
Figure B3 Linear viscoelastic moduli (closed: G', open: G") as a function of temperature at an angular frequency ω = 25 rad/s from Fig. 3.1. The error bars are standard errors from 3 independent frequency-sweep measurements.
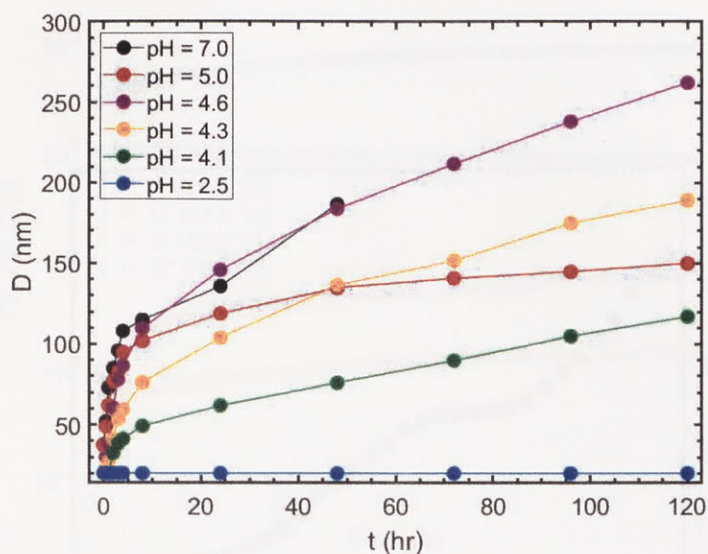
Figure B4 Nanoemulsion droplet size as a function of pH over a course of several days at room temperature. The nanoemulsion at pH = 7 phase separate after 48 hours. The pH was adjusted using NaOH.
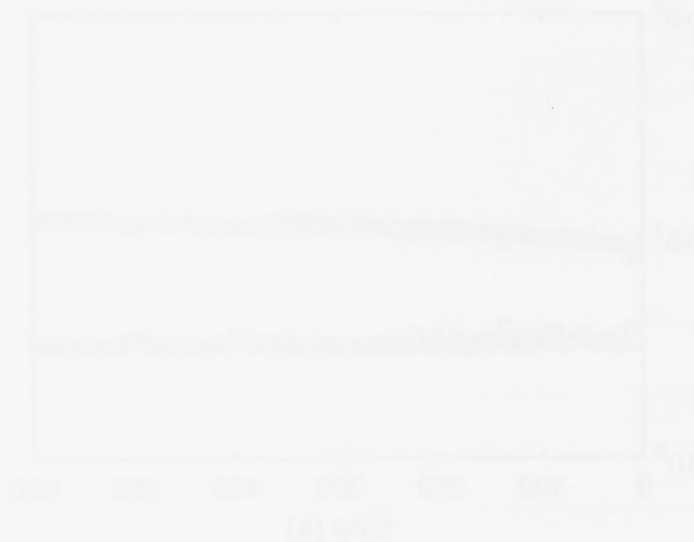
Appendix C
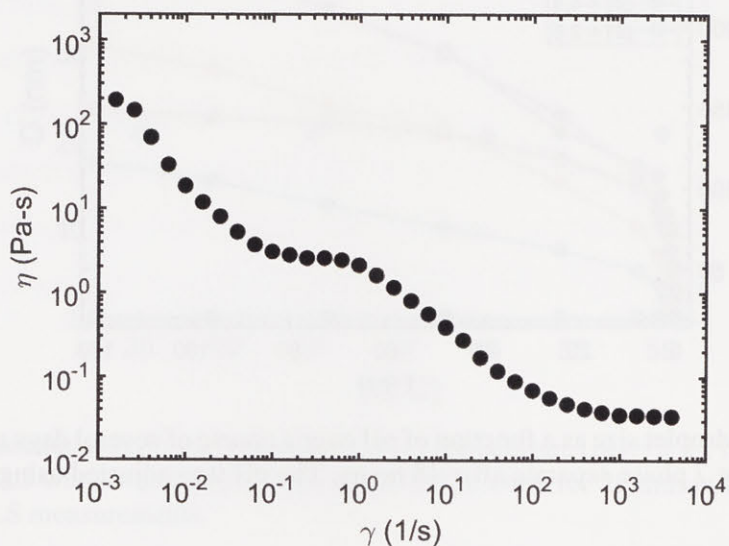
Figure C1 Flow curve of the nanoemulsion with [NaCl] = 0.07 M at T = 20.0 °C.
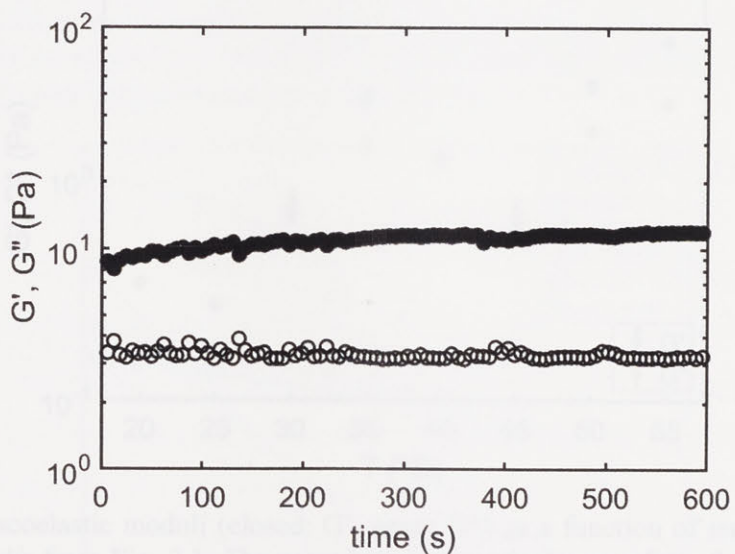
Figure C2 Linear viscoelastic moduli (G': closed symbols, G": open symbols) of the nanoemulsion with [NaCl] = 0.07 M at T = 20.0 °C as a function of time. The measurement starts right after the pre-shear step (rejuvenation). Angular frequency $\omega = 10$ rad s^{-1} and shear strain $\gamma = 0.05\%$.
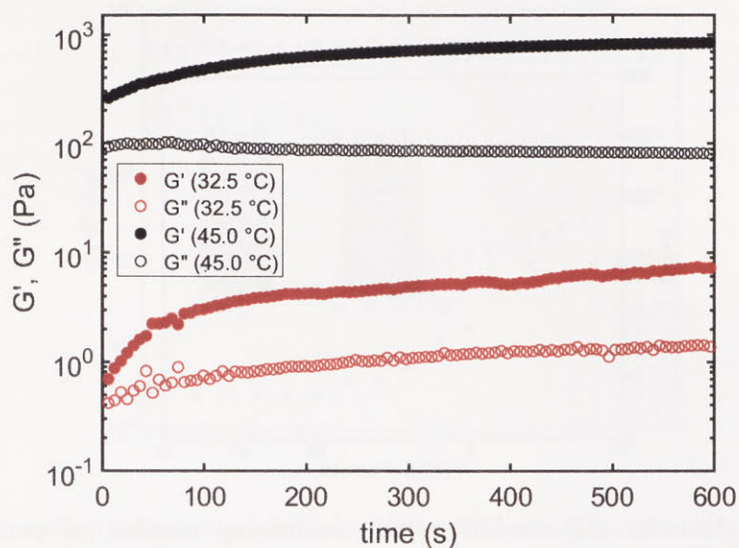
Figure C3 Linear viscoelastic moduli (G': closed symbols, G": open symbols) of the nanoemulsion with [NaCl] = 0 M as a function of time at T = 32.5 °C (red) and 50.0 °C (black). The measurement starts right after the sample reaches the target temperature. Angular frequency $\omega = 10$ rad s^{-1} and shear strain $\gamma = 0.05\%$.

Appendix D
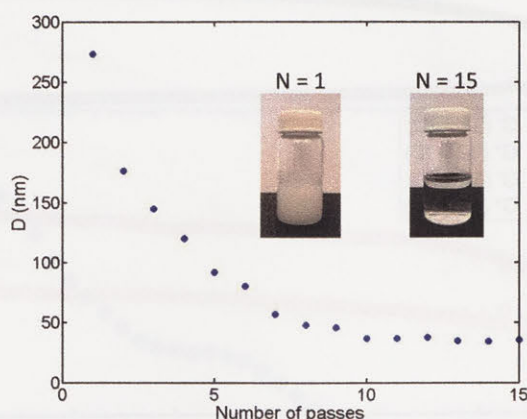
Figure D1 Oil droplet diameter (D) evolution with increasing number of pass (N) through the homogenization. Inset photos show the appearance of the emulsion with N = 1 (opaque) and N = 15 (transparent).
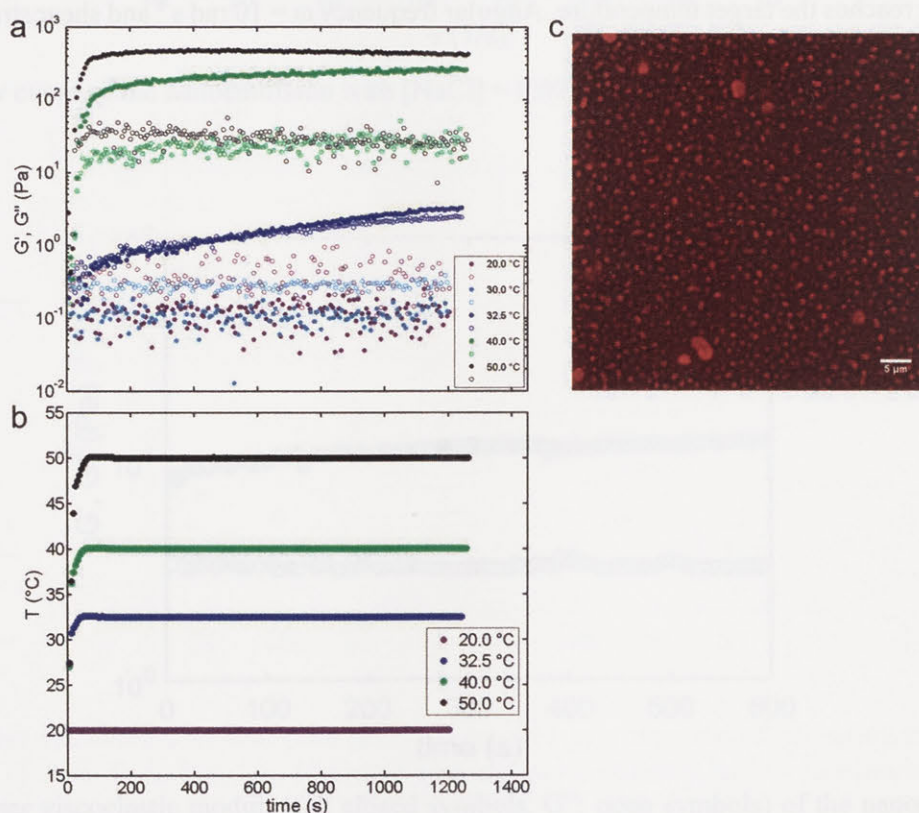
Figure D2 (a) Rheological response of the nanoemulsion with one-step temperature jump. The plot shows the measurements with initial temperature increasing from T = 20.0 °C to the target temperature. Closed symbols denote G' and open symbols denote G". (b) Complete temperature history during the rheology measurement. (c) Confocal image of the nanoemulsion at T = 30.0 °C. The image shows the microstructure is composed of freely-suspended clusters and the rheology at T = 30.0 °C shows liquid-like behavior without increase in viscoelasticity in (a). Therefore, we believe that the freely-suspended clusters at T = 32.5 °C (quantified as $L_{C,2}$ in Chapter 5) are not stress-bearing structures.

188
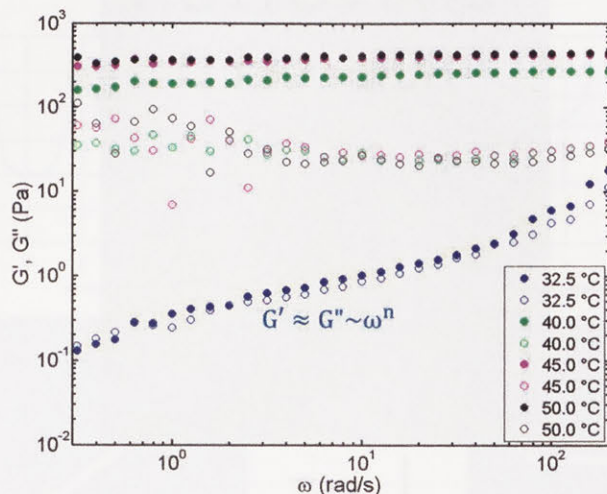
Figure D3 Frequency-sweep linear viscoelastic moduli of the nanoemulsion at various temperatures. The measurements start after T reaches the target temperature for 10 minutes. Closed symbols denote G' and open symbols denote G".
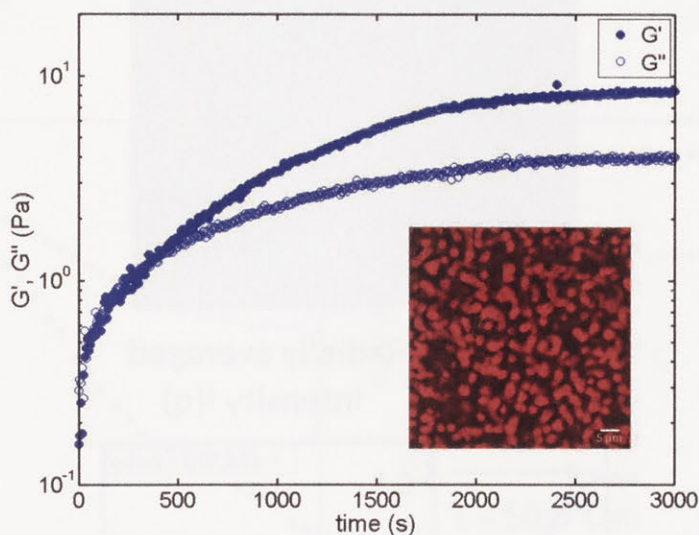
Figure D4 Time-dependent viscoelastic moduli (G' and G") of the nanoemulsion at T = 32.5 °C. Both G' and G" become nearly constant after t = 45 min, suggesting a pseudo-steady state is achieved. The inset confocal image shows the microstructure captured at t = 50 min, where no discernible freely-suspended clusters are observed, suggesting the inclusion of every cluster in the network.
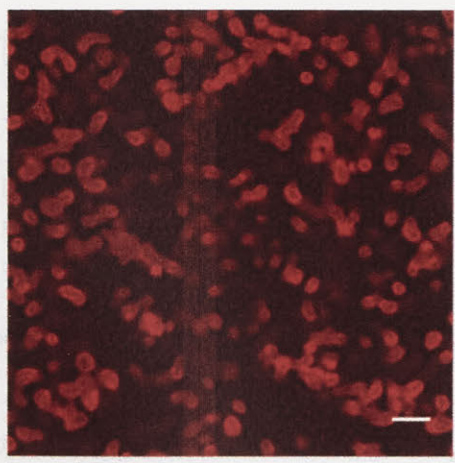
FFT
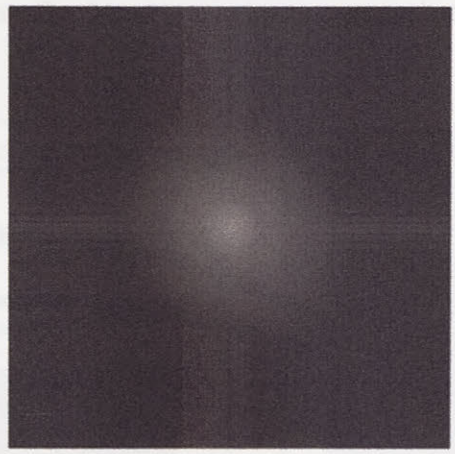
Radially averaged
intensity I(q)

$L_{C,1}$

$L_{C,2}$

$L_{C,3}$
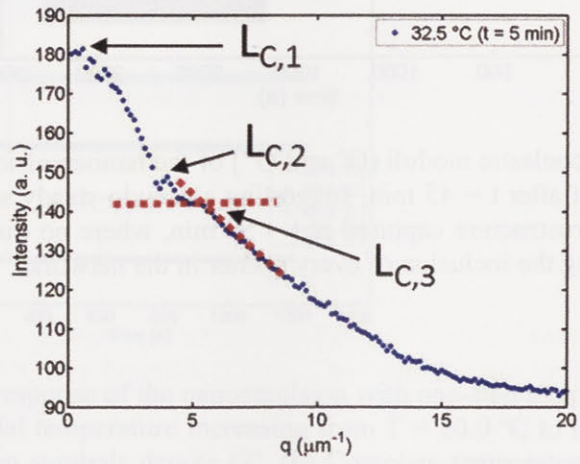
Figure D5 An example to show the procedure to determine L_C using the software ImageJ. Scale bar = 5μm. Dashed red lines are local fits to the data. The inflection point is then determined by the intersection of the fitted lines.
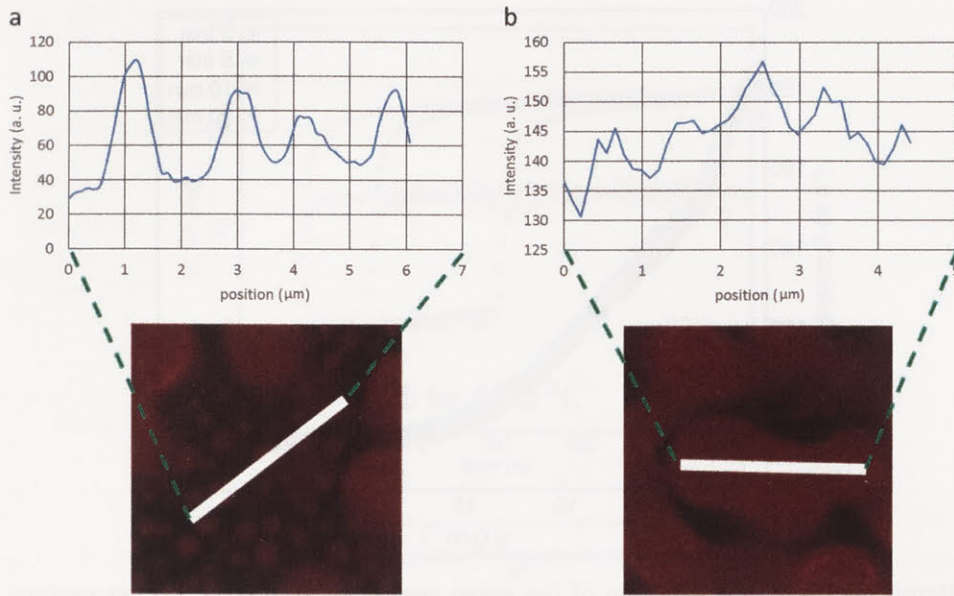
Figure D6 (a) Intensity profile of the region where only freely suspended clusters are present. (b) Intensity profile inside the droplet-rich phase for $L_{C,3}$ validation. Profiles are taken from the nanoemulsion held at T = 32.5 °C for 20 minutes.
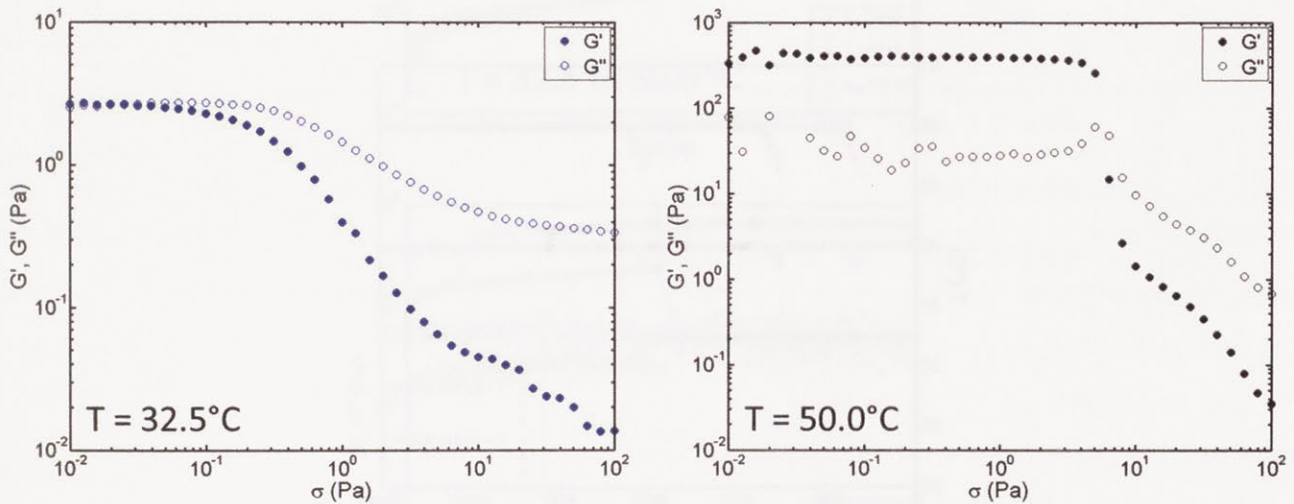
Figure D7 Large amplitude oscillatory shear rheology of viscoelastic moduli (G' and G") versus oscillatory shear stress (σ) of the nanoemulsion at T = 32.5 °C and 50.0 °C. At T = 50.0 °C, the measurement shows a typical two-step yielding with a maximum in G", suggesting the gel network is of a hierarchical nature (primary: droplet-rich strands and secondary: 'building blocks' clusters, as shown in Fig. 5.2E. At T = 32.5 °C, the nanoemulsion only shows a weak two-stage yielding in G", while a simple yielding is present in G", which may be because this temperature is at the critical gel point where the stress-bearing network is just established.
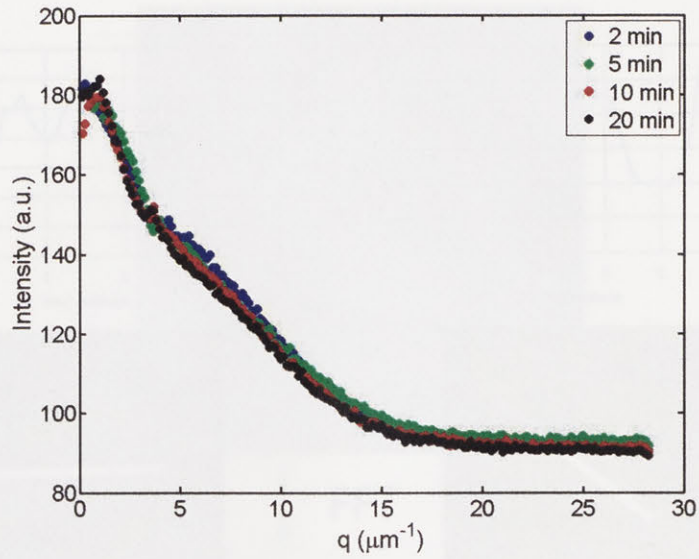
Figure D8 Scattered intensity as a function of the wave vector, q, at T = 32.5 °C at various times. For q smaller than ≈ 2μm^{-1}, which corresponds to primary length scale ($L_{C,1}$), the intensity increases with time. This is consistent with more droplet-rich strands formed with time, as shown in Fig. 5.1D. For 3 μm^{-1} ≤ q ≤ 5 μm^{-1}, which corresponds to secondary correlation length ($L_{C,2}$), the intensity decreases with time. This is consistent with fewer freely suspended clusters present with time, as shown in Fig. 5.1D.
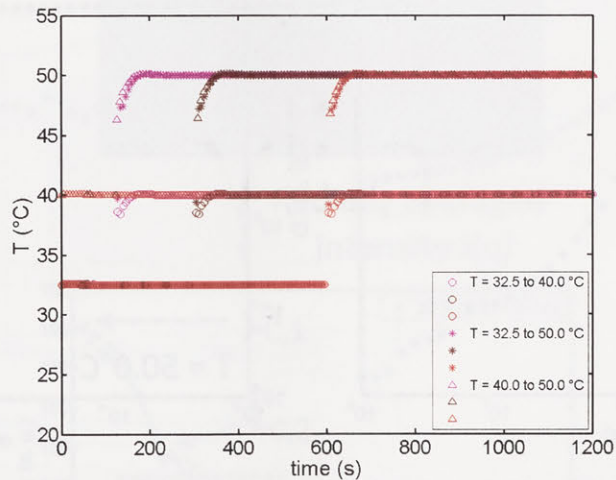
Figure D9 Complete temperature history of thermally processed samples during the rheology measurement. The shape indicates the different thermal processing route. Circle: 32.5 to 40.0 °C. Star: 32.5 to 50.0 °C. Triangle: 40.0 to 50.0 °C. The color indicates the different holding time. Purple: T_{hold} = 2 min. Brown: t_{hold} = 5 min. Red: T_{hold} = 10 min.
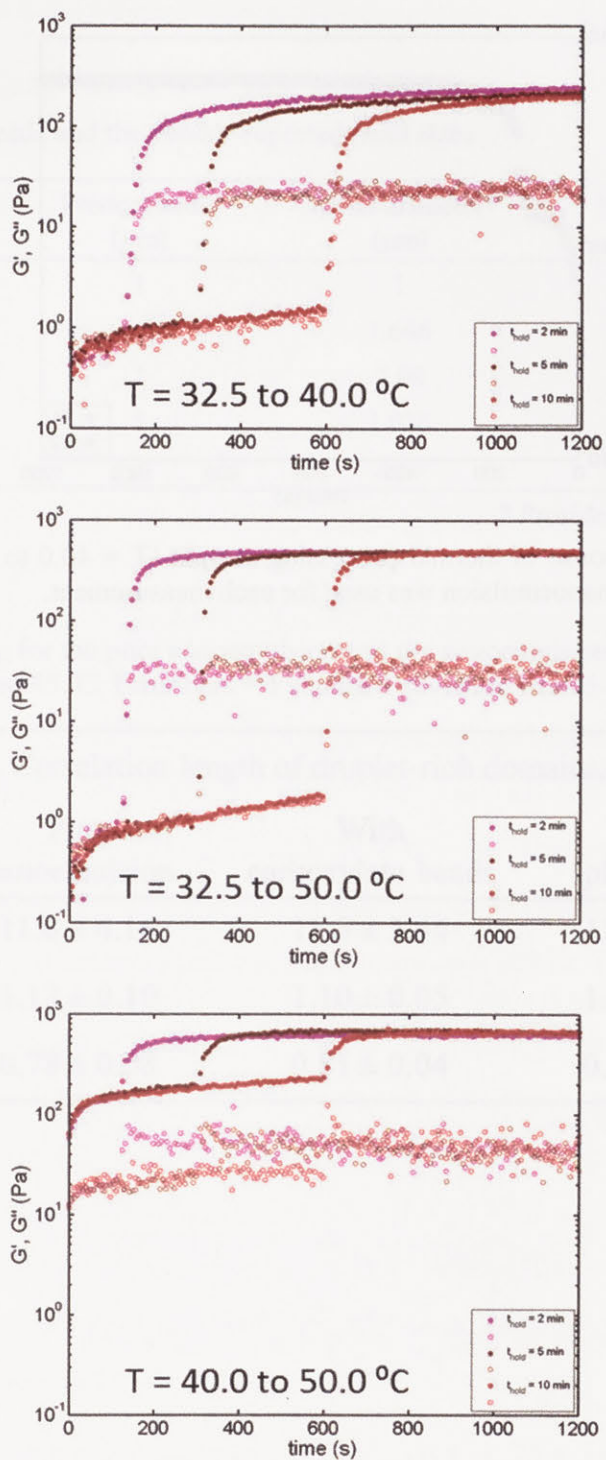
Figure D10 Temporal viscoelastic moduli, G' (closed symbols) and G" (open symbols), of the nanoemulsion undergoing two-step temperature jump.
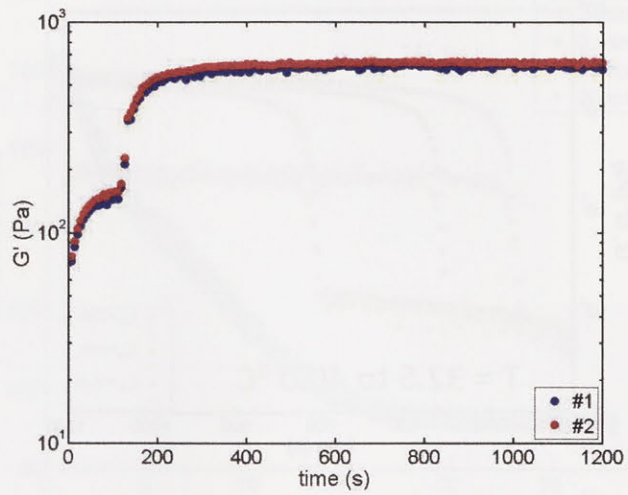
Figure D11 Rheological response of thermal processing sample (T = 40.0 to 50.0 °C, t_{hold} = 2 min) is reproducible. Freshly loaded nanoemulsion was used for each measurement.

Appendix E

Table E1 Static errors of beads and the vendor-reported bead sizes.

Bead type	Product name (μm)	Actual diameter* (μm)	Static error (μm²)
Carboxylate	1	1	2.5×10^{-5}
	1.5	1.646	2.2×10^{-5}
	2	2.08	1.8×10^{-5}
Plain	1	1.036	2.5×10^{-5}
	2	2.16	1.8×10^{-5}

* Provided by the vendor.

Table E2 Comparison of L_C for the pure nanoemulsion and the nanoemulsion mixed with carboxylate and plain beads at T = 35, 40 and 45 °C. Error bars = 1 standard deviation from 5-8 images.

T (°C)	Correlation length of droplet-rich domains, L_C (μm)		
	Pure nanoemulsion	With carboxylate beads	With plain beads
35	11.0 ± 4.16	11.3 ± 3.94	11.3 ± 3.94
40	1.13 ± 0.10	1.10 ± 0.05	1.11 ± 0.05
45	0.78 ± 0.08	0.81 ± 0.04	0.80 ± 0.05

Schematic of the chamber for particle tracking experiments

Fig. E1 shows the detailed dimensions of the custom-built chamber used in particle tracking. The temperature difference is $\leq 0.2\ ^\circ C$ across the chamber (blue region) when mounting on the heating stage which controls the temperature of the sample.
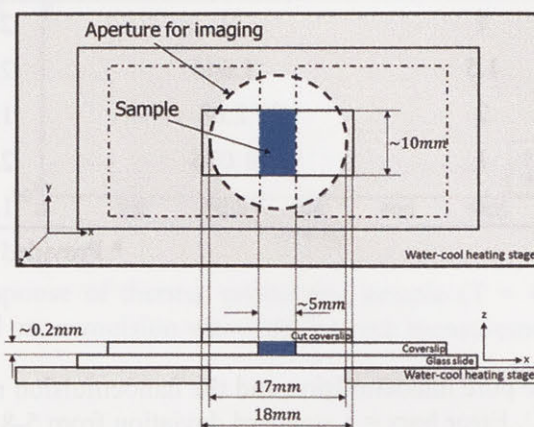
Figure E1 Schematic of the chamber for particle tracking. The slides are stuck by the UV-curing glue. After the sample is loaded, both ends are sealed by epoxy glue. Dimensions are indicated.

Viscoelastic moduli of the nanoemulsion after the temperature is jump to 30 °C

Fig. E2 shows the G' and G'' of the nanoemulsion after the temperature is jumped to 30 °C at the beginning of the measurement (t = 0). The moduli do not change over a wide period of time for at least 20 minutes.
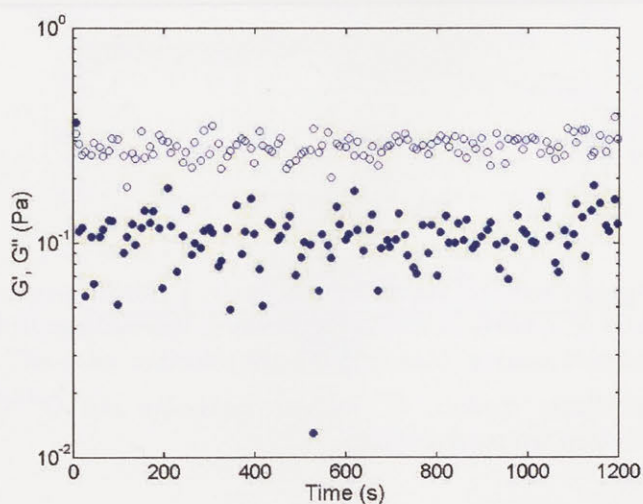
Figure E2 Viscoelastic moduli of the nanoemulsion after T is jumped to 30 °C at t = 0. The moduli do not change for at least 20 min. The rheometer parameters: $\gamma = 0.05\%$, $\omega = 20$ rad/s.

Measuring L_C, L_{rich} and L_{poor} using ImageJ software

Fig. E3 shows an example of how L_C is determined from confocal images. First, the fast Fourier transform (FFT) is applied to the image to obtain the scattered light intensity profile in q-space. Then, the radially averaged light intensity I(q) of the processed image is calculated, where q is the wave vector. Finally, we computed the correlation length as $L_C = 2\pi/q_{max}$, where q_{max} is the wave vector of the maximum averaged light intensity.

Fig. E4 shows an example of how L_{rich} is calculated from a 2D confocal image using the image processing software ImageJ. First, the image is processed with a built-in function "Threshold" that allows the objects of interest (here, the droplet-rich domains) to be distinguished from the background. Second, this processed image is analyzed by the built-in function "Analyze particles" that outlines detected objects. We then use ImageJ to calculate the Feret diameter. The Feret diameter is defined as the distance between any two parallel lines that are tangential to the outline of a 2D object, as shown in Fig. E4. We use the minimum Feret diameter, the smallest distance between two tangential lines, for defining L_{rich}. Finally, we set the averaged minimum Feret diameter of the detected objects to be L_{rich}. We chose to use the minimum Feret diameter to define L_{rich} since the gelled structure resembles percolated strands of clustered droplets and this measure would most closely correlate to the strand width.

A similar procedure is performed for L_{poor}. However, the white/black values of raw 2D images were first inverted before thresholding. This step allows the droplet-poor domains (i.e. the dark regions in the original images) to be the objects of interest. After this step, the same procedure as described above is applied to obtain L_{poor}. However, at T = 30.0 to 35.0 °C, due to the lack of isolated droplet-poor domains, L_{poor} was computed by measuring the separation distance between two near droplet-rich domains (Fig. E5 for an example). At least 50 measurements of distance were obtained at each temperature.

An additional step is performed for computing L_{rich} at T = 32.5 and 35.0 °C. At these two temperatures, the histogram of sizes of droplet-rich domains has a bimodal distribution with a local minimum in the probability distribution at 2 μm, distinguishing the two populations. This bimodal distribution can qualitatively be seen in Fig. 6.2 in Chapter 6. Therefore, for these two temperatures we calculate and report two averaged minimum Feret diameters.
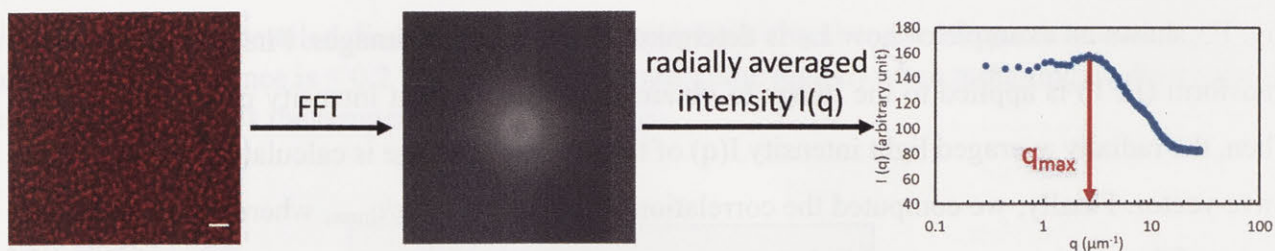
Figure E3 Procedure to determine L_C using the software ImageJ. Scale bar = 5µm.
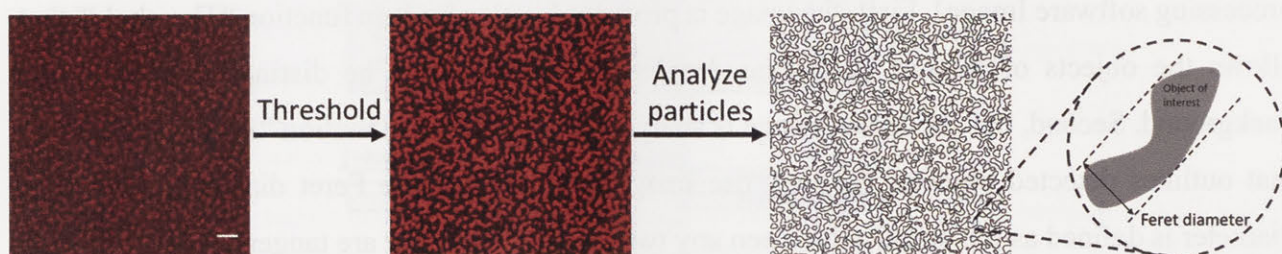
Figure E4 Procedure to determine L_{rich} using the software ImageJ. Scale bar = 5µm.
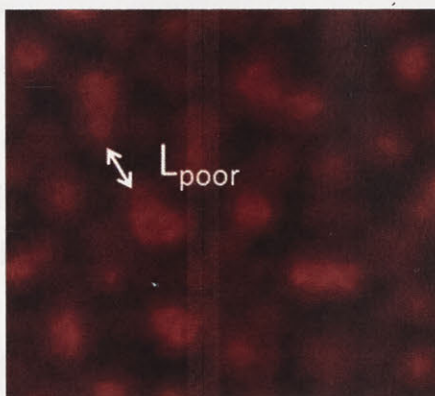
Figure E5 Determine L_{poor} by measuring the separation distance between two nearby droplet-rich domains.

Nanoemulsion mixed with probes at higher bead concentration

In the main text, the bead volume fraction was kept ≈ 0.02 % to minimize influence of beads on the nanoemulsion. Here, we increase the bead volume fraction to 0.08 % to have a larger ensemble to show the selectivity of beads residing in the droplet-rich and droplet-poor phases is controllable.

198

The results are shown in Fig. E6. The carboxylate beads are still in the droplet-poor phase and the plain beads are in the droplet-rich phase.
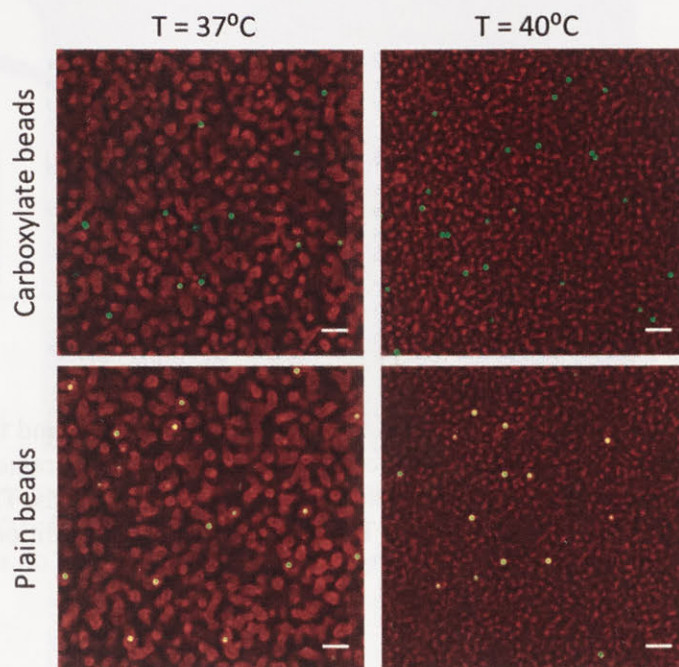
Figure E6 Representative confocal images of the nanoemulsion mixed with particle tracking beads at higher bead volume fractions (0.08%). Carboxylate beads still reside in the droplet-poor phase and plain beads still reside in the droplet-rich phase. Diameter of droplets = 55 nm. Scale bars = 5 μm.

Addition of beads has negligible influence on the nanoemulsion bulk rheology

As shown in Fig. 6.3, the nanoemulsion microstructures are not influenced by the addition of beads. To further verify the argument, we measured the temperature-ramp viscoelasticity. The results are shown in Fig. E7. Comparing to the pure nanoemulsion, the addition of beads has negligible effect on the nanoemulsion rheology, no matter the surface chemistry and size of the beads.
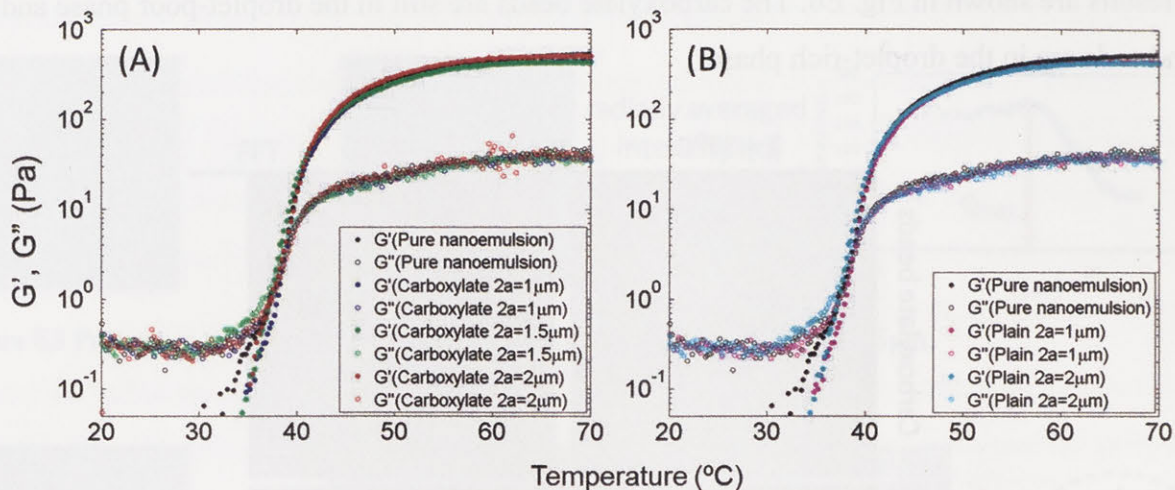
Figure E7 Temperature-ramp viscoelastic moduli of the pure nanoemulsion and the nanoemulsion mixed with beads of different sizes and different surface chemistries. Rheometer parameters: $\gamma = 0.05\%$, $\omega = 20$ rad/s and $\Delta T = 2$ °C/s. The beads are (A) carboxylate beads and (B) plain beads. The bead concentration is the same as in the MPT experiment (≈ 0.02 % v/v). The data shows that the addition of beads has negligible effect on the nanoemulsion rheology.

Plain beads do not induce droplet aggregation

Plain beads associating with colloid-rich phase introduces an interesting question whether plain beads serve as nucleation sites for droplet aggregation. To investigate this, we design an experiment that we mixed the plain beads with the nanoemulsion at lower oil volume fraction (= 0.05). At this oil loading, the nanoemulsion shows various microstructures at high temperatures. The result is shown in Fig. E8. As can be seen, the nanoemulsion shows various droplet aggregations and plain beads can reside in each of them. The droplet-rich region associating with plain beads do not show a regular pattern.

200
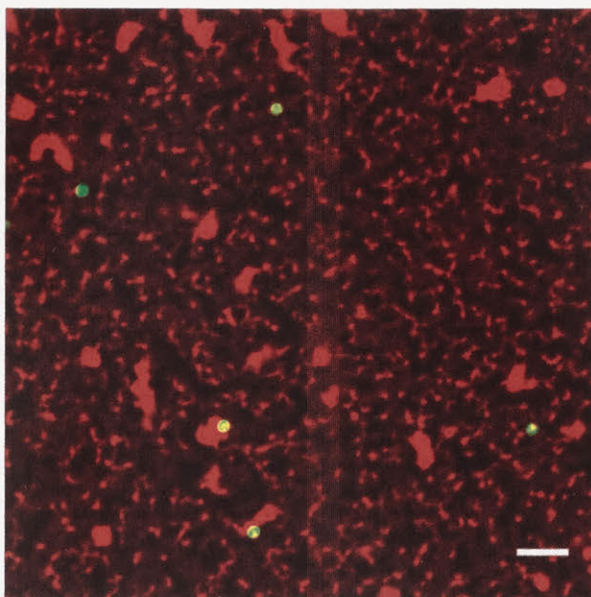
Figure E8 Confocal microscopy images of the nanoemulsion at $\phi = 0.05$ mixed with plain beads with diameter = 1 μm at 40 °C. Plain beads can reside in various droplet-rich regions, which supports the statement that plain beads do not induce the droplet aggregation. Scale bar = 5 μm.

Viscosity of continuous phase as a function of temperature
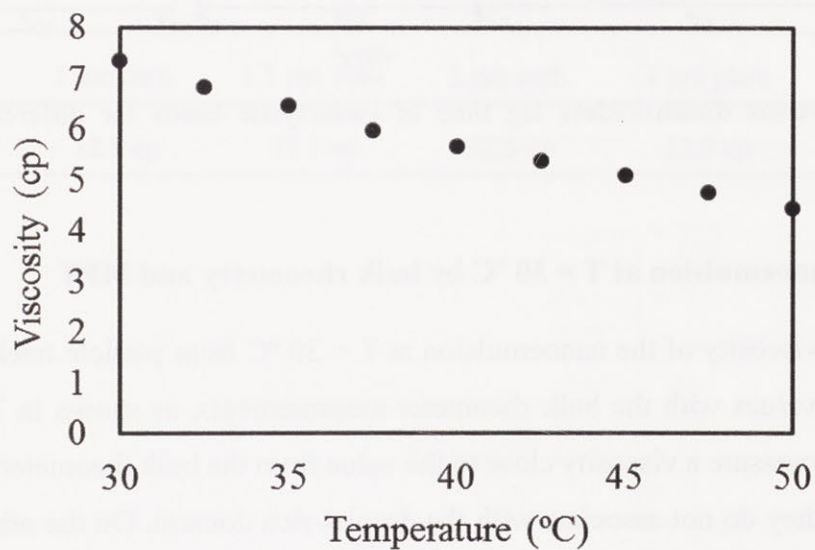
Figure E9 Viscosity of the aqueous continuous phase (P = 0.33, [SDS] = 0.175M) as a function of temperature. The viscosity decreases as T increases.

Plot of MSD versus dimensionless lag time for carboxylate beads

To examine the role of the continuous phase viscosity on the MSDs of carboxylate beads, we normalized the lag times by D/a^2 where D is the bead diffusion coefficient in the continuous phase. We used the Stokes-Einstein relation to obtain D, and viscosities of the continuous phase from Fig. E9. For 1 μm and 1.5 μm beads, the MSDs are collapsed at $T = 30.0$ to 37.5 °C, which supports the claim that the initial increase in MSDs in Fig. 6.7 is due to the viscosity decrease of the continuous phase. This collapse does not hold when the confinement from the droplet-rich phase becomes significant when the temperature is increased, and when the size of beads is close to the size of droplet-poor phase.
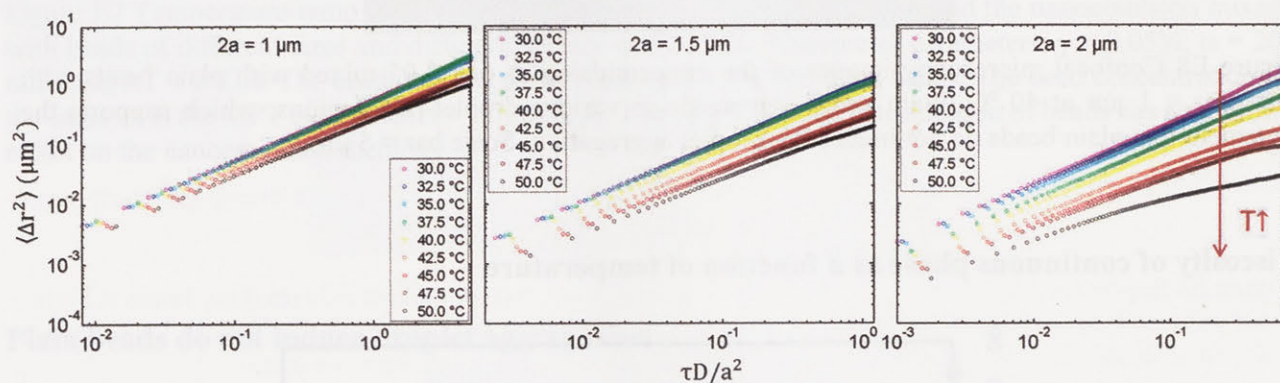
Figure E10 MSD versus dimensionless lag time of carboxylate beads for different sizes at rising temperatures.

Viscosity of the nanoemulsion at T = 30 °C by bulk rheometry and MPT

We calculated the viscosity of the nanoemulsion at $T = 30$ °C from particle tracking of all beads and compared the values with the bulk rheometer measurements, as shown in Table E3 below. Carboxylate beads measure a viscosity close to the value from the bulk rheometer, which supports our argument that they do not associate with the droplet-rich domain. On the other hand, a more viscous fluid is measured by the 1 μm plain beads, and an even higher viscosity is obtained with the 2 μm plain beads. We calculated the effective plain bead size by using the viscosities in Table E3 and the Stokes-Einstein relation:

$$D = \frac{k_B T}{6\pi\eta a},$$

where k_B is Boltzmann constant, T is the absolute temperature, η is the viscosity and a is the radius of the beads. From the diffusion coefficient obtained in MPT, one can either calculate the viscosity assuming a known probe size (Table E3), or calculate the effective probe size assuming a known viscosity. To calculate the effective probe size, we used the viscosity measured by bulk rheometry (12.7 cp).

The effective diameter is 1.13 μm for 1 μm plain beads (actual vendor-reported diameter = 1.036 μm, Table E1), and 2.87 μm for 2 μm plain beads (actual vendor-reported diameter = 2.16 μm, Table E1). There are two factors that can contribute to the increased effective size. First, the clusters associate with the plain beads due to the PEGDA bridging as discussed in Chapter 6, and the larger beads have more association due to a larger surface area. Second, droplets can form layers on beads or beads reside in the larger clusters in the nanoemulsions at T = 30 °C. Nonetheless, the data shown here again suggests the plain beads associate with the droplet-rich domains in the nanoemulsion.

Table E3 Viscosity of the nanoemulsion at T = 30 °C as measured by bulk rheometry and MPT.

Rheometer	1 μm carb.	1.5 μm carb.	2 μm carb.	1 μm plain	2 μm plain
12.7 cp	12.9 cp	13.1 cp	12.6 cp	13.9 cp	16.8 cp

Viscoelasticity of the nanoemulsions by MPT
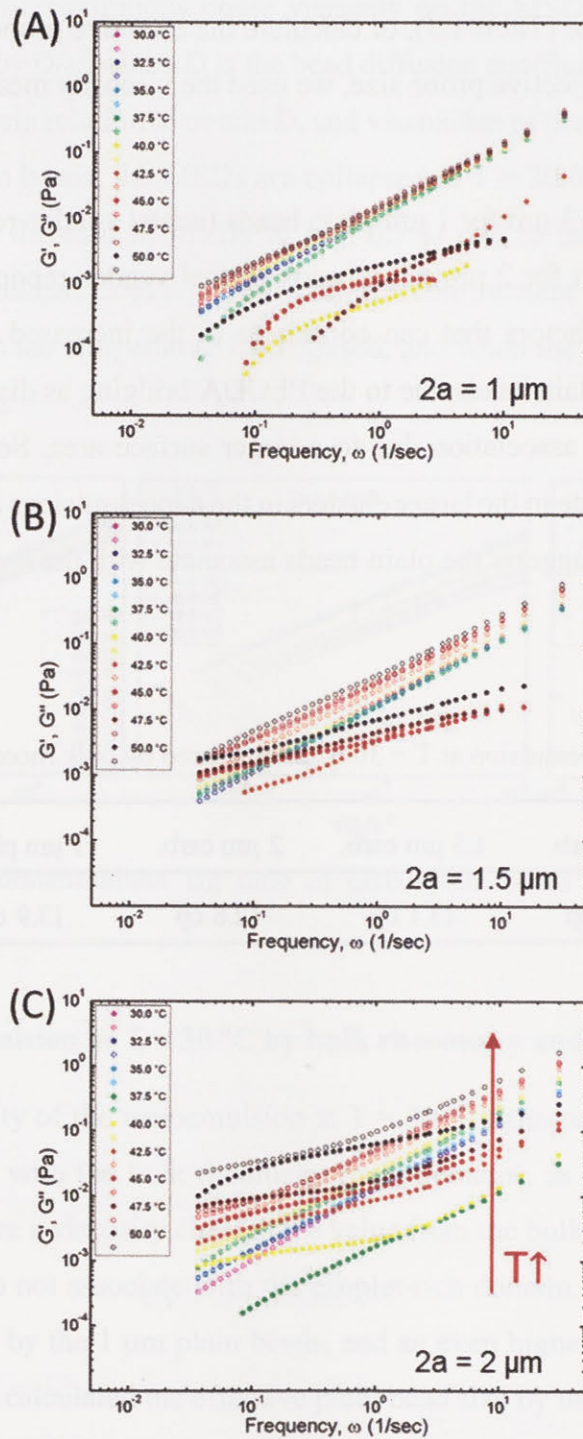
Figure E11 Viscoelastic moduli calculated from MSDs in Fig. 6.7 (carboxylate beads) by using the generalized Stokes-Einstein relation. The diameters of probes are (A) 1 μm, (B) 1.5 μm and (C) 2 μm. Filled symbols: G' and open symbols: G".
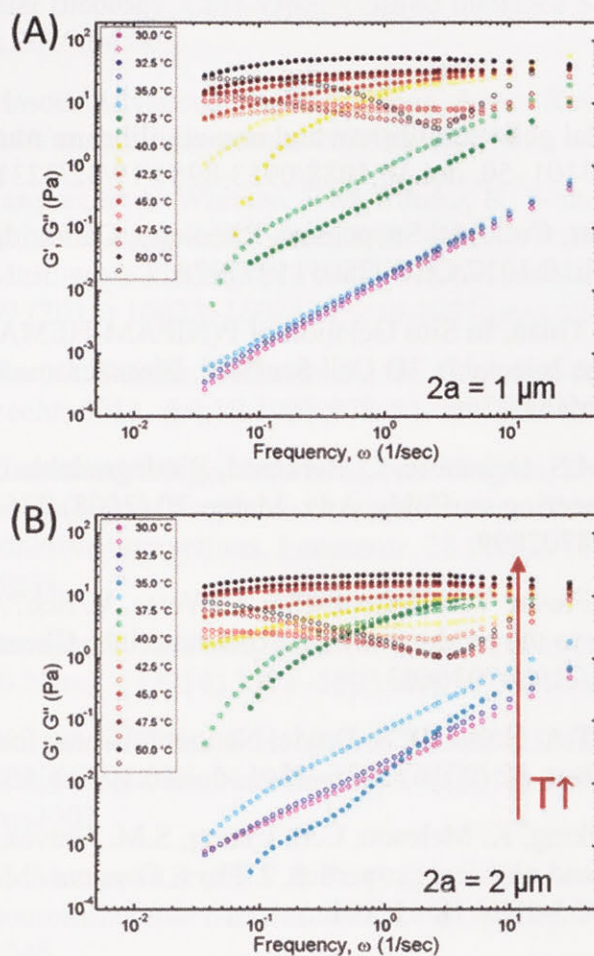
Figure E12 Viscoelastic moduli calculated from MSDs in Fig. 6.9 (plain beads) by using the generalized Stokes-Einstein relation. The diameters of probes are (A) 1 μm and (B) 2 μm. Filled symbols: G' and open symbols: G".
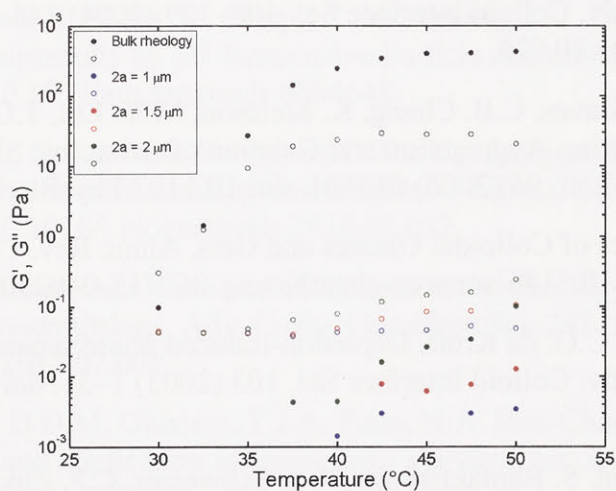
Figure E13 Comparison of the viscoelastic moduli from bulk rheology and microrheology using carboxylate beads at frequency ω = 20 rad/s. Filled symbols = G'; open symbols = G".

205

Bibliography

[1]   E. Zaccarelli, Colloidal gels: equilibrium and non-equilibrium routes, J. Phys. Condens. Matter. 19 (2007) 323101–50. doi:10.1088/0953-8984/19/32/323101.

[2]   J. Mewis, N.J. Wagner, Colloidal Suspension Rheology, Cambridge University Press, Cambridge, 2011. doi:10.1017/CBO9780511977978.

[3]   T. Gan, Y. Zhang, Y. Guan, In Situ Gelation of P(NIPAM-HEMA) Microgel Dispersion and Its Applications as Injectable 3D Cell Scaffold, Biomacromolecules. 10 (2009) 1410–1415. doi:10.1021/bm900022m.

[4]   Q. Wang, L. Wang, M.S. Detamore, C. Berkland, Biodegradable colloidal gels as moldable tissue engineering scaffolds, Adv. Mater. 20 (2008) 236–239. doi:10.1002/adma.200702099.

[5]   D.F. Schmidt, C. Du Fresne Von Hohenesche, A. Weiss, V. Sch??dler, Colloidal gelation as a general approach to the production of porous materials, Chem. Mater. 20 (2008) 2851–2853. doi:10.1021/cm7036603.

[6]   A. Gupta, H.B. Eral, T.A. Hatton, P.S. Doyle, Nanoemulsions: formation, properties and applications, Soft Matter. 12 (2016) 2826–2841. doi:10.1039/C5SM02958A.

[7]   T.G. Mason, J.N. Wilking, K. Meleson, C.B. Chang, S.M. Graves, Nanoemulsions: formation, structure, and physical properties, J. Phys. Condens. Matter. 18 (2006) R635–R666. doi:10.1088/0953-8984/18/41/R01.

[8]   M.E. Helgeson, Colloidal behavior of nanoemulsions: Interactions, structure, and rheology, Curr. Opin. Colloid Interface Sci. 25 (2016) 39–50. doi:10.1016/j.cocis.2016.06.006.

[9]   O. Sonneville-Aubrun, J.-T. Simonnet, F. L'Alloret, Nanoemulsions: a new vehicle for skincare products, Adv. Colloid Interface Sci. 108–109 (2004) 145–149. doi:10.1016/j.cis.2003.10.026.

[10]   J.N. Wilking, S.M. Graves, C.B. Chang, K. Meleson, M.Y. Lin, T.G. Mason, Dense Cluster Formation during Aggregation and Gelation of Attractive Slippery Nanoemulsion Droplets, Phys. Rev. Lett. 96 (2006) 015501. doi:10.1103/PhysRevLett.96.015501.

[11]   Y.M. Joshi, Dynamics of Colloidal Glasses and Gels, Annu. Rev. Chem. Biomol. Eng. 5 (2014) 181–202. doi:10.1146/annurev-chembioeng-060713-040230.

[12]   R. Tuinier, J. Rieger, C.G. de Kruif, Depletion-induced phase separation in colloid-polymer mixtures, Adv. Colloid Interface Sci. 103 (2003) 1–31. doi:10.1016/S0001-8686(02)00081-7.

[13]   S.A. Shah, Y.-L. Chen, S. Ramakrishnan, K.S. Schweizer, C.F. Zukoski, Microstructure of dense colloid–polymer suspensions and gels, J. Phys. Condens. Matter. 15 (2003) 4751–4778. doi:10.1088/0953-8984/15/27/308.

[14]   L.C. Hsiao, S. Pradeep, Experimental synthesis and characterization of rough particles for

colloidal and granular rheology, Curr. Opin. Colloid Interface Sci. 43 (2019) 94–112. doi:10.1016/j.cocis.2019.04.003.

[15] M.M. Fryd, T.G. Mason, Advanced Nanoemulsions, Annu. Rev. Phys. Chem. 63 (2012) 493–518. doi:10.1146/annurev-physchem-032210-103436.

[16] J.W. Swan, P.A. Vasquez, P.A. Whitson, E.M. Fincke, K. Wakata, S.H. Magnus, F.D. Winne, M.R. Barratt, J.H. Agui, R.D. Green, N.R. Hall, D.Y. Bohman, C.T. Bunnell, A.P. Gast, E.M. Furst, Multi-scale kinetics of a field-directed colloidal phase transition, Proc. Natl. Acad. Sci. 109 (2012) 16023–16028. doi:10.1073/pnas.1206915109.

[17] H.N.W. Lekkerkerker, R. Tuinier, Colloids and the Depletion Interaction, Springer Netherlands, Dordrecht, 2011. doi:10.1007/978-94-007-1223-2.

[18] A.P.R. Eberle, R. Castañeda-Priego, J.M. Kim, N.J. Wagner, Dynamical arrest, percolation, gelation, and glass formation in model nanoparticle dispersions with thermoreversible adhesive interactions, Langmuir. 28 (2012) 1866–1878. doi:10.1021/la2035054.

[19] M. Grzelczak, J. Vermant, E.M. Furst, L.M. Liz-Marzán, Directed Self-Assembly of Nanoparticles, ACS Nano. 4 (2010) 3591–3605. doi:10.1021/nn100869j.

[20] L. Di Michele, F. Varrato, J. Kotar, S.H. Nathan, G. Foffi, E. Eiser, Multistep kinetic self-assembly of DNA-coated colloids, Nat. Commun. 4 (2013) 2007. doi:10.1038/ncomms3007.

[21] M.E. Helgeson, S.E. Moran, H.Z. An, P.S. Doyle, Mesoporous organohydrogels from thermogelling photocrosslinkable nanoemulsions, Nat. Mater. 11 (2012) 344–352. doi:10.1038/nmta3248.

[22] P.C. Hiemenz, R. Rajagopalan, Principles of Colloid and Surface Chemistry, CRC Press, Taylor & Francis Group, 6000 Broken Sound Parkway NW, Suite 300, Boca Raton, FL 33487-2742, 1997. doi:10.1201/9781315274287.

[23] T. Sekido, S. Wooh, R. Fuchs, M. Kappl, Y. Nakamura, H.-J. Butt, S. Fujii, Controlling the Structure of Supraballs by pH-Responsive Particle Assembly, Langmuir. 33 (2017) 1995–2002. doi:10.1021/acs.langmuir.6b04648.

[24] Q. Wang, J. Wang, Q. Lu, M.S. Detamore, C. Berkland, Injectable PLGA based colloidal gels for zero-order dexamethasone release in cranial defects, Biomaterials. 31 (2010) 4980–4986. doi:10.1016/j.biomaterials.2010.02.052.

[25] H.S. Kim, T.G. Mason, Advances and challenges in the rheology of concentrated emulsions and nanoemulsions, Adv. Colloid Interface Sci. 247 (2017) 397–412. doi:10.1016/j.cis.2017.07.002.

[26] M.N. Yukuyama, D.D.M. Ghisleni, T.J.A. Pinto, N.A. Bou-Chacra, Nanoemulsion: process selection and application in cosmetics - a review, Int. J. Cosmet. Sci. 38 (2016) 13–24. doi:10.1111/ics.12260.

[27] O. Sonneville-Aubrun, M.N. Yukuyama, A. Pizzino, Application of Nanoemulsions in Cosmetics, Elsevier Inc., 2018. doi:10.1016/B978-0-12-811838-2.00014-X.

[28] J.S. Komaiko, D.J. McClements, Formation of Food-Grade Nanoemulsions Using Low-Energy Preparation Methods: A Review of Available Methods, Compr. Rev. Food Sci. Food Saf. 15 (2016) 331–352. doi:10.1111/1541-4337.12189.

[29] H.B. Eral, M. O'Mahony, R. Shaw, B.L. Trout, A.S. Myerson, P.S. Doyle, Composite hydrogels laden with crystalline active pharmaceutical ingredients of controlled size and loading, Chem. Mater. 26 (2014) 6213–6220. doi:10.1021/cm502834h.

[30] V. Mahendran, J. Philip, An optical technique for fast and ultrasensitive detection of ammonia using magnetic nanofluids, Appl. Phys. Lett. 102 (2013). doi:10.1063/1.4792055.

[31] J.N. Wilking, C.B. Chang, M.M. Fryd, L. Porcar, T.G. Mason, Shear-Induced Disruption of Dense Nanoemulsion Gels, Langmuir. 27 (2011) 5204–5210. doi:10.1021/la200021r.

[32] Y. Gao, J. Kim, M.E. Helgeson, Microdynamics and arrest of coarsening during spinodal decomposition in thermoreversible colloidal gels, Soft Matter. 11 (2015) 6360–6370. doi:10.1039/C5SM00851D.

[33] L.C. Hsiao, A.Z.M. Badruddoza, L.-C. Cheng, P.S. Doyle, 3D Printing of Self-Assembling Thermoresponsive Nanoemulsions into Hierarchical Mesostructured Hydrogels, Soft Matter. 13 (2017) 921–929. doi:10.1039/C6SM02208A.

[34] A. Gupta, H.B. Eral, T.A. Hatton, P.S. Doyle, Controlling and predicting droplet size of nanoemulsions: scaling relations with experimental validation., Soft Matter. 12 (2016) 1452–1458. doi:10.1039/c5sm02051d.

[35] A. Gupta, V. Narsimhan, T.A. Hatton, P.S. Doyle, Kinetics of the Change in Droplet Size during Nanoemulsion Formation, Langmuir. 32 (2016) 11551–11559. doi:10.1021/acs.langmuir.6b01862.

[36] P. Fernandez, V. André, J. Rieger, A. Kühnle, Nano-emulsion formation by emulsion phase inversion, Colloids Surfaces A Physicochem. Eng. Asp. 251 (2004) 53–58. doi:10.1016/j.colsurfa.2004.09.029.

[37] C. Solans, I. Solé, Nano-emulsions: Formation by low-energy methods, Curr. Opin. Colloid Interface Sci. 17 (2012) 246–254. doi:10.1016/j.cocis.2012.07.003.

[38] A.H. Saberi, Y. Fang, D.J. McClements, Thermal reversibility of vitamin E-enriched emulsion-based delivery systems produced using spontaneous emulsification, Food Chem. 185 (2015) 254–260. doi:10.1016/j.foodchem.2015.03.080.

[39] A. Gupta, A.Z.M. Badruddoza, P.S. Doyle, A General Route for Nanoemulsion Synthesis Using Low-Energy Methods at Constant Temperature, Langmuir. 33 (2017) 7118–7123. doi:10.1021/acs.langmuir.7b01104.

[40] K. Bouchemal, S. Briançon, E. Perrier, H. Fessi, Nano-emulsion formulation using spontaneous emulsification: Solvent, oil and surfactant optimisation, Int. J. Pharm. 280 (2004) 241–251. doi:10.1016/j.ijpharm.2004.05.016.

[41] D. Morales, J.M. Gutiérrez, M.J. García-Celma, Y.C. Solans, A study of the relation between bicontinuous microemulsions and oil/water nano-emulsion formation, Langmuir.

19 (2003) 7196–7200. doi:10.1021/la0300737.

[42]   L.C. Peng, C.H. Liu, C.C. Kwan, K.F. Huang, Optimization of water-in-oil nanoemulsions by mixed surfactants, Colloids Surfaces A Physicochem. Eng. Asp. 370 (2010) 136–142. doi:10.1016/j.colsurfa.2010.08.060.

[43]   J. Feng, C. Solans, T.F. Tadros, J. Esquena, J.C. Dederen, N. Azemar, P. Izquierdo, M.J. Garcia, The influence of surfactant mixing ratio on nano-emulsion formation by the pit method, J. Colloid Interface Sci. 285 (2004) 388–394. doi:10.1016/j.jcis.2004.10.047.

[44]   E. Dickinson, M. Golding, M.J.W. Povey, Creaming and Flocculation of Oil-in-Water Emulsions Containing Sodium Caseinate, J. Colloid Interface Sci. 185 (1997) 515–529. doi:10.1006/jcis.1996.4605.

[45]   J. Bibette, D. Roux, F. Nallet, Depletion interactions and fluid-solid equilibrium in emulsions, Phys. Rev. Lett. 65 (1990) 2470–2473. doi:10.1103/PhysRevLett.65.2470.

[46]   V.V. Erramreddy, S. Tu, S. Ghosh, Rheological reversibility and long-term stability of repulsive and attractive nanoemulsion gels, RSC Adv. 7 (2017) 47818–47832. doi:10.1039/c7ra09605d.

[47]   S.S. Datta, D.D. Gerrard, T.S. Rhodes, T.G. Mason, D.A. Weitz, Rheology of attractive emulsions, Phys. Rev. E. 84 (2011) 041404. doi:10.1103/PhysRevE.84.041404.

[48]   E. Dickinson, M. Golding, Rheology of Sodium Caseinate Stabilized Oil-in-Water Emulsions, J. Colloid Interface Sci. 191 (1997) 166–176. doi:10.1006/jcis.1997.4939.

[49]   D.J. McClements, Ultrasonic determination of depletion flocculation in oil-in-water emulsions containing a non-ionic surfactant, Colloids Surfaces A Physicochem. Eng. Asp. 90 (1994) 25–35. doi:10.1016/0927-7757(94)02881-8.

[50]   L. Bécu, S. Manneville, A. Colin, Yielding and Flow in Adhesive and Nonadhesive Concentrated Emulsions, Phys. Rev. Lett. 96 (2006) 138302. doi:10.1103/PhysRevLett.96.138302.

[51]   V.V. Erramreddy, S. Ghosh, Influence of droplet size on repulsive and attractive nanoemulsion gelation, Colloids Surfaces A Physicochem. Eng. Asp. 484 (2015) 144–152. doi:10.1016/j.colsurfa.2015.07.027.

[52]   V.V. Erramreddy, S. Ghosh, Influence of emulsifier concentration on nanoemulsion gelation, Langmuir. 30 (2014) 11062–11074. doi:10.1021/la502733v.

[53]   K. Kadiya, S. Ghosh, Conversion of Viscous Oil-in-Water Nanoemulsions to Viscoelastic Gels upon Removal of Excess Ionic Emulsifier, Langmuir. 35 (2019) 17061–17074. doi:10.1021/acs.langmuir.9b02558.

[54]   A. Meller, J. Stavans, Stability of Emulsions with Nonadsorbing Polymers, Langmuir. 12 (1996) 301–304. doi:10.1021/la950440h.

[55]   A. Meller, T. Gisler, D.A. Weitz, J. Stavans, Viscoelasticity of Depletion-Induced Gels in Emulsion–Polymer Systems, Langmuir. 15 (1999) 1918–1922. doi:10.1021/la9812424.

[56]   S. Aben, C. Holtze, T. Tadros, P. Schurtenberger, Rheological Investigations on the

Creaming of Depletion-Flocculated Emulsions, Langmuir. 28 (2012) 7967–7975. doi:10.1021/la300221m.

[57]   U. Steiner, A. Meller, J. Stavans, Entropy Driven Phase Separation in Binary Emulsions, Phys. Rev. Lett. 74 (1995) 4750–4753. doi:10.1103/PhysRevLett.74.4750.

[58]   J. Philip, T. Jaykumar, P. Kalyanasundaram, B. Raj, O. Mondain-Monval, Effect of polymer-surfactant association on colloidal force, Phys. Rev. E. 66 (2002) 011406. doi:10.1103/PhysRevE.66.011406.

[59]   J. Philip, G.G. Prakash, T. Jaykumar, P. Kalyanasundaram, O. Mondain-Monval, B. Raj, Interaction between Emulsion Droplets in the Presence of Polymer–Surfactant Complexes, Langmuir. 18 (2002) 4625–4631. doi:10.1021/la0256477.

[60]   J. Kim, Y. Gao, C. Hebebrand, E. Peirtsegaele, M.E. Helgeson, Polymer–surfactant complexation as a generic route to responsive viscoelastic nanoemulsions, Soft Matter. 9 (2013) 6897–6910. doi:10.1039/c3sm50301a.

[61]   K.C. Tam, E. Wyn-Jones, Insights on polymer surfactant complex structures during the binding of surfactants to polymers as measured by equilibrium and structural techniques, Chem. Soc. Rev. 35 (2006) 693. doi:10.1039/b415140m.

[62]   R.D. Lundberg, F.E. Bailey, R.W. Callard, Interactions of inorganic salts with poly(ethylene oxide), J. Polym. Sci. Part A-1 Polym. Chem. 4 (1966) 1563–1577. doi:10.1002/pol.1966.150040620.

[63]   B. Cabane, R. Duplessix, Neutron scattering study of water-soluble polymers adsorbed on surfactant micelles, Colloids and Surfaces. 13 (1985) 19–33. doi:10.1016/0166-6622(85)80003-2.

[64]   S. Dai, K.C. Tam, Isothermal Titration Calorimetry Studies of Binding Interactions between Polyethylene Glycol and Ionic Surfactants, J. Phys. Chem. B. 105 (2001) 10759–10763. doi:10.1021/jp0110354.

[65]   L. Bernazzani, S. Borsacchi, D. Catalano, P. Gianni, V. Mollica, M. Vitelli, F. Asaro, L. Feruglio, On the Interaction of Sodium Dodecyl Sulfate with Oligomers of Poly(Ethylene Glycol) in Aqueous Solution, J. Phys. Chem. B. 108 (2004) 8960–8969. doi:10.1021/jp049673k.

[66]   R. Mészáros, I. Varga, T. Gilányi, Effect of Polymer Molecular Weight on the Polymer/Surfactant Interaction, J. Phys. Chem. B. 109 (2005) 13538–13544. doi:10.1021/jp051272x.

[67]   Y.J. Nikas, D. Blankschtein, Complexation of Nonionic Polymers and Surfactants in Dilute Aqueous Solutions, Langmuir. 10 (1994) 3512–3528. doi:10.1021/la00022a026.

[68]   R.D. Groot, Mesoscopic Simulation of Polymer–Surfactant Aggregation, Langmuir. 16 (2000) 7493–7502. doi:10.1021/la000010d.

[69]   A.M. Howe, A. Clarke, T.H. Whitesides, Viscosity of Emulsions of Polydisperse Droplets with a Thick Adsorbed Layer, Langmuir. 13 (1997) 2617–2626. doi:10.1021/la960871f.

[70] A.M. Howe, A.R. Pitt, Rheology and stability of oil-in-water nanoemulsions stabilised by anionic surfactant and gelatin 2) addition of homologous series of sugar-based co-surfactants, Adv. Colloid Interface Sci. 144 (2008) 30–37. doi:10.1016/j.cis.2008.08.004.

[71] S. Damodaran, K. Anand, Sulfhydryl–Disulfide Interchange-Induced Interparticle Protein Polymerization in Whey Protein-Stabilized Emulsions and Its Relation to Emulsion Stability, J. Agric. Food Chem. 45 (1997) 3813–3820. doi:10.1021/jf970319b.

[72] A. Caciagli, M. Zupkauskas, A. Levin, T.P.J. Knowles, C. Mugemana, N. Bruns, T. O'Neill, W.J. Frith, E. Eiser, DNA-Coated Functional Oil Droplets, Langmuir. 34 (2018) 10073–10080. doi:10.1021/acs.langmuir.8b01828.

[73] Y. Zhang, A. McMullen, L.-L. Pontani, X. He, R. Sha, N.C. Seeman, J. Brujic, P.M. Chaikin, Sequential self-assembly of DNA functionalized droplets, Nat. Commun. 8 (2017) 21. doi:10.1038/s41467-017-00070-0.

[74] M. Hadorn, E. Boenzli, K.T. Sorensen, H. Fellermann, P. Eggenberger Hotz, M.M. Hanczyc, Specific and reversible DNA-directed self-assembly of oil-in-water emulsion droplets, Proc. Natl. Acad. Sci. 109 (2012) 20320–20325. doi:10.1073/pnas.1214386109.

[75] W.B. Russel, D.A. Saville, W.R. Schowalter, Colloidal Dispersions, Cambridge University Press, Cambridge, 1989. doi:10.1017/CBO9780511608810.

[76] J. Bibette, T.G. Mason, H. Gang, D.A. Weitz, P. Poulin, Structure of adhesive emulsions, Langmuir. 9 (1993) 3352–3356. doi:10.1021/la00036a006.

[77] P. Poulin, J. Bibette, D.A. Weitz, From colloidal aggregation to spinodal decomposition in sticky emulsions, Eur. Phys. J. B. 7 (1999) 277–281. doi:10.1007/s100510050614.

[78] J. Bibette, T.G. Mason, Hu Gang, D.A. Weitz, Kinetically induced ordering in gelation of emulsions, Phys. Rev. Lett. 69 (1992) 981–984. doi:10.1103/PhysRevLett.69.981.

[79] A. Lozsan, Salt-induced fast aggregation of nano-emulsions: structural and kinetic scaling, Colloid Polym. Sci. 290 (2012) 1561–1566. doi:10.1007/s00396-012-2680-4.

[80] H. Casanova, E. Dickinson, Influence of Protein Interfacial Composition on Salt Stability of Mixed Casein Emulsions, J. Agric. Food Chem. 46 (1998) 72–76. doi:10.1021/jf970600q.

[81] A. Patel, N. Longmore, A. Mohanan, S. Ghosh, Salt and pH-Induced Attractive Interactions on the Rheology of Food Protein-Stabilized Nanoemulsions, ACS Omega. 4 (2019) 11791–11800. doi:10.1021/acsomega.8b03360.

[82] T.D. Dimitrova, F. Leal-Calderon, Bulk Elasticity of Concentrated Protein-Stabilized Emulsions, Langmuir. 17 (2001) 3235–3244. doi:10.1021/la001805n.

[83] T.D. Dimitrova, F. Leal-Calderon, Rheological properties of highly concentrated protein-stabilized emulsions, Adv. Colloid Interface Sci. 108–109 (2004) 49–61. doi:10.1016/j.cis.2003.10.002.

[84] A. Torcello-Gómez, M. Wulff-Pérez, M.J. Gálvez-Ruiz, A. Martín-Rodríguez, M. Cabrerizo-Vílchez, J. Maldonado-Valderrama, Block copolymers at interfaces:

Interactions with physiological media, Adv. Colloid Interface Sci. 206 (2014) 414–427. doi:10.1016/j.cis.2013.10.027.

[85]   M. Wulff-Pérez, A. Martín-Rodríguez, M.J. Gálvez-Ruiz, J. de Vicente, The effect of polymeric surfactants on the rheological properties of nanoemulsions, Colloid Polym. Sci. 291 (2013) 709–716. doi:10.1007/s00396-012-2780-1.

[86]   L. Alison, S. Menasce, F. Bouville, E. Tervoort, I. Mattich, A. Ofner, A.R. Studart, 3D printing of sacrificial templates into hierarchical porous materials, Sci. Rep. 9 (2019) 409. doi:10.1038/s41598-018-36789-z.

[87]   T.M. Squires, T.G. Mason, Fluid Mechanics of Microrheology, Annu. Rev. Fluid Mech. 42 (2010) 413–438. doi:10.1146/annurev-fluid-121108-145608.

[88]   J.P. Rich, G.H. McKinley, P.S. Doyle, Size dependence of microprobe dynamics during gelation of a discotic colloidal clay, J. Rheol. (N. Y. N. Y). 55 (2011) 273–299. doi:10.1122/1.3532979.

[89]   J. Bibette, Monodisperse ferrofluid emulsions, J. Magn. Magn. Mater. 122 (1993) 37–41. doi:10.1016/0304-8853(93)91034-5.

[90]   J. Liu, E.M. Lawrence, A. Wu, M.L. Ivey, G.A. Flores, K. Javier, J. Bibette, J. Richard, Field-Induced Structures in Ferrofluid Emulsions, Phys. Rev. Lett. 74 (1995) 2828–2831. doi:10.1103/PhysRevLett.74.2828.

[91]   R.N. Zia, B.J. Landrum, W.B. Russel, A micro-mechanical study of coarsening and rheology of colloidal gels: Cage building , cage hopping, and Smoluchowski's ratchet, J. Rheol. 58 (2014) 1121–1157. doi:10.1122/1.4892115.

[92]   V. Trappe, P. Sandkühler, Colloidal gels — Low-density disordered solid-like states, Curr. Opin. Colloid Interface Sci. 8 (2004) 494–500. doi:10.1016/j.cocis.2004.01.002.

[93]   T.A. Waigh, Microrheology of complex fluids, Reports Prog. Phys. 68 (2005) 685–742. doi:10.1088/0034-4885/68/3/R04.

[94]   W.M. Deen, Introduction to Chemical Engineering Fluid Mechanics, Cambridge University Press, 2016.

[95]   M. Rubinstein, R.H. Colby, Polymer Physics, Oxford University Press, 2003.

[96]   J. Kim, D. Merger, M. Wilhelm, M.E. Helgeson, Microstructure and nonlinear signatures of yielding in a heterogeneous colloidal gel under large amplitude oscillatory shear, J. Rheol. (N. Y. N. Y). 58 (2014) 1359–1390. doi:10.1122/1.4882019.

[97]   T.G. Mason, Estimating the viscoelastic moduli of complex fluids using the generalized Stokes-Einstein equation, Rheol. Acta. 39 (2000) 371–378. doi:10.1007/s003970000094.

[98]   M.E. Helgeson, Y. Gao, S.E. Moran, J. Lee, M. Godfrin, A. Tripathi, A. Bose, P.S. Doyle, Homogeneous percolation versus arrested phase separation in attractively-driven nanoemulsion colloidal gels, Soft Matter. 10 (2014) 3122–3133. doi:10.1039/c3sm52951g.

[99]   E. Dickinson, Stabilising emulsion-based colloidal structures with mixed food ingredients,

J. Sci. Food Agric. 93 (2013) 710–721. doi:10.1002/jsfa.6013.

[100] T. Gibaud, N. Mahmoudi, J. Oberdisse, P. Lindner, J.S. Pedersen, C.L.P. Oliveira, A. Stradner, P. Schurtenberger, New routes to food gels and glasses, Faraday Discuss. 158 (2012) 267. doi:10.1039/c2fd20048a.

[101] L.-C. Cheng, L.C. Hsiao, P.S. Doyle, Multiple particle tracking study of thermally-gelling nanoemulsions, Soft Matter. 13 (2017) 6606–6619. doi:10.1039/c7sm01191a.

[102] C. He, S.W. Kim, D.S. Lee, In situ gelling stimuli-sensitive block copolymer hydrogels for drug delivery, J. Control. Release. 127 (2008) 189–207. doi:10.1016/j.jconrel.2008.01.005.

[103] P.J. Lu, E. Zaccarelli, F. Ciulla, A.B. Schofield, F. Sciortino, D.A. Weitz, Gelation of particles with short-range attraction, Nature. 453 (2008) 499–503. doi:10.1038/nature06931.

[104] L.C. Hsiao, R.S. Newman, S.C. Glotzer, M.J. Solomon, Role of isostaticity and load-bearing microstructure in the elasticity of yielded colloidal gels, Proc. Natl. Acad. Sci. 109 (2012) 16029–16034. doi:10.1073/pnas.1206742109.

[105] L.-C. Cheng, P.D. Godfrin, J.W. Swan, P.S. Doyle, Thermal processing of thermogelling nanoemulsions as a route to tune material properties, Soft Matter. 14 (2018) 5604–5614. doi:10.1039/c8sm00814k.

[106] Z.M. Sherman, D. Ghosh, J.W. Swan, Field-Directed Self-Assembly of Mutually Polarizable Nanoparticles, Langmuir. 34 (2018) 7117–7134. doi:10.1021/acs.langmuir.8b01135.

[107] H. Hoekstra, J. Mewis, T. Narayanan, J. Vermant, Multi length scale analysis of the microstructure in sticky sphere dispersions during shear flow, Langmuir. 21 (2005) 11017–11025. doi:10.1021/la051488q.

[108] W.H. Shih, W.Y. Shih, S. Il Kim, J. Liu, I.A. Aksay, Scaling behavior of the elastic properties of colloidal gels, Phys. Rev. A. 42 (1990) 4772–4779. doi:10.1103/PhysRevA.42.4772.

[109] S. Lindman, I. Lynch, E. Thulin, H. Nilsson, K.A. Dawson, S. Linse, Systematic Investigation of the Thermodynamics of HSA Adsorption to N-tert-Butylacrylamide Copolymer Nanoparticles . Effects of Particle Size and Hydrophobicity, Nano Lett. 7 (2007) 914–920. doi:10.1021/nl062743.

[110] S. Paula, W. Sues, J. Tuchtenhagen, A. Blume, Thermodynamics of Micelle Formation as a Function of Temperature: A High Sensitivity Titration Calorimetry Study, J. Phys. Chem. 99 (1995) 11742–11751. doi:10.1021/j100030a019.

[111] H.H. Winter, F. Chambon, Analysis of Linear Viscoelasticity of a Crosslinking Polymer at the Gel Point, J. Rheol. (N. Y. N. Y). 30 (1986) 367–382. doi:10.1122/1.549853.

[112] F. Chambon, H.H. Winter, Linear Viscoelasticity at the Gel Point of a Crosslinking PDMS with Imbalanced Stoichiometry, J. Rheol. (N. Y. N. Y). 31 (1987) 683–697. doi:10.1122/1.549955.

[113] H.H. Winter, Gel Point, in: Encycl. Polym. Sci. Technol., John Wiley & Sons, Inc., Hoboken, NJ, USA, 2016: or. 1–15. doi:10.1002/0471440264.pst476.pub2.

[114] S.R. Bhatia, A. Mourchid, Gelation of Micellar Block Polyelectrolytes: Evidence of Glassy Behavior in an Attractive System, Langmuir. 18 (2002) 6469–6472. doi:10.1021/la025732e.

[115] C.G. Malmberg, A.A. Maryott, Dielectric constant of water from 0 to 100 C, J. Res. Natl. Bur. Stand. (1934). 56 (1956) 1. doi:10.6028/jres.056.001.

[116] R.J. Sengwa, K. Kaur, R. Chaudhary, Dielectric properties of low molecular weight poly(ethylene glycol)s, Polym. Int. 49 (2000) 599–608. doi:10.1002/1097-0126(200006)49:6<599::AID-PI425>3.0.CO;2-K.

[117] K. Arnold, A. Herrmann, L. Pratsch, K. Gawrisch, The dielectric properties of aqueous solutions of poly(ethylene glycol) and their influence on membrane structure, BBA - Biomembr. 815 (1985) 515–518. doi:10.1016/0005-2736(85)90381-5.

[118] S. Ramakrishnan, V. Gopalakrishnan, C.F. Zukoski, Clustering and Mechanics in Dense Depletion and Thermal Gels †, Langmuir. 21 (2005) 9917–9925. doi:10.1021/la050830w.

[119] S. Ramakrishnan, Y.-L. Chen, K.S. Schweizer, C.F. Zukoski, Elasticity and clustering in concentrated depletion gels, Phys. Rev. E. 70 (2004) 040401. doi:10.1103/PhysRevE.70.040401.

[120] Z.M. Sherman, J.W. Swan, Dynamic, Directed Self-Assembly of Nanoparticles via Toggled Interactions, ACS Nano. 10 (2016) 5260–5271. doi:10.1021/acsnano.6b01050.

[121] Z.M. Sherman, H. Rosenthal, J.W. Swan, Phase Separation Kinetics of Dynamically Self-Assembling Nanoparticles with Toggled Interactions, Langmuir. 34 (2018) 1029–1041. doi:10.1021/acs.langmuir.7b02902.

[122] S. Asakura, F. Oosawa, Interaction between particles suspended in solutions of macromolecules, J. Polym. Sci. 33 (1958) 183–192. doi:10.1002/pol.1958.1203312618.

[123] D.N. Petsev, N.D. Denkov, P.A. Kralchevsky, Flocculation of Deformable Emulsion Droplets, J. Colloid Interface Sci. 176 (1995) 201–213. doi:10.1006/jcis.1995.0023.

[124] G. Duplâtre, M.F. Ferreira Marques, M. da Graça Miguel, Size of Sodium Dodecyl Sulfate Micelles in Aqueous Solutions as Studied by Positron Annihilation Lifetime Spectroscopy, J. Phys. Chem. 100 (1996) 16608–16612. doi:10.1021/jp960644m.

[125] S.S. Shah, N.U. Jamroz, Q.M. Sharif, Micellization parameters and electrostatic interactions in micellar solution of sodium dodecyl sulfate (SDS) at different temperatures, 178 (2001) 199–206.

[126] K. Sainath, P. Ghosh, Stabilization of Silicone Oil-in-Water Emulsions by Ionic Surfactant and Electrolytes: The Role of Adsorption and Electric Charge at the Interface, Ind. Eng. Chem. Res. 52 (2013) 15808–15816. doi:10.1021/ie401490c.

[127] A. Koh, G. Gillies, J. Gore, B.R. Saunders, Flocculation and Coalescence of Oil-in-Water Poly(dimethylsiloxane) Emulsions, J. Colloid Interface Sci. 227 (2000) 390–397.

doi:10.1006/jcis.2000.6909.

[128] K.A. Whitaker, Z. Varga, L.C. Hsiao, M.J. Solomon, J.W. Swan, E.M. Furst, Colloidal gel elasticity arises from the packing of locally glassy clusters, Nat. Commun. 10 (2019) 2237. doi:10.1038/s41467-019-10039-w.

[129] F. Cardinaux, T. Gibaud, A. Stradner, P. Schurtenberger, Interplay between spinodal decomposition and glass formation in proteins exhibiting short-range attractions, Phys. Rev. Lett. 99 (2007) 1–4. doi:10.1103/PhysRevLett.99.118301.

[130] Y.L. Chen, K.S. Schweizer, Microscopic theory of gelation and elasticity in polymer-particle suspensions, J. Chem. Phys. 120 (2004) 7212–7222. doi:10.1063/1.1683077.

[131] D.J. McClements, E. Dickinson, S.R. Dungan, J.E. Kinsella, J.G. Ma, M.J.W. Povey, Effect of Emulsifier Type on the Crystallization Kinetics of Oil-in-Water Emulsions Containing a Mixture of Solid and Liquid Droplets, J. Colloid Interface Sci. 160 (1993) 293–297. doi:10.1006/jcis.1993.1399.

[132] H. Lee, R.M. Venable, A.D. MacKerell, R.W. Pastor, Molecular dynamics studies of polyethylene oxide and polyethylene glycol: Hydrodynamic radius and shape anisotropy, Biophys. J. 95 (2008) 1590–1599. doi:10.1529/biophysj.108.133025.

[133] N. Anton, J.-P. Benoit, P. Saulnier, Design and production of nanoparticles formulated from nano-emulsion templates—A review, J. Control. Release. 128 (2008) 185–199. doi:10.1016/j.jconrel.2008.02.007.

[134] K. Landfester, Miniemulsion Polymerization and the Structure of Polymer and Hybrid Nanoparticles, Angew. Chemie Int. Ed. 48 (2009) 4488–4507. doi:10.1002/anie.200900723.

[135] D.J. McClements, Food Emulsions, CRC Press, 2015. doi:10.1201/b18868.

[136] V. Mahendran, J. Philip, Sensing of Biologically Important Cations Such as Na + , K + , Ca 2+ , Cu 2+ , and Fe 3+ Using Magnetic Nanoemulsions, Langmuir. 29 (2013) 4252–4258. doi:10.1021/la400502b.

[137] V. Mahendran, J. Philip, Non-enzymatic glucose detection using magnetic nanoemulsions, Appl. Phys. Lett. 105 (2014). doi:10.1063/1.4896522.

[138] L.-C. Cheng, Z.M. Sherman, J.W. Swan, P.S. Doyle, Colloidal Gelation through Thermally Triggered Surfactant Displacement, Langmuir. 35 (2019) 9464–9473. doi:10.1021/acs.langmuir.9b00596.

[139] S.M. Hashemnejad, A.Z.M. Badruddoza, B. Zarket, C. Ricardo Castaneda, P.S. Doyle, Thermoresponsive nanoemulsion-based gel synthesized through a low-energy process, Nat. Commun. 10 (2019) 2749. doi:10.1038/s41467-019-10749-1.

[140] E. Lee, B. Kim, Smart delivery system for cosmetic ingredients using pH-sensitive polymer hydrogel particles, Korean J. Chem. Eng. 28 (2011) 1347–1350. doi:10.1007/s11814-010-0509-8.

[141] J. Hu, H. Meng, G. Li, S.I. Ibekwe, A review of stimuli-responsive polymers for smart

textile applications, Smart Mater. Struct. 21 (2012). doi:10.1088/0964-1726/21/5/053001.

[142] N. Hashimah Alias, N. Aimi Ghazali, T. Amran Tengku Mohd, S. Adieb Idris, E. Yahya, N. Mohd Yusof, Nanoemulsion Applications in Enhanced Oil Recovery and Wellbore Cleaning: An Overview, Appl. Mech. Mater. 754–755 (2015) 1161–1168. doi:10.4028/www.scientific.net/amm.754-755.1161.

[143] L.C. Hsiao, P.S. Doyle, Celebrating Soft Matter's 10th Anniversary: Sequential phase transitions in thermoresponsive nanoemulsions, Soft Matter. 11 (2015) 8426–8431. doi:10.1039/C5SM01581B.

[144] J.C.-W. Lee, L. Porcar, S.A. Rogers, Unveiling Temporal Nonlinear Structure–Rheology Relationships under Dynamic Shearing, Polymers (Basel). 11 (2019) 1189. doi:10.3390/polym11071189.

[145] J.C.-W. Lee, K.M. Weigandt, E.G. Kelley, S.A. Rogers, Structure-Property Relationships via Recovery Rheology in Viscoelastic Materials, Phys. Rev. Lett. 122 (2019) 248003. doi:10.1103/PhysRevLett.122.248003.

[146] L. Kass, E.D. Cardenas-Vasquez, L.C. Hsiao, Composite double network hydrogels with thermoresponsive colloidal nanoemulsions, AIChE J. 65 (2019) 1–8. doi:10.1002/aic.16817.

[147] I. Solè, C.M. Pey, A. Maestro, C. González, M. Porras, C. Solans, J.M. Gutiérrez, Nano-emulsions prepared by the phase inversion composition method: Preparation variables and scale up, J. Colloid Interface Sci. 344 (2010) 417–423. doi:10.1016/j.jcis.2009.11.046.

[148] K. Sue, T. Usami, K. Arai, Determination of Acetic Acid Dissociation Constants to 400 °C and 32 MPa by Potentiometric pH Measurements, J. Chem. Eng. Data. 48 (2003) 1081–1084. doi:10.1021/je030142j.

[149] K. Sue, F. Ouchi, K. Minami, K. Arai, Determination of Carboxylic Acid Dissociation Constants to 350 °C at 23 MPa by Potentiometric pH Measurements, J. Chem. Eng. Data. 49 (2004) 1359–1363. doi:10.1021/je049923q.

[150] H.S. Harned, R.W. Ehlers, The Dissociation Constant of Propionic Acid from 0 to 60°, J. Am. Chem. Soc. 55 (1933) 2379–2383. doi:10.1021/ja01333a024.

[151] G.A. Poskrebyshev, P. Neta, R.E. Huie, Temperature Dependence of the Acid Dissociation Constant of the Hydroxyl Radical, J. Phys. Chem. A. 106 (2002) 11488–11491. doi:10.1021/jp020239x.

[152] V. Ferrari, D.J. Cutler, Temperature Dependence of the Acid Dissociation Constants of Chloroquine, J. Pharm. Sci. 76 (1987) 554–556. doi:10.1002/jps.2600760714.

[153] H. Bao, L. Li, L.H. Gan, H. Zhang, Interactions between Ionic Surfactants and Polysaccharides in Aqueous Solutions, Macromolecules. 41 (2008) 9406–9412. doi:10.1021/ma801957v.

[154] Y. Li, R. Xu, D.M. Bloor, J. Penfold, J.F. Holzwarth, E. Wyn-Jones, Moderation of the Interactions between Sodium Dodecyl Sulfate and Poly(vinylpyrrolidone) Using the Nonionic Surfactant Hexaethyleneglycol Mono- n -dodecyl Ether C 12 EO 6 : an

Electromotive Force, Microcalorimetry, and Small-Angle Neutron Scattering Study, Langmuir. 16 (2000) 8677–8684. doi:10.1021/la000292h.

[155] M. Almgren, J. Van Stam, C. Lindblad, P. Li, P. Stilbs, P. Bahadur, Aggregation of poly(ethylene oxide)-poly(propylene oxide)-poly(ethylene oxide) triblock copolymers in the presence of sodium dodecyl sulfate in aqueous solution, J. Phys. Chem. 95 (1991) 5677–5684. doi:10.1021/j100167a055.

[156] M. Bjoerling, G. Karlstroem, P. Linse, Conformational adaption of poly(ethylene oxide): A carbon-13 NMR study, J. Phys. Chem. 95 (1991) 6706–6709. doi:10.1021/j100170a060.

[157] W.F. Polik, W. Burchard, Static light scattering from aqueous poly(ethylene oxide) solutions in the temperature range 20-90°C, Macromolecules. 16 (1983) 978–982. doi:10.1021/ma00240a030.

[158] R. Kjellander, E. Florin, Water structure and changes in thermal stability of the system poly(ethylene oxide)–water, J. Chem. Soc. Faraday Trans. 1 Phys. Chem. Condens. Phases. 77 (1981) 2053. doi:10.1039/f19817702053.

[159] G. Karlstroem, A new model for upper and lower critical solution temperatures in poly(ethylene oxide) solutions, J. Phys. Chem. 89 (1985) 4962–4964. doi:10.1021/j100269a015.

[160] G. Karlstroem, A. Carlsson, B. Lindman, Phase diagrams of nonionic polymer-water systems: experimental and theoretical studies of the effects of surfactants and other cosolutes, J. Phys. Chem. 94 (1990) 5005–5015. doi:10.1021/j100375a045.

[161] S. Hocine, M.H. Li, Thermoresponsive self-assembled polymer colloids in water, Soft Matter. 9 (2013) 5839–5861. doi:10.1039/c3sm50428j.

[162] D. Hui, M. Nawaz, D.P. Morris, M.R. Edwards, B.R. Saunders, Study of pH-triggered heteroaggregation and gel formation within mixed dispersions, J. Colloid Interface Sci. 324 (2008) 110–117. doi:10.1016/j.jcis.2008.05.035.

[163] Y. Arai, H. Nakajima, K. Ohno, F. Application, P. Data, P. Examiner, A. Diamond, Emulsion for Hair Treatment, USOO5817155A, 1998.

[164] J. Tang, P.J. Quinlan, K.C. Tam, Stimuli-responsive Pickering emulsions: recent advances and potential applications, Soft Matter. 11 (2015) 3512–3529. doi:10.1039/C5SM00247H.

[165] T.P. Sari, B. Mann, R. Kumar, R.R.B. Singh, R. Sharma, M. Bhardwaj, S. Athira, Preparation and characterization of nanoemulsion encapsulating curcumin, Food Hydrocoll. 43 (2015) 540–546. doi:10.1016/j.foodhyd.2014.07.011.

[166] M. Rondón, P. Bouriat, J. Lachaise, J.-L. Salager, Breaking of Water-in-Crude Oil Emulsions. 1. Physicochemical Phenomenology of Demulsifier Action, Energy & Fuels. 20 (2006) 1600–1604. doi:10.1021/ef060017o.

[167] C.W. Angle, Y. Hua, Phase Separation and Interfacial Viscoelasticity of Charge-Neutralized Heavy Oil Nanoemulsions in Water, J. Chem. Eng. Data. 56 (2011) 1388–1396. doi:10.1021/je101162n.

[168] A.K. Fraga, L.F.I. Souza, J.R. Magalhães, C.R.E. Mansur, Development and evaluation of oil in water nanoemulsions based on polyether silicone as demulsifier and antifoam agents for petroleum, J. Appl. Polym. Sci. 131 (2014). doi:10.1002/app.40889.

[169] F. Shehzad, I.A. Hussein, M.S. Kamal, W. Ahmad, A.S. Sultan, M.S. Nasser, Polymeric Surfactants and Emerging Alternatives used in the Demulsification of Produced Water: A Review, Polym. Rev. 58 (2018) 63–101. doi:10.1080/15583724.2017.1340308.

[170] M.D. Seymour, Q. Fernando, Effect of Ionic Strength on Equilibrium Constants, J. Chem. Educ. 54 (1977) 225. doi:10.1021/ed054p225.

[171] C. Rey-Castro, R. Herrero, M.E. Sastre de Vicente, Gibbs–Donnan and specific-ion interaction theory descriptions of the effect of ionic strength on proton dissociation of alginic acid, J. Electroanal. Chem. 564 (2004) 223–230. doi:10.1016/j.jelechem.2003.10.023.

[172] M.E. Krahl, The Effect of Variation in Ionic Strength and Temperature on the Apparent Dissociation Constants of Thirty Substituted Barbituric Acids., J. Phys. Chem. 44 (1940) 449–463. doi:10.1021/j150400a010.

[173] D.A. Dikin, M. Mehta, C.W. Bark, C.M. Folkman, C.B. Eom, V. Chandrasekhar, Coexistence of Superconductivity and Ferromagnetism in Two Dimensions, Phys. Rev. Lett. 107 (2011) 056802. doi:10.1103/PhysRevLett.107.056802.

[174] M. Ataman, E.A. Boucher, Properties of aqueous salt solutions of poly(ethylene oxide), J. Polym. Sci. Polym. Phys. Ed. 20 (1982) 1585–1592. doi:10.1002/pol.1982.180200907.

[175] B. Briscoe, P. Luckham, S. Zhu, On the effects of water solvency towards non–ionic polymers, Proc. R. Soc. London. Ser. A Math. Phys. Eng. Sci. 455 (1999) 737–756. doi:10.1098/rspa.1999.0332.

[176] E.A. Boucher, P.M. Hines, Effects of inorganic salts on the properties of aqueous poly(ethylene oxide) solutions, J. Polym. Sci. Polym. Phys. Ed. 14 (1976) 2241–2251. doi:10.1002/pol.1976.180141209.

[177] K.P. Ananthapadmanabhan, E.D. Goddard, Aqueous biphase formation in polyethylene oxide-inorganic salt systems, Langmuir. 3 (1987) 25–31. doi:10.1021/la00073a005.

[178] A. Vintiloiu, J.C. Leroux, Organogels and their use in drug delivery - A review, J. Control. Release. 125 (2008) 179–192. doi:10.1016/j.jconrel.2007.09.014.

[179] E. Dickinson, Colloids in Food: Ingredients, Structure, and Stability, Annu. Rev. Food Sci. Technol. 6 (2015) 211–233. doi:10.1146/annurev-food-022814-015651.

[180] S. Asakura, F. Oosawa, On interaction between two bodies immersed in a solution of macromolecules, J. Chem. Phys. 22 (1954) 1255–1256. doi:10.1063/1.1740347.

[181] L.-C. Cheng, S.M. Hashemnejad, B. Zarket, S. Muthukrishnan, P.S. Doyle, Thermally and pH-responsive gelation of nanoemulsions stabilized by weak acid surfactants, J. Colloid Interface Sci. 563 (2020) 229–240. doi:10.1016/j.jcis.2019.12.054.

[182] A.G. Kanellopoulos, M.J. Owen, Adsorption of sodium dodecyl sulphate at the silicone

fluid/water interface, Trans. Faraday Soc. 67 (1971) 3127–3138. doi:10.1039/TF9716703127.

[183] P.N. Segrè, V. Prasad, A.B. Schofield, D.A. Weitz, Glasslike kinetic arrest at the colloidal-gelation transition, Phys. Rev. Lett. 86 (2001) 6042–6045. doi:10.1103/PhysRevLett.86.6042.

[184] W.D. Callister, D.G. Rethwisch, Materials science and engineering: An Introduction, 9. arg., John Wiley and Sons, 2013. doi:10.1126/science.8134833.

[185] M. Chen, Mechanical Behavior of Metallic Glasses: Microscopic Understanding of Strength and Ductility, Annu. Rev. Mater. Res. 38 (2008) 445–469. doi:10.1146/annurev.matsci.38.060407.130226.

[186] S. Nakamura, T. Mukai, M. Senoh, N. Iwasa, Thermal Annealing Effects on P-Type Mg-Doped GaN Films, Jpn. J. Appl. Phys. 31 (1992) 139–142.

[187] S. Malik, C. Roberts, R. Murray, M. Pate, Tuning self-assembled InAs quantum dots by rapid thermal annealing, Appl. Phys. Lett. 71 (1997) 1987–1989. doi:10.1063/1.119763.

[188] T. Kitatani, K. Nakahara, M. Kondow, K. Uomi, T. Tanaka, Mechanism analysis of improved GaInNAs optical properties through thermal annealing, J. Cryst. Growth. 209 (2000) 345–349. http://www.sciencedirect.com/science/article/pii/S0022024899005680.

[189] W. Prellier, A. Fouchet, B. Mercey, Oxide-diluted magnetic semiconductors: a review of the experimental status, J. Phys. Condens. Matter. 15 (2003) 1583–1601. doi:10.1088/0953-8984/15/37/R01.

[190] G. Ziegler, J. Heinrich, G. Wötting, Relationships between processing, microstructure and properties of dense and reaction-bonded silicon nitride, J. Mater. Sci. 22 (1987) 3041–3086. doi:10.1007/BF01161167.

[191] H. Chen, M.B. Müller, K.J. Gilmore, G.G. Wallace, D. Li, Mechanically strong, electrically conductive, and biocompatible graphene paper, Adv. Mater. 20 (2008) 3557–3561. doi:10.1002/adma.200800757.

[192] K. Kim, M.W. Schulze, A. Arora, R.M. Lewis III, M.A. Hillmyer, K.D. Dorfman, F.S. Bates, Thermal processing of diblock copolymer melts mimics metallurgy, Science (80-.). 356 (2017) 520–523.

[193] M.-S. She, T.-Y. Lo, R.-M. Ho, Long-range ordering of block copolymer cylinders driven by combining thermal annealing and substrate functionalization, ACS Nano. 7 (2013) 2000–2011. doi:10.1021/nn305725q.

[194] V. Olszowka, M. Hund, V. Kuntermann, S. Scherdel, L. Tsarkova, A. Böker, Electric field alignment of a block copolymer nanopattern: direct observation of the microscopic mechanism, ACS Nano. 3 (2009) 1091–1096. doi:10.1021/nn900081u.

[195] Y. Lu, Y. Zhang, G. Zhang, M. Yang, S. Yan, D. Shen, Influence of thermal processing on the perfection of crystals in polyamide 66 and polyamide 66/clay nanocomposites, Polymer (Guildf). 45 (2004) 8999–9009. doi:10.1016/j.polymer.2004.10.025.

[196] S.O. Lumsdon, E.W. Kaler, O.D. Velev, Two-Dimensional Crystallization of Microspheres by a Coplanar AC Electric Field, Langmuir. 20 (2004) 2108–2116. doi:10.1021/la035812y.

[197] J.W. Swan, J.L. Bauer, Y. Liu, E.M. Furst, Directed colloidal self-assembly in toggled magnetic fields, Soft Matter. 10 (2014) 1102–1109. doi:10.1039/C3SM52663A.

[198] M.B. Gordon, C.J. Kloxin, N.J. Wagner, The rheology and microstructure of an aging thermoreversible colloidal gel, J. Rheol. (N. Y. N. Y). 61 (2017) 23–34. doi:10.1122/1.4966039.

[199] Z.M. Sherman, H. Rosenthal, J.W. Swan, Phase separation kinetics of dynamically self-assembling nanoparticles with toggled interactions, Langmuir. (2017) acs.langmuir.7b02902. doi:10.1021/acs.langmuir.7b02902.

[200] E. Wetterskog, C. Jonasson, D.-M. Smilgies, V. Schaller, C. Johansson, P. Svedlindh, Colossal Anisotropy of the Dynamic Magnetic Susceptibility in Low-Dimensional Nanocube Assemblies, ACS Nano. (2018) acsnano.7b07745. doi:10.1021/acsnano.7b07745.

[201] C. Yilmaz, A. Sirman, A. Halder, A. Busnaina, High-Rate Assembly of Nanomaterials on Insulating Surfaces Using Electro-Fluidic Directed Assembly, ACS Nano. 11 (2017) 7679–7689. doi:10.1021/acsnano.6b07477.

[202] L. Lin, X. Peng, M. Wang, L. Scarabelli, Z. Mao, L.M. Liz-Marzán, M.F. Becker, Y. Zheng, Light-Directed Reversible Assembly of Plasmonic Nanoparticles Using Plasmon-Enhanced Thermophoresis, ACS Nano. 10 (2016) 9659–9668. doi:10.1021/acsnano.6b05486.

[203] H. Mehling, G. Hautzinger, O. Nilsson, J. Fricke, R. Hofmann, O. Hahn, Thermal diffusivity of semitransparent materials determined by the laser-flash method applying a new analytical model, Int. J. Thermophys. 19 (1998) 941–949. doi:10.1023/A:1022611527321.

[204] S. Wassén, N. Lorén, K. van Bemmel, E. Schuster, E. Rondeau, A.-M. Hermansson, Effects of confinement on phase separation kinetics and final morphology of whey protein isolate-gellan gum mixtures, Soft Matter. 9 (2013) 2738–2749. doi:10.1039/c2sm27804a.

[205] P.J. Lu, D.A. Weitz, Colloidal Particles : Crystals , Glasses , and Gels, Annu. Rev. Condens. Matter Phys. 4 (2013) 217–233. doi:10.1146/annurev-conmatphys-030212-184213.

[206] L. Cipelletti, L. Ramos, Slow dynamics in glasses, gels and foams, Curr. Opin. Colloid Interface Sci. 7 (2002) 228–234. doi:10.1016/S1359-0294(02)00051-1.

[207] L. Ramos, L. Cipelletti, Ultraslow Dynamics and Stress Relaxation in the Aging of a Soft Glassy System, Phys. Rev. Lett. 87 (2001) 245503. doi:10.1103/PhysRevLett.87.245503.

[208] O. Lieleg, J. Kayser, G. Brambilla, L. Cipelletti, A.R. Bausch, Slow dynamics and internal stress relaxation in bundled cytoskeletal networks, Nat. Mater. 10 (2011) 236–242. doi:10.1038/nmat2939.

[209] C.J. Dibble, M. Kogan, M.J. Solomon, Structure and dynamics of colloidal depletion gels: Coincidence of transitions and heterogeneity, Phys. Rev. E - Stat. Nonlinear, Soft Matter Phys. 74 (2006) 1–11. doi:10.1103/PhysRevE.74.041403.

[210] L.C. Hsiao, H. Kang, K.H. Ahn, M.J. Solomon, Role of shear-induced dynamical heterogeneity in the nonlinear rheology of colloidal gels, Soft Matter. 10 (2014) 9254–9259. doi:10.1039/C4SM01375A.

[211] Y. Guan, Y. Zhang, PNIPAM microgels for biomedical applications: from dispersed particles to 3D assemblies, Soft Matter. 7 (2011) 6375–6384. doi:10.1039/c0sm01541e.

[212] D. van den Ende, E.H. Purnomo, M.H.G. Duits, W. Richtering, F. Mugele, Aging in dense suspensions of soft thermosensitive microgel particles studied with particle-tracking microrheology, Phys. Rev. E - Stat. Nonlinear, Soft Matter Phys. 81 (2010) 1–9. doi:10.1103/PhysRevE.81.011404.

[213] L.H. Wong, N.A. Kurniawan, H.-P. Too, R. Rajagopalan, Spatially resolved microrheology of heterogeneous biopolymer hydrogels using covalently bound microspheres, Biomech. Model. Mechanobiol. 13 (2014) 839–849. doi:10.1007/s10237-013-0538-4.

[214] A. Kowalczyk, C. Oelschlaeger, N. Willenbacher, Visualization of micro-scale inhomogeneities in acrylic thickener solutions: A multiple particle tracking study, Polymer (Guildf). 58 (2015) 170–179. doi:10.1016/j.polymer.2014.12.041.

[215] C. Oelschlaeger, F. Bossler, N. Willenbacher, Synthesis, Structural and Micromechanical Properties of 3D Hyaluronic Acid-Based Cryogel Scaffolds, Biomacromolecules. 17 (2016) 580–589. doi:10.1021/acs.biomac.5b01529.

[216] T. Moschakis, Microrheology and particle tracking in food gels and emulsions, Curr. Opin. Colloid Interface Sci. 18 (2013) 311–323. doi:10.1016/j.cocis.2013.04.011.

[217] T. Moschakis, B.S. Murray, E. Dickinson, On the kinetics of acid sodium caseinate gelation using particle tracking to probe the microrheology, J. Colloid Interface Sci. 345 (2010) 278–285. doi:10.1016/j.jcis.2010.02.005.

[218] T. Moschakis, B.S. Murray, E. Dickinson, Particle Tracking Using Confocal Microscopy to Probe the Microrheology in a Phase-Separating Emulsion Containing Nonadsorbing Polysaccharide, Langmuir. 22 (2006) 4710–4719.

[219] T.G. Mason, K. Ganesan, J.H. van Zanten, D. Wirtz, S.C. Kuo, Particle Tracking Microrheology of Complex Fluids, Phys. Rev. Lett. 79 (1997) 3282–3285. doi:10.1103/PhysRevLett.79.3282.

[220] B.S. Chae, E.M. Furst, Probe surface chemistry dependence and local polymer network structure in F-actin microrheology, Langmuir. 21 (2005) 3084–3089. doi:10.1021/la0480890.

[221] B.R. Dasgupta, D.A. Weitz, Microrheology of cross-linked polyacrylamide networks, Phys. Rev. E - Stat. Nonlinear, Soft Matter Phys. 71 (2005) 1–9. doi:10.1103/PhysRevE.71.021504.

[222] Q. Lu, M.J. Solomon, Probe size effects on the microrheology of associating polymer solutions, Phys. Rev. E - Stat. Nonlinear, Soft Matter Phys. 66 (2002) 1–11. doi:10.1103/PhysRevE.66.061504.

[223] A. Maestro, L.J. Bonales, H. Ritacco, T.M. Fischer, R.G. Rubio, F. Ortega, Surface rheology: Macro- and microrheology of poly(tert-butyl acrylate) monolayers, Soft Matter. 7 (2011) 7761–7771. doi:10.1039/c1sm05225j.

[224] J.L. McGrath, J.H. Hartwig, S.C. Kuo, The mechanics of F-actin microenvironments depend on the chemistry of probing surfaces., Biophys. J. 79 (2000) 3258–3266. doi:10.1016/S0006-3495(00)76558-1.

[225] M.T. Valentine, Z.E. Perlman, M.L. Gardel, J.H. Shin, P. Matsudaira, T.J. Mitchison, D.A. Weitz, Colloid Surface Chemistry Critically Affects Multiple Particle Tracking Measurements of Biomaterials, Biophys. J. 86 (2004) 4004–4014. doi:10.1529/biophysj.103.037812.

[226] J.C. Crocker, D.G. Grier, Methods of Digital Video Microscopy for Colloidal Studies, J. Colloid Interface Sci. 179 (1996) 298–310. doi:10.1006/jcis.1996.0217.

[227] T. Savin, P.S. Doyle, Static and dynamic errors in particle tracking microrheology., Biophys. J. 88 (2005) 623–638. doi:10.1529/biophysj.104.042457.

[228] A. Kowalczyk, C. Oelschlaeger, N. Willenbacher, Tracking errors in 2D multiple particle tracking microrheology, Meas. Sci. Technol. 26 (2015) 1–15. doi:10.1088/0957-0233/26/1/015302.

[229] K.M. Schultz, E.M. Furst, Microrheology of biomaterial hydrogelators, Soft Matter. 8 (2012) 6198–6205. doi:10.1039/c2sm25187f.

[230] C.J. Rueb, C.F. Zukoski, Viscoelastic properties of colloidal gels, J. Rheol. (N. Y. N. Y). 41 (1997) 197–218. doi:10.1122/1.550812.

[231] P.D. Godfrin, N.E. Valadez-Pérez, R. Castañeda-Priego, N.J. Wagner, Y. Liu, Generalized phase behavior of cluster formation in colloidal dispersions with competing interactions, Soft Matter. 10 (2014) 5061–5071. doi:10.1039/C3SM53220H.

[232] S. Mossa, F. Sciortino, P. Tartaglia, E. Zaccarelli, Ground-state clusters for short-range attractive and long-range repulsive potentials, Langmuir. 20 (2004) 10756–10763. doi:10.1021/la048554t.

[233] J.C. Conrad, H.M. Wyss, V. Trappe, S. Manley, K. Miyazaki, L.J. Kaufman, A.B. Schofield, D.R. Reichman, D.A. Weitz, Arrested fluid-fluid phase separation in depletion systems: Implications of the characteristic length on gel formation and rheology, J. Rheol. (N. Y. N. Y). 54 (2010) 421–438. doi:10.1122/1.3314295.

[234] Y. Gao, M.E. Helgeson, Texture analysis microscopy: quantifying structure in low-fidelity images of dense fluids., Opt. Express. 22 (2014) 10046–63. doi:10.1364/OE.22.010046.

[235] N.W. Song, K.M. Park, I.-H. Lee, H. Huh, Uncertainty estimation of nanoparticle size distribution from a finite number of data obtained by microscopic analysis, Metrologia. 46 (2009) 480–488. doi:10.1088/0026-1394/46/5/012.

[236] H.G. Merkus, Particle Size Measurements: Fundamentals, Practice, Quality, Springer, 2009.

[237] R.A. Lauten, A.-L. Kjøniksen, B. Nyström, Adsorption and Desorption of Unmodified and Hydrophobically Modified Ethyl (hydroxyethyl) cellulose on Polystyrene Latex Particles in the Presence of Ionic Surfactants Using Dynamic Light Scattering, Langmuir. 16 (2000) 4478–4484.

[238] R.A. Lauten, A.-L. Kjøniksen, B. Nyström, Colloid polymer interactions and aggregation in aqueous mixtures of polystyrene latex, sodium dodecyl sulfate, and a hydrophobically modified polymer: A dynamic light scattering study, Langmuir. 17 (2001) 924–930. doi:10.1021/la001307e.

[239] M.A. Cohen-Stuart, Experimental aspects of polymer adsorption at solid/solution interfaces, Adv. Colloid Interface Sci. 24 (1986) 143–239.

[240] A. Courvoisier, F. Isel, J. François, M. Maaloum, End-adsorbed telechelic polymer chains at surfaces: Bridging and elasticity, Langmuir. 14 (1998) 3727–3729. doi:10.1021/la971041k.

[241] H. Bagger-Jörgensen, L. Coppola, K. Thuresson, U. Olsson, K. Mortensen, Phase Behavior, Microstructure, and Dynamics in a Nonionic Microemulsion on Addition of Hydrophobically End-Capped Poly(ethylene oxide), Langmuir. 13 (1997) 4204–4218. doi:10.1021/la010359g.

[242] E. Michel, M. Filali, R. Aznar, G. Porte, J. Appell, Percolation in a model transient network: Rheology and dynamic light scattering, Langmuir. 16 (2000) 8702–8711. doi:10.1021/la000317c.

[243] G. Porte, C. Ligoure, J. Appell, R. Aznar, Bridging interactions due to telechelic linkers balanced by screened Coulombic repulsions, J. Stat. Mech. Theory Exp. 2006 (2006) 1–14. doi:10.1088/1742-5468/2006/05/P05005.

[244] V. Testard, O. Julian, C. Ligoure, Monte Carlo simulations of colloidal pair potential induced by telechelic polymers: Statistics of loops and bridges, Macromolecules. 41 (2008) 7219–7226. doi:10.1021/ma8005813.

[245] S. Panmai, R.K. Prud'homme, D.G. Peiffer, Rheology of hydrophobically modified polymers with spherical and rod-like surfactant micelles, Colloids Surfaces A Physicochem. Eng. Asp. 147 (1999) 3–15. doi:10.1016/S0927-7757(98)00741-9.

[246] T. Savin, P.S. Doyle, Statistical and sampling issues when using multiple particle tracking, Phys. Rev. E - Stat. Nonlinear, Soft Matter Phys. 76 (2007) 1–15. doi:10.1103/PhysRevE.76.021501.

[247] I.Y. Wong, M.L. Gardel, D.R. Reichman, E.R. Weeks, M.T. Valentine, A.R. Bausch, D.A. Weitz, Anomalous diffusion probes microstructure dynamics of entangled F-actin networks, Phys. Rev. Lett. 92 (2004) 1–4. doi:10.1103/PhysRevLett.92.178101.

[248] R. Metzler, J.-H. Jeon, A.G. Cherstvy, E. Barkai, Anomalous diffusion models and their properties: non-stationarity, non-ergodicity, and ageing at the centenary of single particle tracking., Phys. Chem. Chem. Phys. 16 (2014) 24128–24164. doi:10.1039/c4cp03465a.

[249] J. He, J.X. Tang, Surface adsorption and hopping cause probe-size-dependent microrheology of actin networks, Phys. Rev. E - Stat. Nonlinear, Soft Matter Phys. 83 (2011) 1–13. doi:10.1103/PhysRevE.83.041902.

[250] M. Ehrenberg, J.L. McGrath, Binding between particles and proteins in extracts: Implications for microrheology and toxicity, Acta Biomater. 1 (2005) 305–315. doi:10.1016/j.actbio.2005.02.002.

[251] L.L. Josephson, E.M. Furst, W.J. Galush, Particle tracking microrheology of protein solutions, J. Rheol. (N. Y. N. Y). 60 (2016) 531–540. doi:10.1122/1.4948427.

[252] S.C. Glotzer, M.J. Solomon, Anisotropy of building blocks and their assembly into complex structures, Nat. Mater. 6 (2007) 557–562. doi:10.1038/nmat1949.

[253] A. Khademhosseini, R. Langer, Microengineered hydrogels for tissue engineering, Biomaterials. 28 (2007) 5087–5092. doi:10.1016/j.biomaterials.2007.07.021.

[254] M.P. Cuchiara, D.J. Gould, M.K. McHale, M.E. Dickinson, J.L. West, Integration of Self-Assembled Microvascular Networks with Microfabricated PEG-Based Hydrogels, Adv. Funct. Mater. 22 (2012) 4511–4518. doi:10.1002/adfm.201200976.

[255] L.A. Hockaday, K.H. Kang, N.W. Colangelo, P.Y.C. Cheung, B. Duan, E. Malone, J. Wu, L.N. Girardi, L.J. Bonassar, H. Lipson, C.C. Chu, J.T. Butcher, Rapid 3D printing of anatomically accurate and mechanically heterogeneous aortic valve hydrogel scaffolds, Biofabrication. 4 (2012) 035005. doi:10.1088/1758-5082/4/3/035005.

[256] C.-C. Lin, K.S. Anseth, PEG Hydrogels for the Controlled Release of Biomolecules in Regenerative Medicine, Pharm. Res. 26 (2009) 631–643. doi:10.1007/s11095-008-9801-2.

[257] J. Malda, J. Visser, F.P. Melchels, T. Jüngst, W.E. Hennink, W.J.A. Dhert, J. Groll, D.W. Hutmacher, 25th Anniversary Article: Engineering Hydrogels for Biofabrication, Adv. Mater. 25 (2013) 5011–5028. doi:10.1002/adma.201302042.

[258] B. V. Slaughter, S.S. Khurshid, O.Z. Fisher, A. Khademhosseini, N.A. Peppas, Hydrogels in Regenerative Medicine, Adv. Mater. 21 (2009) 3307–3329. doi:10.1002/adma.200802106.

[259] L.-W. Xia, R. Xie, X.-J. Ju, W. Wang, Q. Chen, L.-Y. Chu, Nano-structured smart hydrogels with rapid response and high elasticity, Nat. Commun. 4 (2013) 2226. doi:10.1038/ncomms3226.

[260] P.B. Welzel, J. Friedrichs, M. Grimmer, S. Vogler, U. Freudenberg, C. Werner, Cryogel Micromechanics Unraveled by Atomic Force Microscopy-Based Nanoindentation, Adv. Healthc. Mater. 3 (2014) 1849–1853. doi:10.1002/adhm.201400102.

[261] P.X. Ma, J.-W. Choi, Biodegradable Polymer Scaffolds with Well-Defined Interconnected Spherical Pore Network, Tissue Eng. 7 (2001) 23–33. doi:10.1089/107632701300003269.

[262] Y.-J. Lee, P.V. Braun, Tunable Inverse Opal Hydrogel pH Sensors, Adv. Mater. 15 (2003) 563–566. doi:10.1002/adma.200304588.

[263] A.N. Stachowiak, A. Bershteyn, E. Tzatzalos, D.J. Irvine, Bioactive Hydrogels with an

Ordered Cellular Structure Combine Interconnected Macroporosity and Robust Mechanical Properties, Adv. Mater. 17 (2005) 399–403. doi:10.1002/adma.200400507.

[264] M.N. Lee, A. Mohraz, Bicontinuous Macroporous Materials from Bijel Templates, Adv. Mater. 22 (2010) 4836–4841. doi:10.1002/adma.201001696.

[265] Y.S. Nam, T.G. Park, Porous biodegradable polymeric scaffolds prepared by thermally induced phase separation, J. Biomed. Mater. Res. 47 (1999) 8–17. doi:10.1002/(SICI)1097-4636(199910)47:1<8::AID-JBM2>3.0.CO;2-L.

[266] H. Diestra-Cruz, E. Bukusoglu, N.L. Abbott, A. Acevedo, Hierarchical Microstructures Formed by Bidisperse Colloidal Suspensions within Colloid-in-Liquid Crystal Gels, ACS Appl. Mater. Interfaces. 7 (2015) 7153–7162. doi:10.1021/am509008m.

[267] V.J. Anderson, H.N.W. Lekkerkerker, Insights into phase transition kinetics from colloid science, Nature. 416 (2002) 811–815. doi:10.1038/416811a.

[268] A. Sydney Gladman, E.A. Matsumoto, R.G. Nuzzo, L. Mahadevan, J.A. Lewis, Biomimetic 4D printing, Nat. Mater. 15 (2016) 413–418. doi:10.1038/nmat4544.

[269] J.R. Tumbleston, D. Shirvanyants, N. Ermoshkin, R. Janusziewicz, A.R. Johnson, D. Kelly, K. Chen, R. Pinschmidt, J.P. Rolland, A. Ermoshkin, E.T. Samulski, J.M. DeSimone, Continuous liquid interface production of 3D objects, Science (80-.). 347 (2015) 1349–1352. doi:10.1126/science.aaa2397.

[270] M.N. Cooke, J.P. Fisher, D. Dean, C. Rimnac, A.G. Mikos, Use of stereolithography to manufacture critical-sized 3D biodegradable scaffolds for bone ingrowth, J. Biomed. Mater. Res. 64B (2003) 65–69. doi:10.1002/jbm.b.10485.

[271] S.C. Ligon, B. Husár, H. Wutzel, R. Holman, R. Liska, Strategies to Reduce Oxygen Inhibition in Photoinduced Polymerization, Chem. Rev. 114 (2014) 557–589. doi:10.1021/cr3005197.

[272] D. Dendukuri, P. Panda, R. Haghgooie, J.M. Kim, T.A. Hatton, P.S. Doyle, Modeling of Oxygen-Inhibited Free Radical Photopolymerization in a PDMS Microfluidic Device, Macromolecules. 41 (2008) 8547–8556. doi:10.1021/ma801219w.

[273] D. Dendukuri, D.C. Pregibon, J. Collins, T.A. Hatton, P.S. Doyle, Continuous-flow lithography for high-throughput microparticle synthesis, Nat. Mater. 5 (2006) 365–369. doi:10.1038/nmat1617.

[274] K.J. LeBlanc, S.R. Niemi, A.I. Bennett, K.L. Harris, K.D. Schulze, W.G. Sawyer, C. Taylor, T.E. Angelini, Stability of High Speed 3D Printing in Liquid-Like Solids, ACS Biomater. Sci. Eng. 2 (2016) 1796–1799. doi:10.1021/acsbiomaterials.6b00184.

[275] B.G. Compton, J.A. Lewis, 3D-Printing of Lightweight Cellular Composites, Adv. Mater. 26 (2014) 5930–5935. doi:10.1002/adma.201401804.

[276] A.A. Pawar, G. Saada, I. Cooperstein, L. Larush, J.A. Jackman, S.R. Tabaei, N.-J. Cho, S. Magdassi, High-performance 3D printing of hydrogels by water-dispersible photoinitiator nanoparticles, Sci. Adv. 2 (2016) e1501381. doi:10.1126/sciadv.1501381.

[277] I. Pinnau, L.G. Toy, Gas and vapor transport properties of amorphous perfluorinated copolymer membranes based on 2,2-bistrifluoromethyl-4,5-difluoro-1,3-dioxole/tetrafluoroethylene, J. Memb. Sci. 109 (1996) 125–133. doi:10.1016/0376-7388(95)00193-X.

[278] T.C. Merkel, V.I. Bondar, K. Nagai, B.D. Freeman, I. Pinnau, Gas sorption, diffusion, and permeation in poly(dimethylsiloxane), J. Polym. Sci. Part B Polym. Phys. 38 (2000) 415–434. doi:10.1002/(SICI)1099-0488(20000201)38:3<415::AID-POLB8>3.0.CO;2-Z.

[279] J. Kim, M.E. Helgeson, Shear-induced clustering of Brownian colloids in associative polymer networks at moderate Péclet number, Phys. Rev. Fluids. 1 (2016) 043302. doi:10.1103/PhysRevFluids.1.043302.

[280] J. Nase, A. Lindner, C. Creton, Pattern Formation during Deformation of a Confined Viscoelastic Layer: From a Viscous Liquid to a Soft Elastic Solid, Phys. Rev. Lett. 101 (2008) 074503. doi:10.1103/PhysRevLett.101.074503.

[281] A.Z.M. Badruddoza, P.D. Godfrin, A.S. Myerson, B.L. Trout, P.S. Doyle, Core–Shell Composite Hydrogels for Controlled Nanocrystal Formation and Release of Hydrophobic Active Pharmaceutical Ingredients, Adv. Healthc. Mater. 5 (2016) 1960–1968. doi:10.1002/adhm.201600266.

[282] N. Doshi, B. Prabhakarpandian, A. Rea-Ramsey, K. Pant, S. Sundaram, S. Mitragotri, Flow and adhesion of drug carriers in blood vessels depend on their shape: A study using model synthetic microvascular networks, J. Control. Release. 146 (2010) 196–200. doi:10.1016/j.jconrel.2010.04.007.

[283] T.W. Sirk, K.S. Khare, M. Karim, J.L. Lenhart, J.W. Andzelm, G.B. McKenna, R. Khare, High strain rate mechanical properties of a cross-linked epoxy across the glass transition, Polymer (Guildf). 54 (2013) 7048–7057. doi:10.1016/j.polymer.2013.10.051.

[284] H.Z. An, M.E. Helgeson, P.S. Doyle, Nanoemulsion composite microgels for orthogonal encapsulation and release, Adv. Mater. 24 (2012) 3838–3844. doi:10.1002/adma.201200214.

[285] H.Z. An, E.R. Safai, H. Burak Eral, P.S. Doyle, Synthesis of biomimetic oxygen-carrying compartmentalized microparticles using flow lithography, Lab Chip. 13 (2013) 4765. doi:10.1039/c3lc50610j.

[286] R.O. Dunn, J.F. Scamehorn, S.D. Christian, Simultaneous removal of dissolved organics and divalent metal cations from water using micellar-enhanced ultrafiltration, Colloids and Surfaces. 35 (1989) 49–56. doi:10.1016/0166-6622(89)80317-8.

[287] C.A. Pons Siepermann, A.S. Myerson, Inhibition of Nucleation Using a Dilute, Weakly Hydrogen-Bonding Molecular Additive, Cryst. Growth Des. 18 (2018) 3584–3595. doi:10.1021/acs.cgd.8b00367.

[288] J.C. Martinez, J. Murciano-Calles, E. S., M. Iglesias-Bexiga, I. Luque, J. Ruiz-Sanz, Isothermal Titration Calorimetry: Thermodynamic Analysis of the Binding Thermograms of Molecular Recognition Events by Using Equilibrium Models, in: Appl. Calorim. a Wide Context - Differ. Scanning Calorimetry, Isothermal Titration Calorim.

Microcalorim., InTech, 2013. doi:10.5772/53311.

[289] H. Joshi, P.S. Shirude, V. Bansal, K.N. Ganesh, M. Sastry, Isothermal titration calorimetry studies on the binding of amino acids to gold nanoparticles, J. Phys. Chem. B. 108 (2004) 11535–11540. doi:10.1021/jp048766z.

[290] N. Welsch, Y. Lu, J. Dzubiella, M. Ballauff, Adsorption of proteins to functional polymeric nanoparticles, Polymer (Guildf). 54 (2013) 2835–2849. doi:10.1016/j.polymer.2013.03.027.

[291] P. Saha, S. Chowdhury, Insight Into Adsorption Thermodynamics, in: Thermodynamics, IntechOpen, 2011. doi:10.5772/13474.

[292] Y. Zeng, S. Grandner, C.L.P. Oliveira, A.F. Thünemann, O. Paris, J.S. Pedersen, S.H.L. Klapp, R. Von Klitzing, Effect of particle size and Debye length on order parameters of colloidal silica suspensions under confinement, Soft Matter. 7 (2011) 10899–10909. doi:10.5935/1984-6835.20120032.

[293] P. Attard, D. Antelmi, I. Larson, Comparison of the zeta potential with the diffuse layer potential from charge titration, Langmuir. 16 (2000) 1542–1552. doi:10.1021/la990487t.

[294] R. Sprycha, Electrical double layer at alumina/electrolyte interface. I. Surface charge and zeta potential, J. Colloid Interface Sci. 127 (1989) 1–11. doi:10.1016/0021-9797(89)90002-7.

[295] L. Rabinovich-Guilatt, P. Couvreur, G. Lambert, D. Goldstein, S. Benita, C. Dubernet, Extensive surface studies help to analyse zeta potential data: The case of cationic emulsions, Chem. Phys. Lipids. 131 (2004) 1–13. doi:10.1016/j.chemphyslip.2004.04.003.

[296] W.R. Gillap, N.D. Weiner, M. Gibaldi, Ideal behavior of sodium alkyl sulfates at various interfaces. Thermodynamics of adsorption at the oil-water interface, J. Phys. Chem. 72 (1968) 2222–2227. doi:10.1021/j100852a059.

[297] M.J. Moreno, M. Bastos, A. Velazquez-Campoy, Partition of amphiphilic molecules to lipid bilayers by isothermal titration calorimetry, Anal. Biochem. 399 (2010) 44–47. doi:10.1016/j.ab.2009.11.015.

[298] A. Tan, A. Ziegler, B. Steinbauer, J. Seelig, Thermodynamics of sodium dodecyl sulfate partitioning into lipid membranes, Biophys. J. 83 (2002) 1547–1556. doi:10.1016/S0006-3495(02)73924-6.